



VALIDATION AND APPLICATIONS OF THE MATERIAL POINT METHOD

Thesis submitted for the degree of

Doctor of Philosophy

At the University of Leicester

By

Ali Tabatabaeian Nimavardi

Department of Engineering

University of Leicester

July 2016

Abstract

The Material Point Method (MPM) is a modern finite element method that is classified as a point based method or meshless method, while it takes the advantage of two kinds of spatial discretisation that are based on an arbitrary Eulerian-Lagrangian description of motion. The referenced continuum is represented by the material points, and the motions are tracked through a computational background mesh, that is an arbitrary constant mesh which does not move the material. Hence, in the MPM mesh distortion especially in the large deformation analysis is naturally avoided.

However, MPM has been employed to simulate difficult problems in the literature, many are still unsatisfactory due to the lack of rigorous validation. Therefore, this thesis firstly provides a series of simple case studies which any numerical method must pass to test the validity of the MPM, and secondly demonstrate the capability of the MPM in simulating difficult problems such as degradation of highly swellable polymers during large swelling that is currently difficult to handle by the standard finite element method. Flory's theory is incorporated into the material point method to study large swelling of polymers, and degradation of highly swellable polymers is modelled by the MPM as a random phenomenon based on the normal distribution of the volumetric strain. These numerical developments represent adaptability of the MPM and enabling the method to be used in more complicated simulations. Furthermore, the advantages of this powerful numerical tool are studied in the modelling of an additive manufacturing technology called Selective Laser Melting (SLM). It is shown the MPM is an ideal numerical method to study SLM manufacturing technique. The focus of this thesis is to validate the MPM and exhibit the simplicity, strength, and accuracy of this numerical tool compared with standard finite element method for very complex problems which requires a complicated topological system.

Key words: Material Point Method (MPM), Non-uniform swelling, Selective Laser Melting (SLM), Degradation of highly swellable polymers

Acknowledgement

I would like to sincerely thank my supervisor, Professor Jingzhe Pan, for all his supports and extensive help during this Ph.D. He offered his time and support without any hesitation whenever it was needed. His amazing approach towards engineering problems and modelling were the most reliable source of help in this Ph.D. He has inspired me in many aspects with his kindness, knowledge and the friendliest way of communication. I much appreciate him for all of this wonderful help. I hope one day I return all these pleasant favours to the Ph.D. students of my own.

I also would like to thank my co-supervisor Dr. Csaba Sinka for his useful advice and supports. Supports from all the staffs as well as colleagues and friends are much respected.

I would like to gratefully acknowledge a partial Ph.D. studentship from the University of Leicester, as well as the opportunity that they offered me to work as a teacher assistant within the engineering department, University of Leicester.

Finally, I would like to dedicate this Ph.D. thesis to my inspiring parents Mostafa and Shahin, for their kindest supports and for being the role models, cheerleading squad and sounding boards I have needed. Certainly, without them, none of my success would be possible. I would like to thank my sister Razieh for all her kind wishes and supports. Last but not least, I would like to thank my wonderful fiancée Farzane who supported me, encouraged me and made the last year of my Ph.D. a delightful year.

Contents

Abstract	2
Acknowledgement	3
List of Symbols	8
List of Figures	12
Chapter 1. Introduction	18
1.1 Overall theme of the thesis.....	18
1.2 Material Point Method (MPM)	19
1.3 Contribution to science.....	20
1.4 The structure of this thesis	21
Chapter 2. Introduction to Nonlinear Finite Element Method	23
2.1 Equilibrium thermodynamic theory of polymer swelling	23
2.1.1 Variational approach.....	23
2.1.2 Calculation of the total work.....	24
2.1.3 Free energy density function for the hydrogels.....	25
2.1.4 Mass Conservation	25
2.1.5 Total Free energy	26
2.2 Non-equilibrium thermodynamic theory.....	29
2.2.1 Variation of total work done by the body force over the volume	29
2.2.2 Gibbs free energy	30
2.2.3 Entropy of mixing	31
2.3 Numerical approach to model large swelling of highly swellable polymers.....	35
2.3.1 Introduction	35
2.3.2 General introduction to Finite Element Method (FEM).....	36
2.4 A brief history of nonlinear finite element method.....	38
2.4.1 Introduction to nonlinear finite element method	39
2.4.2 Stress-strain laws	41
2.4.3 Nonlinear elasticity	41
2.4.4 Finite Element Method for non-linear large deformation.....	42
2.5 The advantages of MPM over traditional FEM	50
2.6 Summary of this chapter	51
Chapter 3. The Material Point Method.....	53
3.1 Introduction	53
3.2 The advantages of MPM over conventional FEM	54

3.3 Material point method and formulation.....	54
3.3.1 Governing equations.....	55
3.3.2 Deformation gradient tensor	57
3.3.3 Green strain tensor	58
3.3.4 Rate of deformation.....	58
3.3.5 Jaumann rate.....	59
3.3.6 Large deformation schemes for incrementally objective integration	60
3.3.7 Mapping procedure.....	60
3.3.8 Time integration loop for the dynamic equations	61
3.4 Topological systems in the MPM	65
3.5 Summary of this chapter	66
Chapter 4. Validation of The Material Point Method for Small Deformation	68
4.1 Introduction	68
4.2 Theoretical background	69
4.3 Numerical approach.....	70
4.3.1 Simulating 1D forced vibration of elastic beams with Finite Element Method	70
4.3.2 Implementing MPM to 1D forced vibration of elastic beams.....	71
4.4 Validation of the Material Point Method using Analytical Solution and Finite Element Analysis.....	74
4.5 Swelling induced by moisture absorption 1D simulation	76
4.5.1 Numerical results for 1D Swelling induced by moisture absorption	81
4.5.2 Validation of the numerical code based on the static FEM	81
4.5.3 Model validation	82
4.5.4 Results of simulating swelling induced by moisture absorption	83
4.5.5 The effect of damping coefficient	84
4.5.6 The effect of diffusion coefficient.....	85
4.5.7 The effect of coefficient of hygroscopic swelling.....	86
4.6 Implementation of MPM for 2D problems	87
4.6.1 Validation method	88
4.7 Numerical results of 2D vibration simulation	89
4.7.1 Case study 1: the effect of Young’s modulus.....	89
4.7.2 Case study 2: the effect of constant stress	92
4.7.3 Case study 3: the effect of density and damping coefficient.....	93
4.7.4 Case study 4: the effect of number material points	95

4.8 Validation of the code by simulating a uniaxial tensile test	96
4.9 Summary of this chapter	100
Chapter 5. Degradation of Highly Swellable Polymers During Large Elastic Swelling	102
5.1 Introduction	102
5.2 Theoretical Background	105
5.2.1 Rate form of constitutive law for hyperelastic materials	105
5.2.2 Derivation of rate form of Flory’s constitutive law	105
5.2.3 Free energy function	106
5.2.4 Calculation of tangent modulus based on Flory’s constitutive law	108
5.3 The numerical methods	110
5.3.1 Material point method for large deformation	110
5.3.2 Some vital issues of implementing MPM for large swelling	112
5.3.3 Special boundary treatments	113
5.4 Validation of the MPM code for large deformation based on Flory’s constitutive law..	116
5.4.1 The analytical approach	116
5.4.2 Uniform swelling results from the MPM code	119
5.4.3 Test 1, the effect of the zero boundary layer	119
5.4.4 Test 2, the effect of the number of background elements	122
5.4.5 The effect of higher constant applied stress	126
5.5 Model validation	129
5.6 Non-uniform swelling	131
5.6.1 Non-uniform swelling VS. Flory’s theory	132
5.6.2 The results of non-uniform swelling	133
5.7 Simulating of degradation of highly swellable polymers	136
5.7.1 The analytical approach in simulating of degradation of highly swellable polymers	137
5.8 Application of polymer degradation in controlled drug delivery systems	140
5.8.1 Drug release	140
5.9 Summary of this chapter	141
Chapter 6. Implementation of MPM to Selective Laser Melting	143
6.1 Selective laser melting	143
6.1.1 Introduction	143
6.1.2 The main problems and issues of SLM	145
6.2 The purpose of this chapter	147

CONTENTS

6.3 Overall numerical algorithm	148
6.3.1 Adapt Material Point Method for SLM	148
6.4 Pre-processing for different scanning strategy in SLM	152
6.5 Results and discussion.....	155
6.5.1 Distribution of von Mises stress for the first scanning strategy	155
6.5.2 Distribution of von Mises stress for the second scanning strategy	156
6.5.3 Distribution of von Mises stress for the third scanning strategy.....	157
6.5.4 Distribution of von Mises stress with different length of cooling period t_c	158
6.6 Summary	160
Chapter 7. Conclusion.....	161
References:	167
APPENDICES	172
Conference Presentations.....	172
Appendix I Reynold's theorem of material time derivative	173
Appendix II Derivatives of tangent modulus based on Flory's constitutive law	175
Appendix III Expected value of a function of random variable	179

List of Symbols

Ω	Volume of the material
Γ	Surface of the material
b_i	Distributed body force
τ_i	Surface traction
$\hat{\mu}$	chemical potential per solvent molecule
Ω_0	Reference volume of the material
Γ_0	Reference surface of the material
δx_i	Variation of the current position
δj_k	Variation of the molecular flux
n_k	Unit normal vector
ρ	Mass density
δG	Variation of the total free energy of the thermodynamic system
$\delta \Phi$	Variation of total free energy of hydrogel
δW	Variation total work
$u(F_{ik}, C)$	Free energy density function
F_{ik}	Deformation gradient tensor
$C(x, t)$	Solvent molecular concentration
$J_k(x, t)$	Flux of the solvent molecules
$\xi(x)$	Test function
t	Time
$s_{ik}(x, t)$	Nominal stress
$\mu(x, t)$	Chemical potential
$\dot{v}(x, t)$	Acceleration
l_i	Length of the elements
F	Body force
n_1	Number of molecules
V	Volume
u	Velocity vector
δu	Variation of the velocity vector
M	Mobility
δj	Variation of the flux of the solvent molecules
G	Total free energy of the thermodynamic system
ΔH	Enthalpy change
ΔS	Entropy change
T	Temperature
G_m	Total free energy of mixing
ΔS_m	Entropy change of mixing
k	Boltzmann's constant

LIST OF SYMBOLS

Φ	Possible number of configurations
n_A and n_B	Total number of spherical particles of materials A and B
x_A and x_B	Mole fractions of materials A and B
c_A and c_B	Concentration of materials A and B
g_m	Total free energy density of mixing
$\delta\dot{G}_m$	Variation of the differential of the total free energy of mixing
$p(t)$	Linear momentum
$v(x,t)$	Velocity field
$H^1(\Omega)$	Hilbert space
σ_{ji}	Cauchy stress tensor
Δv_i	Virtual velocity field
\tilde{u} and \tilde{v}	Displacement of nodal points within the elements in X and Y direction
$N_I(x_i)$	Shape functions
m	Mass
f^{ext}	External forces
f^{int}	Internal forces
\dot{v}	Acceleration
\mathcal{E}	Strain tensor
D	Tensor of rate of deformation
C_{ijkl}^{SE}	Tangent modulus for the second Piola-Kirchhoff stress strain tensor
λ_0 and μ_0	Lame constants
J	Jacobian
E	Young's modulus
ν	Poisson ratio
E_{ij}	Green strain tensor
X_i	Material coordinates (Lagrangian coordinate)
u	displacement function
x_i	Spatial coordinate system
W_{ij}	Spin tensor
$\sigma^{\nabla J}$	Objective stress rate
$\tilde{\delta}$	Dirac delta function
M_p	Mass of a material point
N_p	Total number of the material points,
Δv	Arbitrary admissible test function
$f(x_0)$	Arbitrary function
$B_I(X_p)$	Spatial gradient of the shape function
∇_0	Left gradient operator
$\Phi(X,t)$	Equation of motion

LIST OF SYMBOLS

δ_{ij}	Kronecker's delta
L_{ij}	Velocity gradient
$Q(t)$	Rotation tensor
Δt	Time interval
C^{α}	Elastic modulus tensor
$t + \Delta t$	Updated for the time step
$J^{t+\Delta t}$	Updated Jacobian
ρ_i	Nodal value of the mass density
$v_I^{t+\Delta t}$	Updated velocity vector
$[K]$	Stiffness matrix
l	Length of each element
$[M]$	Mass matrix
$\{F\}$	Force vector
i	Nodal indicator
$V_p^{t+\Delta t}$	Updated material point velocity
$v_I^{t+\Delta t}$	Updated nodal velocity
$\sigma^{t+\Delta t}$	Updated stress values
$\dot{\sigma}^{t+\Delta t}$	Updated rate of stress
$D^{t+\Delta t}(X_p^t)$	Updated rate of deformation
$\sigma_0(X_p)$	Constant applied stress
ε^s	Swelling strain
α^s	Volumetric change in the swollen hydrogel
V_0 and V_1	Initial and swollen volume of the hydrogel
α	Constant coefficient of hygroscopic swelling
c_∞	Constant concentration on surface
c_0	Uniform initial concentration
D	Diffusion coefficient
\tilde{x}	Dimensionless parameter position per length
u^e	Elastic displacement
u^s	displacement due to swelling
u^t	Total displacement
F_i^s and F_i^d	swelling force and damping force
d	Constant damping coefficient
\dot{X}_i	Nodal velocities
\ddot{X}_i^t	Nodal acceleration
$(-\sigma_0)$	Sintering stress
$\sigma_{von-Mises}$	Von Mises stress
$\omega(E)$	Potential function

LIST OF SYMBOLS

$\psi(C)$	Stored energy potential
$U_e(F)$	Elastic free energy density of hydrogel
$U_m(C)$	Free energy of hydrogel due to mixing
λ_1, λ_2 and λ_3	Principal stretches
$Nk_B T$	Initial shear modulus of an elastomer
χ	Dimensionless quantity that characterizes the interaction energy between the solvent and polymer
v	Volume per small molecule
$\hat{U}(F, \mu)$	Legendre transformation of the free energy density function
H_{ijkl}	Fourth order tensor
$\Pi(x, t)$	Lagrange multiplier
Gf^{int}	Summation of the internal nodal forces
$N(\mu, \sigma)$	Probability density function
σ	Standard deviation
μ	Mean value
r	A random value
ε_{vr}	Random volumetric strain
η	Derivative of Gibbs free energy with respect to concentration

List of Figures

FIGURE 2-1 SCHEMATIC DEFORMATION OF THE REFERENCE CONFIGURATION. M. KANG AND R. HUANG (2010) 24

FIGURE 2-2 SCHEMATIC DIAGRAM OF A POLYMER NETWORK UNDER A BODY FORCE F AND A VELOCITY FIELD U 29

FIGURE 2-3 SCHEMATIC DIAGRAM, SHOWS EMPTY LATTICE THAT CAN BE FILLED WITH TWO DIFFERENT SPHERICAL MOLECULES RANDOMLY. PAINTER P. C., COLEMAN M. M., (2009). 31

FIGURE 2-4 SCHEMATIC DIAGRAM SHOWS A FILLED LATTICE WITH SMALL SIZE (LOW MOLECULAR WEIGHT) MOLECULES REPRESENT SOLVENT MOLECULES IN BLUE AND CONNECTED RED BALLS REPRESENT SEGMENTS OF A POLYMER CHAIN. PAINTER P. C., COLEMAN M. M., (2009). 32

FIGURE 2-5 ILLUSTRATE 2D DISCRETISED COMPUTATIONAL DOMAINS WITH TRIANGULAR ELEMENTS FOR DIFFERENT GEOMETRIES. 38

FIGURE 2-6 FIGURE SHOWS A 3D GEOMETRY WHICH HAS BEEN DISCRETISED WITH TRIANGULAR ELEMENTS. 38

FIGURE 2-7 THE CONSTANT STIFFNESS METHOD. I. M. SMITH AND D. V. GRIFFITHS (2004)..... 40

FIGURE 2-8 THE VARIABLE OR TANGENT STIFFNESS METHOD. I. M. SMITH AND D. V. GRIFFITHS (2004). 41

FIGURE 2-9 SCHEMATIC DIAGRAM SHOWS MATERIAL BODY REPRESENTED DEFORMS AS A FUNCTION OF TIME AND POSITION. 42

FIGURE 2-10 SHOWS AN EXTREMELY SOLID ROTATION OF A BAR UNDER AN INITIAL STRESS, THAT CHANGE THE VALUE STRESS WITHOUT CHANGING THE VALUE OF STRAIN AS AN EFFECT OF SOLID ROTATION. F. LI (2008)..... 50

FIGURE 3-1 THREE MAIN STEPS OF MPM ALGORITHM: (A) INITIALISATION OF THE MATERIAL POINTS, (B) DEFORMATION OF THE MATERIAL POINTS (LAGRANGIAN PHASE), (C) RESETTING THE MESH, BY USING THE MAPPING SYSTEM (CONVECTIVE PHASE) (PHUONG ET AL. 2015) 55

FIGURE 3-2 SCHEMATIC PICTURE OF BOUNDARY CELLS THAT NEED SPECIAL CARE, AS THE NODAL LUMPED MASS WILL BE SMALL ESPECIALLY AT THE CORNER CELLS WHICH MAY NEED DISTINCT TREATMENTS..... 64

FIGURE 3-3 TOPOLOGICAL SYSTEM OF THE RECTANGULAR MESH 65

FIGURE 4-1 CANTILEVER BEAM UNDER A CONSTANT FORCE..... 69

FIGURE 4-2 SCHEMATIC MODEL OF MASS SPRING..... 69

FIGURE 4-3 THE DISCRETISED GEOMETRY USING LINEAR ELEMENTS 70

FIGURE 4-4 SCHEMATIC DISCRETISED SYSTEM IN 1D MPM, THE BLUE POINTS REPRESENTS THE MATERIAL POINTS AND THE BLACK POINTS REPRESENT THE ELEMENTAL NODES. 72

FIGURE 4-5 FLOWCHART OF MPM FOR SMALL DEFORMATION..... 73

FIGURE 4-6 SHOWS MPM VS. FEM RESULTS OF DISPLACEMENT OF THE LAST NODE FOR VIBRATION OF A BAR WITH TOTAL LENGTH OF $l = 849.375mm$, YOUNG'S MODULUS OF $E = 50Mpa$, CROSS SECTION AREA OF $A = 10mm^2$, THE BODY FORCE $F = 0.5N$, MASS OF EACH MATERIAL POINT IS 0.13 GR AND SEVEN MATERIAL POINTS IS USED IN EACH MESH IN MPM, 173 ELEMENTS IS USED IN FEM, AND LUMPED MASS OF EACH NODE IN FEM IS 0.91GR. THE TIME STEP IS $\Delta t = 0.001$ SECOND OF EACH ITERATION..... 74

FIGURE 4-7 SHOWS MPM VS. FEM RESULTS OF DISPLACEMENT OF THE LAST NODE FOR VIBRATION OF A BAR WITH TOTAL LENGTH OF $l = 849.375mm$, YOUNG'S MODULUS OF $E = 10Mpa$, CROSS SECTION AREA OF $A = 10mm^2$, THE BODY FORCE $F = 0.5N$, MASS OF EACH MATERIAL POINT IS 0.13 GR AND SEVEN MATERIAL POINTS IS USED IN EACH MESH IN MPM, 167 ELEMENTS IS USED

IN FEM, AND THE LUMPED MASS OF EACH NODE IN FEM IS 0.91GR. THE TIME STEP IS $\Delta t = 0.001$ SECOND OF EACH ITERATION..... 75

FIGURE 4-8 SHOWS MPM VS. FEM RESULTS OF DISPLACEMENT OF THE LAST NODE FOR VIBRATION OF A BAR WITH TOTAL LENGTH OF $l = 849.00mm$, YOUNG'S MODULUS OF $E = 30Mpa$, CROSS SECTION AREA OF $A = 10mm^2$, THE BODY FORCE $F = 0.5N$, MASS OF EACH MATERIAL POINT IS 0.225 GR AND FOUR MATERIAL POINTS IS USED IN EACH MESH IN MPM, 170 ELEMENTS IS USED IN FEM AND LUMPED MASS OF EACH NODE IN FEM IS 0.9GR. THE TIME STEP IS $\Delta t = 0.001$ SECOND OF EACH ITERATION..... 76

FIGURE 4-9 THE CONCENTRATION OF THE SOLVENT AT THE LENGTH PARAMETER \tilde{x} 78

FIGURE 4-10 THE FLOWCHART OF FEM CODE IN FORTRAN FOR 1D SWELLING INDUCED BY MOISTURE ABSORPTION 80

FIGURE 4-11 STATIC AND DYNAMIC RESPONSE OF FORCED VIBRATION OF THE ELASTIC BAR WITH DAMPING. THE VERTICAL AXIS SHOWS THE LENGTH OF THE BEAM. THE HORIZONTAL AXIS SHOWS THE ITERATION NUMBER. THE TIME STEP IS $\Delta t = 0.001$ SECOND OF EACH ITERATION..... 83

FIGURE 4-12 POSITION OF DIFFERENT NODES DUE TO MOISTURE ABSORPTION, NODES 20, 14, 9 AND 4 SHOWN FROM SERIES 1 TO SERIES 4 RESPECTIVELY. THE VERTICAL AXIS SHOWS THE LENGTH OF THE BEAM. THE HORIZONTAL AXIS SHOWS THE ITERATION NUMBER. THE TIME STEP IS $\Delta t = 0.001$ SECOND OF EACH ITERATION..... 84

FIGURE 4-13 THE EFFECT OF DIFFERENT DAMPING COEFFICIENT ON THE SWELLING INDUCED BY MOISTURE ABSORPTION. THE GREEN LINE SHOWS THE SYSTEM IS VERY SLOW AND NOT YET REACHED AN EQUILIBRIUM STATE. FOR ALL THE THREE CASES DIFFUSION COEFFICIENT IS $D = 1000$ AND COEFFICIENT OF HYGROSCOPIC SWELLING IS $\alpha = 1$. THE VERTICAL AXIS SHOWS THE LENGTH OF THE BEAM. THE HORIZONTAL AXIS SHOWS THE ITERATION NUMBER. THE TIME STEP IS $\Delta t = 0.001$ SECOND OF EACH ITERATION. 85

FIGURE 4-14 THE EFFECT OF THE DIFFERENT DIFFUSION COEFFICIENT ON THE SWELLING INDUCE BY MOISTURE ABSORPTION. THE DAMPING COEFFICIENT IS $d = 1$ AND COEFFICIENT OF HYGROSCOPIC SWELLING IS $\alpha = 1$ FOR ALL THE CASES. THE TIME STEP IS $\Delta t = 0.001$ SECOND OF EACH ITERATION. 86

FIGURE 4-15 THE EFFECT OF DIFFERENT COEFFICIENT OF HYGROSCOPIC SWELLING OF THE MATERIAL. THE DAMPING COEFFICIENT IS $d = 1$ AND THE DIFFUSION COEFFICIENT IS $D = 1000$ FOR ALL THE CASES. THE TIME STEP IS $\Delta t = 0.001$ SECOND OF EACH ITERATION. 87

FIGURE 4-16 THE SCHEMATIC PICTURE OF A 2DIMENSIONAL MPM WITH FREE MESHES..... 88

FIGURE 4-17 THE FLUCTUATING LINE SHOWS THE RESULTS MPM CODE WITH YOUNG'S MODULUS $E=10$ MPA, POISSON'S RATIO $\nu = 0.4$, THE DENSITY OF 1000 KG/M^3 , 100 MATERIAL POINTS IS USED IN EACH COMPUTATIONAL CELL, INITIAL NEGATIVE STRESS $\sigma_0(X_p) = -70KPa$, AND DAMPING $C(X_p) = 1000000000$, AND THE RED LINE SHOWS THE EQUILIBRIUM STATE OF DEFORMATION. THE TIME STEP IS $\Delta t = 0.001$ SECOND OF EACH ITERATION. 90

FIGURE 4-18 THE FLUCTUATING LINE SHOWS THE RESULTS MPM CODE FOR A STRAIN WITH YOUNG'S MODULUS $E=250$ MPA, POISSON'S RATIO $\nu = 0.4$, THE DENSITY OF 1000 KG/M^3 , 100 MATERIAL POINTS IS USED IN EACH COMPUTATIONAL CELL, INITIAL NEGATIVE STRESS $\sigma_0(X_p) = -70KPa$, AND DAMPING $C(X_p) = 1000000000$, AND THE RED LINE SHOWS THE EQUILIBRIUM STATE OF DEFORMATION. THE TIME STEP IS $\Delta t = 0.001$ SECOND OF EACH ITERATION. 91

FIGURE 4-19 THE FLUCTUATING LINE SHOWS THE RESULTS MPM CODE FOR A STRAIN WITH YOUNG'S MODULUS $E=500$ MPA, POISSON'S RATIO $\nu = 0.4$, THE DENSITY OF 1000 KG/M^3 , 100 MATERIAL

LIST OF FIGURES

POINTS IS USED IN EACH COMPUTATIONAL, INITIAL NEGATIVE STRESS $\sigma_0(X_p) = -70KPa$, AND DAMPING $C(X_p) = 1000000000$, AND THE RED LINE SHOWS THE EQUILIBRIUM STATE OF DEFORMATION. THE TIME STEP IS $\Delta t = 0.001$ SECOND OF EACH ITERATION..... 91

FIGURE 4-20 THE FLUCTUATING LINE SHOWS THE RESULTS MPM CODE FOR A STRAIN WITH YOUNG'S MODULUS $E=10$ MPA, POISSON'S RATIO $\nu = 0.4$, THE DENSITY OF 1000 KG/M^3 , 100 MATERIAL POINTS IS USED IN EACH COMPUTATIONAL CELL, INITIAL NEGATIVE STRESS $\sigma_0(X_p) = -1Pa$, AND DAMPING $C(X_p) = 1000000000$, AND THE RED LINE SHOWS THE EQUILIBRIUM STATE OF DEFORMATION. THE TIME STEP IS $\Delta t = 0.001$ SECOND OF EACH ITERATION..... 92

FIGURE 4-21 THE FLUCTUATING LINE SHOWS THE RESULTS MPM CODE FOR A STRAIN WITH YOUNG'S MODULUS $E=10$ MPA, POISSON'S RATIO $\nu = 0.4$, THE DENSITY OF 1000 KG/M^3 , 100 MATERIAL POINTS IS USED IN EACH COMPUTATIONAL CELL, INITIAL POSITIVE STRESS $\sigma_0(X_p) = 70Pa$, AND DAMPING $C(X_p) = 1000000000$, AND THE RED LINE SHOWS THE EQUILIBRIUM STATE OF DEFORMATION. THE TIME STEP IS $\Delta t = 0.001$ SECOND OF EACH ITERATION..... 93

FIGURE 4-22 THE FLUCTUATING LINE SHOWS THE RESULTS OF MPM CODE FOR A STRAIN WITH YOUNG'S MODULUS $E=10$ MPA, POISSON'S RATIO $\nu = 0.4$, THE DENSITY OF 2000 KG/M^3 , 100 MATERIAL POINTS IS USED IN EACH COMPUTATIONAL CELL, INITIAL POSITIVE STRESS $\sigma_0(X_p) = 70Pa$, AND DAMPING $C(X_p) = 1000000000$, AND THE RED LINE SHOWS THE EQUILIBRIUM STATE OF DEFORMATION. THE TIME STEP IS $\Delta t = 0.001$ SECOND OF EACH ITERATION. 94

FIGURE 4-23 THE FLUCTUATING LINE SHOWS THE RESULTS OF MPM CODE FOR A STRAIN WITH YOUNG'S MODULUS $E=10$ MPA, POISSON'S RATIO $\nu = 0.4$, THE DENSITY OF 2000 KG/M^3 , 100 MATERIAL POINTS IS USED IN EACH COMPUTATIONAL CELL, INITIAL POSITIVE STRESS $\sigma_0(X_p) = 70Pa$, AND DAMPING $C(X_p) = 1500000000$, AND THE RED LINE SHOWS THE EQUILIBRIUM STATE OF DEFORMATION. THE TIME STEP IS $\Delta t = 0.001$ SECOND OF EACH ITERATION. 94

FIGURE 4-24 THE FLUCTUATING LINE SHOWS THE RESULTS MPM CODE FOR A STRAIN WITH YOUNG'S MODULUS $E=10$ MPA, POISSON'S RATIO $\nu = 0.4$, THE DENSITY OF 2000 KG/M^3 , 94 MATERIAL POINTS IS USED IN EACH COMPUTATIONAL CELL, INITIAL POSITIVE STRESS $\sigma_0(X_p) = 70Pa$, AND DAMPING $C(X_p) = 1500000000$, AND THE RED LINE SHOWS THE EQUILIBRIUM STATE OF DEFORMATION. THE TIME STEP IS $\Delta t = 0.001$ SECOND OF EACH ITERATION..... 96

FIGURE 4-25 THE VALUE OF YOUNG'S MODULUS IS CALCULATED VIA DIVIDING STRESS BY STRAIN WHICH IS OBTAINED FROM MPM IN THE X DIRECTION. THE TIME STEP IS $\Delta t = 0.001$ SECOND OF EACH ITERATION. 98

FIGURE 4-26 THE VALUE OF POISSON'S RATIO IS CALCULATED VIA DIVIDING STAIN IN THE Y DIRECTION BY STRAIN IN THE X DIRECTION. THE TIME STEP IS $\Delta t = 0.001$ SECOND OF EACH ITERATION..... 98

FIGURE 4-27 THE VALUE OF YOUNG'S MODULUS IS CALCULATED VIA DIVIDING STRESS BY STRAIN WHICH IS OBTAINED FROM MPM IN THE X DIRECTION. THE TIME STEP IS $\Delta t = 0.001$ SECOND OF EACH ITERATION. 99

FIGURE 4-28 THE GRAPH SHOWS THE DIVISION OF NEGATIVE OF STRAIN IN THE Y DIRECTION BY STRAIN IN THE X DIRECTION WHICH IS EQUAL TO THE POISSON'S RATIO. THE TIME STEP IS $\Delta t = 0.001$ SECOND OF EACH ITERATION..... 99

LIST OF FIGURES

FIGURE 5-1 SHOWS A SCHEMATIC DIAGRAM OF SOLVENT MOLECULES DIFFUSED INSIDE THE POLYMER
E. M. AYDT AND R. HENTSCHE (1999)..... 103

FIGURE 5-2 THE INTERNAL TOPOLOGICAL SYSTEM IN THE MPM CODE..... 112

FIGURE 5-3 SCHEMATICS OF 2D HOMOGENEOUS SWELLING 116

FIGURE 5-4 THE STRESS STRETCH DIAGRAM 119

FIGURE 5-5 SHOWS A FOUR BY FOUR ELEMENT SET UP FOR THE INITIAL UN-DEFORMED SHAPE OF THE
BODY. THE MIDDLE TWO BY TWO ELEMENTS INDICATED BY THE GREEN BOUNDARY IS THE MAIN
REFERENCED BODY. THE ZERO LIMITS ARE ALSO SHOWN BY RED BOUNDARIES..... 120

FIGURE 5-6 SHOWS THE CONVERGED STRESS VALUE, THE INPUT SINTERING STRESS IS $\sigma_0 = 1100000$
PA. THE ITERATION TIME STEP IS $\Delta t = 0.001$ 121

FIGURE 5-7 SHOWS THE STEADY STATE VALUE OF SWELLING DEFORMATION WHEN SINTERING STRESS
IS $\sigma_0 = 1100000$ PA. THE ITERATION TIME STEP IS $\Delta t = 0.001$ 121

FIGURE 5-8 SHOWS THE DEFORMED SHAPE OF THE BODY WHEN THE VALUE OF STRESS IS
 $\sigma_0 = 1100000$ PA. THE GREEN BOUNDARIES REPRESENT THE DEFORMED MAIN BODY. THE ZERO
LIMITS ARE ALSO SHOWN BY RED BOUNDARIES. 122

FIGURE 5-9 SHOWS A 14*14 ELEMENT SET UP FOR THE INITIAL UN-DEFORMED SHAPE OF THE BODY.
THE MIDDLE 8*8 ELEMENTS INDICATED BY THE GREEN BOUNDARY IS THE MAIN REFERENCED
BODY. THE ZERO LIMITS ARE ALSO SHOWN BY RED BOUNDARIES. 123

FIGURE 5-10 SHOWS THE DEFORMED SHAPE OF THE BODY WHEN THE VALUE OF STRESS IS
 $\sigma_0 = 1100000$ PA. THE GREEN BOUNDARIES REPRESENT THE DEFORMED MAIN BODY. THE ZERO
LIMITS ARE ALSO SHOWN BY RED BOUNDARIES. 124

FIGURE 5-11 SHOWS A 32*32 ELEMENT SET UP FOR THE INITIAL UN-DEFORMED SHAPE OF THE BODY.
THE MIDDLE 20*20 ELEMENTS INDICATED BY THE GREEN BOUNDARY IS THE MAIN REFERENCED
BODY. THE ZERO LIMITS ARE ALSO SHOWN BY RED BOUNDARIES. 125

FIGURE 5-12 SHOWS THE DEFORMED SHAPE OF THE BODY WHEN THE VALUE OF STRESS IS
 $\sigma_0 = 1100000$ PA. THE GREEN BOUNDARIES REPRESENT THE DEFORMED MAIN BODY. THE ZERO
LIMITS ARE ALSO SHOWN BY THE RED BOUNDARIES. 125

FIGURE 5-13 SHOWS THE CONVERGED STRESS VALUE, THE INPUT SINTERING STRESS IS $\sigma_0 = 1600000$
PA. THE ITERATION TIME STEP IS $\Delta t = 0.001$ 126

FIGURE 5-14 SHOWS THE STEADY STATE VALUE OF SWELLING DEFORMATION WHEN SINTERING STRESS
IS $\sigma_0 = 1600000$ PA. THE ITERATION TIME STEP IS $\Delta t = 0.001$ 127

FIGURE 5-15 SHOWS THE DEFORMED SHAPE OF THE BODY WHEN THE VALUE OF STRESS IS
 $\sigma_0 = 1600000$ PA..... 127

FIGURE 5-16 SHOWS THE CONVERGED STRESS VALUE, THE INPUT SINTERING STRESS IS $\sigma_0 = 2300000$
PA. THE ITERATION TIME STEP IS $\Delta t = 0.001$ 128

FIGURE 5-17 SHOWS THE STEADY STATE VALUE OF SWELLING DEFORMATION WHEN SINTERING STRESS
IS $\sigma_0 = 2300000$ PA. THE ITERATION TIME STEP IS $\Delta t = 0.001$ 128

FIGURE 5-18 SHOWS THE DEFORMED SHAPE OF THE BODY WHEN THE VALUE OF STRESS IS
 $\sigma_0 = 2300000$ PA. 129

FIGURE 5-19 THE VERTICAL AXIS IS THE VALUE OF STRESS, AND THE HORIZONTAL AXIS IS THE VALUE OF
THE CORRESPONDING STRETCH. THIS FIGURE SHOWS A PERFECT MATCH BETWEEN THE
ANALYTICAL RESULTS PRESENTED BY THE RED LINE AND THE RESULTS FROM THE MPM CODE
THAT IS REPRESENTED BY THE STARS. THIS IS THE MOST IMPORTANT FIGURE IN THIS CHAPTER, AS
IT TESTS THE VALIDITY OF MPM IN LARGE ELASTIC DEFORMATION. THE NON-LINEAR

CONSTITUTIVE LAW WHICH IS BASED ON FLORY'S CONSTITUTIVE LAW HAS BEEN FED TO THE MPM CODE, AND THE RESULTS ARE PERFECTLY MATCHED WITH THE ANALYTICAL RESULTS, THAT WERE DISCUSSED IN SECTION 5.4.1. 130

FIGURE 5-20 THE SCHEMATIC DIAGRAM OF THE MULTI-LAYERED TABLET DURING THE NON-UNIFORM SWELLING, THE UN-DEFORMED STATE, AND THE DEFORMED STATE ARE SHOWN..... 132

FIGURE 5-21 REPRESENT THE MULTI-LAYERED TABLET, IN WHICH THE BLACK ZONE SHOWS THE HARD CORE OF THE TABLET, THE TWO GREEN ZONES ON THE TOP AND BOTTOM OF THE HARD CORE ARE THE SOFTER ZONES, AND THE ZERO LIMITS ARE ALSO SHOWN BY RED BOUNDARIES. 133

FIGURE 5-22 SHOWS THE NON-UNIFORM DEFORMED SHAPE OF THE BODY WHEN THE VALUE OF STRESS IN THE HARD CORE SECTION IS $\sigma_0 = 500000 \text{ PA}$, AND STRESS IN THE SOFT SECTIONS ARE $\sigma_0 = 1000000 \text{ PA}$. THE SHEAR MODULUS OF ELASTOMER IN BOTH HARD AND SOFT CORE ARE $Nk_B T = 600000$, AND THE SHEAR MODULUS OF ELASTOMER IN THE EXTRA MATERIAL POINTS IS $Nk_B T = 600$ 134

FIGURE 6-1 SCHEMATIC OF THE SLM PROCESS L. E. LOH ET AL. (2014) 145

FIGURE 6-2 CRACK SURFACES OF TI-6-4 SPECIMENS FOLLOWING SLM PROCESSING, SUBSEQUENT HIP TREATMENT AND FATIGUE AT A STRESS AMPLITUDE OF 620 MPA. FATIGUE LIVES OF THE SAMPLES SHOWN WERE FAIRLY LOW (A, C: 188,103 CYCLES; B, D: 845,383 CYCLES) DUE TO REMAINING POROSITY. THE CRACK INITIATION SITES FOR TWO DIFFERENT SAMPLES ARE SHOWN IN LOW MAGNIFICATION IN (A) AND (B); (C) AND (D) DEPICT THE CORRESPONDING MAGNIFIED VIEW OF THE UNDERLYING DEFECTS. S. LEUDERS ET AL. (2012). 146

FIGURE 6-3 THE DISTRIBUTION OF THE SINTERING STRESS ON THE MATERIAL POINT OVER TIME. 150

FIGURE 6-4 THE GEOMETRY OF THE CIRCULAR PIPE WITH A SEPARATION WALL. ALL THE DIMENSIONS ARE IN CM. 153

FIGURE 6-5 THE LASER MOVES Laterally AND IS PERPENDICULAR TO THE PLANE OF POWDERS. 154

FIGURE 6-6 THE LASER MOVES ON A CIRCULAR BASE, PERPENDICULAR TO THE PLAIN OF POWDERS.. 154

FIGURE 6-7 THE LASER FIRST SCANS THE EDGES AND THEN SCANS BETWEEN THE EDGES. 154

FIGURE 6-8 DISTRIBUTION OF VON MISES STRESS FOR THE FIRST SCANNING STRATEGY WITH COOLING TIME $t_c = 500$ AND MAXIMUM SINTERING STRESS $\sigma_0 = -500 \text{ MPa}$ (ALL THE UNITS IN THE FIGURE ARE $- \text{MPa}$). THE NUMBER OF SCANNED MATERIAL POINTS: (A) 1530; (B) 5100; (C) 7650; (D) 10200..... 156

FIGURE 6-9 DISTRIBUTION OF VON MISES STRESS FOR THE THIRD STRATEGY WITH COOLING TIME $t_c = 500$ AND MAXIMUM SINTERING STRESS IS $\sigma_0 = -500 \text{ MPa}$ (ALL THE UNITS IN THE FIGURE ARE $- \text{MPa}$). THE NUMBER OF MATERIAL POINTS: (A) 600 ;(B) 3500 ;(C) 4500(D) 6150;(E) 6500 ;(F) 7200;(G) 8000 157

FIGURE 6-10 DISTRIBUTION OF VON MISES STRESS FOR THE THIRD STRATEGY WITH COOLING TIME $t_c = 500$ AND MAXIMUM SINTERING STRESS IS $\sigma_0 = -500 \text{ MPa}$ (ALL THE UNITS IN THE FIGURE ARE $- \text{MPa}$). THE NUMBER OF MATERIAL POINTS: (A) 500 ;(B) 1100 ;(C) 2400 (D) 3930 ;(E) 10050 ;(F) 12600 158

FIGURE 6-11 DISTRIBUTION OF VON MISES STRESS FOR THE FIRST STRATEGY WITH MAXIMUM SINTERING STRESS $\sigma_0 = -500 \text{ MPa}$, THE NUMBER OF MATERIAL POINTS 1530 (ALL THE UNITS IN THE FIGURE ARE $- \text{MPa}$). COOLING TIME t_c IS: (A) 20; (B) 100; (C) 500. 159

FIGURE 6-12 DISTRIBUTION OF VON MISES STRESS FOR THE THIRD STRATEGY WITH MAXIMUM SINTERING STRESS $\sigma_0 = -500 \text{ MPa}$, (ALL THE UNITS IN THE FIGURE ARE $- \text{MPa}$). NUMBER OF MATERIAL POINTS 2502 AND COOLING TIME t_c IS: (A) 20; (B) 100; (C) 500. 159

List of tables

TABLE 1 SHOWS DISCRETISATION OF DIFFERENT TERMS IN THE FEM.....	46
TABLE 2 THE MAIN VARIABLES USED IN THE FE CODE.	81
TABLE 3 SHOWS THE INITIAL INPUT FOR CASE STUDY 1	90
TABLE 4 SHOWS THE INITIAL INPUT FOR CASE STUDY 2	92

Chapter 1. Introduction

The theme of this thesis is to take advantage of a modern Finite Element method called Material Point Method (MPM) to simulate difficult problems such as the swelling behaviour and large deformation coupled with degradation in highly swellable polymers. Also, a rigorous validation of the MPM against a set of simple problems has been conducted. Furthermore, we have demonstrated the capability of this strong numerical tool to study an additive manufacturing technology called Selective Laser Melting (SLM). The aim of this thesis is to clearly demonstrate the advantages of MPM over the traditional Finite Element Method (FEM) to simulate difficult problems which require complex topological systems.

1.1 Overall theme of the thesis

The general idea in Material Point Method (MPM) first was introduced by Harlow (1964) in fluid dynamics that is called Particle-In-Cell (PIC) method. Further applications of this method in solid mechanics were done by Burgess et al. (1995) and Sulsky et al. (1994, 1995). Following their work, the algorithm of Material Point Method was discussed and analytically formulated and applied in publications by Wiezckowski et al. (1999) and Wiezckowski (2004). Recently F. Li et al. (2011) have used MPM in the modelling of brittle impact failure of disc particles. Also, the same group has used MPM to model adhesive contact between fine particles. Material Point Method has been recently developed in the literature as a strong numerical tool to simulate some rigorous cases. X. Ma et al. (2012) have used MPM for axisymmetric computation of Taylor cylinder impacts of ductile and brittle materials, they have also used a dual domain MPM and compared the results with the original MPM and found that compared to the other numerical methods, MPM has more accurate results especially on severely deformed specimens. B. Wang, et al. (2016) carried out an investigation of retrogressive and progressive slope failure mechanics using the material point method. They found that MPM is a promising method to simulate slope failure and it is mainly useful to capture the post-failure of slopes.

Although MPM has been used for many difficult case studies in the literature, many still suffer from the rigorous validation of the method. History has shown promising numerical methods have failed to pass some basic case studies. Therefore, the purpose of this work is to test the MPM using firstly a set of simple case studies which any numerical method has to pass and secondly apply the MPM to a few difficult problems such as simulation of degradation of highly swellable materials during large swelling and also simulation of Selective Laser Melting (SLM) manufacturing process as two complex examples that are challenging for the standard finite element method.

1.2 Material Point Method (MPM)

Simulating extremely large deformation of structures and materials is often too complicated and there are no fully analytical solutions to deal with extremely large elastic deformation in materials. For example, there is no analytical solution to model particularly large elastic swelling of highly swellable polymers. Therefore a specific numerical method is required to solve the problem with a numerical approach as the modern computers are getting more and more powerful. For example, in order to simulate the swelling problem for highly swellable polymers the numerical method has to be capable of simulating large deformation of polymers due to contact with a solvent, along with degradation of polymers due to breakage of the polymer chains, or for example, in order to simulate Selective Laser Melting (SLM) the numerical method should be able to deal with both discrete powders and the solidified material at the same time.

The general attitude of MPM is to represent a material body with some discrete points called material points. Material Point Method is using the advantage of an arbitrary Lagrangian-Eulerian description of motion and could be categorised as a mesh-less method Wierzchowski (2004). In the Material Point Method the mass of the body is lumped on the material points, also all the state variables such as stresses, densities, and velocities are traced at the material points. Further to material points an independent Eulerian mesh is defined (computational mesh) on which all the equations of motion are formulated and solved. This Eulerian mesh is a constant background mesh that is defined in an arbitrary way, so the problem of mesh distortion which is an important issue in the Lagrangian mesh is avoided. The computational mesh has to

cover all the possible domain of the motion of the main body. So, particularly for large swelling problems, there should be quite a lot of free meshes around the body to include the final swelled body. The background mesh is related to the material points through a mapping system. The computational mesh is used to determine the accelerations of the nodes, and also the stress rates. After calculating the nodal accelerations and stress rates at each time step, as opposed to the conventional finite element methods that the nodes will be moved, the velocity of each node will be mapped into the material points and the new position of the material points will be determined. After finding the new positions of the material points a new relationship between material points and computational mesh can be defined, so it avoids mesh tangling or distortion. Another advantage of computational mesh is for contact problems in which contact boundary conditions of impenetrability and contact forces will be easily satisfied. Therefore, MPM is a powerful numerical method to simulate extremely large deformations such as swelling or shrinking problems of polymers, as well as simulating of degradation in polymers, since it can effectively control the topological relationships in extremely large deformations or in those problems that deal with discrete powders and solidified parts at the same time such as the SLM technique. This method can be perfectly used for simulation of material breakage or material degradation. F. Li et al. (2011) have used MPM for modelling brittle impact failure of disc particles using material point method.

1.3 Contribution to science

As it was discussed earlier, the lack of rigorous validation for the MPM in the literature is unsatisfactory. Therefore, the main focus of this thesis is to first test the validity of the MPM via a series of simple tests, such as a 1D forced vibration, 2D forced vibration and 2D large tensile test. Secondly, MPM is implemented to case studies such as Selective Laser Melting (SLM) and polymer degradation during large swelling which is currently difficult to handle using traditional Finite Element Method. A topological system is presented for the MPM coding, firstly to deal with two different systems of discretization that are based on an arbitrary Lagrangian-Eulerian description of motion, and secondly to reduce the computational costs to a minimum. Hence, all the codes are developed by the author of this thesis from scratch in order to have full control of the

numerical implementation. Ultimately, the theme of this thesis is to test the validity of MPM as well as to demonstrate its capabilities.

1.4 The structure of this thesis

In Chapter 1 an overview of the theme of this thesis is presented. The resolution of this thesis is to first, test the validity of MPM code that is entirely written by the author of this thesis by solving some simple case studies, and then demonstrate the capability of MPM for much more complex systems such as polymer degradation during large elastic swelling and an additive manufacturing technique called Selective Laser Melting (SLM). In chapter 2 first, a review of the current literature is presented to model swelling of polymers based on the equilibrium thermodynamic theory. The theory has been improved by the author via adding two more terms to the main governing equation. Although it still lacks the capability of modelling highly swellable polymers. To tackle this, an alternative non-equilibrium theory is developed based on the Gibbs free energy by the author to explain large swelling of highly swellable polymers. Last but not least, a new numerical method is suggested to analyse the degradation of highly swellable polymers during large swelling.

In chapter 3, a detailed literature review of material point method is conducted and is later used as the main numerical approach in this thesis. Furthermore, the topological systems that have been used in my code are discussed in details that come along with a flowchart of the MPM code.

In chapter 4, the MPM code that is developed by the author is validated for a 1D simple forced vibration problem against the results of conventional FEM. Furthermore, in this chapter, the MPM code is validated through a series of 2D tensile tests.

In chapter 5, firstly, a rate form of a nonlinear constitutive law for hyperelastic materials is developed based on Flory's theory. Secondly, the nonlinear constitutive law is fitted in the MPM code through a convenient tangent modulus and the code is validated via a series of large tensile tests. Next, non-uniform swelling is discussed and the MPM code is tailored to model large non-uniform swelling of polymers. Finally, it is demonstrated that MPM is a robust numerical tool to simulate the degradation of highly swellable polymers during large non-uniform swelling in different applications such as in controlled drug delivery systems.

Chapter 6 is demonstrating the capability of MPM to simulate an additive manufacturing method called Selective Laser Melting (SLM) as an industrial application of the MPM for small deformation analysis. In this chapter, the main concerns in the simulation of the SLM are discussed. Generally, conventional finite element methods struggle to deal with the SLM process. Therefore, a simple case study is modelled with the validated MPM in two dimensions to prove this method is strong enough to perfectly solve real cases for industrial purposes.

This thesis will be finished with the conclusion in chapter 7.

Chapter 2. Introduction to Nonlinear Finite Element Method

This chapter is to first provide a review of the current literature detailing the simulation of materials such as polymers under large deformations, based on equilibrium thermodynamic theory and secondly, to present a non-equilibrium thermodynamic theory for large deformation of highly swellable polymers due to solvent mixing. Furthermore, a discussion is provided on why traditional numerical tools such as conventional Finite Element methods cannot be used for problems such as degradation of highly swellable polymers during large swelling and also for simulation of Selective Laser Melting. Last but not least Material Point Method is introduced briefly as a robust numerical tool to model the swelling and degradation of highly swellable polymers.

2.1 Equilibrium thermodynamic theory of polymer swelling

In this chapter, polymer swelling is used as an example to demonstrate the underlying theory for large deformation of materials. Following the works are done by W. Hong et al. (2007) and M. Kang and R. Huang (2010) in this section a field theory of the gels is explained which is based on the classic works done by J.W. Gibbs (1878) and M.A. Biot (1941).

2.1.1 Variational approach

A polymer network in the hydrogel state is considered at the current state with the volume Ω and the surface Γ . The hydrogel body is subjected to a distributed body force b_i and a surface traction τ_i . Furthermore, a chemical potential $\hat{\mu}$ (per solvent molecule) is subjected to the hydrogel body as it is dipped in a solvent. Solvent molecules can go across the surface Γ and also through the body of the hydrogel. Figure 2-1 shows a schematic hydrogel of the reference configuration with volume Ω_0 and surface Γ_0 at the initial time that changes through the time and finally reaches the equilibrium state.

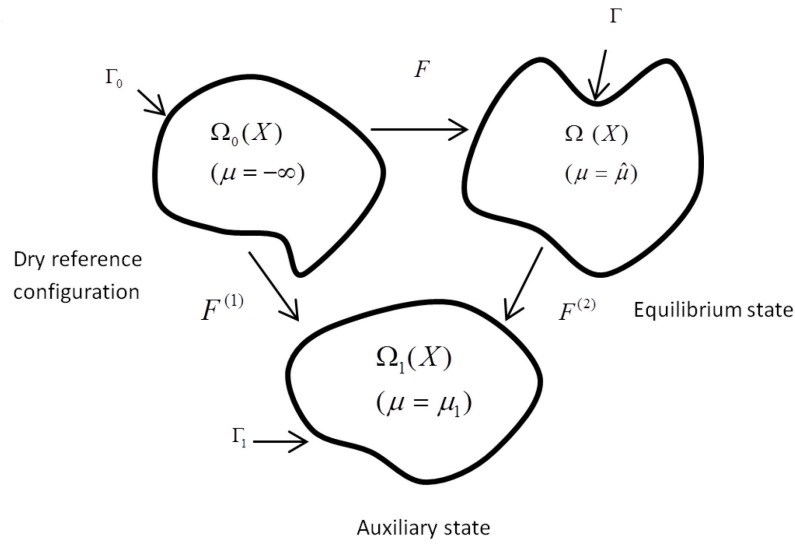


Figure 2-1 Schematic deformation of the reference configuration. M. Kang and R. Huang (2010)

2.1.2 Calculation of the total work

According to the virtual work principle, in order to calculate the total work done to the hydrogel, including mechanical forces such as the body force and the surface traction and chemical work due to the absorption of the solvent molecules, an infinitesimal displacement is assumed in either mechanical displacement and/or molecular transport. Eq. (2-1) is calculating the total work:

$$\delta W = \int_{\Omega} \rho b_i \delta x_i d\Omega + \oint_{\Gamma} \tau_i \delta x_i d\Gamma - \oint_{\Gamma} \hat{\mu} n_k \delta i_k d\Gamma \quad (2-1)$$

In Eq. (2-1) δx_i represents the variation of the current position of the body, and δi_k represents the variation of the molecular flux that is equal to the number of solvent molecules going through, per unit area of the element with respect to the unit normal vector in the direction of x_k . n_k is the unit normal vector with positive outwards direction, and $-n_k \delta i_k$ is the vector product that gives the number of solvent molecules entering the polymer network across the surface per unit area of the surface. ρ is the mass density, b is the body force, and τ is the surface traction and $\hat{\mu}$ is a solvent environment chemical potential (per solvent molecules). Other terms such as work done by temperature or magnetic field could be considered in the above formula that is

beyond the scope of this thesis. Also, mass transport from solvent to the polymer network is considered to be only due to chemical potential and any distributed pump is ignored in this thesis.

The variation of the total free energy of the thermodynamic system which is including the gel, the mechanical fields and the field of chemical potential is based on the variation of the free energy of the hydrogel and the mechanical/chemical environment that is shown in Eq. (2-2).

$$\delta G = \delta \Phi - \delta W \quad (2-2)$$

In Eq.(2-2) δG is a variation of the total free energy of the thermodynamic system, $\delta \Phi$ is a variation of total free energy of hydrogel and δW is total work done to the hydrogel. Based on the general principals of thermodynamics, any system tends to reduce its total free energy, so for any thermodynamically permissible variation $\delta G \leq 0$. The equality is for the thermodynamical equilibrium state.

2.1.3 Free energy density function for the hydrogels

Based on Flory's work (1953), a free energy density function is assumed as $u(F, C)$, which is a function of deformation gradient tensor F and solvent molecular concentration in the hydrogel C . Hence, a variation of the total free energy of the hydrogel is shown in Eq. (2-3).

$$\delta \Phi = \delta \left(\int_{\Omega} u d\Omega \right) \quad (2-3)$$

Therefore, in order to be able to analyse the swelling deformation of the hydrogel, a functional form of the free energy density u is required, this is introduced in chapter 6 and is based on Flory's theory (1953).

2.1.4 Mass Conservation

According to the conservation of mass the below equations can be obtained:

$$\frac{\partial C(x, t)}{\partial t} + \frac{\partial J_k(x, t)}{\partial x_k} = 0 \quad (2-4)$$

$$(J_k^+(x, t) - J_k^-(x, t))n_k(x, t) = 0 \quad (2-5)$$

In Eq. (2-5) $J_k(x, t)n_k$ represents the number of solvent molecules going through the element of area, whereas $C(x, t)$ in Eq. (2-4) signifies the number of solvent molecules in an element of volume.

By using a test function $\xi(x)$ and integrating Eq. (2-4) over the total volume of the gel we have:

$$\int_{\Omega} \frac{\partial C}{\partial t} \xi d\Omega + \int_{\Omega} \frac{\partial J_k}{\partial x_k} \xi d\Omega = 0 \quad (2-6)$$

By applying divergence theorem to Eq. (2-6) and using Eq. (2-4).

$$\int_{\Omega} \frac{\partial C}{\partial t} \xi d\Omega = \int_{\Omega} J_k \frac{\partial \xi}{\partial x_k} d\Omega \quad (2-7)$$

2.1.5 Total Free energy

As it was mentioned in section 2.1.2 the total free energy of the thermodynamic system G is cumulating of the total free energy of the hydrogel, potential energy of the mechanical forces and chemical potential energy. By using Eq. (2-1), Eq. (2-2), and Eq. (2-3) the rate of changes in total free energy will be obtained as below:

$$\frac{\delta G}{\delta t} = \int_{\Omega} \frac{\delta u}{\delta t} d\Omega - \int_{\Omega} \rho b_i \frac{\delta x_i}{\delta t} d\Omega - \int_{\Gamma} \tau_i \frac{\delta x_i}{\delta t} d\Gamma + \int_{\Gamma} \hat{\mu} m_k \frac{\delta i_k}{\delta t} d\Gamma \quad (2-8)$$

By substituting the mathematical variation of the free energy of the hydrogel as it is given in Eq. (2-9) in the first term of the right hand side of Eq. (2-8), and also using the dynamic force balance in continuum mechanics as in Eq. (2-10) and (2-11) We will obtain Eq.(2-12).

$$\delta u = \frac{\partial u}{\partial F} \delta F_{ik} + \frac{\partial u}{\partial C} \delta C \quad \text{in } \Omega \quad (2-9)$$

$$\frac{\partial s_{ik}}{\partial x_k} + \rho_i b_i(x, t) = \rho_i \dot{v}_i(x, t) \quad \text{in } \Omega \quad (2-10)$$

$$(s_{ik}^-(x, t) - s_{ik}^+(x, t))n_k(x, t) - \tau_i(x, t) = \rho_i l_i \dot{v}_i(x, t) \quad \text{on } \Gamma \quad (2-11)$$

Where $s_{ik}(x, t)$ in Eq. (2-10) is the nominal stress tensor and $\dot{v}(x, t)$ is the acceleration, l_i in Eq. (2-11) is the length of each element of the mesh.

$$\begin{aligned} \frac{\delta G}{\delta t} = & \int_{\Omega} \frac{\partial u}{\partial F_{ik}} \frac{\delta F_{ik}}{\delta t} d\Omega + \int_{\Omega} \frac{\partial u}{\partial C} \frac{\delta C}{\delta t} d\Omega - \int_{\Omega} \frac{\partial s_{ik}}{\partial x_k} - \rho_i \dot{v}_i(x, t) \frac{\delta x_i}{\delta t} d\Omega - \\ & \int_{\Gamma} (s_{ik} n_k - \rho_i x_i \dot{v}_i(x, t)) \frac{\delta x_i}{\delta t} d\Gamma + \int_{\Gamma} \hat{\mu} n_k \frac{\delta \tilde{t}_k}{\delta t} d\Gamma \end{aligned} \quad (2-12)$$

Furthermore, by applying the divergence theorem Eq. (2-12) can be written as:

$$\begin{aligned} \frac{\delta G}{\delta t} = & \int_{\Omega} \left(\frac{\partial u}{\partial F_{ik}} - s_{ik} \right) \frac{\delta F_{ik}}{\delta t} d\Omega + \int_{\Omega} J_k \frac{\partial}{\partial x_k} \left(\frac{\partial u}{\partial C} \right) d\Omega - \int_{\Omega} \rho_i \dot{v}_i(x, t) \frac{\delta x_i}{\delta t} d\Omega + \\ & \int_{\Gamma} \rho_i x_i \dot{v}_i(x, t) \frac{\delta x_i}{\delta t} d\Gamma - \int_{\Gamma} \left(\frac{\partial u}{\partial C} - \hat{\mu} \right) n_k \frac{\delta \tilde{t}_k}{\delta t} d\Gamma \end{aligned} \quad (2-13)$$

As it was discussed in section 2.1.2, based on the thermodynamic principles, the total free energy of a system must be decreasing, i.e. $\delta G \leq 0$, which means this should be true for any arbitrary J_k and $\frac{\delta x_i}{\delta t}$.

In Eq. (2-13) each term represents a specific mechanism of energy dissipation. While the first term on the right hand side expresses the local rearrangement of the small molecules, the second term represents the long-term migration of the small molecules. The third and fourth terms denote acceleration of the molecules inside the volume and on the surface respectively. As opposed to (Hong et. al. 2007) in this thesis the process of local rearrangement of the molecules is not assumed to be instantaneous. Basically, they have assumed the process is made of a series of small processes that each one is in mechanical equilibrium conditions. (i.e. viscosity of the hydrogel in local rearrangement of the molecules is ignored in their theory). Therefore, the third and fourth terms on the right hand side of Eq. (2-13) are added to consider the effect of viscosity of the hydrogel either inside the gel or on the surface. The last term on the right hand side of Eq. (2-13) signifies chemical potential of the solvent molecules that is diffused into the hydrogel.

A hydrogel evolves over time when it is under the mechanical loads, which is held constant through the time. Two different limiting states can be analysed based on the time evolution of the hydrogel. In short time limit, the solvent molecules that are penetrated inside the hydrogel has not yet redistributed, but the mechanical governing equation can be obtained from the dynamic force balance in continuum mechanics as shown in Eq. (2-10) and Eq. (2-11). So, if $C(X)$ assumed to be the concentration field

of solvent molecules at the time that load changes, then the short time limit of the hydrogel will be governed by the dynamic forces, stresses that are shown in Eq. (2-14) and also chemical potential that is achieved through Eq. (2-15). The short time limit is as a result of a local rearrangement of molecules.

In the Long time limit, thermodynamic equilibrium state can be assumed in the hydrogel between mechanical load and the external solvent. Therefore, the free energy of the hydrogel should be the minimum that leads to $\delta G / \delta t = 0$ so that the second integrand in the right hand side of Eq. (2-13) must be zero. Accordingly, at the equilibrium state, the chemical potential is homogeneous inside the gel, which can be obtained from the external solvent. This should be mentioned that thermodynamic equilibrium state is different from mechanical equilibrium state. As the system is thermodynamically in the equilibrium state and the left hand side of Eq. (2-13) is zero, so the third and the fourth integrand must vanish which leads to zero acceleration of the solvent molecules inside the hydrogel and at the surface of the hydrogel at the equilibrium state. So, the long time limit state will be determined by force balance equations in Eq. (2-10), and Eq. (2-11) while the acceleration terms inside the hydrogel and at the surface are both zero, also Eq. (2-14) and Eq.(2-15) are the stresses and chemical potential inside the hydrogel.

Furthermore, as at the equilibrium state $\delta G = 0$, so the left hand side of Eq. (2-13) is zero, therefore by using the advantage of variational approach each term on the right hand side can be zero. Consequently, the first integrand in Eq. (2-13) vanishes, leading to

$$s_{ik} = \frac{\partial u(F, C)}{\partial F_{ik}} \quad (2-14)$$

Furthermore, local equilibrium is assumed between small molecules. Therefore, the fifth integrand in Eq. (1. 13) vanishes, leading to

$$\mu = \frac{\partial u(F, C)}{\partial C} \quad (2-15)$$

Hence, by assuming the local equilibrium condition, the stress values can be obtained from the derivative of the free energy density of the hydrogel with respect to the deformation gradient, and the chemical potential of the solvent molecules that are

penetrated inside the hydrogel is equal to the derivative of the free energy density of the hydrogel with respect to the concentration of the solvent molecules inside the hydrogel. Therefore, a functional form of the free energy density $u(F, C)$ is required to be able to derive the equations of state. Flory's approach is taken in chapter 5 to define a functional form of the free energy density of the hydrogel and derive the equations of state.

However, the above Equilibrium thermodynamic theory looks like a decent theory to analyse the behaviour of the hydrogel, (i.e. the polymer in contact with solvents), still cannot be used for highly swellable materials. As it was discussed earlier, the short time limit is when the solvent molecules are not yet redistributed, while highly swellable materials extremely deform in this situation. Therefore, equilibrium thermodynamic theory is not capable of analysing fast changes of the hydrogel for highly swellable materials in the short time limit. Hence, another non-equilibrium thermodynamic theory is required to deal with the short time limit.

2.2 Non-equilibrium thermodynamic theory

2.2.1 Variation of total work done by the body force over the volume

In this approach, another field theory of the gels is developed by the author that is based on the variational approach that leads to a non-equilibrium thermodynamic theory. A polymer network in the hydrogel state is considered at the current state with the volume Ω and the surface Γ . Figure 2-2 shows a polymer network, in which P_i is a body force applied to the molecules, m_1 is the number of molecules that move due to the body force and u_i is the drift velocity vector. The differential form of the variation of the total work done by the body force over the volume Ω is given in Eq. (2-16).

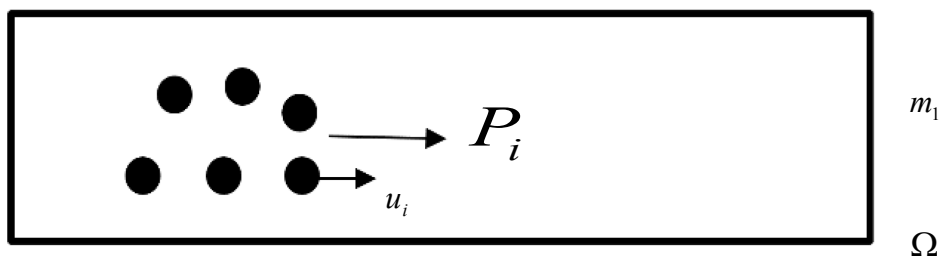


Figure 2-2 schematic diagram of a polymer network under a body force F and a velocity field u .

$$\delta\dot{W} = m_1.P_i.\delta u_i \quad (2-16)$$

The total work per unit volume can be written as

$$\delta\dot{w} = \frac{m_1}{\Omega}.P_i.\delta u_i = c_1.P_i.\delta u_i \quad (2-17)$$

In Eq. (2-17) c_1 is the number of the molecules per unit volume inside the hydrogel, and δu is the variation of the drift velocity vector.

Next, a linear relationship between drift velocity and the body force is assumed, which is shown in Eq. (2-18).

$$u_i = M.P_i \quad (2-18)$$

In which M is the mobility. Furthermore, flux can be defined as below

$$j_i = c_1 u_i \quad (2-19)$$

Therefore, the variational form of the flux can be written as

$$\delta j_i = c_1 \delta u_i \quad (2-20)$$

Hence, by substituting Eq. (2-18) and Eq. (2-20) into Eq. (2-17) it changes to

$$\delta\dot{w} = \frac{j_i}{M c_1} \delta j_i \quad (2-21)$$

Finally, the variation of total work done by the body force over the volume is

$$\delta\dot{W} = \int_{\Omega} \frac{j_i}{M c_1} \delta j_i d\Omega \quad (2-22)$$

2.2.2 Gibbs free energy

The Gibbs free energy of the total system for a constant pressure process is

$$G = \Delta H - T\Delta S \quad (2-23)$$

In which ΔH is the enthalpy change at constant pressure, and ΔS is the entropy change of the system, and T is the temperature. Eq. (2-23) shows when the entropy change is positive, there is a negative change in the total free energy of the system. As all the parameters in the free energy equation are defined in terms of changes in the system, we only need to simply check whether or not the free energy change is negative for a

given mixing problem. By simplifying Eq. (2-23) for a swelling problem, we can assume that

$$G_m = -T\Delta S_m \quad (2-24)$$

For any mixing problem obviously the entropy of the system will be increased, hence the free energy change should be negative. As the entropy of the system is related to the energy of interaction between the molecules and the number of arrangements available to the system, so it would be rational to relate the entropy to the molecular quantities.

2.2.3 Entropy of mixing

According to the Boltzmann's equation shown in Eq. (2-25) and considering statistical mechanics the entropy of the system is equal to

$$S = k \ln \Phi \quad (2-25)$$

In which Φ is the total number of configurations that is possible to happen in the mixing of two different materials, and k is the Boltzmann's constant.

For the simplest problem of mixing two materials with the same spherical size particles A and B the total number of possible configuration can be proved to be

$$\Phi = \frac{(n_A + n_B)!}{n_A!n_B!} \quad (2-26)$$

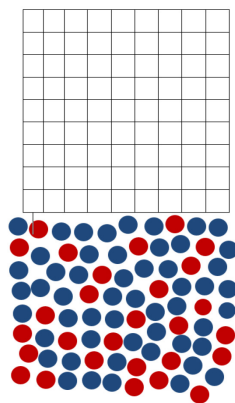


Figure 2-3 Schematic diagram, shows empty lattice that can be filled with two different spherical molecules randomly. Painter P. C., Coleman M. M., (2009).

In which n_A and n_B are the total number of spherical particles of materials A and B respectively. Therefore, the Boltzmann's equation can be written in terms of mole fractions as shown below by using Stirling approximation ($\ln(n!) \approx n \ln(n) - n$)

$$-\Delta S_m = k(n_A \ln x_A + n_B \ln x_B) \quad (2-27)$$

In Eq. (2-27) x_A and x_B are the mole fractions of materials A and B respectively that are given in Eq. (2-28) and Eq. (2-29) respectively.

$$x_A = \frac{n_A}{n_A + n_B} \quad (2-28)$$

$$x_B = \frac{n_B}{n_A + n_B} \quad (2-29)$$

But, mixing of two different materials with different particle size is desirable in the swelling problem, as the polymer chains (molecules) are far larger than the solvent molecules. Following an earlier suggestion by Fowler and Guggenheim (1941), Flory and Huggins (1953) independently used a model which assumes larger molecules such as a polymer can be treated as a set of linked segments Painter P. C., Coleman M.M. (2009). By substituting Eq. (2-27) into Eq. (2-24)

$$G_m = -T\Delta S_m = Tk(n_A + n_B)(x_A \ln x_A + x_B \ln x_B) \quad (2-30)$$

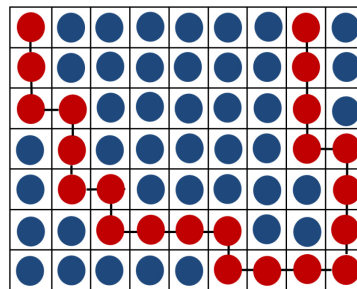


Figure 2-4 Schematic diagram shows a filled lattice with small size (low molecular weight) molecules represent solvent molecules in blue and connected red balls represent segments of a polymer chain. Painter P. C., Coleman M. M., (2009).

Where n_A and n_B are the total number of solvent molecules and polymer molecules respectively. Also x_A and x_B are the mole fractions of materials A and B (i.e. solvent and polymer) as before.

In order to get the free energy density, both side of Eq. (2-30) should be divided by the total volume Ω . Let's take $Z = \Omega / (n_A + n_B)$ and define c_A and c_B as the concentration of the solvent molecules and polymer molecules respectively as shown in Eq. (2-31) and Eq. (2-32).

$$c_A = \frac{x_A}{Z} \quad (2-31)$$

$$c_B = \frac{x_B}{Z} \quad (2-32)$$

Furthermore, the concentration of the solvent molecules is far more than the concentration of the polymer molecules, due to the sizes of the molecules. Hence, approximately the total free energy density is equal to

$$g_m = \frac{G_m}{\Omega} \approx kT [c_A \ln(c_A Z)] \quad (2-33)$$

Therefore, the total free energy of mixing over the volume is equal to

$$G_m = \int_{\Omega} g_m d\Omega = \int_{\Omega} kT [c_A \ln(c_A Z)] d\Omega \quad (2-34)$$

By differentiating Eq. (2-34) with respect to time and using the chain rule we have

$$\dot{G}_m = \int_{\Omega} \frac{\partial g_m}{\partial c_A} \frac{\partial c_A}{\partial t} d\Omega = \int_{\Omega} \eta \frac{\partial c_A}{\partial t} d\Omega \quad (2-35)$$

In which $\eta = \frac{\partial g_m}{\partial c_A}$ can be obtained from Eq. (2-33). Hence, the variational form of Eq.

(2-35) can be written as

$$\delta \dot{G}_m = \int_{\Omega} \eta \delta \left(\frac{\partial c_A}{\partial t} \right) d\Omega \quad (2-36)$$

According to the conservation of the energy in the system, the summation of the total free energy of mixing of the system should be equal to the negative of the total work done by the force, or it can be written as

$$\delta\dot{W}_m + \delta\dot{G}_m = 0 \quad (2-37)$$

By substituting Eq. (2-22) and Eq. (2-36) into Eq. (2-37) it can be shown that:

$$\int_{\Omega} \left[\frac{j}{Mc_1} \delta\dot{j} + \eta \delta \left(\frac{\partial c_A}{\partial t} \right) \right] d\Omega = 0 \quad (2-38)$$

Following Eq. (2-4) it can be shown that,

$$\delta \left(\frac{\partial c_A}{\partial t} \right) = - \frac{\partial \delta\dot{j}}{\partial x} \quad (2-39)$$

Therefore by substituting Eq. (2-39) into Eq. (2-38) it gives

$$\int_{\Omega} \left[\frac{j}{Mc_1} \delta\dot{j} - \eta \frac{\partial}{\partial x} (\delta\dot{j}) \right] d\Omega = 0 \quad (2-40)$$

By simplifying Eq. (2-40) in 1D it can be shown that

$$\int_x \left[\frac{j}{Mc_1} \delta\dot{j} - \frac{\partial}{\partial x} (\eta \delta\dot{j}) + \frac{\partial \eta}{\partial x} \delta\dot{j} \right] dx = 0 \quad (2-41)$$

By applying the integration over the above equation it can be written as

$$\int_x \left[\frac{j}{Mc_1} + \frac{\partial \eta}{\partial x} \right] (\delta\dot{j}) dx - \eta \delta\dot{j} \Big|_x = 0 \quad (2-42)$$

In Eq. (2-42) each term represents a specific mechanism of the flux of the solvent molecules. Taking the advantage of variational approach, the second term on the left hand side which represent the flux over the boundary must vanish means there is no flux in or out at the boundaries.

The first term on the left hand side of Eq. (2-42) must also vanish, that leads to an equation of flux of solvent molecules inside the hydrogel, as shown below

$$j = -Mc_A \frac{\partial \eta}{\partial x} \quad (2-43)$$

According to Eq. (2-33) η can be shown as below

$$\eta = \frac{\partial g_m}{\partial c_A} = kT \left[\ln(c_A Z) + \frac{1}{Z} \right] \quad (2-44)$$

Therefore,

$$\frac{\partial \eta}{\partial x} = \frac{kT}{c_A} \frac{\partial c_A}{\partial x} \quad (2-45)$$

By substituting Eq. (2-45) to Eq. (2-43)

$$j = -MkT \frac{\partial c_A}{\partial x} \quad (2-46)$$

Eq. (2-46) is very similar to the Fick's law of diffusion that can explain the behaviour of solvent molecules inside the hydrogel. By comparing Eq. (2-46) and Fick's law of diffusion given in Eq. (2-47) a constant value will be obtained for M .

$$j = -D \frac{\partial c_A}{\partial x} \quad (2-47)$$

Therefore,

$$M = \frac{D}{kT} \quad (2-48)$$

So, our initial assumption in Eq. (2-18) is now proved that, there is a linear relationship between the force which is applied to the solvent molecules and the velocity vector. Therefore, in the numerical simulation of the swelling problem, a constant stress is applied to all the material points through the time. This simulation is based on Material Point Method that is discussed in chapter 3.

2.3 Numerical approach to model large swelling of highly swellable polymers

2.3.1 Introduction

Highly swellable polymers form a jelly phase when they are in contact with a solvent. Hydrogels can undergo large and recoverable deformations. Swelling of a polymer is also a large deformation procedure that can happen as a result of diffusion of solvent molecules into the polymer network due to chemical potential, and form an aggregate that is called a polymeric hydrogel. By increasing the number of solvent molecules inside the hydrogel, hydrogen bonding breaks between the polymer chains. Therefore, polymer chains achieve more rotational freedom and finally swelling happens as a result of decreasing the forces between the polymer networks. Therefore, polymer swelling is brought about by the concentration of the solvent molecules which is diffused inside

the polymer due to the chemical potential. Hence, in order to calculate the nominal stresses, the governing equations in Eq.(2-14) and Eq.(2-15) must be solved for stresses and chemical potential. Based on the non-equilibrium thermodynamic theory that was discussed in section 2.2, it was proposed there is a linear relationship between the applied body force to the polymer and the displacement as stated in Eq. (2-18). In this thesis instead of solving the governing equations, we have only focused on the large elastic deformations as a consequence of the nominal stresses. Therefore, a computer program based on the MPM is designed to work for a range of arbitrary constant stresses. Hence, instead of solving the actual governing equations for nominal stresses and chemical potential, alternatively, we have assumed a range of known constant stresses which are each applied to the polymer like an initial body force. Therefore, the computer program will be able to work for more realistic values of stresses and chemical potential when required. In section 2.4.4 the numerical approach that is used in this thesis is discussed and the MPM is reviewed in details in chapter 3.

2.3.2 General introduction to Finite Element Method (FEM)

Over the last few decades, testing of the prototypes via computer aided design has been enormously increased. The most significant effect of the computer aided design is to increase the speed of simulations and testing. Partial differential equations (PDE) that are used in mathematical modelling of different physical, chemical and biological phenomena are often too complicated to be analytically solved. Therefore, there is a large range of numerical schemes for solving these PDEs. Numerical simulations all have their own limitations. Finite Element Method (FEM) is a powerful numerical technique which can be used to find an approximate solution for PDEs, which is used to simulate engineering problems, for both evaluations of early designs and also testing details of the final design. Another significant advantage of FEM is that it can be used for the problem especially with complicated and irregular geometries and also with complicated boundary conditions. FEM is based on the classical works done by Leonard Euler (1707-1783) that is based on the minimum total potential energy principle. There are various techniques in the conventional FE analysis to simulate different problems including linear/non-linear, static/dynamic, steady state/transient, and coupled or uncoupled problems in 1D, 2D or 3D. Conventional nonlinear FEM has been used in

many fields of manufacturing such as casting, sheet-metal processing, aviation industries as well as automotive industries. However, these days different commercial packages of FE are available, understanding the fundamental concepts of non-linear FE is essential for both analysts and developers. Also, the key reason of why we need a nonlinear FE analysis in our project has been clarified. Furthermore, it has been discussed why material point method has been employed for numerical modelling and why the conventional FE methods are not sufficient enough to simulate the targeted problem in this thesis.

Generally, in order to solve PDEs by using finite element method, first of all, the PDEs must be transformed into a set of equivalent variational or weak forms based on the variational principle. Next, the geometry needs to be discretised; therefore a finite element mesh needs to be generated following the listed guidelines below:

1. The mesh should be an accurate representation of the geometry of the computational domain and the load distribution of the problem.
2. The mesh should be fine enough to accurately represent large gradients in the solutions.
3. The mesh can consist of different types or orders (i.e. triangular and quadrilateral, linear and quadratic)

Choosing the type and order of the mesh is very problem-dependent (i.e. one mesh may perfectly work for one problem but may not work well for another). There is always a concern to use a sufficient refined mesh for the problem to be converged. Therefore, an analyst should have a physical insight view of the problem to make a better choice of the elements and handle the simulating process. The simulation will be started with using a fair course mesh that should meet all the three requirements listed above and evaluate the results, that should be in light of a physical understanding of the problem and give an approximate analytical and/or experimental information which is available. In Figure 2-5 and Figure 2-6 a few different computational domain have been illustrated that are discretised by a set of triangular elements.

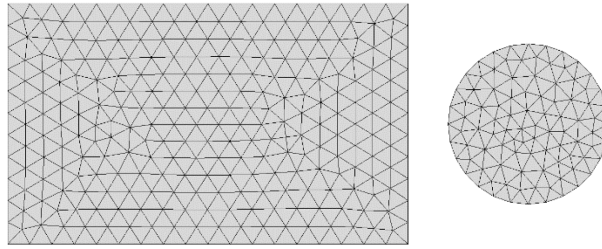


Figure 2-5 illustrate 2D discretised computational domains with triangular elements for different geometries.

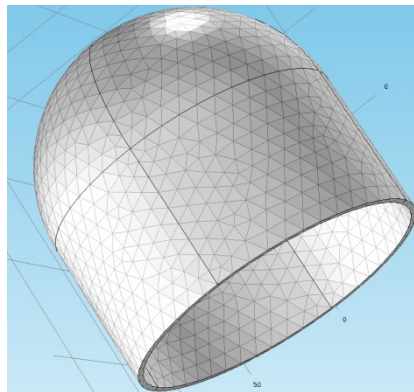


Figure 2-6 Figure shows a 3D geometry which has been discretised with triangular elements.

In order to solve partial differential equations globally with FEM, the total computational domain should be transformed to a set of subdomains and therefore, by using the approximation functions the PDEs can be replaced by a set of matrix equations that take the form of linear and non-linear algebraic equations, or maybe ordinary differential equations in the time variable. As it was mentioned in earlier by using the shape functions PDEs can be replaced with a set of matrix equations that can be linear and non-linear algebraic equations. Using non-linear shape functions or non-linear constitutive laws (stress-strain laws) in some cases such as when there is material non-linearity or geometrical non-linearity is inevitable. The structure in this thesis is based on the non-linear large elastic deformation of hyper-elastic materials. Therefore, it is necessary to introduce non-linear finite element methods as well.

2.4 A brief history of nonlinear finite element method

Due to the extensive applications of nonlinear finite element methods, several books and articles have already been published. A Book such as Oden (1972) which is

particularly important as Oden pioneered the field of nonlinear finite element method. Furthermore, some books are written particularly in the nonlinear FE field such as Belytschko and Hughes (1983), Zienkiewicz and Tylor (1991). One recent book is written by Wu and Gu (2012). One of the most recent papers on nonlinear, transient finite element method is published by N. Bouklas et.al. (2015).

2.4.1 Introduction to nonlinear finite element method

A combination of three different fields represents the nonlinear finite element method: (1) Linear finite element methods that are based on the matrix methods of structural analysis; (2) Nonlinear continuum mechanics; and (3) mathematics, including numerical analysis. Two kinds of nonlinearity can happen in finite element analysis of solid materials: (1) Nonlinearity due to the material, as a result of complicated nonlinear relationship between stresses and strains that cause the equation coefficients to be depending on the solution; (2) Geometrical nonlinearity, which is also known as 'large strain' or 'large deformation' analysis. It is always simpler to implement material nonlinearity than geometrical nonlinearity. In practice, there are two main approaches that can be adopted to simulate material nonlinearity. The first method involves constant stiffness that means by iteratively modifying the right hand side loads vector the introduced nonlinearity will be addressed. Therefore, the elastic global stiffness matrix is formed once only. This means each iteration includes a static equilibrium elastic analysis of solids. So convergence can be tested when the generated stresses by the loads can satisfy yield or failure criterion within prescribed tolerances. The load's vector at each iteration includes external forces and also body forces. Basically, the effect of the body forces is to redistribute stresses or (moments) within the system, but they don't change the net loading of the system, as they are self-equilibrating. The constant stiffness method is shown schematically in Figure 2-7. The problem with this method is that elastic constant global stiffness matrix highly overestimate the material stiffness, therefore it requires a huge number of iterations. I. M. Smith and D. V. Griffiths, (2004).

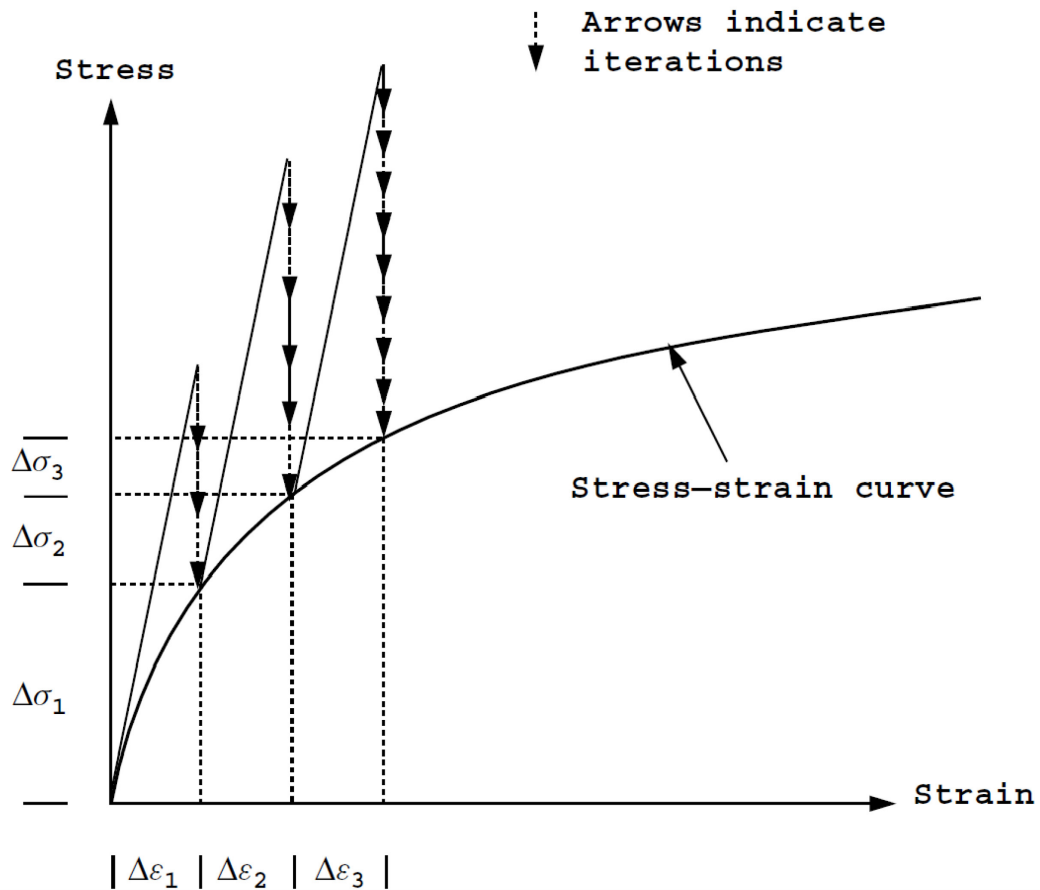


Figure 2-7 the constant stiffness method. I. M. Smith and D. V. Griffiths (2004)

The second approach is called variable or tangent stiffness method. This method considers the reduction of stiffness of the material as failure is approached. This method is equivalent to the explicit Euler method if small enough load steps are taken. Practically in this method, the global stiffness matrix will be updated on a periodic basis, and body load iterations are used to finally achieve convergence. Variable stiffness method is shown graphically in Figure 2-8. The advantage of variable stiffness method over the constant stiffness method is that it needs fewer iterations, but on the other hand it has an extra cost of reforming and factorising the global stiffness matrix. In the next section, a brief discussion is given about the types of constitutive laws (stress-strain laws) that should be adopted for these introduced methods I. M. Smith and D. V. Griffiths (2004).

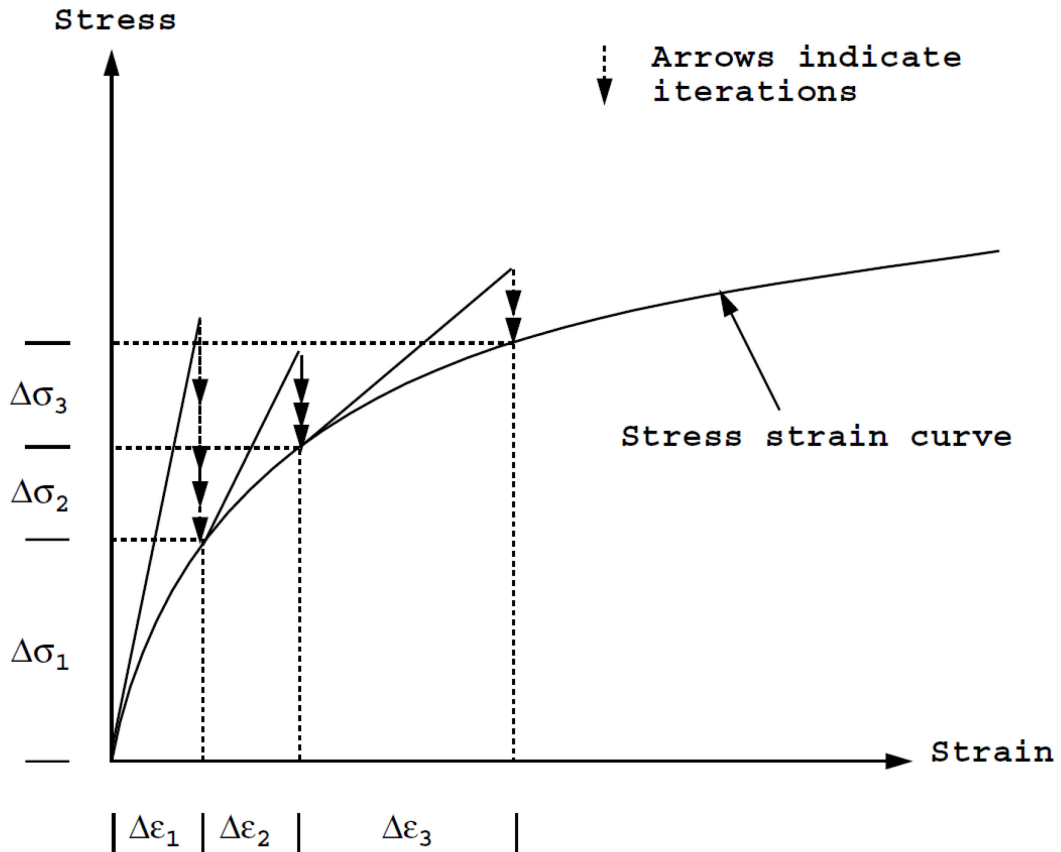


Figure 2-8 the variable or tangent stiffness method. I. M. Smith and D. V. Griffiths (2004).

2.4.2 Stress-strain laws

In nonlinear FEM analysis, it is essential to use a nonlinear constitutive law which means a nonlinear relationship between the stresses and strains. In solid mechanics, it depends on the nature of the problem whether the material is going through large elastic deformation or it undergoes plastic deformation. Different constitutive laws are available that are coming from elasticity theories or plasticity theories. Here in this thesis, we have focused on the large nonlinear elasticity.

2.4.3 Nonlinear elasticity

The constitutive law for elastic large deformation can be simply illustrated in the special case of Kirchhoff material, which is actually a straightforward generalization of linear elasticity for large elastic deformations, such as many engineering problems that involve small strains and large rotations. The criterion to measure the elasticity of the material model is the degree of path independency, which is related to the reversibility and non-dissipative behaviour of the material. Hypo-elastic materials are the most weakly path-

independent in the category of elastic materials and followed by Cauchy elasticity, that the stress is path-independent but the energy is not. Hyper-elastic or Green elastic materials are fully reversible and path-independent, and the stress values can be derived from strain energy potential. In this thesis, a simulation of large swelling of hyper-elastic materials is presented in chapter 6, so their mechanical behaviour will be explained in details in chapter 6.

2.4.4 Finite Element Method for non-linear large deformation

Finite element method is basically an accurate method to deal with large deformation simulations. In which normally a numerical constitutive law i.e. stress-strain curve will be fed to the numerical system as an input. The Finite Element Method (FEM) is a robust numerical tool that is frequently used to solve swelling behaviour of polymers Hong et al. (2007). As it was mention earlier FEM is used to find numerical approximations of PDEs. The background dynamic PDE description of polymer swelling can be derived based on the force method as following. As schematically shown in Figure 2-5 a material body with the referenced volume Ω_0 , boundary Γ_0 , initial position x_0 , and initial velocity v_0 deforms through the time with the displacement field u . At any specific time t , the material body occupies volume Ω , surface Γ , at the position x , and the new velocity v . Therefore, the total applied mechanical force to the material body is given by Eq. (2-49).

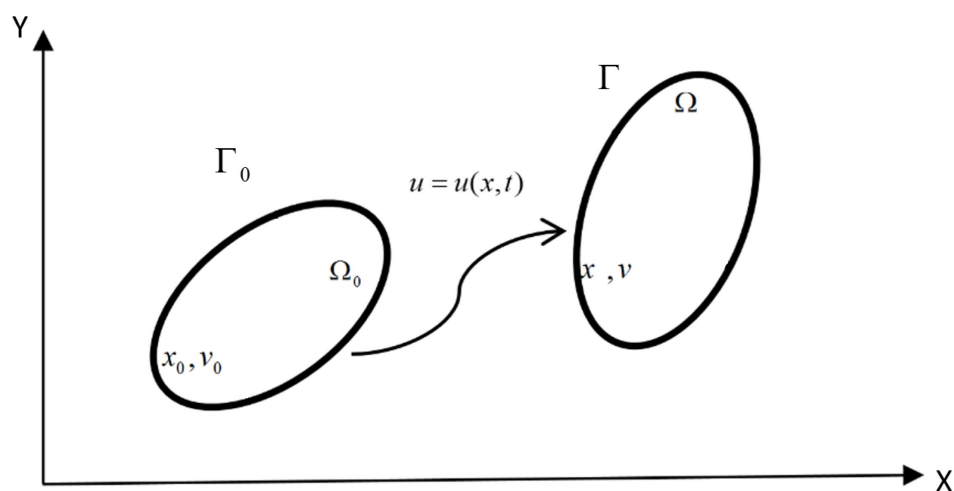


Figure 2- 9 schematic diagram shows material body represented deforms as a function of time and position.

$$f_i(t) = \int_{\Omega} \rho b_i(x,t) d\Omega + \int_{\Gamma} \tau_i(x,t) d\Gamma \quad (2-49)$$

In Eq. (2-49) ρ is the density, b_i is the body force, x_i is the spatial coordinate system, and τ_i is the surface traction. Furthermore, the force due to the chemical potential of the solvent molecules is ignored, as this field is not solved in our numerical calculation in this thesis. Further details are presented in chapter 5. The linear momentum of the body is $p_i(t)$ that is represented by

$$p_i(t) = \int_{\Omega} \rho v_i(x,t) d\Omega \quad (2-50)$$

In which $v_i(x,t)$ is the inertial velocity field of the material body.

Momentum conservation dictates that

$$\begin{aligned} \frac{dp_i(t)}{dt} &= f_i(t) \quad \text{That gives} \\ \frac{d}{dt} \int_{\Omega} \rho v_i(x,t) d\Omega &= \int_{\Omega} \rho b_i(x,t) d\Omega + \int_{\Gamma} \tau_i(x,t) d\Gamma \end{aligned} \quad (2-51)$$

According to Reynold's theorem, (see APPENDIX I) the time derivative of the left hand side of Eq. (2-51) gives

$$\begin{aligned} \frac{d}{dt} \int_{\Omega} \rho v_i(x,t) d\Omega &= \int_{\Omega} \left(\frac{d(\rho v_i(x,t))}{dt} + \rho v_i(x,t) \nabla \cdot (v_i(x,t)) \right) d\Omega = \\ &= \int_{\Omega} \left(\rho \frac{d(v_i(x,t))}{dt} + v_i(x,t) \left(\frac{d\rho}{dt} + \rho \nabla \cdot (v_i(x,t)) \right) \right) d\Omega \end{aligned} \quad (2-52)$$

According to the statement of conservation of mass,

$$\frac{d\rho}{dt} + \rho \nabla \cdot (v_i(x,t)) = 0 \quad (2-53)$$

Therefore, from Eq. (2-51), Eq. (2-52) and Eq. (2-53) can be shown that

$$\int_{\Omega} \rho \frac{d(v_i(x,t))}{dt} d\Omega = \int_{\Omega} \rho b_i(x,t) d\Omega + \int_{\Gamma} \tau_i(x,t) d\Gamma \quad (2-54)$$

By using Gauss theorem which is shown in Eq. (2-55) all the terms in Eq. (2-54) can be merged

$$\int_{\Gamma} \tau_i(x, t) d\Gamma = \int_{\Gamma} n_j \cdot \sigma_{ij}(x, t) d\Gamma = \int_{\Omega} \nabla \cdot \sigma_{ij}(x, t) d\Omega \quad (2-55)$$

Where, σ_{ij} is the Cauchy stress tensor, and n_j is the unit normal vector of the surface Γ the subjected boundary condition in Eq. (2-54) is

$$n_j \cdot \sigma_{ij}(x, t) = \tau_i(x, t) \text{ On } \Gamma . \quad (2-56)$$

Eq. (1. 1) then can be written as

$$\int_{\Omega} \rho \frac{d(v_i(x, t))}{dt} d\Omega = \int_{\Omega} \rho b_i(x, t) d\Omega + \int_{\Omega} \nabla \cdot \sigma_{ij}(x, t) d\Omega \quad (2-57)$$

Or in the differential form, Eq.(2-57) can be written as

$$\rho b_i + \nabla \cdot \sigma_{ij} = \rho \dot{v}_i \quad (2-58)$$

Eq. (2-57) is normally called the strong form, and cannot be solved analytically since it needs the spatial derivative of the stress field. Therefore, a weak form is required to be able to solve this PDE. The weak form is obtained by using virtual work principle.

Hence, Eq. (2-58) can be integrated over the volume

$$\int_{\Omega} \Delta v (\rho b_i + \nabla \cdot \sigma_{ij} - \rho \dot{v}_i) d\Omega = 0 \quad (2-59)$$

By expanding Eq.(2-59) and using indicial form it can be written as

$$\int_{\Omega} \Delta v_i \frac{\partial \sigma_{ji}}{\partial x_i} d\Omega = \int_{\Omega} (-\Delta v_i \rho b_i + \Delta v_i \rho \dot{v}_i) d\Omega \quad (2-60)$$

In which i, j denotes the components of the vectors. According to the chain rule, the left hand side of Eq.(2-60) can be written as

$$\int_{\Omega} \Delta v_i \frac{\partial \sigma_{ji}}{\partial x_i} d\Omega = \int_{\Omega} \frac{\partial}{\partial x_i} (\Delta v_i \sigma_{ji}) d\Omega - \int_{\Omega} \frac{\partial \Delta v_i}{\partial x_j} \sigma_{ji} d\Omega \quad (2-61)$$

Hence by applying the Gauss theorem on the first term of the right hand side of Eq. (2-61), then it changes to

$$\int_{\Omega} \Delta v_i \frac{\partial \sigma_{ji}}{\partial x_i} d\Omega = \int_{\Gamma} \Delta v_i \tau_i d\Gamma - \int_{\Omega} \frac{\partial \Delta v_i}{\partial x_j} \sigma_{ji} d\Omega \quad (2-62)$$

Therefore, by substituting Eq. (2-62) into Eq. (2-61) and rearranging it, the weak form of the Eq. (2-61) will be obtained that can be used as the governing equation in the numerical solutions, as there is no continuity of the stress field in this equation.

$$\int_{\Omega} \frac{\partial \Delta v_i}{\partial x_j} \sigma_{ji} d\Omega - \int_{\Gamma} \Delta v_i \tau_i d\Gamma - \int_{\Omega} \Delta v_i \rho b_i d\Omega + \int_{\Omega} \Delta v_i \rho \dot{v}_i d\Omega = 0 \quad (2-63)$$

The weak form of Eq. (2-63) is used to generate a Lagrangian frame on a finite element mesh in 1D in chapter 3, to validate the results of Material Point Method which is the main numerical frame work of this thesis. Basically, FEM takes the advantage of shape functions to represent the deformation of the material body. The shape functions differ based on the shape of the finite element and number of nodes of each element. Eq. (2-63) can be discretised over each element by using the proper shape functions for the elements, by using the below equations:

$$\tilde{u}_1(x, y, t) = [N_1 \quad N_2 \quad N_3 \quad N_4] \begin{Bmatrix} u_1 \\ u_2 \\ u_3 \\ u_4 \end{Bmatrix} = [N] \{u\} = N_I(x, y) u_I(t) \quad (2-64)$$

$$\tilde{v}_2(x, y, t) = [N_1 \quad N_2 \quad N_3 \quad N_4] \begin{Bmatrix} v_1 \\ v_2 \\ v_3 \\ v_4 \end{Bmatrix} = [N] \{v\} = N_I(x, y) v_I(t) \quad (2-65)$$

Where, \tilde{u} and \tilde{v} are displacement of any points within the elements in X and Y direction respectively. $N_I(x, y)$ is the shape function, and u_I, v_I are the values of displacements of nodes in X and Y direction of a 2D plane respectively and I is the index of nodes. Hence, the velocity of the points can be described as

$$\frac{d\tilde{u}(x, y, t)}{dt} = N_I(x, y) \frac{du_I(t)}{dt} \quad (2-66)$$

$$\frac{d\tilde{v}(x, y, t)}{dt} = N_I(x, y) \frac{dv_I(t)}{dt} \quad (2-67)$$

In order to use the shape functions to discretise equation (2-63), (I.M. Smith and D.V. Griffiths) suggest Table 1:

Terms in Differential equations	Terms in matrix equation	Symmetry
u	$\int N_i N_j dx$	Yes
$\frac{du}{dx}$	$\int N_i \frac{dN_j}{dx} dx$	No
$\frac{d^2u}{dx^2}$	$-\int \frac{dN_i}{dx} \frac{dN_j}{dx} dx$	Yes
$\frac{d^4u}{dx^4}$	$\int \frac{d^2N_i}{dx^2} \frac{d^2N_j}{dx^2} dx$	Yes

Table 1 shows discretisation of different terms in the FEM.

As it was mentioned, by using the shape functions the weak form equation can be discretised as

$$\int_{\Omega} \Delta v_{il} N_I(x_i) \rho \dot{v}_{il} N_I(x_i) d\Omega = \int_{\Gamma} \Delta v_{il} N_I(x_i) \tau_i d\Gamma + \int_{\Omega} \Delta v_{il} N_I(x_i) \rho b_i d\Omega - \int_{\Omega} \left(\Delta v_{il} \frac{\partial N_I(x_i)}{\partial x_j} \sigma_{ji} \right) d\Omega \quad (2-68)$$

By eliminating Δv_{il} from Eq.(2-68) gives

$$\int_{\Omega} N_I(x_i) \rho \dot{v}_{il} N_I(x_i) d\Omega = \int_{\Gamma} N_I(x_i) \tau_i d\Gamma + \int_{\Omega} N_I(x_i) \rho b_i d\Omega - \int_{\Omega} \left(\frac{\partial N_I(x_i)}{\partial x_j} \sigma_{ji} \right) d\Omega \quad (2-69)$$

Eq. (2-69) can be shortly represented at nodes as

$$m \dot{v}_{il} = f_{il}^{ext} - f_{il}^{int} \quad (2-70)$$

In which,

$$m = \int_{\Omega} \rho N_I^T(x_i) N_I(x_i) d\Omega \quad (2-71)$$

$$f_{li}^{int} = \int_{\Omega} \left(\frac{\partial N_I(x_i)}{\partial x_j} \sigma_{ji} \right) d\Omega = \int_{\Omega} (B_{lj} \sigma_{ji}) d\Omega \quad (2-72)$$

$$f_{li}^{ext} = \int_{\Gamma} N_I(x_i) \tau_i d\Gamma + \int_{\Omega} N_I(x_i) \rho b_i d\Omega \quad (2-73)$$

In Which i defines the directions in x,y,z in the Cartesian coordinate system and I represents the node number. The ultimate goal of FEM is to find the deformation of the material body under the applied forces. The equation of motion shown in Eq. (2-70) should be solved at each time step in a Lagrangian framework to find the deformation of each node. Hence, a specific constitutive law is required for the material to find the values of stresses at each node from the strains inside each element. The Constitutive law depends on the material properties, for example, Hook's law is the simplest constitutive law that represents the linear relationship between stress and strain in the elastic zone. Hence, Constitutive laws can be shown as below

$$\sigma = C : \varepsilon \quad (2-74)$$

In which the strains ε are directly calculated from the deformation gradient tensor as introduced in Eq. (2-86), or alternatively, from Eq. (2-76). Also, C is defined in (2-78) that is the tensor of the material properties.

Alternatively, the rate form of constitutive law is shown below

$$\dot{\sigma} = C : D \quad (2-75)$$

D is the tensor of the rate of deformation that is shown in Eq. (2-77) and C is the tensor of the material properties or the tangent modulus. As it was discussed, constitutive laws vary based on the material. Therefore, the tensor of material properties should vary as well. In chapter 5 we have used a specific tangent modulus which is based on the Flory approach. For example, tangent modulus for Neo-Hookean materials will be defined as in Eq. (2-78).

$$\varepsilon = \frac{\partial u}{\partial x} \text{ or } \varepsilon_{ij} = \frac{1}{2} \left(\frac{\partial u_i}{\partial x_j} + \frac{\partial u_j}{\partial x_i} \right) \quad (2-76)$$

$$D = \frac{\partial \dot{u}}{\partial x} \text{ or } D_{ij} = \frac{1}{2} \left(\frac{\partial \dot{u}_i}{\partial x_j} + \frac{\partial \dot{u}_j}{\partial x_i} \right) \quad (2-77)$$

$$C_{ijkl} = \lambda C_{ij}^{-1} C_{kl}^{-1} + \mu (C_{ik}^{-1} C_{jl}^{-1} + C_{il}^{-1} C_{kj}^{-1}) \quad (2-78)$$

Where in the above equations, u_i and \dot{u}_i are the displacements and the velocity term respectively, C_{ijkl} is the tangent modulus for the second Piola-Kirchhoff stress strain tensor, C_{ij} is defined in Eq. (2-83), λ are μ introduced in below.

$$\lambda = \lambda_0 \quad (2-79)$$

$$\mu = \mu_0 - \lambda \ln J \quad (2-80)$$

In which λ_0 and μ_0 are Lamé constants of the linearized theory which are given in Eq. (2-81) and Eq. (2-82) respectively, in terms of Young's modulus and Poisson ratio and $J = \det F$ in which F is the deformation gradient tensor as it is defined in Eq. (2-86).

$$\lambda_0 = \frac{\nu E}{(1-2\nu)(1+\nu)} \quad (2-81)$$

$$\mu_0 = \frac{E}{2(1+\nu)} \quad (2-82)$$

In Eq. (2-78) C_{ij} can be achieved from Green strains as below

$$E_{ij} = (C_{ij} - I) / 2 \quad (2-83)$$

Where, I is the identity matrix, and E_{ij} is the Green strain that is defined as

$$E_{ij} = \frac{1}{2} \left(\frac{\partial u_i}{\partial X_j} + \frac{\partial u_j}{\partial X_i} + \frac{\partial u_k}{\partial X_i} \frac{\partial u_k}{\partial X_j} \right) \quad (2-84)$$

In which X is the material coordinates (Lagrangian coordinate) and u is the displacement function, which is defined as below

$$u_i = x_i - X_i \quad (2-85)$$

We can also define deformation gradient tensor in terms of the displacement function u as below

$$F_{ij} = \begin{bmatrix} \frac{\partial x_1}{\partial X_1} & \frac{\partial x_1}{\partial X_2} \\ \frac{\partial x_2}{\partial X_1} & \frac{\partial x_2}{\partial X_2} \end{bmatrix} = \begin{bmatrix} \frac{\partial u_1}{\partial X_1} + 1 & \frac{\partial u_1}{\partial X_2} \\ \frac{\partial u_2}{\partial X_1} & \frac{\partial u_2}{\partial X_2} + 1 \end{bmatrix} \quad (2-86)$$

Therefore, the Jacobian determinant can also be defined in terms of displacement function.

$$J = \det F = \left(\frac{\partial u_1}{\partial X_1} + 1 \right) \left(\frac{\partial u_2}{\partial X_2} + 1 \right) - \frac{\partial u_1}{\partial X_2} \frac{\partial u_2}{\partial X_1} \quad (2-87)$$

In Eq. (2-86) spatial coordinates are denoted by a small letter x which is also called Eulerian coordinates. As it is shown in Eq. (2-78) the elasticity tensor (tangent modulus) is a fourth-order tensor, but in the 2D simulation, we only need nine component of this tensor. In Eq. (2-88) we have shown Voigt matrix notation of tangent moduli in 2D.

$$\begin{Bmatrix} \dot{S}_{11} \\ \dot{S}_{22} \\ \dot{S}_{12} \end{Bmatrix} = \begin{bmatrix} C_{1111} & C_{1122} & C_{1112} \\ C_{2211} & C_{2222} & C_{2212} \\ C_{1211} & C_{1222} & C_{1212} \end{bmatrix} \begin{Bmatrix} \dot{E}_{11} \\ \dot{E}_{22} \\ \dot{E}_{12} \end{Bmatrix} \quad (2-88)$$

In which \dot{S}_{ij} are the stresses and \dot{E}_{ij} are the rate of green strains that is introduced in Eq.(2-84). It should be mentioned that second elasticity tensor C_{ijkl} has both major and minor symmetry, which means $C_{ijkl} = C_{klij}$ gives major symmetry, and as it relates symmetric measures of stress rate and strain rate, therefore it also has the minor symmetries.

Furthermore, the constitutive laws are shown in Eq. (2-74) and Eq. (2-75) cannot be true in large deformation as shown by Belytschko et al. (2000), because of the wrong measure of stress and strain. Basically, solid rotation in large deformation should be counted, in the stress and strain measures. Figure 2-10 shows an extreme situation of solid rotation of a bar under an initial stress. However the bar undergoes a solid rotation in this figure and the value of strain remain zero, the stress in the X direction changes from σ_0 to zero and stress in the Y direction changes from zero to σ_0 . Therefore, in large deformation analysis, the constitutive laws mentioned earlier have some inappropriate values.

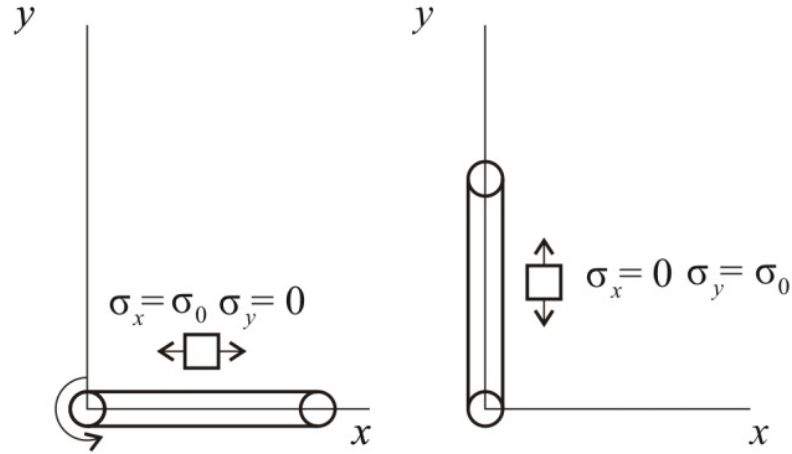


Figure 2-10 Shows an extremely solid rotation of a bar under an initial stress, that change the value stress without changing the value of strain as an effect of solid rotation. F. Li (2008)

In order to cover the effect of solid rotation in large deformation different objective stress rates are defined. Here in this thesis, Jaumann rate is used that is defined as below

$$\dot{\sigma}^{\nabla J} = \dot{\sigma} - W \cdot \sigma - \sigma \cdot W^T \quad (2-89)$$

Where W is the spin tensor that is shown as below

$$W_{ij} = \frac{1}{2} \left(\frac{\partial \dot{u}_i}{\partial x_j} - \frac{\partial \dot{u}_j}{\partial x_i} \right) \quad (2-90)$$

Hence, the rate form of the constitutive law shown in Eq. (2-75) in large deformation should be changed to

$$\dot{\sigma}^{\nabla J} = C : D \quad (2-91)$$

Therefore, the stress rate will be defined as

$$\dot{\sigma} = W \cdot \sigma + \sigma \cdot W^T + \dot{\sigma}^{\nabla J} \quad (2-92)$$

Further discussions and applications of the objective stress rates are given in Chapter 6.

2.5 The advantages of MPM over traditional FEM

The material point method (MPM) is a developed finite element method which is based on the Lagrangian-Eulerian formulation to describe the deformations. This method takes the advantage of two different kinds of spatial discretisation. One characterises the motion of the material points which represents the deformation of the continuum body. The movement of the material points is traced against a constant background

computational mesh. These two meshes are related to each other via a mapping system. The two main advantages of MPM over the conventional FEM are first, due to the constant background mesh which can be chosen arbitrarily. Therefore, mesh distortion that is a major difficulty and a fatal error in conventional FEM which usually happens in extremely large deformation analysis can be avoided. However, there are different numerical techniques to deal with large deformation problems based on the conventional FEM, but as it was mentioned earlier constantly modifying the stiffness matrix, re-meshing and changing of the topological inter-relationships and/or modifying the force matrix is required, that suggests to develop a robust numerical method that makes it easier to simulate large deformations. The second advantage of MPM over conventional FEM is the flexibility in changing the main computational domain in the MPM. Adding material to or losing material from the total computational domain during the analysis is quite a difficult task in the conventional FEM, as it requires to constantly changing the mesh system and all the topological relationships need to be defined again. So, conventional FEM has a major problem to deal with some problems such as crack propagations, degradations of the materials, and also additive manufacturing simulations.

2.6 Summary of this chapter

In this chapter, the current literature detailing the simulation of materials such as polymers under large deformation is reviewed based on the equilibrium thermodynamic theory. Therefore, polymer swelling is used as an example to demonstrate the underlying theory for large deformation of materials. Highly swellable materials that are in contact with a solvent first form a hydrogel phase and finally falling apart due to degradation. However, equilibrium thermodynamic theory sounds applicable to simulate the swelling behaviour of the hydrogels, it cannot be used for highly swellable polymers, since the theory does not consider the short time limit of the swelling process and only deals with the long time limit and the final swelling ratio in the equilibrium stage. Therefore, a decent theory is required to deal with the fast changes of the hydrogels for highly swellable polymers. Instead, the non-equilibrium thermodynamic theory was introduced and its mathematical framework was presented to model the swelling behaviour of highly swellable polymers. A simplified version of

the non-equilibrium thermodynamic theory is applied to model swelling induced by moisture absorption in chapter 4.

Furthermore, the numerical approach that is used to the model swelling behaviour of the hydrogels is discussed that is based on the Material Point Method (MPM). Therefore, a rate form of the material constitutive law is required to fit with the MPM. A rating form of the linear constitutive law (Hook's law) is used for the elastic small deformation. Furthermore, a rate form of the constitutive law based on Flory's theory is used for extremely large deformation of highly swellable polymers. In addition, in order to cover the effect of solid rotation in large deformation, an objective stress rate was introduced that is based on the Jaumann rate. Further details of the rate form of material constitutive law and the objective stress rates is discussed in details in Chapter 5.

Finally, a glimpse of conventional Finite Element Method (FEM) in nonlinear modelling was discussed to clarify the reasons why conventional FEM is not capable of modelling extremely large deformation of highly swellable polymers that finally falling apart due to degradation. Therefore, Material Point Method (MPM) was introduced as a robust numerical technique to simulate the swelling behaviour of highly swellable hydrogels. In Chapter 3 the MPM is reviewed in detail.

Chapter 3. The Material Point Method

Material Point Method (MPM) is an advanced Finite Element numerical tool. This method takes advantage of Lagrangian-Eulerian description of motion. Therefore, the topological system used in this method can effectively deal with extremely large deformations, such as large swelling in highly swellable polymers. Furthermore, this method can be efficiently applied to difficult problems that deal with discrete elements and continuum bodies at the same time, such as the modelling of Selective Laser Melting technique and degradation of highly swellable polymers during large swelling. This chapter is to provide a review of MPM detailing the mathematical formulations and declare the advantages of MPM over conventional FEM. Additionally, the topological system in MPM that is used in our code is discussed.

3.1 Introduction

Over the last few decades, computational techniques have been enormously developed for different applications. Recently, by developing the capacities of computers numerical techniques are advanced to simulate even more demanding problems. Material Point Method is an advanced numerical tool that can be used to model complex problems such as granular flow, and plastic forming according to Z. Wieckowski (2004). Furthermore, MPM can be conducted for those problems that either the discrete elements solidify and make a continuum body such as the simulation of SLM technique, or a continuum body starts to disintegrate such as degradation of highly swellable polymers during large swelling, that are currently difficult to handle for the traditional finite element method. In the new numerical techniques, it is attempted to avoid the problem of mesh distortion which is a common problem in the traditional finite element method, especially in the large deformation analysis. Therefore, there is no need for regular re-meshing systems, and adding or losing materials to/from the main computational body are also possible. In the next section, the advantages of MPM over the traditional FEM is discussed.

3.2 The advantages of MPM over conventional FEM

Precisely speaking, dealing with extremely large deformation in conventional FEM is too difficult because of mesh distortion and tangling which could be fatal for the numerical solution. Conventional FEM in solid mechanics is based on the Lagrangian mesh that is deforming with the material. In the large deformation simulation such as swelling, the mesh can be distorted rigorously and therefore the accuracy of interpolations loses quickly. Tangled mesh in large deformation can also be fatal for FEM simulation because it ends up with an ill conditioned stiffness matrix. Therefore, we may need to use re-meshing technics to avoid fatal errors. However, accuracy in mapping variables from the old mesh to the new mesh; and an adaptive algorithm to decide when to re-mesh are the two important considerations in any re-meshing technics. Furthermore, FEM is developed to deal with continuous problems, while degradation problem involves some sort of discontinuity at the breaking sections of the material parts of the main body. Thus, by losing material we need to re-mesh the body again and again. According to these restrictions, application of conventional FEM for extremely large deformation of polymers accompanied with degradation is not suggested. Hence, in order to simulate swelling and degradation problems a simple but robust numerical method is required. Recently, different generalized Finite Element Methods and mesh free methods have been developed. By using the advantage of Eulerian mesh, such as the Arbitrary Eulerian-Lagrangian (ALE) mesh Liu et al. (1988), Level set boundary tracking method Hettich and Ramm, (2006) and etc. some large deformation problems have been solved. The numerical method used in this thesis is based on the newly developed method called Material Point Method (MPM) that is explained in details in the next section.

3.3 Material point method and formulation

In this chapter algorithm and governing equations of MPM is introduced in detail and, a few examples are solved to demonstrate the accuracy and capability of the MPM code. A schematic figure is shown in Figure 3-1 to represent the MPM solution algorithm.

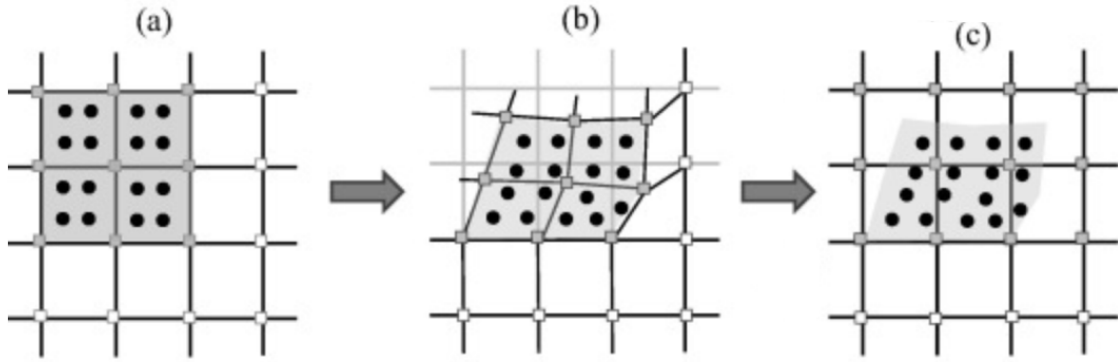


Figure 3-1 Three main steps of MPM algorithm: (a) Initialisation of the material points, (b) deformation of the material points (Lagrangian phase), (c) Resetting the mesh, by using the mapping system (convective phase) (Phuong et al. 2015)

3.3.1 Governing equations

Most of the materials in this section are taken from Z. Wieckowski (2004) and Ted Belytschko et al. (2005).

The basic idea in MPM is the discretisation of the solid body into groups of material points through applying density concentration function. Using Dirac delta function $\tilde{\delta}$ gives:

$$\rho = \sum_{p=1}^{N_p} M_p \tilde{\delta}(x - X_p) \quad (3-1)$$

In Eq.(3-1) ρ is the density, M_p is the mass of a material point, N_p is the total number of the material points, $\tilde{\delta}$ is the Dirac delta function, x is the vector of the spatial coordinate and X_p is the vector of the material points position (the p subscript indicates the variables on the material points)

In standard FE weak form, Dirac delta function is defined as:

$$\tilde{\delta}(x - X_p) = \begin{cases} 1 & \text{if } x = X_p \\ 0 & \text{if } x \neq X_p \end{cases} \quad (3-2)$$

As it was discussed in chapter 1 the standard weak form in the tensor notation of the governing equation, on the material domain Ω with the boundary Γ is written as

$$\int_{\Omega} \Delta v_i \rho \dot{v}_i d\Omega = - \int_{\Omega} \nabla(\Delta v_i) \sigma d\Omega + \int_{\Gamma} \Delta v_i \tau_i d\Gamma + \int_{\Omega} \Delta v_i \rho b_i d\Omega \quad (3-3)$$

In Eq. (3-3) v is the velocity vector, Δv is a test function and \dot{v} is acceleration (the dot denotes first order time derivative), σ is the Cauchy stress tensor, τ and b are the vectors of surface traction and body force respectively.

The discretized form of Eq. (3-3) for MPM is attained as:

$$\sum_{p=1}^{N_p} M_p \left\{ \dot{v}(X_p) \Delta v(X_p) + \rho_p^{-1} \sigma \nabla [\Delta v(X_p)] \right\} = \sum_{p=1}^{N_p} M_p b(X_p) \Delta v(X_p) + \int_{\Gamma} \Delta v \tau d\Gamma \quad (3-4)$$

Where in the second term of the left hand side of Eq. (3-4) ρ_p^{-1} is the inverse of the density, which is different from conventional FEM. In order to calculate the velocity of the material points, a background mesh is required. By using the Eulerian shape functions $N_I(X)$ in which I denotes the nodal index of the computational mesh, and by substituting $v_I = N_I(X)v_I(t)$, and $\Delta v_I = N_I(X)\Delta v_I(t)$ in Eq. (3-4) the discretised form is as below:

$$\begin{aligned} \sum_{p=1}^{N_p} M_p N_I^T(X_p) N_I(X_p) \dot{v}_I &= - \sum_{p=1}^{N_p} M_p B_I^T(X_p) \rho_p^{-1} \sigma(X_p) \\ &+ \sum_{p=1}^{N_p} M_p N_I(X_p) b(X_p) + \int_{\Gamma} N_I(X_p) \tau d\Gamma \end{aligned} \quad (3-5)$$

This can briefly be shown as the conventional FEM notation that was introduced in Eq. (2-70):

$$m \dot{v}_I = f_I^{ext} - f_I^{int} \quad (3-6)$$

In Eq. (3-6) m , f_I^{ext} and f_I^{int} are the consistent mass matrix, nodal external forces, and nodal internal forces on the computational mesh, respectively.

In Eq. (3-5) $B_I(X_p)$ is the spatial gradient of the shape function $N_I(X_p)$ defined as:

$$B_I(X_p) = \frac{\partial N_I(X_p)}{\partial x} \quad (3-7)$$

In this thesis, the lower case letters represent the spatial/nodal tensor variables of the computational mesh, and the upper case letters denote the tensor variables of the material points. Another difference between MPM and conventional FEM is in employing mass matrix. In the MPM, a lumped mass matrix in explicit time integration

that is shown in Eq. (3-8) is used instead of the consistent mass matrix such as shown in the left hand side of Eq. (3-5)

$$m_I = \sum_{p=1}^{N_p} M_p N_I(X_p) \quad (3-8)$$

In MPM, all the state variables such as stresses and density and material point velocities are traced on the material points. In comparison with conventional FEM material points in MPM are used as numerical volume integration points instead of Gauss points to calculate the volume integration. The first term on the right hand side of Eq. (3-5) is the nodal internal forces. Which is given below

$$f_I^{int} = \sum_{p=1}^{N_p} M_p B_I^T(X_p) \rho_p^{-1} \sigma(X_p) \quad (3-9)$$

The nodal external forces including all the body forces and surface tractions in Eq. (3-5) is given as:

$$f_I^{ext} = \sum_{p=1}^{N_p} M_p N_I(X_p) b(X_p) + \int_{\Gamma} N_I(X_p) t d\Gamma \quad (3-10)$$

Material Point Method is a very convenient numerical method to simulate extremely large deformation. Therefore, in the next section, we discuss nonlinear continuum mechanics such as the deformation gradient tensor, the Green (Green- Lagrange) strain tensor E , the rate of deformation tensor D , the spin tensor W and Jaumann rate of Cauchy stress that is used to explicitly update the stress in each time step.

3.3.2 Deformation gradient tensor

The two essential part of the nonlinear continuum mechanics is the description of deformation and the measure of strain. Therefore, deformation gradient is an important variable in characterization of the deformation, which is defined by

$$F_{ij} = \frac{\partial x_i}{\partial X_j} \quad (3-11)$$

Where x_i and X_j refer to the computational coordinates and the material coordinates respectively. The deformation gradient in a rectangular coordinate system in 2D is given

by Eq. (2-86) and the determinant of the F which is called Jacobian determinant is defined in Eq. (2-87).

With the Jacobian determinant, the integrals in the current and reference configurations can be related, which is an essential definition of updating the material configuration in MPM.

$$\int_{\Omega} f(x,t)d\Omega = \int_{\Omega_0} f(x,t)Jd\Omega_0 \quad (3-12)$$

In which x is the position of the material point X at time t , and Ω_0, Ω are the initial state of the configuration and the current configuration respectively.

3.3.3 Green strain tensor

The most widely used measure of strain especially in finite element method is the Green strain. In order to avoid nonzero strains or nonzero stresses, the measure of strain should vanish for any rigid body motion, and especially for rigid body rotation. This is the most important reason that linear strain displacement equations are restricted in nonlinear theories. By using the definition of the deformation gradient tensor the Green strain tensor is defined as in Eq. (2-84).

3.3.4 Rate of deformation

The rate of deformation D or the velocity strain is another important kinematic measure in continuum mechanics that is used in MPM. First, consider the velocity gradient L which is defined on the material points.

$$L_{ij} = \frac{\partial V_i}{\partial x_j} \quad (3-13)$$

By dividing the velocity gradient tensor into symmetric and skew-symmetric parts it becomes

$$L_{ij} = \frac{1}{2}(L_{ij} + L_{ji}) + \frac{1}{2}(L_{ij} - L_{ji}) \quad (3-14)$$

The symmetric part of the velocity gradient tensor is defined as the rate of deformation D that is shown in the Eq.(3-15), and the skew-symmetric part is defined as the spin W which is shown in Eq. (3-16).

$$D_{ij} = \frac{1}{2} \left(\frac{\partial V_i}{\partial x_j} + \frac{\partial V_j}{\partial x_i} \right) \quad (3-15)$$

$$W_{ij} = \frac{1}{2} \left(\frac{\partial V_i}{\partial x_j} - \frac{\partial V_j}{\partial x_i} \right) \quad (3-16)$$

In this thesis, the capital letters are used for the material coordinate system, and the small letters are used to represent the spatial coordinate system.

3.3.5 Jaumann rate

Objective rates in constitutive equations are required for Cauchy stress tensor, to consider the solid rotation of the material. Therefore, the objective rate of the stress tensor can be used to account for the material rotation that is also called a frame invariant rate. In this thesis Jaumann rate of Cauchy stress is used that is given as

$$\sigma_{ij}^{\nabla J} = \frac{D\sigma_{ij}}{Dt} - W_{ik} \cdot \sigma_{kj} - \sigma_{ik} \cdot W_{kj}^T \quad (3-17)$$

Where, W is the spin tensor given in Eq. (2. 2) which is also traced on the material points as well as stresses.

The superscript ∇ in both equations describes an objective rate. The hypo-elastic constitutive equation that is used in this thesis is as below:

$$\sigma^{\nabla J} = C^{\alpha J} : D \quad (3-18)$$

Where $C^{\alpha J}$ is the constitutive law and D is the rate of deformation that was introduced in Eq.(3-15) and the first term on the right hand side of Eq. (3-17) is the material rate for the Cauchy stress tensor, which is given as:

$$\frac{D\sigma}{Dt} = \sigma^{\nabla J} + W \cdot \sigma + \sigma \cdot W^T = \underbrace{C^{\alpha J} : D}_{\text{material}} + \underbrace{W \cdot \sigma + \sigma \cdot W^T}_{\text{rotation}} \quad (3-19)$$

As it is represented in Eq. (3-19) the material time derivative of the Cauchy stress contains two parts. The first term on the right hand side of Eq. (3-19) is the rate of change due to the material response which is identified as an objective stress rate called Jaumann rate. The second term is a change of the stress due to the rotation.

3.3.6 Large deformation schemes for incrementally objective integration

In large deformation analysis, the rigid rotation is an important factor. The idea of incremental objectivity is presented by Huges and Winget (1980) that means an update algorithm is incrementally objective. Precisely speaking, in a rigid rotation where $F_{n+1} = Q_{ij}(t) \cdot F_n$ in which Q_{ij} is the rotation tensor and $\det Q_{ij} = 1$. The Cauchy stress is given by $\sigma_{ij(n+1)} = Q_{ij}(t) \cdot \sigma_{ij(n)} \cdot Q_{ij}^T(t)$. Simo and Hughes (1998) have an extensive discussion of objective stress update algorithms. In this thesis, a simple update scheme is used based on Jaumann rate. The stress update scheme is given by

$$\sigma_{n+1} = Q_{n+1} \cdot \sigma_n \cdot Q_{n+1}^T + \Delta t \sigma^{\nabla J} \quad (3-20)$$

In Eq.(3-20) $Q_{ij(n+1)} = \exp[W_{ij} \Delta t]$ is the incremental rotation tensor which is related to the spin W_{ij} , which is introduced in Eq.(3-15). By substituting Eq. (3-19) for the Jaumann rate in Eq. (3-20).

$$\sigma_{n+1} = Q_{n+1} \cdot \sigma_n \cdot Q_{n+1}^T + \Delta t C^{\sigma J} : D \quad (3-21)$$

In Eq. (3-21) n is the increment number and D is the rate of deformation. Δt is the time interval and $C^{\sigma J}$ is the elastic modulus tensor which will be discussed in details in chapter 5.

3.3.7 Mapping procedure

According to the basic concept of MPM, a mapping procedure is required to map the state variables such as velocity, acceleration, and etc. forward and backward between the material points and the computational mesh. Similar to the conventional FEM, by using the spatial shape functions the information from the nearby material points will be transferred to the nodal points of the computational mesh. The first step in mapping procedure is to calculate the lumped mass matrix. Hence, spatial shape functions can be used to map the mass of the nearby material points to the nodes of the computational mesh as it was given in Eq. (3-8).

In order to map the velocities of the material points to the nodes of the computational mesh, first the momentum of the material points are mapped, according to the conservation of the momentum we have

$$m_I v_I = \sum_{p=1}^{N_p} M_p V_p N_I(X_p) \quad (3-22)$$

In the next step, in order to calculate the nodal velocities, the momentum of the nodal points will be divided by the mass of the nodes. In MPM, the procedure of mapping back the nodal velocities to the material points follows the standard interpolation procedure.

$$V_p = \sum_I v_I N_I(X_p) \quad (3-23)$$

3.3.8 Time integration loop for the dynamic equations

As all the state variables are defined on the material points, the time integration of the dynamic equations starts from the material points. Depend on the initial conditions of the problem, the different starting point can be considered. i.e. if an initial velocity is assigned to the material points the time integration of the dynamic equations should be started from mapping the mass and velocity of the material points to the nodes of the computational mesh by using Eq. (3-8) and Eq. (3-22). If an initial stress is assigned to the material points, then the loop will be started by mapping the stress terms from the material points to the nodes of the computational mesh to calculate the internal nodal forces by using the Eq. (3-26). Generally, the time integration should follow the bellow algorithm.

Map the material point's mass to the nodes of the computational mesh, as it was explained earlier

$$m_I^t = \sum_{p=1}^{N_p} M_p N_I(X_p^t) \quad (3-24)$$

Calculate the nodal velocity of the computational mesh,

$$v_I^t = \frac{1}{m_I^t} \sum_{p=1}^{N_p} M_p V_p^t N_I(X_p^t) \quad (3-25)$$

Update the internal nodal forces, by using Eq. (3-27), some extra term can be added to this equation, to model damping of the system or to model constant stresses. In chapter 3 two more terms will be added to the internal nodal forces for damping force and to model constant stresses.

$$(f_I^{\text{int}})^t = \sum_{p=1}^{N_p} M_p B_I^T(X_p^t) \frac{1}{\rho_p^t} \sigma^t(X_p^t) \quad (3-26)$$

Similarly, we can update the external nodal forces by using

$$(f_I^{\text{ext}})^t = \sum_{p=1}^{N_p} M_p N_I(X_p^t) b^t(X_p^t) + \int_{\Gamma} N_I(X_p^t) \tau^t d\Gamma \quad (3-27)$$

By using the second law of Newton, nodal acceleration of the nodal points can be updated for the time step $t + \Delta t$ as bellow

$$\dot{v}_I^{t+\Delta t} = \frac{1}{m_I^t} [(f_I^{\text{int}})^t - (f_I^{\text{ext}})^t] \quad (3-28)$$

Eq. (3-29) can be used to update the material point's velocity, which is the backward difference mapping procedure:

$$V_p^{t+\Delta t} = V_p^t + \Delta t \sum_I \dot{v}_I^{t+\Delta t} N_I(X_p^t) \quad (3-29)$$

In order to update the nodal velocities of the computational mesh, the calculated nodal acceleration can be used:

$$v_I^{t+\Delta t} = v_I^t + \Delta t \dot{v}_I^{t+\Delta t} \quad (3-30)$$

The next step is to calculate the rate of deformation, by using Eq. (3-31) we can calculate the rate of deformation as shown below

$$D^{t+\Delta t}(X_p^t) = B_I(X_p^t) v_I^{t+\Delta t} \quad (3-31)$$

In which $B_I(X_p)$ is the derivative of the shape functions.

In order to update the stress in MPM Eq. (3-32) can be used as shown below

$$\sigma^{t+\Delta t} = \sigma^t + \Delta t \dot{\sigma}^{t+\Delta t} \quad (3-32)$$

The second term on the right hand side of Eq. (3-32) is the stress rate. Depends on the constitutive law we can use a different method to find the stress rate. As we discussed in Eq. (3-21) by using an incrementally objective algorithm, we are able to find the stress rate in large deformation analysis.

The mass density field is calculated on the material points and will be updated at each time increment. Eq. (3-33) can be used to update the mass density field

$$\rho^{t+\Delta t} = (J^{t+\Delta t})^{-1} \rho^t \quad (3-33)$$

Where ρ^t and $\rho^{t+\Delta t}$ are the density values of each material points at time step t and $t + \Delta t$ respectively, and $J^{t+\Delta t}$ is the Jacobian that is the determinant of deformation gradient tensor as it is discussed earlier at the time $t + \Delta t$ which is related to the material configuration at time step t . According to Wieckowski (2004) in some problems especially, when stresses are equal to zero at the beginning of the process, Eq. (3-33) is not very accurate and can lead to a major numerical error. In such cases, Wieckowski suggested using the current position of the material points to approximate the density by using equation below

$$\rho(x) = \sum N_i \rho_i \quad (3-34)$$

In Eq. (3-34) N_i are the shape functions, and ρ_i are the nodal value of the mass density, in which for a rectangular mesh with linear shape functions can be calculated by:

$$\rho_I = \frac{\sum_I \sum_{p=1}^{N_p} M_p N_I(X_p)}{\sum_I (vol)_I} \quad (3-35)$$

In which $\sum_I (vol)_I$ is the average volume of the elements around the node I that are filed with material points (i.e. the volume of the free elements around the boundary do not count). The last step is to update the position of the material points by mapping the nodal velocities to the material points as

$$X_p^{t+\Delta t} = X_p^t + \Delta t \sum_I N_I(X_p^t) v_I^{t+\Delta t} \quad (3-36)$$

In the above time integration procedure, there are two different methods to update the nodal velocity vector $v_I^{t+\Delta t}$ for the next time step, either Eq. (3-25) can be used via conservation of linear momentum or directly updating the nodal velocities via acceleration of the nodal points for the next time step as it is shown in Eq. (3-30). The nodal velocities are important in MPM as they have used to both updates the stresses

and also to update material point's positions. In some cases, there are some numerical errors especially for those material points located near to the boundary. As it is shown in Figure 3-2, when there are a small number of material points in one computational cell, the nodal mass m_i^t tends to zero while the calculated nodal forces from Eq. (3-26) do not tend to be zero (especially in the case of having an extra term of constant stress which will be discussed in chapter 3), hence a large nodal acceleration will be obtained that leads to large nodal velocity which causes material points separation.

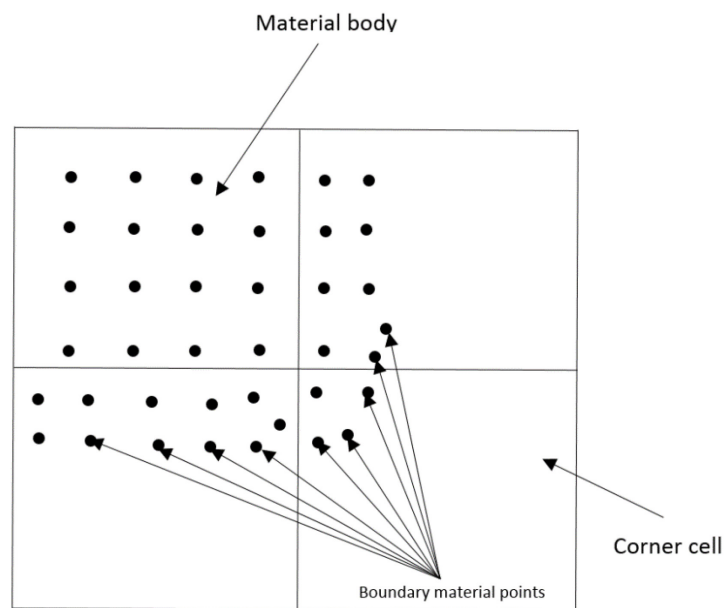


Figure 3-2 Schematic picture of boundary cells that need special care, as the nodal lumped mass will be small especially at the corner cells which may need distinct treatments.

A smoothing technique of Eq. (3-25) is suggested by Sulsky et al. (1995) to resolve this problem. In our numerical calculation, we have observed both Eq. (3-25) and Eq. (3-30) have almost the same results for small elastic deformations, however, Eq. (3-25) has much better results for extremely large deformations to update the nodal velocities. It has been tested that this method will not have any material point separation or numerical problems at the boundary cells of the computational mesh. In Chapter 5 a discussion is provided for different possible sources of numerical errors in MPM for extremely large deformation's applications.

3.4 Topological systems in the MPM

As Material Point Method utilises two distinctly different discretization methods which require a complicated mapping system to link between the computational mesh and the discrete material points. There should be an active way of tracking the material points on the computational mesh at every time step. Perhaps for small deformation analysis, it can be assumed that the material points are not leaving the initial computational cell, which makes the tracking system to be much easier, while for large deformation analysis a full tracking system is required. Therefore, there must be three different numbering system as shown in Figure 3-3.

- A specific number should be assigned to all the cells of the computational mesh
- A specific number should be assigned to all the nodal points of the computational mesh
- A specific number should be assigned to all the material points

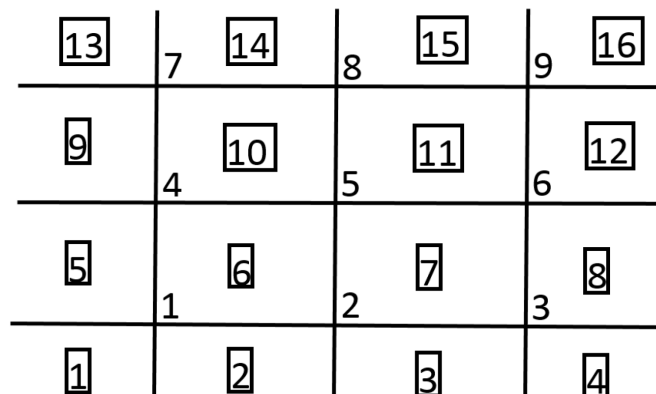


Figure 3-3 topological system of the rectangular mesh

The topological relationships between the cell's number and the node's number in the computational mesh in the MPM is easier than the topological relationships in the normal Lagrangian mesh that is used in the conventional FEM, because computational mesh remains constant in the MPM, and for example the four neighbourhood cells around point 5 are always cells number 6,7,10 and 11. Hence, the two main subroutines for this purpose should be defined as below

1. The input is the node's index number, and the output is the four cell's index numbers around the node.

2. The input is the cell's index number, and the output is the four node's index numbers around the cell.

Furthermore, there should be active relationships between the material points and the computational mesh. In the simulation of extremely large deformation (i.e. 100% expansion in each direction) the material points move to the other computational cells, and the path cannot be predicted, hence a tracking system is required to track the MPs and needs to be updated at each time step. Therefore, the first it is required to know the total number of MPs that exist in the cell at each time step, and the second, it is essential to investigate the exact index numbers of the MPs that are in each cell, since all the other state variables such as stress, velocity, and position vectors and also shape functions and derivatives of the shape functions are defined based on the index numbers of the MPs. Therefore, three subroutines are required to be able to track the MPs.

1. The input is the cell's index number, and the output is the total number of existing MPs in the cell.
2. The input is the material point's index number, and the output is the cell's index number.
3. The input is the cell's index number, and the output is the index numbers of all the existing MPs in the cell.

These five subroutines are almost essential to be able to fully track the material points for extremely large deformation, in which the material points may move to many different cells through the simulation.

3.5 Summary of this chapter

In this chapter, the numerical framework of Material Point Method (MPM), is discussed in detail. The most important advantages of the MPM are mentioned as below

- It does not require any extra computer modelling for re-meshing systems to deal with mesh distortion and especial boundary conditions such as polymer degradation or erosion, which is a major difficulty of conventional Finite Elements Method.

- The MPM is a robust tool to simulate discrete systems that turn into a continuum system through a sintering or powder impact process.
- Easy to deal with adding material or losing material in every time step.
- Easy to define complicated geometries. As oppose to the conventional FEM the computational mesh is independent of the geometry so the material body can be easily defined through an initiation of the material points in a global coordinate system.

Ultimately, due to the two different discretization techniques in the MPM and the required mapping system between the two meshes, and all the other topological relationships that are required for the MPM make this numerical method more computationally demanding compared to the conventional FEM, however, it is observed in our code that the computational cost of the MPM is also reasonable as long as the code considers no multi-dimensional arrays should be used for the material points and for the nodal points (i.e. Every component of material point's position, velocity and stress or nodal position, velocity, acceleration and internal forces should be defined separately in different X, Y and Z directions). As it was mentioned earlier in the conventional FEM the difficulty of mesh construction is directly related to the complication of the computational geometry, and usually commercial mesh generators are required to construct a convergent mesh for the body, while in the MPM the situation is much easier when a simple background computational mesh can be defined and it remains unchanged. Furthermore the material points can be easily positioned within a global coordinate system and build a large collection of material points in multi-dimensional space with specific boundary profile, however, then a fairly complicated topological system is required to track the material points at every time step, especially in large deformations that material points move far from their initial computational cell, and at every time step the tracking information should be updated. Also, either global or local mesh refinement is possible in the MPM. In addition, modelling of two different material in the same computational mesh is possible which suits for simulation of composite materials or functionally graded materials as well.

Chapter 4. Validation of The Material Point Method for Small Deformation

Very few benchmark tests have been presented in the literature for MPM. Therefore, this chapter presents a series of basic test case studies to demonstrate the validity of the MPM. A range of basic tests from 1D small vibration to 2D tensile test are chosen as the benchmark and the results of the MPM code that is written by the author are tested against either analytical results or standard FEM results. Furthermore, swelling induced by moisture absorption has been tackled as an application of the 1D small deformation and also to open an introduction to the simulation of a large swelling process for highly swellable polymers that is mainly discussed in chapter 5.

4.1 Introduction

The MPM was implemented for small deformation by the author to validate the method. A series of basic test case studies are chosen that all have analytical results. In the first case, a simple 1D forced vibration problem is considered. The results of MPM implementation is compared with the results of conventional FEM, for elastic small deformation. In the second case, MPM is implemented for 2D problems, and a tensile test is chosen as the benchmark. Therefore, in this case, study, the final equilibrium state of the deformation is checked with the analytical solution. Also, in order to check the accuracy of the implemented linear constitutive law, a series of final results for Young's modulus and Poisson ratio are checked with the initial inputs for these parameters. Furthermore, the same dynamic model has been used to simulate swelling induced by moisture absorption. This is to demonstrate moisture absorption, swelling, and moisture distribution as a result of longitudinal diffusion of solvent molecules into the dry polymeric 1D beam. The model is used for small deformation to predict the final swelling ratio and solvent distribution in the polymer. This example is to provide a basic mathematical framework for the swelling process, and also to use the general idea of the non-equilibrium thermodynamic theory that is discussed in chapter 2 and finally,

provides an introduction to a large swelling process for highly swellable polymers which is discussed in chapter 5.

4.2 Theoretical background

Consider a one-dimensional cantilever beam with length L and Young's modulus E with a constant cross section are of A and density ρ as shown in Figure 4-1.

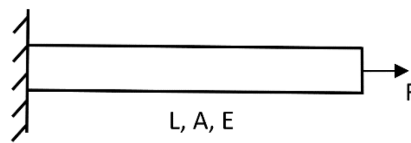


Figure 4-1 Cantilever beam under a constant force

Generally, conventional Finite Element Method is based on the principle of minimum potential energy. We have used an explicit time integration to simulate a forced vibration problem of an elastic bar, using 2-node bar elements. In order to simulate the system with FEM, the system can be modelled with a series of mass and springs as shown in Figure 4-2, the springs can be regarded as finite elements and masses can be regarded as nodes. The elasticity of the springs depends on the material properties, in which for a homogeneous bar the elasticity of the spring is given later. Therefore, having finite elements (i.e. springs and masses) simulate a closer system to the solid body.

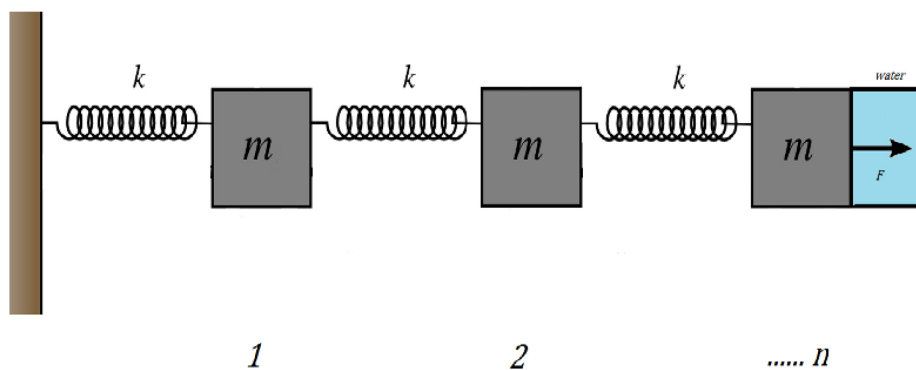


Figure 4-2 Schematic model of mass spring

The ultimate goal of dynamic finite element analysis is to find the vibration behaviour of the system. As it is shown in Figure 4-2 the boundary conditions and the boundary

load are exactly taken the same as section 4.2, to be able to compare the results of MPM and FEM.

In Figure 4-2 F is the external load which is applied to the right hand side of the body. The other boundary conditions are as below:

1. The initial velocity of the entire system is set to be zero
2. The left boundary is fixed by setting zero horizontal velocity and acceleration for the nodes at left side of the boundary
3. An external force F is applied to the right boundary

Figure 4-3 shows a discretised solid bar with linear elements.

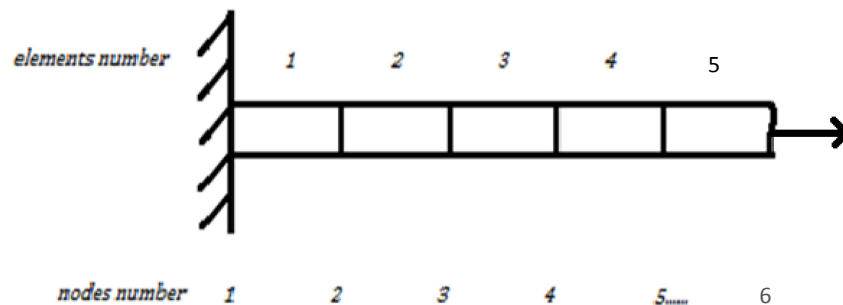


Figure 4-3 the discretised geometry using linear elements

4.3 Numerical approach

4.3.1 Simulating 1D forced vibration of elastic beams with Finite Element Method

Basically, a solid long bar can be considered as a mass-spring system. Springs are considered to be weightless and representing the elements and their lengths, and the mass of each element is lumped on the nodes. The stiffness of the springs is related to the properties of the material. For a homogeneous solid bar, the stiffness of the linear springs is related to Young's modulus, cross section area and the length of the element as it is shown in Eq.(4-1).

$$K_i = \frac{E_i A_i}{l_i} \quad (4-1)$$

The FEM code calculates the dynamic response of the system of mass-springs to a combination of constant applied nodal forces.

$$[M]\{\ddot{x}_i\} + [K]\{x_i\} = \{F\} \quad (4-2)$$

In which dot notations denotes time derivatives, $[M]$ is the lumped mass matrix, $[K]$ is the stiffness matrix and $\{F\}$ is the force matrix. At each time step, the value of the nodal acceleration will be obtained from the internal nodal forces, as it is shown in Eq.(4-3).

$$\ddot{x}_i = \frac{f_i^{\text{int}} - f_{i-1}^{\text{int}}}{M_i} \quad (4-3)$$

Where, i is the elemental indicator and f_i^{int} is the nodal force and is influenced by the elastic strain of the spring, which is simply shown in Eq. (4-4).

$$f_i^{\text{int}} - f_{i-1}^{\text{int}} = K_i(x_{i+1} - 2x_i + x_{i-1}) \quad (4-4)$$

In order to apply the boundary condition on the left hand side K_1 is given a very big number so that node number one that is shown in Figure 4-3 will be fixed. Also, a constant force F_0 is applied to node number n on the right hand side in Figure 4-3.

$$M_i^t \ddot{X}_i^t + K_i^t X_i^{t+1} = f_i^{\text{int}} - f_{i-1}^{\text{int}} \quad (4-5)$$

Therefore, at each time step, Eq.(4-5) Should be solved linearly for X_i and find the new positions of the nodes, and again this loop must be repeated.

In the next section, we have compared the results from MPM and FEM for 1D forced vibration that is shown in Figure 4-3.

4.3.2 Implementing MPM to 1D forced vibration of elastic beams

As it is shown in Figure 4-4 a simple 1D discretised body is considered. In order to get similar results from both MPM and FEM code, we need to have consistent inputs. The left hand side of the boundary is fixed, by giving zero nodal velocity and zero nodal displacement to the left hand side node of the first mesh. A constant force is applied to the right hand side node of the last mesh on the right hand side of the boundary. Therefore, by using 1D shape functions in Eq.(4-6) and (4-7) that are based on the local coordinate system the nodal masses can be obtained as shown in Eq.(4-8).

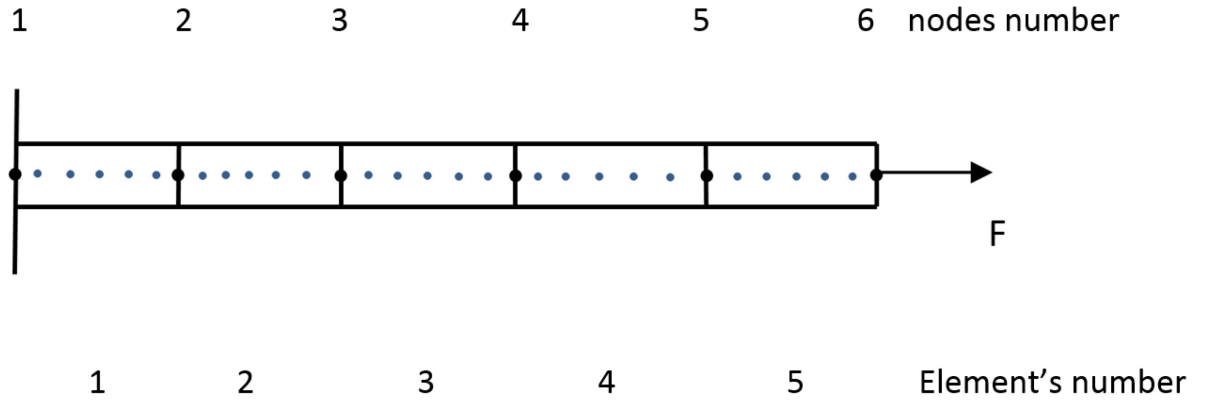


Figure 4-4 Schematic discretised system in 1D MPM, the blue points represents the material points and the black points represent the elemental nodes.

$$N_1(X_p) = \frac{1+\xi}{2} \quad (4-6)$$

$$N_2(X_p) = \frac{1-\xi}{2} \quad (4-7)$$

$$m_I = \sum_{p=1}^{N_p} M_p N_I(X_p^t) \quad (4-8)$$

By having the nodal masses and according to the conservation of linear momentum, nodal velocities can be found as it was shown in Eq. (3-25).

Calculating the out of balance force at each node is a part of the solution in each time step, i.e. it is unknown before the problem is solved and is the key to finding the acceleration and finally the deformation of the body at each increment. On the other hand, as there is no external forces exerted on the body, nodal forces are only updated via internal forces between the material points, as argued in Eq.(3-26). Hence, nodal accelerations are calculated as shown in Eq.(3-28).

In order to update the velocity of the material points, Eq. (3-29) is used. Hence, it maps back the nodal velocities to the material points for the next time step.

Therefore, there are two different ways to update the nodal velocities that are shown in Eq.(4-9) and Eq.(4-10).

$$v_I^{t+\Delta t} = v_I^t + \Delta t \dot{v}_I^{t+\Delta t} \quad (4-9)$$

$$m_I v_I^{t+\Delta t} = \sum_{p=1}^{N_p} M_p V_p^{t+\Delta t} N_I(X_p^t) \quad (4-10)$$

In Material Point Method, stresses will be updated through the rate of strains as it is discussed in Eq.(4-11) by using linear elastic constitutive law which is based on the rate of strain Eq. (4-12) simply can be written as

$$\sigma^{t+\Delta t} = \sigma^t + \Delta t \dot{\sigma}^{t+\Delta t} \quad (4-11)$$

$$\dot{\sigma}^{t+\Delta t} = ED^{t+\Delta t}(X_p^t) \quad (4-12)$$

In which E is Young's modulus and D is the rate of deformation that can be updated as shown in Eq.(3-31).

The final steps are updating the new positions of the material points through Eq.(3-36) and updating the density by using Eq. (3-34) and Eq.(3-35).

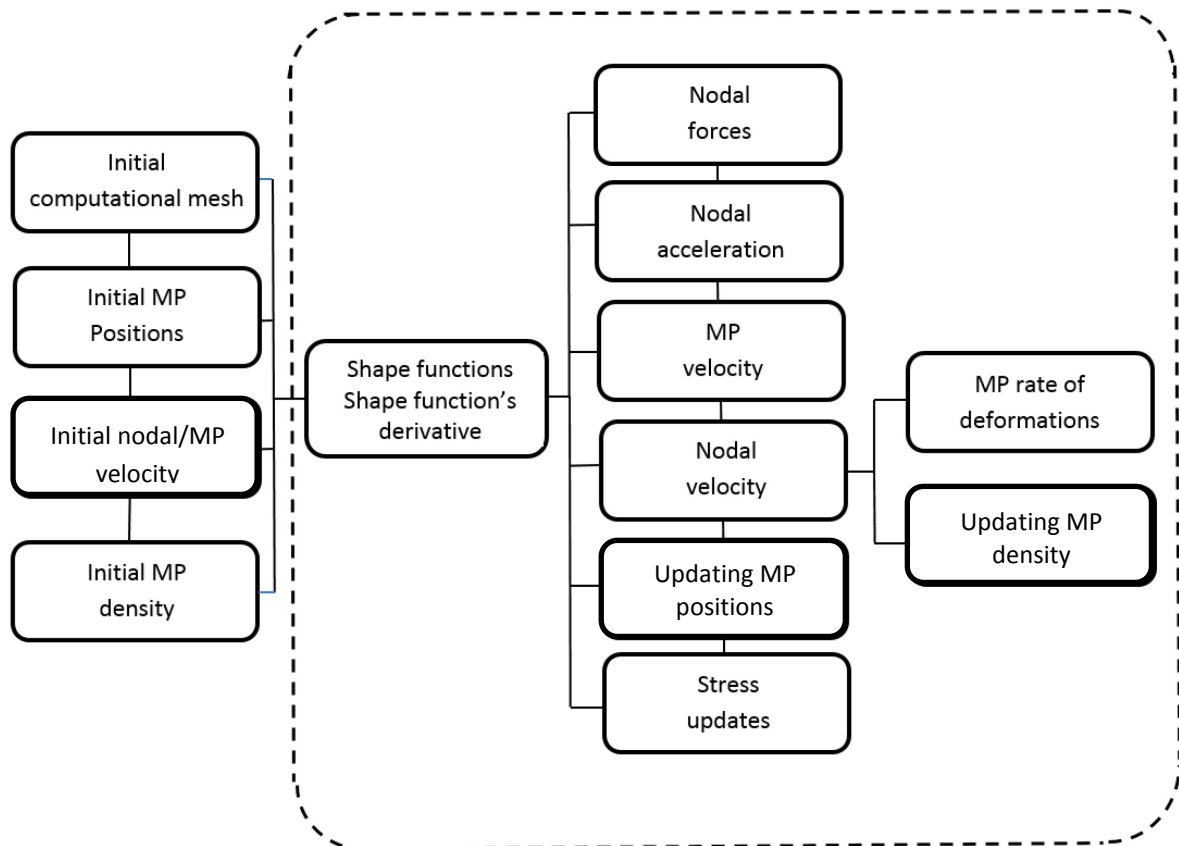


Figure 4-5 Flowchart of MPM for small deformation.

4.4 Validation of the Material Point Method using Analytical Solution and Finite Element Analysis

The validation consists of several stages, starts with a comparison between the results for a 1D small vibration problem simulated by Material Point Method and conventional FEM also with the analytical solution, followed by simulating a simple elastic tensile test to check the accuracy of the linear constitutive law and the final equilibrium state in 2D. A code is developed in FORTRAN to simulate the same vibration problem based on the MPM that was discussed earlier and the flowchart is given in Figure 4-5 In order to validate the results of MPM computer code, the same problem is solved with conventional FEM. Both results are compared and a good match was found as shown in Figure 4-6, Figure 4-7, and Figure 4-8 also both method consistently can prove the analytical equilibrium state of the system.

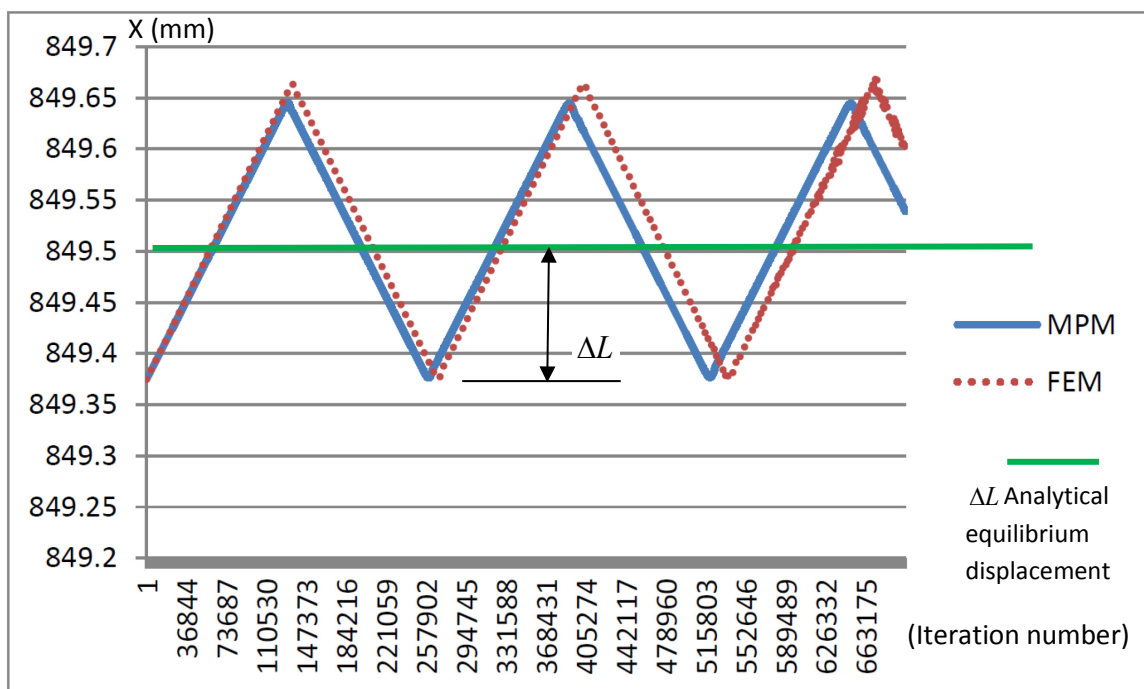


Figure 4-6 shows MPM vs. FEM results of displacement of the last node for vibration of a bar with total length of $l = 849.375\text{mm}$, Young's modulus of $E = 50\text{Mpa}$, cross section area of $A = 10\text{mm}^2$, the body force $F = 0.5\text{N}$, mass of each material point is 0.13 gr and seven material points is used in each mesh in MPM, 173 elements is used in FEM, and lumped mass of each node in FEM is 0.91gr . The time step is $\Delta t = 0.001$ second of each iteration.

$$F = \frac{EA}{nL} \Delta L \tag{4-13}$$

In which F is the applied force E , A and L are Young’s modulus, cross section area, and the original length respectively. n is representing the number of the elements, since by breaking the bar into finite elements it works as a series of springs, therefore the stiffness of the equal spring is divided by the total number of the springs.

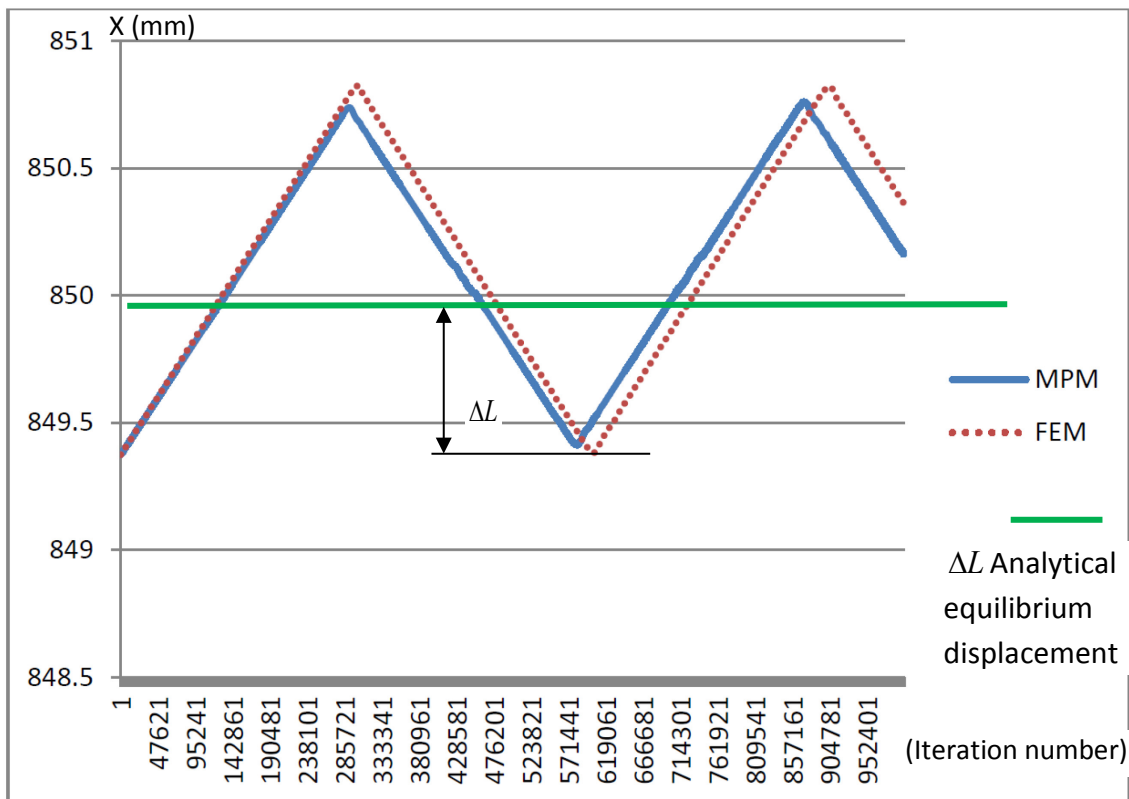


Figure 4-7 shows MPM vs. FEM results of displacement of the last node for vibration of a bar with total length of $l = 849.375\text{mm}$, Young’s modulus of $E = 10\text{Mpa}$, cross section area of $A = 10\text{mm}^2$, the body force $F = 0.5\text{N}$, mass of each material point is 0.13 gr and seven material points is used in each mesh in MPM, 167 elements is used in FEM, and the lumped mass of each node in FEM is 0.91gr . The time step is $\Delta t = 0.001$ second of each iteration.

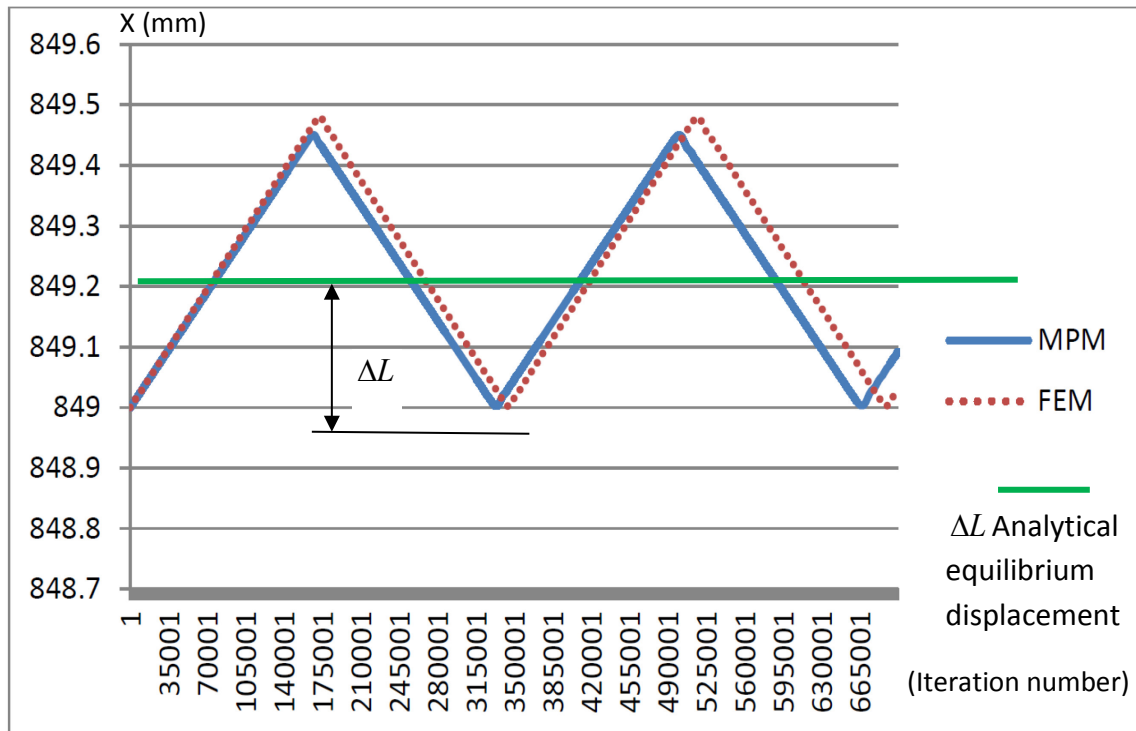


Figure 4-8 shows MPM vs. FEM results of displacement of the last node for vibration of a bar with total length of $l = 849.00\text{mm}$, Young's modulus of $E = 30\text{Mpa}$, cross section area of $A = 10\text{mm}^2$, the body force $F = 0.5\text{N}$, mass of each material point is 0.225 gr and four material points is used in each mesh in MPM, 170 elements is used in FEM and lumped mass of each node in FEM is 0.9gr . The time step is $\Delta t = 0.001$ second of each iteration.

4.5 Swelling induced by moisture absorption 1D simulation

The work presented in this section was carried out by Hai Yan as his MSc project using my FEM code under my co-supervision. (Hai Yan, 2013)

According to Flory, the total deformation in the hydrogels is as a result of both elastic strain and the corresponding swelling strain. Basically, swelling strain is formed due to solvent (i.e. water) absorption in the hydrogel. Therefore, the total strain in the hydrogel is obtained as

$$\varepsilon = \frac{\sigma}{E} + \varepsilon^s \quad \text{in 1D} \quad (4-14)$$

By assuming molecular incompressibility for the hydrogel, the volumetric change in the swollen hydrogel is

$$\alpha^s = \frac{V_1}{V_0} = \frac{V_0 + V_2}{V_0} = 1 + \frac{V_2}{V_0} = 1 + \frac{n \cdot v}{N \cdot V_0} \quad (4-15)$$

In Eq.(4-15) V_0 and V_1 are the initial and swollen volume of the hydrogel, V_2 is the volume of the absorbed solvent, and v is the molar volume of the solvent, n is the number of solvent molecules in the hydrogel and N is the Avogadro's number. So, the volumetric swelling strain is defined as

$$\varepsilon^s = \frac{V_1 - V_0}{V_0} = \frac{V_1}{V_0} - 1 = \alpha^s - 1 = \frac{n \cdot v}{N \cdot V_0} \quad (4-16)$$

Hence, the swelling strain in the hydrogel is a linear function of solvent concentration as below

$$\varepsilon^s = \alpha \cdot c \quad (4-17)$$

In which, α (m^3) is a constant coefficient of hygroscopic swelling and $c = \frac{n}{N \cdot V_0}$ is the number density of the solvent. Hence, for any sort of moisture absorption field, the constitutive model is obtained from Eq.(4-17) which is called hygroscopic swelling strain.

As concentration field is a nonhomogeneous and time depending field, it should be solved separately by using Fick's second law and Flory's theorem as followed next.

Fick's second law describes the concentration changes with respect to time and space as shown below

$$\frac{\partial c}{\partial t} = \nabla \cdot (D_{dif} \nabla c) \quad (4-18)$$

Where, D_{dif} is the diffusion coefficient, c is the solvent concentration, t is the time and ∇ is the gradient operator. Analytical solution of Fick's second law is available for an infinite plane sheet of thickness 1. The analytical solution of the concentration field in an infinite plane sheet of thickness equal to 1 and boundary conditions which are premediated in one dimension is shown in Eq.(4-19). Crank J. (1975)

$$\frac{c_t - c_0}{c_\infty - c_0} = 1 - \frac{4}{\pi} \sum_{n=0}^{\infty} \frac{(-1)^n}{2n+1} \exp\left\{-\frac{D_{dif} (2n+1)^2 \pi^2 t}{4l^2}\right\} \cos \frac{(2n+1)\pi x}{2l} \quad (4-19)$$

In which, c_∞ is a constant concentration on the surface, c_0 is the uniform initial concentration, and x is the Cartesian coordinate system in one dimension from $-l/2$ to $l/2$.

In Eq.(4-19) diffusion coefficient is assumed to be $D_{dif} = 1$. A dimensionless parameter is defined for the length as $\tilde{x} = x/l$ and assumed to be $\tilde{x} = 1$. Therefore, Eq. (4-19) will be simplified to Eq.(4-20) in which α is a time depending parameter, that can be calculated at any time. In Eq. (4-20) the value of $n=0$ is assumed since for any higher value of n the second term on the right hand side of Eq. (4-19) will so small which can be neglected compared to the situation when $n=0$.

$$\tilde{c} = \frac{c_t - c_0}{c_\infty - c_0} = 1 - \alpha(t) \cos\left(\frac{\pi \cdot \tilde{x}}{2}\right) \quad (4-20)$$

The concentration field in Eq. (4-20) for various time computed in MATLAB is shown in Figure 4-9. The horizontal axis shows the length parameter $\tilde{x} = x/l$ and the vertical axis represents the concentration distribution in the plane sheet. Each curve demonstrates the concentration distribution at a specific time in the plane sheet.

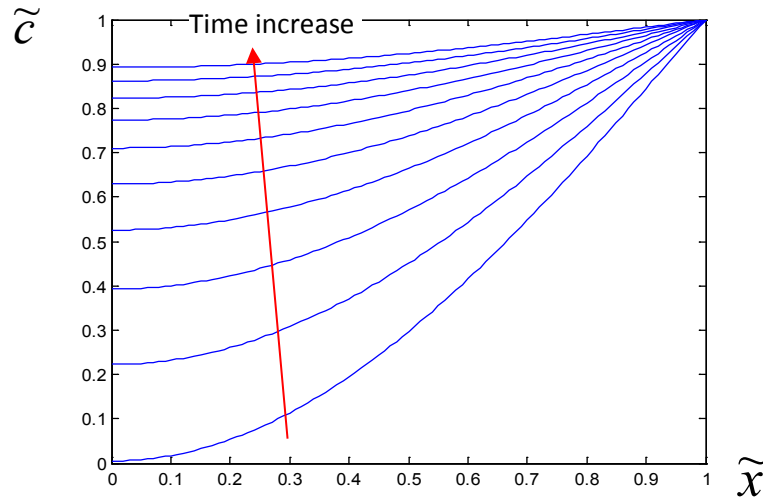


Figure 4-9 the concentration of the solvent at the length parameter \tilde{x} in a plane sheet.

In Figure 4-9 each curve represents a concentration distribution profile, based on the different time parameter of $D_{dif}t/l^2$ that is changing from 0.1 to 1, t is time and l is the length. According to Eq. (4-24) as it is shown in Figure 4-9 in the dry state (i.e. $c_0 = 0$) the concentration profile can be expressed by c_t/c_∞ . Hence, the concentration

distribution profile can be obtained for 1 dimensional beam through Fick's second law. Concentration profile plays an important role in swelling problems that is discussed in details in chapter 5.

Therefore, according to Eq.(4-18) the displacement of element in swelling is made of two parts

$$u^t = u^e + u^s \quad (4-21)$$

Where u^e is the elastic displacement and u^s is the displacement due to the swelling. By substituting the elastic force as $u^e = f^e / K$ in which K is the element stiffness and by rearranging Eq.(4-25) then we have

$$f^e = Ku^t - Ku^s \quad (4-22)$$

As it was discussed earlier concentration profile is nonhomogeneous, hence Eq.(4-17) can be rearranged as

$$du^s = \alpha c \cdot dx \quad (4-23)$$

Therefore, from Eq.(4-20) combined with Eq.(4-23) swelling strain due to moisture absorption can be expressed as

$$u_s = \alpha \cdot (1 - a \cos(\frac{\pi \cdot \tilde{x}}{2})) \quad (4-24)$$

By adding a damper to the initial model which is introduced later in this section along with simulating moisture absorption, the governing equation that was introduced in Eq.(4-22) will be slightly changed. As it was discussed previously, nodal forces are obtained in Eq.(4-22). In case there are other internal forces such as damping forces, or swelling forces as a result of moisture absorption in swellable polymers, out of balance nodal internal forces for element (i) can be calculated as below

$$f_i^{\text{int}} = K_i(X_{i+1} - X_i) + F_i^s + F_i^d \quad (4-25)$$

Where, F_i^s and F_i^d are the swelling force and damping force respectively, that are obtained as below in Eq.(4-26) and Eq.(4-27) respectively.

$$F_i^d = -d \cdot (\dot{X}_{i+1} - \dot{X}_i) \quad (4-26)$$

$$F_i^s = -K \cdot (u_{i+1}^s - u_i^s) \quad (4-27)$$

In which, d is a constant damping coefficient, and \dot{X}_i are the nodal velocities, that are calculated as in Eq.(4-30) and finally u^s the swelling displacement can be calculated through Eq.(4-24).

Time integration of the dynamic model

Time integration of the dynamic equations of FEM for simulating moisture absorption begins with calculating the nodal forces.

$$(f_i^{\text{int}})^t = K_i(X_{i+1}^t - X_i^t) - d.(\dot{X}_{i+1}^t - \dot{X}_i^t) + (F_i^s)^t \quad (4-28)$$

The nodal acceleration can be updated from the equation of motion as

$$\ddot{X}_i^{t+\Delta t} = \frac{1}{m_i}(f_i^{\text{int}})^t \quad (4-29)$$

And the nodal velocities are updated based on the forward difference method

$$\dot{X}_i^{t+\Delta t} = \dot{X}_i^t + \Delta t.\ddot{X}_i^{t+\Delta t} \quad (4-30)$$

Finally, the new position of the nodes will be updated trough Eq.(4-31) and then the loop turns back to Eq.(4-25) to calculate the forces.

$$X_i^{t+\Delta t} = X_i^t + \Delta t.\dot{X}_i^{t+\Delta t} \quad (4-31)$$

The Flowchart of the FEM code that is written in FORTRAN is shown in Figure 4-10.

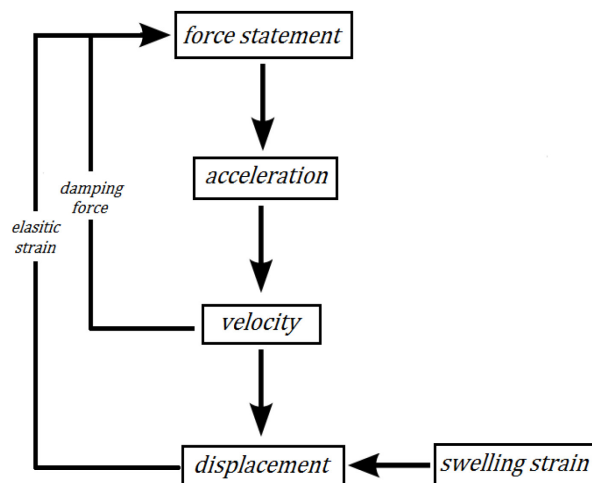


Figure 4-10 the flowchart of FEM code in FORTRAN for 1D Swelling induced by moisture absorption

4.5.1 Numerical results for 1D Swelling induced by moisture absorption

The dynamic nature of swelling induced by moisture utilizes the idea of dynamic FEM. Therefore, a one-dimensional finite element code is written in FORTRAN. The code will be running until it reaches a steady state which is the prediction of the material swelling due to moisture absorption. The main variables that are used in the program are given in Table 2.

Type of elements	1D 2noded elements
Number of elements	19
Length of elements	5
Coefficient of hygroscopic swelling(α)	1
Damping coefficient	1
Time step	0.0001
Coefficient of elasticity (K)	100
Initial Load	100

Table 2 the main variables used in the FE code.

4.5.2 Validation of the numerical code based on the static FEM

Initially, the 1D FEM code was developed to validate the 1D MPM code that was discussed earlier. As both methods well supported each other and also match with the analytical results, therefore, the 1D simulation of swelling induced by moisture absorption is done based on the dynamic FEM, however, the steady state swelling is also checked via a simple static FEM that is briefly explained below.

According to Hooke's law,

$$[K]\{u\} = \{F\} \quad (4-32)$$

In which $[K]$ is the global stiffness matrix for the entire meshed system, and $\{u\}$ is the vector of nodal displacements, and $\{F\}$ is the vector of nodal forces.

Hence, by producing the global stiffness matrix $[K]$ and by applying the boundary conditions to the nodal displacement vector as well as load conditions to the nodal force vector, Eq.(4-32) can be solved easily. The global stiffness matrix for one-dimensional 2-nodded elements can be updated as in Eq.(4-33).

$$[K]= \begin{bmatrix} k & -k & 0 & \vdots & 0 \\ -k & 2k & -k & \ddots & \vdots \\ 0 & -k & 2k & \ddots & 0 \\ \vdots & \ddots & \ddots & \ddots & -k \\ 0 & \dots & 0 & -k & k \end{bmatrix} \quad (4-33)$$

Hence, Eq.(4-32) for our model with the same number of elements that was introduced in Table 2 will be changed to a set of simultaneous linear equations, the boundary condition, and load condition is applied as it was shown in Figure 4-3 in 1 dimension.

$$\begin{bmatrix} k & -k & 0 & \vdots & 0 \\ -k & 2k & -k & \ddots & \vdots \\ 0 & -k & 2k & \ddots & 0 \\ \vdots & \ddots & \ddots & \ddots & -k \\ 0 & \dots & 0 & -k & k \end{bmatrix} \begin{bmatrix} 0 \\ u_2 \\ u_3 \\ \vdots \\ u_{20} \end{bmatrix} = \begin{bmatrix} 0 \\ 0 \\ 0 \\ \vdots \\ F \end{bmatrix} \quad (4-34)$$

4.5.3 Model validation

Figure 4-11 shows a damping forced vibration of the 1D problem that was shown in Figure 4-2, in which the blue line is simulated with the dynamic FEM and is the dynamic response of the system that is started from the initial length of $L = 95$ and is damped over the equilibrium state of the system, all the other variables are taken the same as presented in Table 2. The horizontal axis shows the number of iterations that took to finally damp the vibration around the equilibrium state.

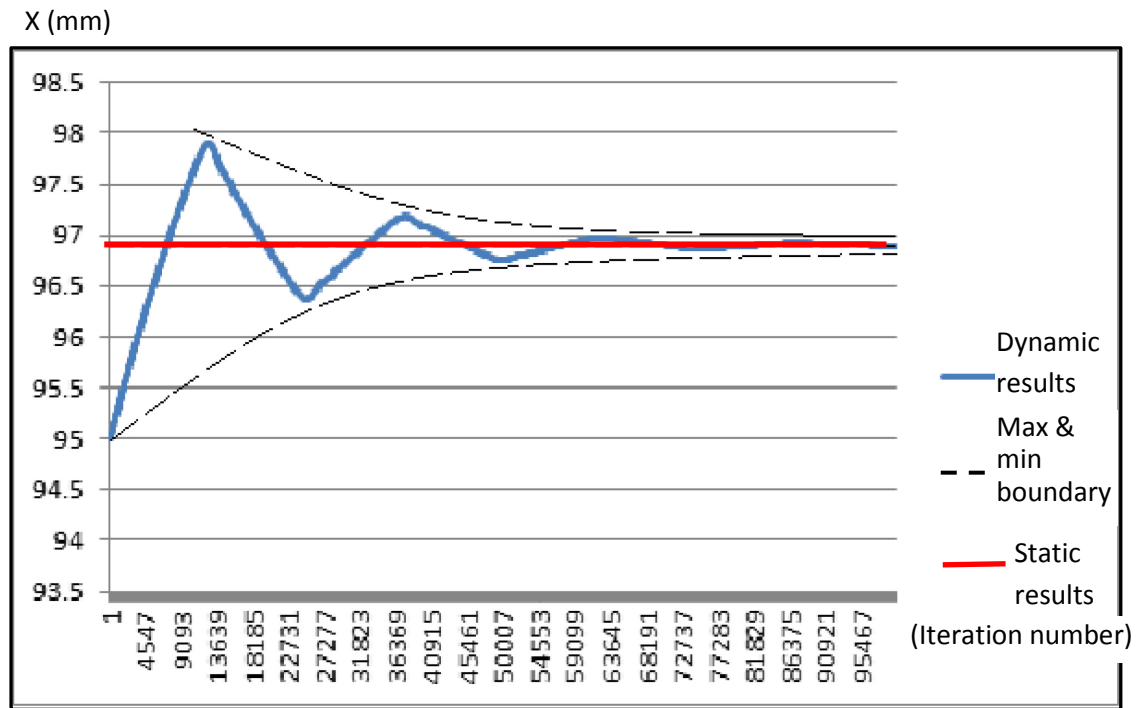


Figure 4-11 Static and dynamic response of forced vibration of the elastic bar with damping. The vertical axis shows the length of the beam. The horizontal axis shows the Iteration number. The time step is $\Delta t = 0.001$ second of each iteration.

In Figure 4-11 the blue line represents the dynamic response of the right hand node as shown in Figure 4-3, the dotted line is demonstrating the analytical solution of steady state displacement of the right hand node which is initially at $L = 95$. As it was mentioned earlier, the applied force is $F = 100$ and the stiffness of each element is $K = 1000$, and the total number of elements are 19.

Therefore, the equilibrium length of the bar after applying the stretching force at the right hand side of the bar is $L_{eq} = L + 1.9 = 96.9$ which is quite close to the steady state value of the dynamic response.

Generally, the analytical solution and the static and dynamic response of the FEM simulation of the forced vibration broadly consist with each other, and not only it can be used to validate the swelling induced by moisture absorption problem in 1D, but also reassure the validation of the 1D MPM code that was discussed earlier in this chapter.

4.5.4 Results of simulating swelling induced by moisture absorption

The result of simulating the 1D swelling induced by moisture absorption is shown in Figure 4-12, in which the total displacement of nodes 20th, 14th, 9th, and 4th are shown

in series 1 to series 4 respectively. The horizontal axis shows the number of iterations to get the final steady state swelling ratio. As it is shown in Figure 4-12, the lower three points start vibrating with a bit of delay. The dotted line in Figure 4-12 highlights the time of affecting each node by the moisture absorption, which indicates the motion in the beam is sequential with respect to the concentration of water molecules which is gradually increasing until it gets to an equilibrium state. Furthermore, it shows an approximately linear moisture absorption in one-dimensional swelling induced problem.

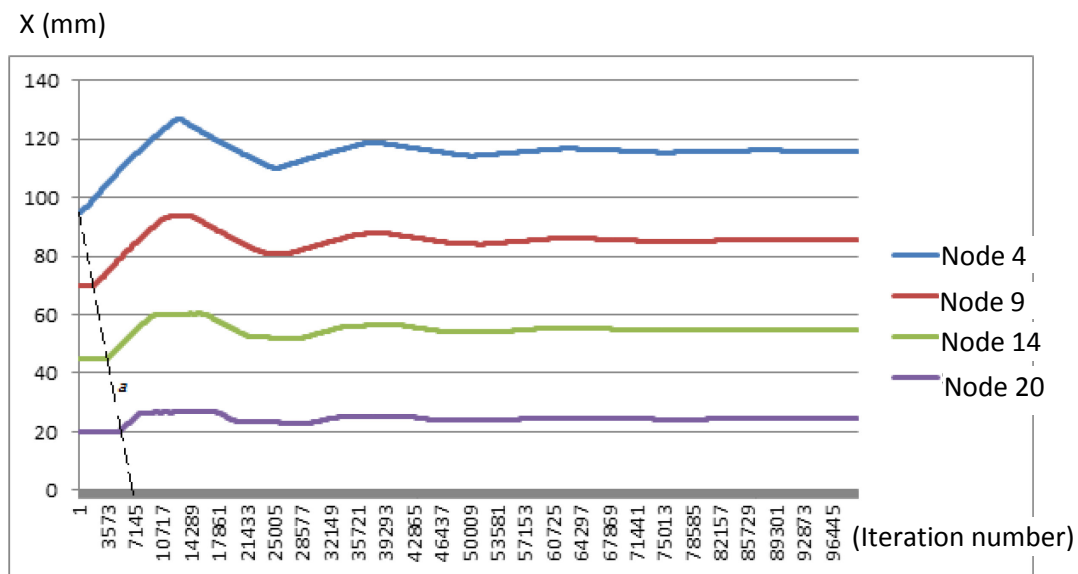


Figure 4-12 Position of different nodes due to moisture absorption, nodes 20, 14, 9 and 4 shown from series 1 to series 4 respectively. The vertical axis shows the length of the beam. The horizontal axis shows the Iteration number. The time step is $\Delta t = 0.001$ second of each iteration.

4.5.5 The effect of damping coefficient

Clearly damping coefficient does not have any effect on the equilibrium state of the system since at equilibrium state the velocity term will be zero and as it is shown in Eq. X (mm) the damping force will be zero. However, higher damping coefficient makes a smoother and slower swelling process as it is shown in Figure 4-13. Therefore, the stability of the system will be increased as there will be fewer fluctuations by using higher damping coefficients, up to about $d=10$.

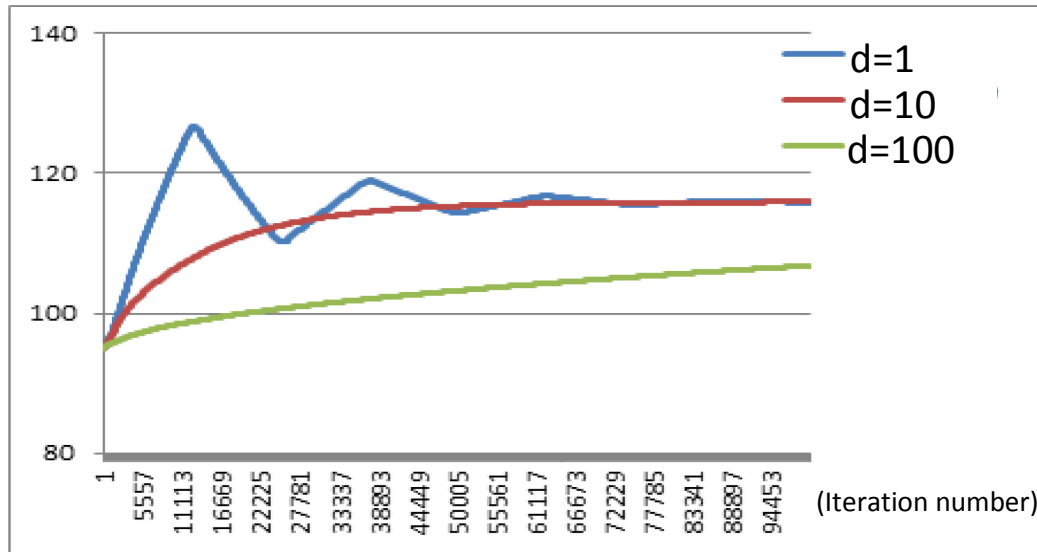


Figure 4-13 the effect of different damping coefficient on the swelling induced by moisture absorption. The green line shows the system is very slow and not yet reached an equilibrium state. For all the three cases diffusion coefficient is $D = 1000$ and Coefficient of hygroscopic swelling is $\alpha = 1$. The vertical axis shows the length of the beam. The horizontal axis shows the iteration number. The time step is $\Delta t = 0.001$ second of each iteration.

4.5.6 The effect of diffusion coefficient

Diffusion coefficient deals with the diffusion of solvent molecules (water molecules) in or out of the material, and directly affects the water concentration. Basically, water absorption reaches a certain value and remains there, the same time that swelling of the polymer reaches an equilibrium state. As it is shown in Figure 4-14 small diffusion coefficient makes the process very slow, however, higher diffusion coefficient may cause a big fluctuation.

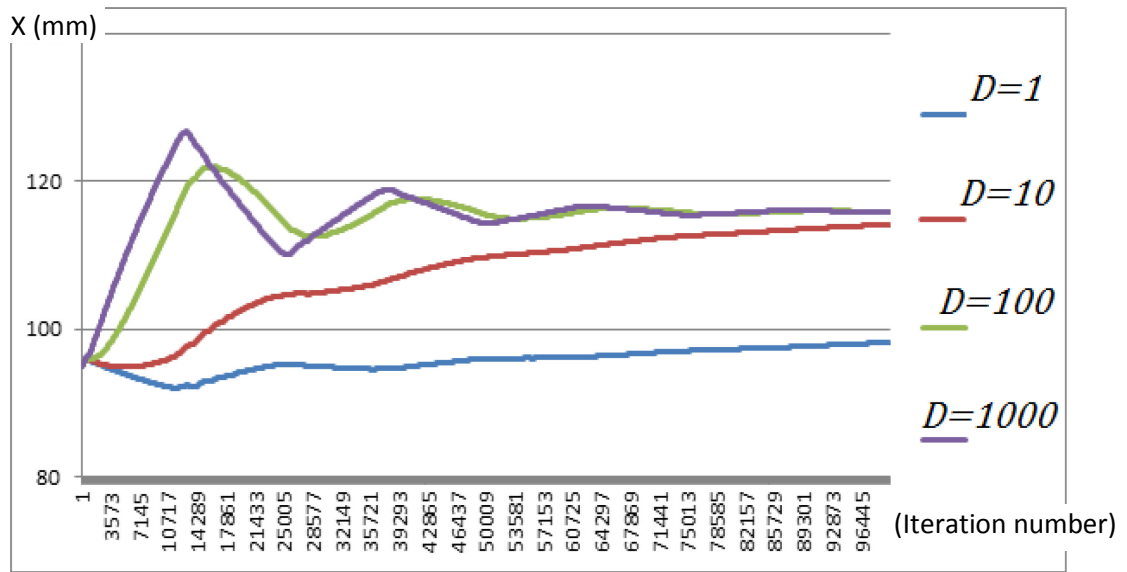


Figure 4-14 the effect of the different diffusion coefficient on the swelling induce by moisture absorption. The damping coefficient is $d = 1$ and Coefficient of hygroscopic swelling is $\alpha = 1$ for all the cases. The time step is $\Delta t = 0.001$ second of each iteration.

4.5.7 The effect of coefficient of hygroscopic swelling

The coefficient of hygroscopic directly impacts on the swelling ratio of the system. As it is shown in Eq.(4-24) higher coefficient of hygroscopic will cause larger swelling strain. Furthermore, Figure 4-15 shows that higher coefficient of hygroscopic increases the amplitude of vibration. According to Eq. (4-27) higher swelling strain provides a larger swelling force that affects the vibration amplitude.

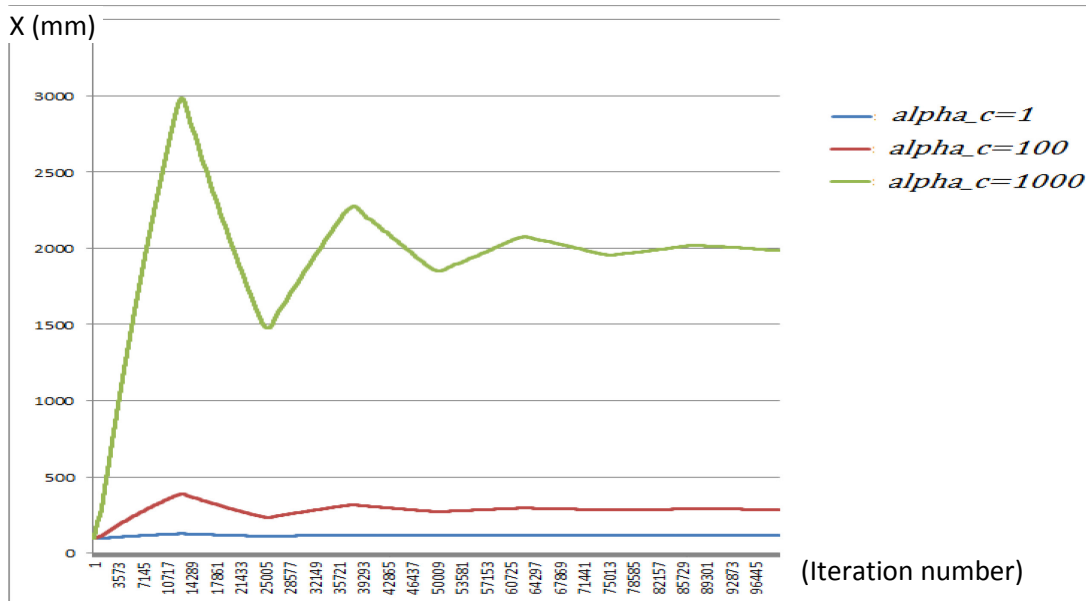


Figure 4-15 the effect of different coefficient of hygroscopic swelling of the material. The damping coefficient is $d = 1$ and the diffusion coefficient is $D = 1000$ for all the cases. The time step is $\Delta t = 0.001$ second of each iteration.

4.6 Implementation of MPM for 2D problems

It is important to validate the proposed Material Point Method scheme to insure the scheme can be used in more complicated applications. To validate the code in 2D, we have again solved a vibration problem with material point method and compared the results with analytical solutions. An elastic two-dimensional square body undertaking free vibration is employed as a benchmark test for our MPM code. As shown in Figure 4-16 the body is discretised into material points and the bottom boundary has been constrained to move in the Y direction, and the left boundary has been constrained to move in the X direction. One freer square of the computational mesh covers the possible domain of deformation of the material points just in case the material points move out of the initial square. Initially, the material points are distributed uniformly in the computational mesh.

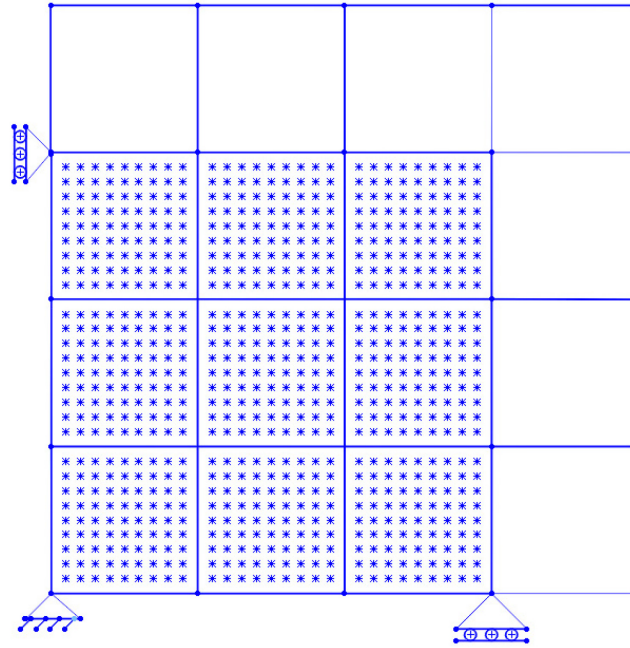


Figure 4-16 the schematic picture of a 2dimensional MPM with free meshes

In this case, an arbitrary constant stress $\sigma_0(X_p)$ is applied to every material point through the time, also a damping effect is assumed for the system to damp the oscillation about the equilibrium state. In order to add the effect of the constant stress and the damper, internal nodal forces in Eq.(4-35) should be updated as bellow in each time step:

$$\begin{aligned}
 (f_I^{\text{int}})^t &= \sum_{p=1}^{N_p} M_p B_I^T(X_p^t) \frac{1}{\rho_p^t} \sigma^t(X_p^t) + \sum_{p=1}^{N_p} M_p B_I^T(X_p^t) \frac{1}{\rho_p^t} \sigma_0^t(X_p^t) \\
 &- \sum_{p=1}^{N_p} M_p B_I^T(X_p^t) \frac{1}{\rho_p^t} C(X_p) B(X_p) W_p(X_p)
 \end{aligned} \tag{4-35}$$

In Eq.(4-35) $\sigma_0(X_p)$ is a constant stress term and $C(X_p)$ is an arbitrary damping effect, that is applied to every material points through the time. The rest of the mapping system is the same as discussed in section 3.3.8.

4.6.1 Validation method

In order to validate the code, different cases with different Young's modulus, different values of density and different initial stresses are examined. The height and width of the

body are 30 mm, and the thickness is 1 mm. Three different Young's modulus $E=10$, $E=250$, and $E=500$ MPa have been used to demonstrate the effect of changing in Young's modulus. Poisson's ratio is $\nu = 0.4$ and the code has been run for two different densities of 1000 Kg/m^3 , and 2000 Kg/m^3 . For all these cases 10 material points are used in each mesh. Furthermore, the number of material points is examined to find the minimum number of material points needed for the convergence of the code. The bottom left corner of the 2 dimensional bodies that is shown in Figure 4-16 is initially positioned at the (0,0) of the computational mesh, the bottom boundary is constrained in the y direction by setting the vertical nodal velocity and the vertical nodal acceleration equal to zero at the bottom of the boundary; and the left boundary is constrained in the x direction by setting zero horizontal velocity and acceleration at the left side of the boundary. A different range of initial negative/positive stresses $\sigma_0(X_p) = -70 \text{ KPa}$, $\sigma_0(X_p) = -1 \text{ Pa}$, $\sigma_0(X_p) = 70 \text{ Pa}$ are employed as the initial stress conditions and a very high damping $C(X_p) = 1000000000$ or $C(X_p) = 1500000000$ are applied to every material point to damp the vibration about the equilibrium state. So, the above conditions are applied one by one and the results are shown in the next section.

4.7 Numerical results of 2D vibration simulation

4.7.1 Case study 1: the effect of Young's modulus

In the first case, the initial inputs are given as presented in Table 3 and three different Young's modulus are tested. In Figure 4-17, Figure 4-18, and Figure 4-19 the value of strain from the dynamic response of the MPM is compared with the analytical solution. The analytical solution can be easily calculated from the generalised Hook's law as shown in Eq.(4-36).

$$\varepsilon_x = \frac{1}{E}(\sigma_x - \nu\sigma_y) \quad (4-36)$$

Thre different Young's modulus for different cases (MPa)	10, 250, 500
Poisson's ratio	0.4
Density of Kg/m ³	1000
Initial negative stress in X and Y direction (KPa)	-70
Number of material points per element	100
Damping coefficient (NS/m)	1000000000

Table 3 shows the initial input for case study 1

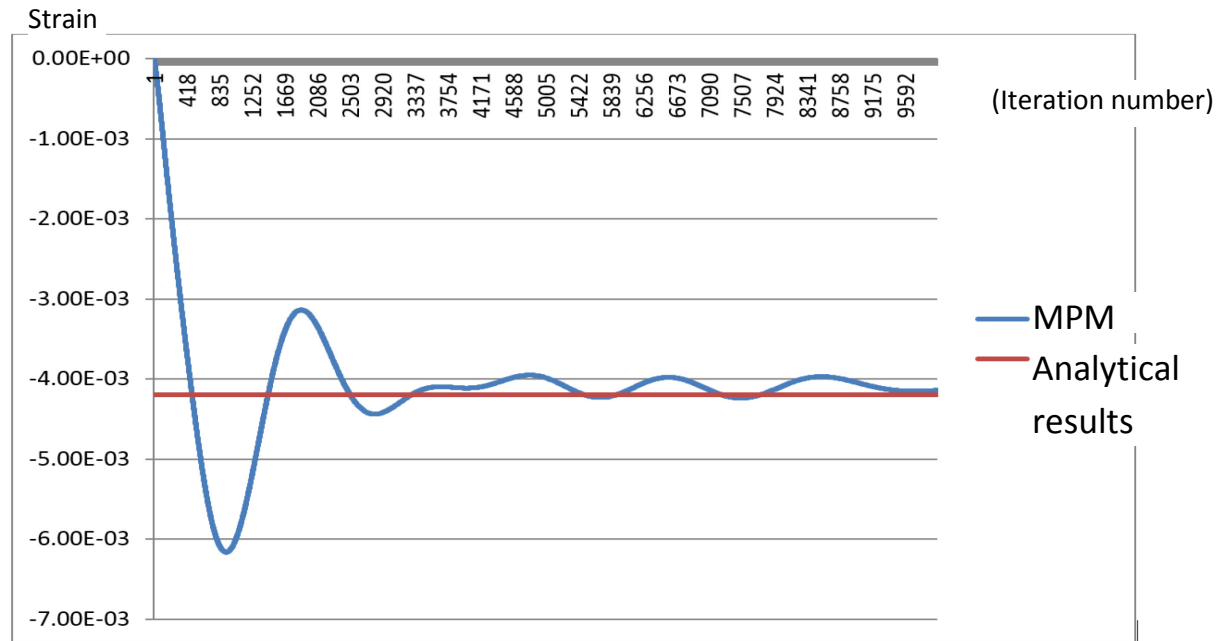


Figure 4-17 the fluctuating line shows the results MPM code with Young's modulus $E=10$ MPa, Poisson's ratio $\nu = 0.4$, the density of 1000 Kg/m^3 , 100 material points is used in each computational cell, initial negative stress $\sigma_0(X_p) = -70 \text{ KPa}$, and damping $C(X_p) = 1000000000$, and the red line shows the equilibrium state of deformation. The time step is $\Delta t = 0.001$ second of each iteration.

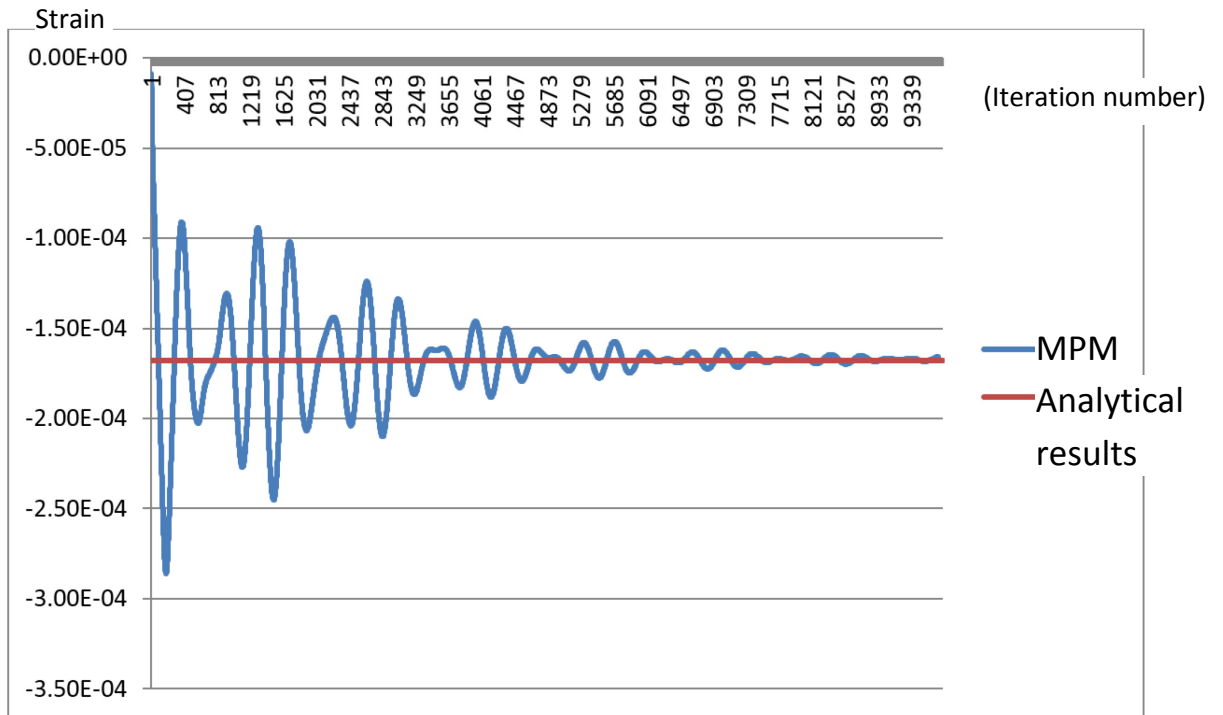


Figure 4-18 the fluctuating line shows the results MPM code for a strain with Young's modulus $E=250$ MPa, Poisson's ratio $\nu = 0.4$, the density of 1000 Kg/m³, 100 material points is used in each computational cell, initial negative stress $\sigma_0(X_p) = -70$ KPa, and damping $C(X_p) = 1000000000$, and the red line shows the equilibrium state of deformation. The time $st_{\epsilon_{Strain}} = 0.001$ second of each iteration.

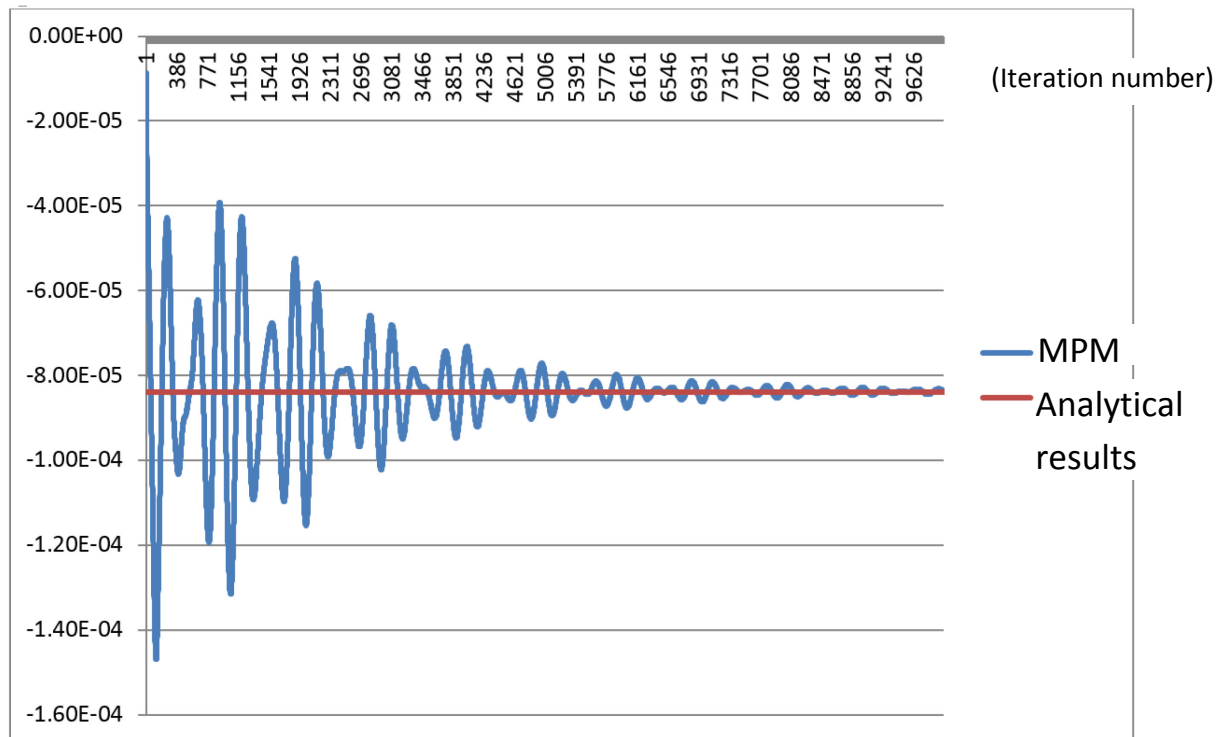


Figure 4-19 the fluctuating line shows the results MPM code for a strain with Young's modulus $E=500$ MPa, Poisson's ratio $\nu = 0.4$, the density of 1000 Kg/m³, 100 material points is used in

each computational, initial negative stress $\sigma_0(X_p) = -70KPa$, and damping $C(X_p) = 1000000000$, and the red line shows the equilibrium state of deformation. The time step is $\Delta t = 0.001$ second of each iteration.

4.7.2 Case study 2: the effect of constant stress

In the second case study, the initial inputs are given as presented in Table 4 with three different values of constant stresses. As it is expected for negative values of the constant stress the body shrinks and for positive values it expands. As it is shown in Figure 4-17, Figure 4-20 and Figure 4-21 strain values from the steady state response of MPM code is quite close to the analytical solution from Generalised Hook’s law.

Young’s modulus (MPa)	10
Poisson’s ratio	0.4
Density of Kg/m ³	1000
Initial stress in X and Y direction(KPa)	-70,-0.001,0.07
Number of material points per element	100
Damping coefficient (NS/m)	1000000000

Table 4 shows the initial input for case study 2

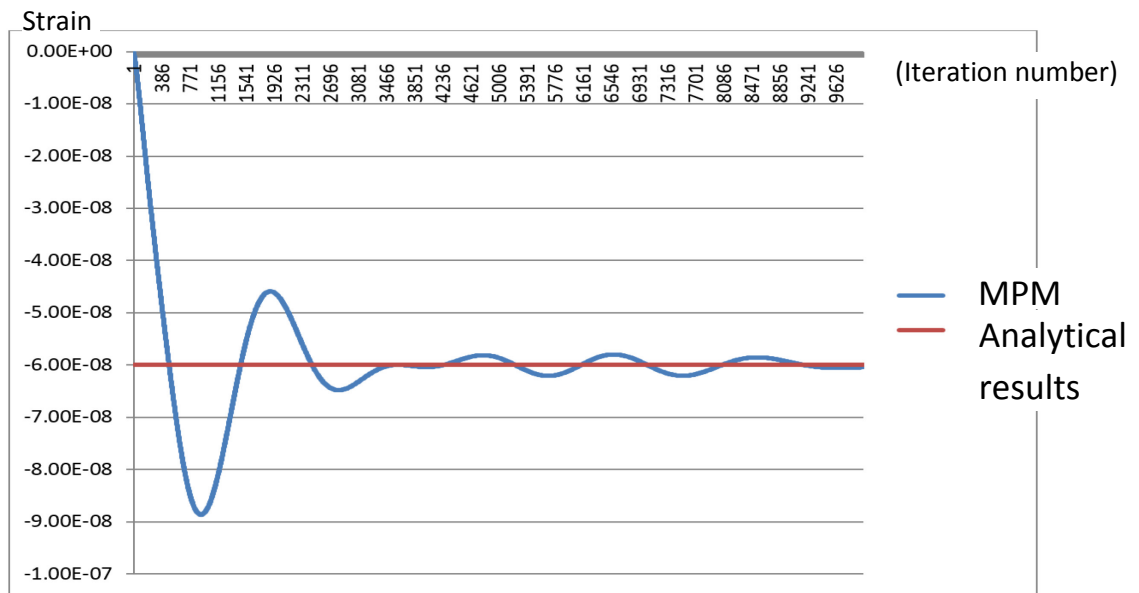


Figure 4-20 the fluctuating line shows the results MPM code for a strain with Young’s modulus $E=10$ MPa, Poisson’s ratio $\nu = 0.4$, the density of 1000 Kg/m³, 100 material points is used in each computational cell, initial negative stress $\sigma_0(X_p) = -1Pa$, and damping $C(X_p) = 1000000000$, and the red line shows the equilibrium state of deformation. The time step is $\Delta t = 0.001$ second of each iteration.

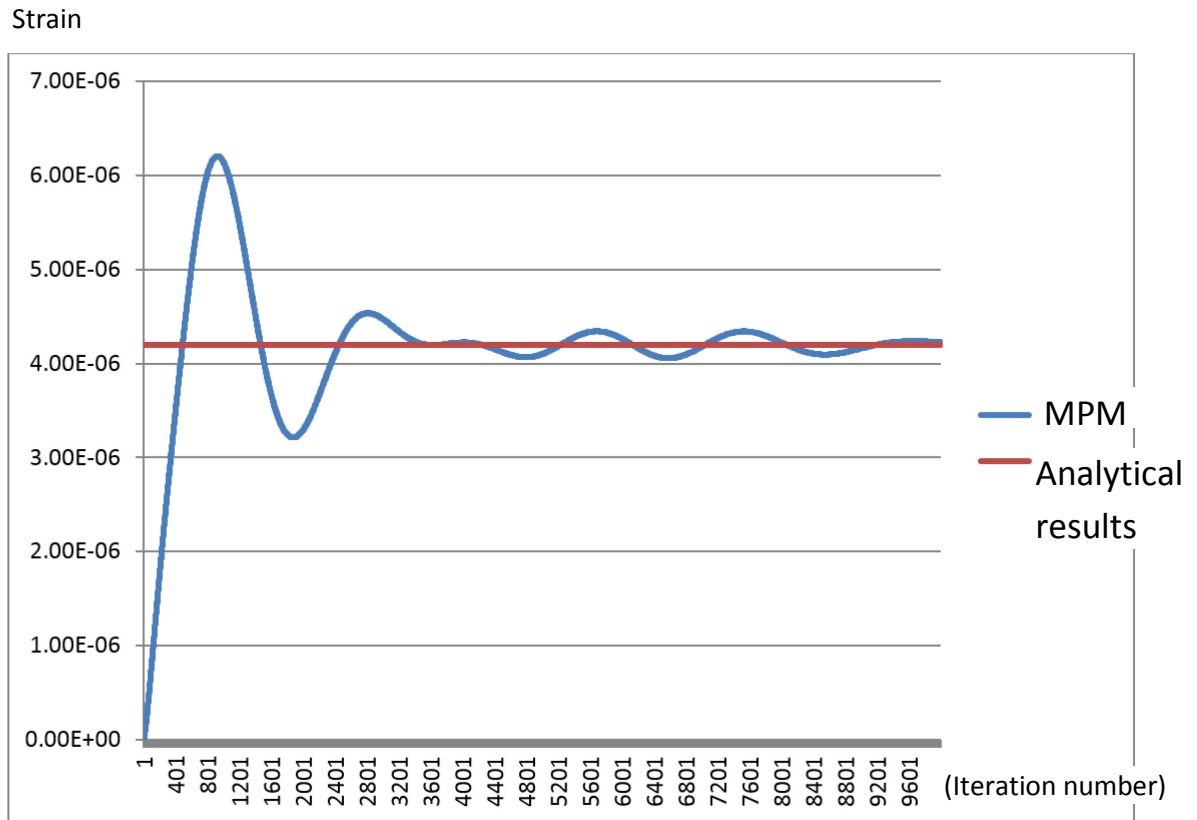


Figure 4-21 the fluctuating line shows the results MPM code for a strain with Young's modulus $E=10$ MPa, Poisson's ratio $\nu = 0.4$, the density of 1000 Kg/m³, 100 material points is used in each computational cell, initial positive stress $\sigma_0(X_p) = 70$ Pa, and damping $C(X_p) = 1000000000$, and the red line shows the equilibrium state of deformation. The time step is $\Delta t = 0.001$ second of each iteration.

4.7.3 Case study 3: the effect of density and damping coefficient

As it was expected the MPM program works for a good range of densities. As it is shown in Figure 4-21 and Figure 4-22 changing the density when the rest of the parameters in Table 1 are kept constant validates almost identical results. This shows the program can deal with a good range of densities. Furthermore, as it was discussed earlier the effect of the damping force here in this simulation is to damp the dynamic response to the steady state situation. Therefore, the value of damping coefficient is not making an important role as finally, the damping force reaches zero at the equilibrium state as the velocity gets to zero, however, and higher coefficient damps the oscillations faster. Figure 4-23 shows the amplitude of oscillations get smaller and the system reached equilibrium state faster compared to the Figure 4-22 in which the rest of the parameters are taken the same in both of them.

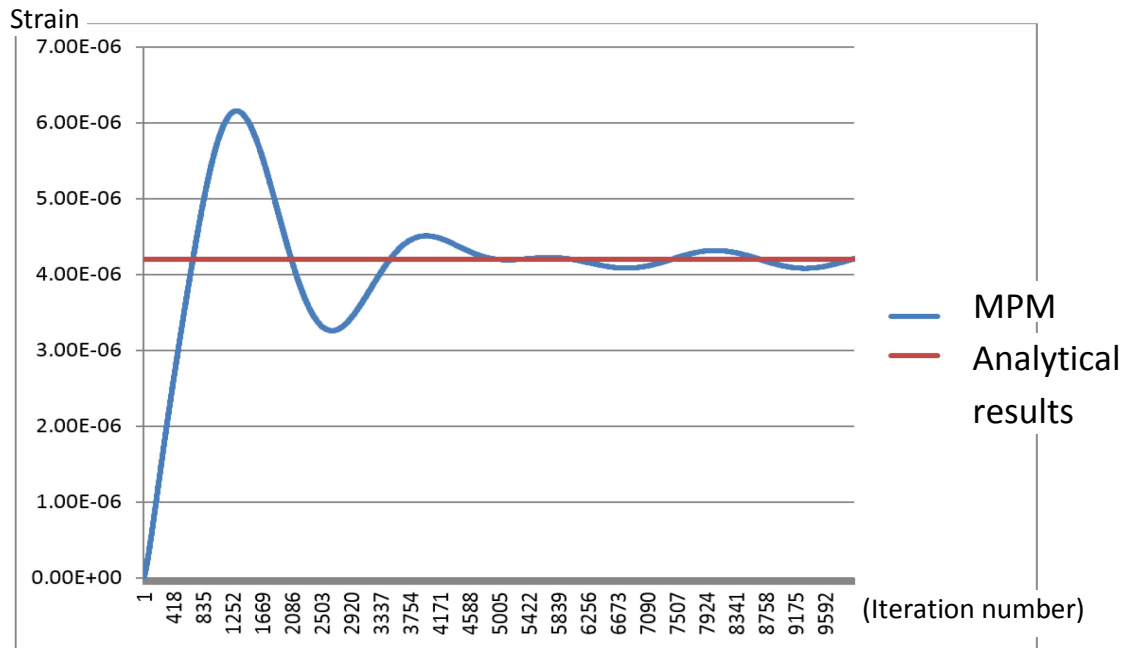


Figure 4-22 the fluctuating line shows the results of MPM code for a strain with Young's modulus $E=10$ MPa, Poisson's ratio $\nu = 0.4$, the density of 2000 Kg/m³, 100 material points is used in each computational cell, initial positive stress $\sigma_0(X_p) = 70$ Pa, and damping $C(X_p) = 1000000000$, and the red line shows the equilibrium state of deformation. The time step is $\Delta t = 0.001$ second of each iteration.

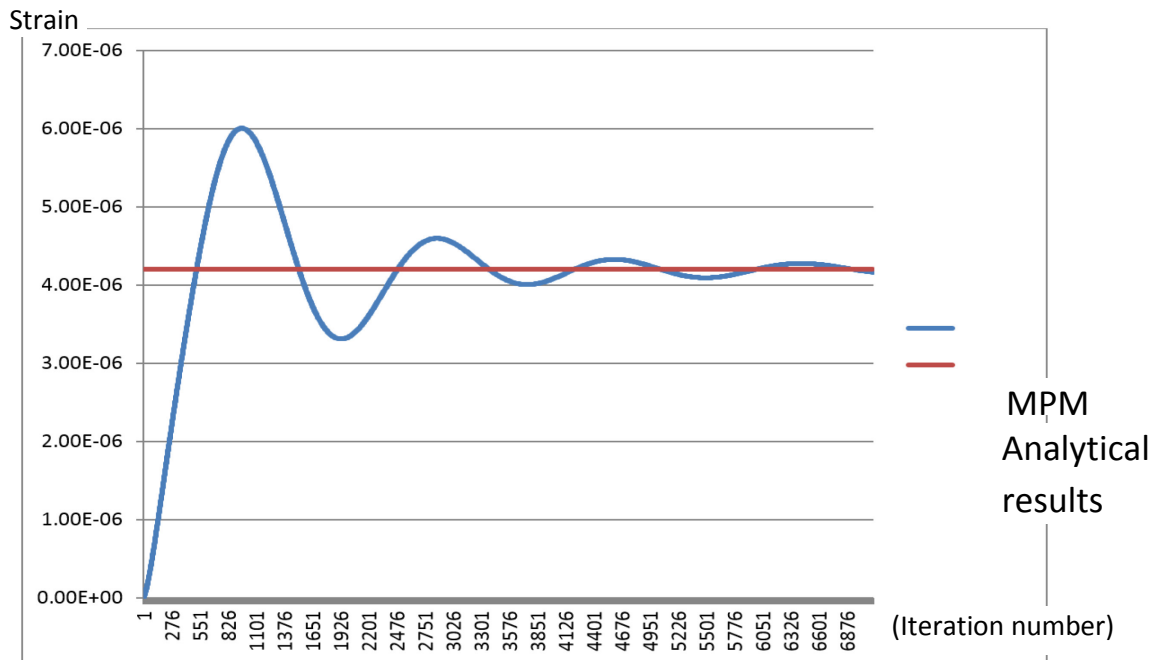


Figure 4-23 the fluctuating line shows the results of MPM code for a strain with Young's modulus $E=10$ MPa, Poisson's ratio $\nu = 0.4$, the density of 2000 Kg/m³, 100 material points is used in each computational cell, initial positive stress $\sigma_0(X_p) = 70$ Pa, and damping

$C(X_p) = 1500000000$, and the red line shows the equilibrium state of deformation. The time step is $\Delta t = 0.001$ second of each iteration.

4.7.4 Case study 4: the effect of number material points

Generally, Material Point Method is a costly numerical technique compared to the conventional finite element method due to its numerical difficulties. As there are complicated topological systems between the material points and the background computational mesh, using minimum possible material points can hugely decrease the cost of numerical analysis. Hence, a convergence test is always suggested specially in small deformation. Fan Li (2008) has carried a convergence test based on three different factors, a number of material points, the number of cells of computational mesh, and material point density (i.e. the average number of material points per unit cell of the computational mesh). He has concluded in his study that the material point density is the most important factor that controls the convergence. Therefore, he suggested 94 material points per unit computational cell as the minimum required for the 2D small deformation analysis based on the convergence test he has carried out in his study. The ultimate goal of this thesis is to apply MPM for large elastic deformation of the materials that is also combined with degradation during large swelling.

In problems with large elastic swelling together with degradation, as the material points travel far from their initial computational cell due to the large swelling, or the material points may be deleted due to the degradation, the material point density may enormously decrease, as a result of a huge volume change. Hence, the initial number of material points should be much more than the minimum required that is suggested by F. Li (2008). Therefore, for the problem of degradation during large swelling the convergence test should be carried out for each example separately, since the required minimum number of material points may increase for those problems that undergo higher elastic swelling. Hence, the MPM should be first validated with a large number of material points per unit computational cell, as it is discussed in chapter 6, and then the minimum number of material points can be achieved by repeating the same modelling for the lower number of material points per unit computational cell, until the same results is no longer achievable. Alternatively, if the final swelling ratio can be

predicted analytically, the initial number of material points per computational cell in the reference body can be assigned wisely. The prediction of the final swelling ratio for large deformation is discussed in chapter 6. In order to avoid an enormous decrease in material point density in the large swelling, especially in the boundary of the main body, we have suggested using extra boundary layer around the main body that is described in detail in chapter 6 as well.

Here in this case study, the same 2D small vibration in Figure 4-23 is repeated with 94 material point per unit computational cell, all the other parameters are taken the same as case 3. By comparing Figure 4-24 and Figure 4-23 the results are almost identical.

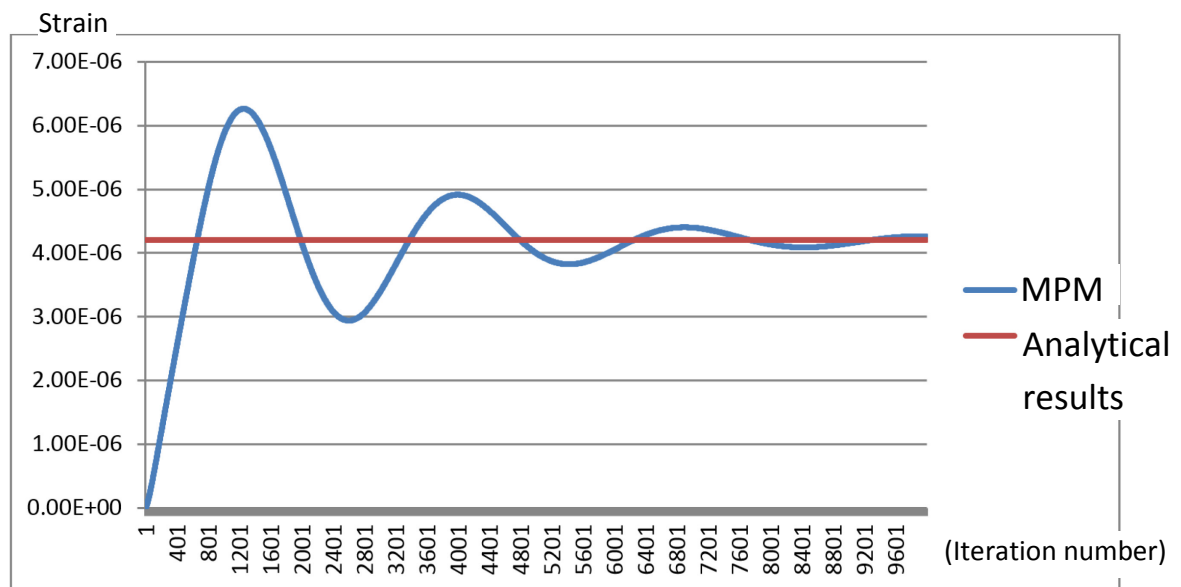


Figure 4-24 the fluctuating line shows the results MPM code for a strain with Young's modulus $E=10$ MPa, Poisson's ratio $\nu = 0.4$, the density of 2000 Kg/m³, 94 material points is used in each computational cell, initial positive stress $\sigma_0(X_p) = 70$ Pa, and damping $C(X_p) = 1500000000$, and the red line shows the equilibrium state of deformation. The time step is $\Delta t = 0.001$ second of each iteration.

4.8 Validation of the code by simulating a uniaxial tensile test

In all the above cases, a constant negative or positive stress is applied to the material points and the final steady state swelling ratio is compared with the analytical value. In a different attempt to validate the code, a time depending stress is applied to the

material points, to simulate a uniaxial tension. Therefore, the value of Young's modulus and Poisson ratio obtaining from the stress strain curve in 2D are compared with the initial inputs. In this case, a body with height and width equal to 30 mm and thickness equal to 1 mm is considered. Instead of applying a uniaxial nodal force which is usual in uniaxial tensile tests, a time depending stress is applied to all the material points. The material constitutive law for updating the stress is the simple linear 2D generalized Hook's law. The boundary is constrained at the bottom in the Y direction, and also is constrained on the left side in the X direction. Two different cases are examined:

In the first case study, the material is under a uniaxial tension in the X direction, and a time depending initial stress $\sigma_0(X_p) = (0.1 * t)Pa$ is applied to all the material points through the time. The initial inputs are, Young's modulus $E=2$ GPa, Poisson's ratio $\nu = 0.4$, damping is $C(X_p) = 1000$.

As it is shown in Figure 4-25, the result of Young's modulus which is obtaining from Hook's law $E = \frac{\sigma_x}{\varepsilon_x}$ is perfectly matched with the initial input for Young's modulus.

Furthermore, Figure 4-26 exhibit an impeccable result for the Poisson's ratio that is the negative ratio of transverse to axial strain that is shown in Eq.(4-37).

$$\nu = -\frac{\varepsilon_y}{\varepsilon_x} \quad (4-37)$$

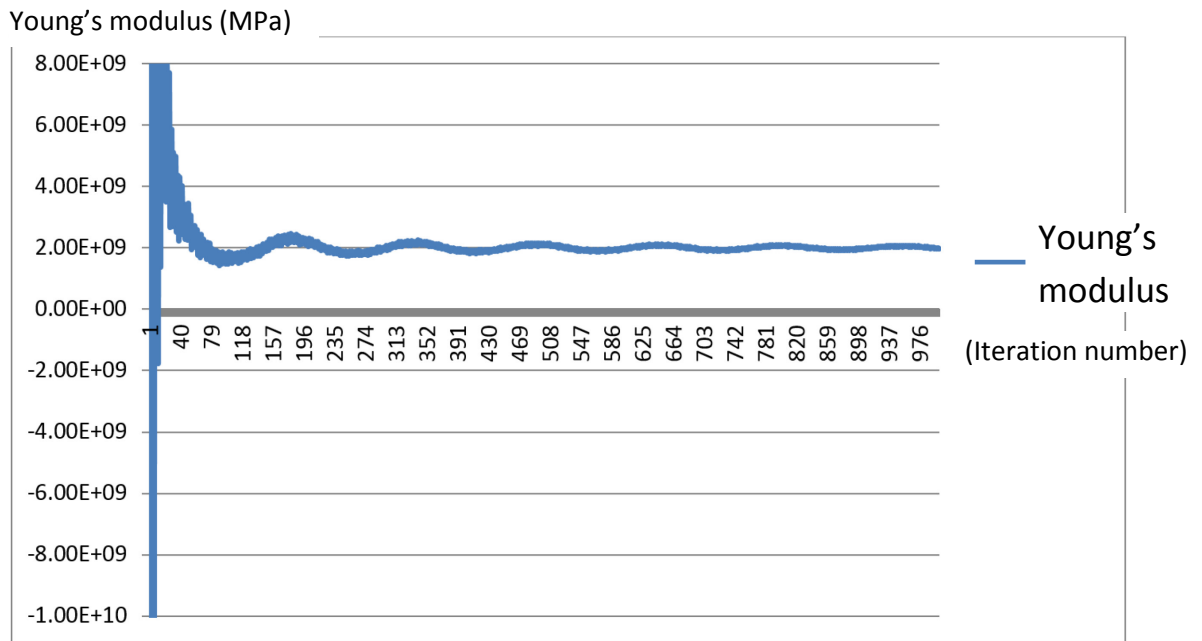


Figure 4-25 the value of Young's modulus is calculated via dividing stress by strain which is obtained from MPM in the X direction. The time step is $\Delta t = 0.001$ second of each iteration.

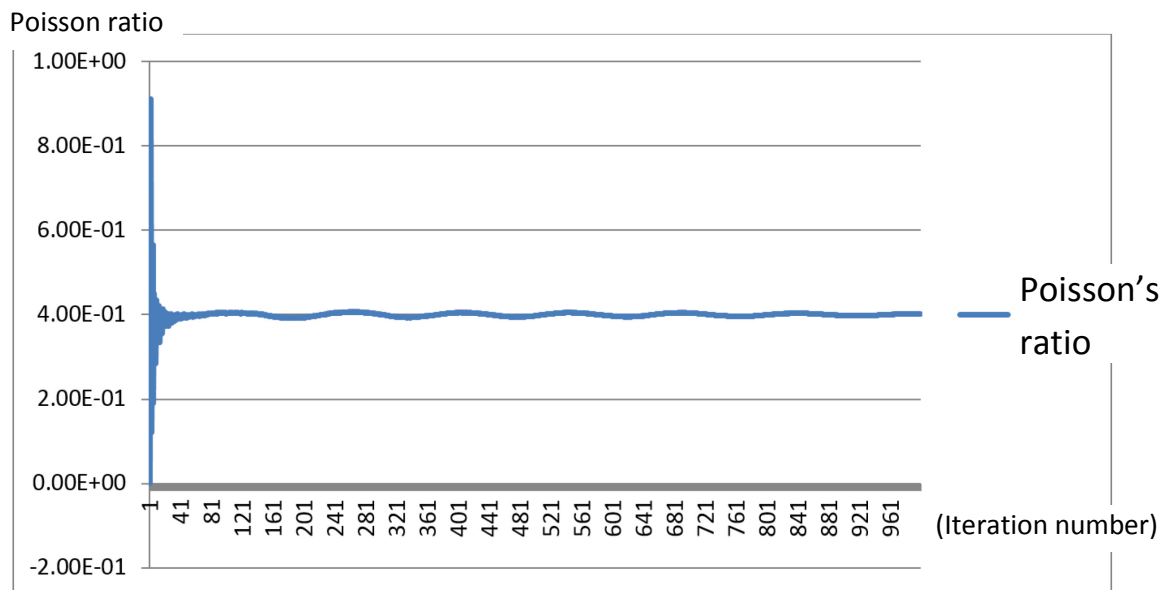


Figure 4-26 the value of Poisson's ratio is calculated via dividing stain in the Y direction by strain in the X direction. The time step is $\Delta t = 0.001$ second of each iteration.

In the second case study, the same uniaxial test with all the same conditions has been carried out, except Young's modulus and Poisson's ratio is set to be $E=500$ MPa and $\nu = 0.2$. As it is shown in Figure 4-27 and Figure 4-28 the steady state value of Young's

modulus and Poisson ratio that comes from the MPM code is almost identical to the initial values.

Young's modulus (MPa)

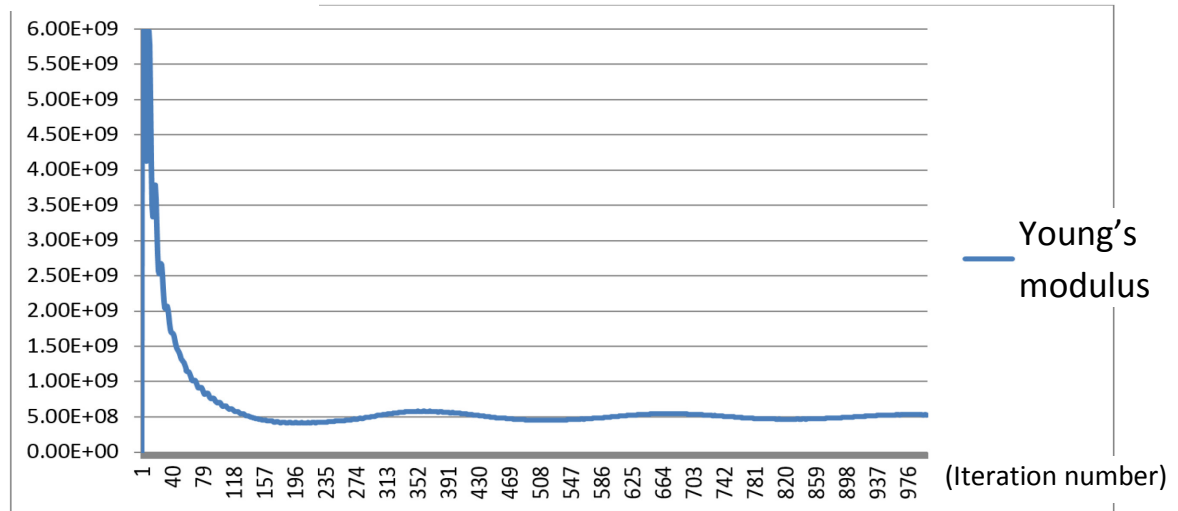


Figure 4-27 the value of Young's modulus is calculated via dividing stress by strain which is obtained from MPM in the X direction. The time step is $\Delta t = 0.001$ second of each iteration.

Poisson ratio

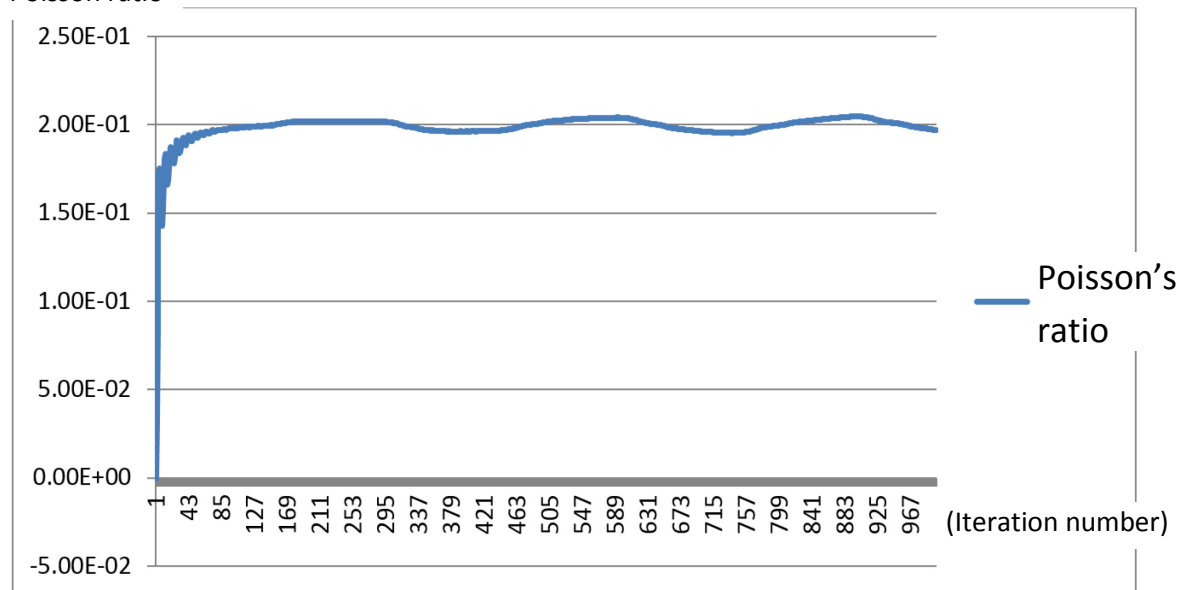


Figure 4-28 the graph shows the division of negative of strain in the Y direction by strain in the X direction which is equal to the Poisson's ratio. The time step is $\Delta t = 0.001$ second of each iteration.

As it is shown in section 4.7 and section 4.8 the code is validated with two different methods. In the first attempt by simulating a forced vibration problem via applying a constant stress to the material points and using a big damping system to damp the

oscillations over the equilibrium state. It has been tested with different conditions and in all the cases the outcomes are perfectly matching with the expecting results. These tests show that the MPM code gives the right value of steady state swelling ratio, while in the second attempt a simple tensile test for small deformation is considered, by applying a time depending uniaxial stress to all the material points. The Young's modulus which has been calculated via dividing the stress and strain at each time is equal to the input value for Young's modulus, and also the value of Poisson's ratio via calculating the ratio of transvers by axial strain has been checked with the initial input for Poisson's ratio which is impeccably matches. The results of the uniaxial test validate that the MPM code returns the correct values of stress and strain at any time. Furthermore, depends on the constitutive law that has been initially used the response of the system is identical. Therefore, the code is surely validated.

4.9 Summary of this chapter

In this chapter in the first case study to validate the MPM code a simple 1D forced vibration is considered as a bench mark. The problem is solved through a dynamic FEM and the result of the steady state situation was compared with the analytical solution for the equilibrium state, and a good match was obtained. Furthermore, the same initial condition was applied to the MPM code in 1D and almost the same respond was achieved for a forced vibration from the MPM code, which can be used to validate the MPM code in 1D.

In the second case study, a 2D tensile test was simulated by the MPM code as the benchmark. Since Material Point Method returns the dynamic response of the vibration, therefore a full validation should include the checking of steady state deformation and also the checking of stress, strain relationship at each time step. In this test not only the final steady state deformation was compared with the analytical solution for equilibrium state, but also the numerical values of Young's modulus and Poisson ratio was compared with the initial inputs. In order to check whether the code only returns the correct steady state solution or it can return a correct relationship between stresses and strains based on the linear constitutive law. Therefore, by checking the numerical values of

Young's modulus and Poisson ratio we can be assured that the linear constitutive law that is defined initially is followed in each time step.

As an application of the non-equilibrium thermodynamic theory that was introduced in chapter 2, a 1D polymer swelling induced by moisture absorption is solved numerically by finite element method. As we initially validated the 1D FEM code, the same FEM code is used to study the diffusion coefficient, damping coefficient and the effect of coefficient of hygroscopic swelling in polymer swelling induced by moisture absorption.

Chapter 5. Degradation of Highly Swellable Polymers During Large Elastic Swelling

The Purpose of this chapter is first to test the validity of MPM for the problem of extremely large deformation, by comparing the constitutive law that has been derived and fed to the numerical method based on Flory's constitutive law. The key result is shown in Figure 5-19. Secondly, the capacity of MPM to model a non-uniform elastic swelling that is difficult to handle by standard FEM is demonstrated. Additionally, degradation during large elastic swelling has been modelled as a random phenomenon and has been applied to the multi-layered tablets for controlled drug released systems.

5.1 Introduction

Highly swellable polymers with cross-linked polymeric chains in contact with solvent molecules (e.g. water) form hydrogels. The small solvent molecules can migrate through three dimensional network structures, and the resulting material that is formed is called elastomer, which is capable of large and reversible deformation in response to external forces or excitations N. Bouklas (2015). A lot of solvent molecules will be diffused inside the polymer to form the hydrogel due to the chemical potential. Figure 5-1 shows a schematic diagram of solvent molecules diffused inside the polymer.

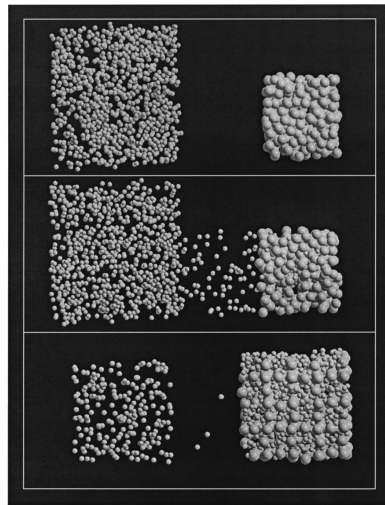


Figure 5-1 shows a schematic diagram of solvent molecules diffused inside the polymer E. M. Aydt and R. Hentschke (1999)

Therefore the solvent molecules in the hydrogel interact with weak physical bonds and may break many of the bindings and locate themselves between adjacent chains. As a result of the broken bonds, the hydrogel gets more freedom in three dimension and swells. Finally, when the swelling ratio reaches a certain value, degradation will be occurring as a result of very weak bonding between the polymer chains. Degradation is a random value, which means the polymer chain may break from either end of the chain and make an oligomer, or it can happen somewhere in the middle of the chain A. Gleadall, et al. (2014). Coupled problem of large deformation and degradation are synthesized for diverse applications such as drug delivery systems and tissue engineering. Many different processes inside the gel may lead to a large deformation and migration as well. For example, when the drug is accommodated inside a highly swellable polymer and it is in contact with a solvent, the solvent molecules diffuse in as a result of chemical potential. Therefore the drug will be dissolved and migrate out due to a change in physiological conditions such as a change in the level of Ph. The rate of the drug release is a function of the deformation of the gel. Furthermore, localized stress in the gel can occur due to swelling. A nonlinear, transient finite element method was suggested by N. Bouklas et al. (2015) to simulate coupled solvent diffusion and large deformation of hydrogels that was based on the mixed FEM with implicit time integration. They have followed Hong et al. (2008), to describe a constitutive behaviour of polymer gel through a free energy density function based on the Flory-Rehner theory.

Hong et al. (2008); Zhang et al. (2009) assumed both polymer and the solvent are incompressible. Therefore, the volumetric strain of the hydrogel should be equal to the solvent concentration N . Bouklas (2015) suggested by adding a quadratic term to the elastic free energy of hydrogels incompressibility assumption for the polymer can be lifted. Therefore, no imposed constraint will be applied on the deformation gradient. But neither of them coupled degradation problem with large deformation of highly swellable polymers. The main difficulty of coupling degradation problem with extremely large deformation is the usage of the appropriate numerical system. Conventional finite element methods are capable of simulating large deformation problems, but modelling degradation problem with conventional FEM is almost impossible. As the main body keeps losing mass, and not only a regular re-meshing system is required, but also it can make a difficult geometry or porous body at extreme cases that are difficult to mesh. Therefore, the topological system should be constantly changed and this will cause a fatal inaccuracy in the conventional FEM.

Over the last decades, polymeric gels are used in various fields of technologies, Medical applications Shahinpoor, Kim (2004), biosensors Gerard, Chaubey, and Malhotra (2002), controlled drug delivery L. Djekic et al. (2015) are a few examples of polymer's applications in industry. But, the focus of this thesis is on the highly swellable materials that are mainly used in drug delivery systems. There has been an increasing interest in the field of controlled drug delivery from non-toxic and highly swellable matrix systems (hydrogels) in pharmaceutical industry. Hydroxypropyl methylcellulose (HPMC) is one of the most used hydrophilic carrier material mainly for oral controlled drug delivery systems Bouklas N., et al. (2015). Being non-toxic and also decent mechanical properties of HPMC such as compression characteristics and also sufficient swelling properties (i.e. corresponding time and the degree of swelling), have made it a very commonly used hydrophilic carrier material. Swellability of the carrier material has a major effect on the release kinetics of an incorporated drug Bouklas N., et al. (2015). Polymer networks upon contact with small molecules (e.g. water or biological fluid) form polymeric hydrogel Siepmann, Peppas, (2000). A hydrogel can swell considerably by absorbing the solvent molecules due to various environmental conditions (e.g. temperature) and finally dissolves Siepmann, Peppas, (2000). Obviously, the mass concentration of the

drug dramatically changes due to swelling of the polymer. According to the Fick's second law, diffusion of the drug out of the polymeric hydrogel is related to the mass concentration of the drug, and decreasing in mass concentration causes decreasing in drug diffusion. Thus, it is necessary to investigate polymer swelling in the drug delivery problem.

5.2 Theoretical Background

5.2.1 Rate form of constitutive law for hyperelastic materials

The majority of the mathematical background should be referenced to T. Belytschko et al. 2005, and M. Kang et al. 2010.

As the rate form of constitutive law is used in the MPM, a general rate form derivative of constitutive law based on Flory's approach is presented in this section. The rating form of stress and strain relationship for hyperelastic materials can be defined as below

$$\dot{S} = 4 \frac{\partial^2 \psi(C)}{\partial C \partial C} : \dot{C} = \frac{\partial^2 \omega(E)}{\partial E \partial E} : \dot{E} = C^{SE} : \dot{C} = C^{SE} : \dot{E} \quad (5-1)$$

Where C^{SE} is called the tensor of tangent modulus tensor, also it is called the second elasticity tensor, and can be obtained as

$$C^{SE} = 4 \frac{\partial^2 \psi(C)}{\partial C \partial C} = \frac{\partial^2 \omega(E)}{\partial E \partial E} \quad (5-2)$$

5.2.2 Derivation of rate form of Flory's constitutive law

In this section derivation of the nominal stresses and also chemical potential based on Flory's approach is discussed in details based on the works done by (Hong et al. 2007). Since the numerical method which is used in this thesis is based on the material point method, a rate form of the constitutive law is required. Therefore, in this chapter, only the rate form of Flory's constitutive law is discussed.

As it was shown in Eq.(5-3) and (5-4) in order to derive nominal stresses and chemical potential, a functional form of the free energy density of the hydrogel is mandatory.

$$s_{ik} = \frac{\partial U(F, C)}{\partial F_{ik}} \quad (5-3)$$

$$\mu = \frac{\partial U(F, C)}{\partial C} \quad (5-4)$$

5.2.3 Free energy function

Based on Flory's theory, the functional form of the free energy density $U(F, C)$ is required for the analysis of the swelling deformation of hydrogels. Therefore, the suggested approach by Flory is to take into account of two separated parts of the free energy function.

$$U(F, C) = U_e(F) + U_m(C) \quad (5-5)$$

According to M. K. Kang and R. Huang (2010) based on the statistical mechanics model of rubber elasticity, was obtained by Flory, the density of the elastic free energy is as

$$u_e(F) = \frac{1}{2} Nk_B T [\lambda_1^2 + \lambda_2^2 + \lambda_3^2 - 3 - \ln(\lambda_1 \lambda_2 \lambda_3)] \quad (5-6)$$

Where, λ_1 , λ_2 and λ_3 are the principal stretches in the principal directions of the deformation gradient tensor F and N is the effective number of polymer chains per unit volume of the hydrogel at the dry state, which is related to the cross-link density of the polymer network. The initial shear modulus of an elastomer is defined as $Nk_B T$ M. K. Kang and R. Huang (2010). Equation (5-6) will be reduced to the familiar strain energy density function for an incompressible neo-Hookean material in which the deformation does not change the volume (i.e. $\lambda_1 \lambda_2 \lambda_3 = 1$). The last term in the bracket of equation (5-6) is as a result of the entropy change associated with the volume change, and to account for the volume change in rubber elasticity many another forms of the free energy function have been suggested. For example, Kang and Huang suggested the following equation:

$$u_e(F) = \frac{1}{2} Nk_B T [\lambda_1^2 + \lambda_2^2 + \lambda_3^2 - 3 - 2 \ln(\lambda_1 \lambda_2 \lambda_3)] \quad (5-7)$$

Note that the principal stretches λ_1 , λ_2 and λ_3 as well as deformation gradient in equation (5-3) and (5-4) are defined with respect to the dry state as the reference, which assumes to be isotropic.

According to the Flory-Huggins polymer solution theory, the free energy change due to the mixing of pure solvent with a polymer network is as below:

$$\Delta F_m = k_B T [n_1 \ln \varphi + \chi n_1 (1 - \varphi)] \quad (5-8)$$

Where, n_1 is the number of solvent molecules, φ is the volume fraction of the solvent, and χ is a dimensionless quantity that characterizes the interaction energy between the solvent and polymer. The first term on the right hand side of Eq. (5-8) comes from the entropy of mixing, and the second term comes from the heat of mixing (enthalpy).

By the assumption of molecular incompressibility, the volume swelling ratio of the hydrogel is

$$J = \frac{V}{V_0} = 1 + \nu C \quad (5-9)$$

Where, ν is the volume per small molecule, and νC is the volume of the small molecules in the gel divided by the volume of the dry polymers, also we have $n_1 = V_0 C$ and $\varphi = \nu C / (1 + \nu C)$. Thus, the free energy of mixing per unit volume is as follows (Kang M.K. and Huang R., 2010)

$$u_m(C) = \frac{\Delta F_m}{V_0} = \frac{k_B T}{\nu} \left(\nu C \ln \frac{\nu C}{1 + \nu C} + \frac{\chi \nu C}{1 + \nu C} \right) \quad (5-10)$$

Eq. (5-10) is slightly different from that given by Hong W. et al. (2007) by a constant, which is insignificant for swelling deformation M. K. Kang and R. Huang (2010). At the dry state $C = 0$, $u_m = 0$ and increasing in the entropy of mixing which causes decreasing of the free energy drives the solvent molecules to enter the polymer network. This tendency to mix may be either opposed $\chi > 0$ (which motivates the small molecules to leave the gel) or enhanced $\chi < 0$ (which motivates the small molecules to enter the gel) by the heat of mixing, depending on the sign of χ . Furthermore, by preceding the process of absorption of the solvent molecules the elastic energy of the network increases as a penalty of swelling. Finally, a state of equilibrium swelling may be obtained, in which the total free energy reaches a minimum. Thus, for the equilibrium swelling state, the condition of molecular incompressibility in Eq. (5-10) can be imposed

as a constraint that relates the solvent concentration, C , to the deformation of the polymer.

Let s_1, s_2 and s_3 be the three principal nominal stresses and can be defined as

$$s_1 = \frac{\partial U}{\partial \lambda_1} = Nk_B T(\lambda_1 - \lambda_1^{-1}) - \Pi \lambda_2 \lambda_3 \quad (5-11)$$

$$s_2 = \frac{\partial U}{\partial \lambda_2} = Nk_B T(\lambda_2 - \lambda_2^{-1}) - \Pi \lambda_3 \lambda_1 \quad (5-12)$$

$$s_3 = \frac{\partial U}{\partial \lambda_3} = Nk_B T(\lambda_3 - \lambda_3^{-1}) - \Pi \lambda_1 \lambda_2 \quad (5-13)$$

Where, $\Pi(x, t)$ is a field of Lagrange multiplier which can be used to enforce the condition of molecular incompressibility, by adding a term $\int \Pi(1 + \nu C - J)d\Omega$ to the free energy, G , of the system.

5.2.4 Calculation of tangent modulus based on Flory's constitutive law

In order to derive an explicit formula for the tangent modulus at the current state, a lengthy derivation is carried out by M. K. Kang and R. Huang (2010). Hence, to find tangent modulus based on Flory's constitutive law, Eqs. (5-11) and (5-12) and (5-13) should be changed into rate form.

M. K. Kang and R. Huang (2010) following Hong et al. (2007) have taken a Legendre transformation of the free energy density function that is shown in Eq. (5-14) to solve the equilibrium swelling deformation with a prescribed chemical potential.

$$\hat{U}(F, \mu) = U(F, C) - \mu C \quad (5-14)$$

In Eq. (5-14) μ is called chemical potential, which is obtained from Eq. (5-15).

$$\mu = \frac{\partial u}{\partial C} = k_B T \left[\ln \frac{\nu C}{1 + \nu C} + \frac{1}{1 + \nu C} + \frac{\chi}{(1 + \nu C)^2} + N\nu \left(\frac{1}{\lambda} - \frac{1}{\lambda^3} \right) \right] \quad (5-15)$$

Therefore, considering the concentration field which is generally inhomogeneous, incompressibility of the hydrogel states that $C = (J - 1) / \nu$. By substituting the $C\nu$ with $(J - 1)$ in Eq. (5-15), and then substitute it into Eq. (5-14), finally they introduced the functional form of Legendre transformation of the free energy density function as below

$$\hat{U}(F, \mu) = \frac{1}{2} Nk_B T (I - 3 - 2 \ln J) + \frac{k_B T}{\nu} [(J-1) \ln \frac{J-1}{J} + \chi \frac{J-1}{J}] - \frac{\mu}{\nu} (J-1) \quad (5-16)$$

Finally, the tensor of tangent modulus has been calculated as below

$$C_{ijkl} = Nk_B T [J^{-1/3} H_{ijkl} + \frac{1}{N\nu} (\ln \frac{J-1}{J} + \frac{1}{J-1} - \frac{\chi}{J^2} - \frac{\mu}{k_B T}) \delta_{ij} \delta_{kl}] \quad (5-17)$$

In Eq. (5-17) H_{ijkl} is also a fourth order tensor which is obtained as below

$$H_{ijkl} = \frac{1}{2} (\bar{B}_{jl} \delta_{ik} + \bar{B}_{ik} \delta_{jl} + \bar{B}_{jk} \delta_{il} + \bar{B}_{il} \delta_{jk}) \quad (5-18)$$

In Eq. (5-18) $\bar{B}_{ij} = J^{-2/3} F_{ik} F_{jk}$ is deviatoric stretch tensor and δ_{ij} is the Kronecker's delta.

Also, J that is shown in Eq. (5-17) is the Jacobian which is the determinant of the deformation gradient tensor. We can also define deformation gradient tensor in terms of the displacement function u as shown in Eq. (5-19) Therefore, the Jacobian determinant can also be defined in terms of displacement function u

$$J = \det F = \left(\frac{\partial u_1}{\partial X_1} + 1 \right) \left(\frac{\partial u_2}{\partial X_2} + 1 \right) - \frac{\partial u_1}{\partial X_2} \frac{\partial u_2}{\partial X_1} \quad (5-19)$$

A full derivative is presented in Appendix 1.

Here in this chapter, we have assumed, there is no chemical potential as an arbitrary constant stress σ_0 have been assumed instead of the chemical potential acting on the polymer. Therefore, instead of the resultant stress on the polymer as a result of mixing of solvent molecules with the polymer, a constant stress value is assumed to be applied to the polymer, and therefore we are only dealing with the elastic free energy of the hydrogel which is discussed in Eq. (5-7) that means we have also ignored free energy of mixing due to the mixing of solvent molecules. Hence, the second term and third term of the right hand side of Eq. (5-16) has been ignored. Therefore, only the first term on the right hand side of Eq. (5-17) is taken for the tangent modulus, that also gives the tangent modulus for an incompressible, neo-Hookean material.

$$C_{ijkl} = Nk_B T [J^{-1/3} H_{ijkl}] \quad (5-20)$$

Hence, $Nk_B T$ have the same meaning introduced in section 5.2.3 and approximately is $Nk_B T = 600000$ (J/mol) for highly swellable materials.

5.3 The numerical methods

5.3.1 Material point method for large deformation

However material point method has been chosen for analysing large swelling of the polymers, the numerical algorithm for nonlinear large deformation is different from small deformation, mainly because the constitutive law for the highly swellable polymers should be changed. In this thesis, Flory constitutive law has been taken to determine the governing equations for nonlinear elastic large deformations. Hence, in the material point method, a few more steps should be calculated such as the deformation gradient tensor, the Jacobian, and also the tangent modulus. The general algorithm of MPM has been introduced in chapter 2, but MPM algorithm has been tailored for large deformation, and some creativity has been applied to increase the speed of the code in this chapter. Furthermore, as we have coupled degradation to our model, a new variable β has been assigned to each material point that is based on the random value of volumetric strain. The degradation simulation is discussed in section 5.7 in detail. Here, the numerical algorithm has been discussed.

As we discussed in chapter 4 the deformation of the material points is calculated from the nodal velocities of the computational mesh that are updated from the nodal acceleration at each time step. Therefore, the main dynamic governing equation with the constant sintering stress and the damping term is

$$\begin{aligned}
 \sum_{p=1}^{N_p} M_p N^T(X_p) N(X_p) \dot{v} = & - \sum_{p=1}^{N_p} M_p B^T(X_p) \rho_p^{-1} \sigma(X_p) + \\
 \sum_{p=1}^{N_p} M_p \rho_p^{-1} B^T(X_p) C(X_p) V(X_p) + & \sum_{p=1}^{N_p} M_p B^T(X_p) \rho_p^{-1} \sigma_0(X_p) + \\
 \sum_{p=1}^{N_p} M_p N^T(X_p) b(X_p) + & \int_{\partial\Omega} N(X_p) \tau ds
 \end{aligned} \tag{5-21}$$

In which internal and external nodal forces are calculated as

$$f^{int} = \sum_{p=1}^{N_p} M_p B_I^T(X_p) \rho_p^{-1} \sigma(X_p) + \sum_{p=1}^{N_p} M_p B_I^T(X_p) \rho_p^{-1} \sigma_0(X_p) + \sum_{p=1}^{N_p} M_p \rho_p^{-1} B^T(X_p) C(X_p) V(X_p) \quad (5-22)$$

$$f^{ext} = \sum_{p=1}^{N_p} M_p N_I(X_p) b(X_p) + \int_{\Gamma} N_I(X_p) \tau d\Gamma \quad (5-23)$$

The third term on the right hand side of Eq. (5-22) is modelling the damping term, hence in order to calculate internal nodal forces the damper coefficient is assigned to each material point. In this chapter, another method has been suggested to add a damping term to the simulation, in order to increase the calculation speed. Basically, the value of the damping is not important in the calculation, since it is only used to damp the dynamic responses of the simulation and return the steady state results. Therefore, instead of applying the damper to the material points it can be added to the nodal points of the computational mesh. As it is shown in Figure 5-2 the global matrix of nodal forces of the computational mesh are calculated from the summation of the internal forces of the proper local nodes of the four neighbour's elements. Hence, instead of the third term on the right hand side of Eq.(5-22), we can add an extra term to the global nodal force of the computational mesh as it is shown in Eq.(5-24). Therefore, the lengthy numerical calculation which is shown in the third term on the right hand side of Eq. (5-22) which should be done for each material point has been substituted by a very simple calculation on the nodes of the computational mesh that are much less than the number of material points. Therefore Eq. (5-22) will be calculated in two steps, for example as it is shown in Figure 5-2 in order to calculate the nodal force of node 5, first we calculate the internal nodal forces of the same point in the cells number 1,2,3, and 4 through Eq.(5-22) then they should be added together through Eq. (5-24).

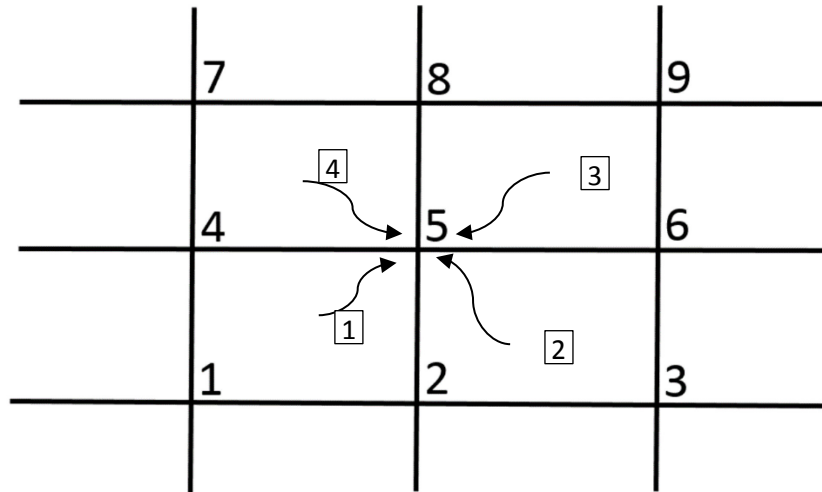


Figure 5-2 the internal topological system in the MPM code

$$Gf^{\text{int}} = \sum_{I=1}^4 f_I^{\text{int}} + C.v \quad (5-24)$$

In Eq.(5-24) the left hand side is the summation of the internal nodal forces for all the four cells around each node. f_I^{int} is the value of internal nodal force for the corresponding node of each element C is the damping coefficient and v is the nodal velocity of the same node.

5.3.2 Some vital issues of implementing MPM for large swelling

In practice, in order to use MPM code for simulating extremely large deformation while we have a constant stress (i.e. σ_0 the sintering stress) can be even more complicated. As in the case of large swelling, material points should move to the new elements, we can see a fatal problem at the boundary of the system. Basically, when only a few material points travel to a free mesh at the boundary, the nodal mass of the corresponding nodes of the element are very small. Furthermore, the nodal forces of the same nodes are calculated from Eq. (5-22), and due to the constant stress applied to all material points, the calculated nodal forces are a big value. Therefore, the nodal acceleration that is calculated from Eq. (3-28) is extremely large, that cause a fatal error at the boundary of the system. Hence, a specific treatment is required for the boundaries. As a very small inconsistency in the main MPM algorithm can cause a fatal

error, hence the special treatment at the boundary should be totally stable. A few different boundary treatments were tested that are introduced in the next section.

5.3.3 Special boundary treatments

5.3.3.1 *Constant velocity at the boundary*

As it was explained, due to the constant stress σ_0 in this problem that is defined on every material point, a large nodal force and therefore, a large nodal acceleration can be calculated at the boundary when only a few MPs have travelled to the new element as a result of small nodal masses. Then, large nodal acceleration leads to large nodal velocities and large material point velocity due to Eq. (3-29), Eq. (3-30) Hence, it causes the MPs at the boundary move faster and finally, the program will crash. So, the suggested treatment was to keep the last velocity of the MP just before it leaves the previous mesh until the number of MPs in the new mesh gets to a certain value so that the nodal masses will increase and the main problem of dividing the large nodal forces by a small nodal masses will not happen in Eq. (3-28). This suggestion can help if the material points in the boundary layer are supposed to move to the free elements only once. Because, if for example the MP velocities are kept constant for half of the MPs of the previous element to move the new mesh, then the new mesh is basically not counted in the MPM algorithm, until the number of MPs in the new mesh, get to a certain value. Also, before the new element gets the certain number of MPs, not only the MP velocities should not be updated normally, but also nodal forces, nodal acceleration, and nodal velocities of the new mesh should not be updated. When the new element gets the certain number of MPs (i.e. half of the MPs of the previous element) then this element should join back to the MPM algorithm. Therefore, as the MP velocities were kept constant since the MP moved to the free meshes, the new updated velocity will be totally wrong, and this cause a big inconsistency between the last two meshes around the boundary layer, and finally cause separation between the material points.

5.3.3.2 Setting a constant zero boundary layer

As the problem of the boundary layer will always exist in the extremely large swelling problems, therefore a new technique has been suggested here to prevent the problem mentioned in section 5.3.2.

In this technique, initially, the domain of the meshes with material points will be defined much bigger than the actually referenced body, such that every possible deformation of the body still remains in the defined domain. In other words, if the actual subject is predicted to have hundred percent swelling in each direction in 2D, then the area of the initial domain of the material points should be defined at least four times bigger than the area of the actually referenced body. Also, in order to prevent the same problem in the new boundary, every material point that reaches this set limit should be deleted. Therefore, the deformation for those material points that represent the actual body will remain in the defined domain, and those extra MPs will be gradually deleted when they reach this set limit.

5.3.3.3 The effect of the extra material points

Generally, material points in the MPM methods represent the mass. Therefore, having some extra material points around the actually referenced body means some extra mass is defined. Hence, this part can resist against the deformation of the referenced body, and also by deleting the MPs that reach the set boundary limit the resistance against deformation of the actual body decreases. Basically, for a homogeneous swelling, this resistance does not take into account, since it will remain uniform everywhere, however, for nonhomogeneous swelling losing material in different sections can apply a different resistance force to the reference body which should be considered carefully. Therefore, in order to reduce the effect of this extra mass on the referenced body, the coefficients of the tangent modulus for those extra MPs have been reduced by choosing a very small $Nk_B T$ just for the sake of numerical simulation. Further results and graphs are shown in the next section.

5.3.3.4 The effect of initial number of material points per unit computational cell

As it is discussed in chapter 4, according to F. Li (2008) the material point density (i.e. the number of material points per unit computational mesh) is the most important factor for MPM to be converged. But, in small deformation analysis, as the material

point density does not change enormously, it is possible to find the minimum number of material points per unit cell of the computational mesh. Furthermore, for large deformation analysis when the volume does not change dramatically, the density of the material points does not decrease massively. Since the total number of the computational cells that cover the deformed body does not change massively. Nevertheless, in order to have a convergent solution, the average number of material points should not be below the minimum required. F. Li (2008) has suggested 94 material point per unit cell is the minimum required for small deformation analysis to be converged. Therefore, the best way is to initially assign enough number of material points to each unit cell of the computational mesh to cover the possibility of the volume change as well. Hence, in order to estimate the final swelling ratio (i.e. volume change), it is possible to use the main constitutive law of the material. In section 5.4.1 the analytical derivation of the material constitutive law based on Flory's theory is presented. Hence, by using Figure 5-4 a good estimation of the final swelling ratio can be obtained, therefore the total number of final computational cells that covers the deformed body can be estimated. Therefore, the initial number of material points that should be assigned to each computational cell at the reference state can be estimated. Additionally, the problem of material point density should be wisely detected for the simulation of degradation during large swelling, as some material points will be deleted randomly when they reach a certain volumetric strain. Therefore, the average number of the material points per unit cell of the computational mesh should not again below the minimum required. So, the initial number of material points that should be assigned to each cell of the reference body should be chosen big enough to cover the possibility of huge volume change and random degradation.

Alternatively, the extra material point that was explained in section 5.3.3.3, can avoid a dramatic decrease in the material point density, especially around the boundary layer of the referenced body.

5.4 Validation of the MPM code for large deformation based on Flory's constitutive law

As the same routine, we used to validate the Material Point Method (MPM) code for small deformation problem in chapter 2 that was based on the linear constitutive law. In this section the main constitutive law has been changed based on Flory's theory to simulate large deformation, therefore the MPM code has been developed based on Flory's constitutive law. Hence, another analytical validation is proposed to validate the MPM code for large deformation problems based on Flory's constitutive law. A simple homogeneous swelling problem due to constant applied stress is modelled through the MPM code. The results of final steady state swelling ratio (i.e. steady state deformation) are compared with an analytical calculation.

5.4.1 The analytical approach

A 2D homogeneous plane shown in Figure 5-3 under equal tensile stresses in both directions is simulated for model validation. The coordinate system is shown by X_1 and X_2 ; u_1 and u_2 are deformations in the first and the second directions respectively.

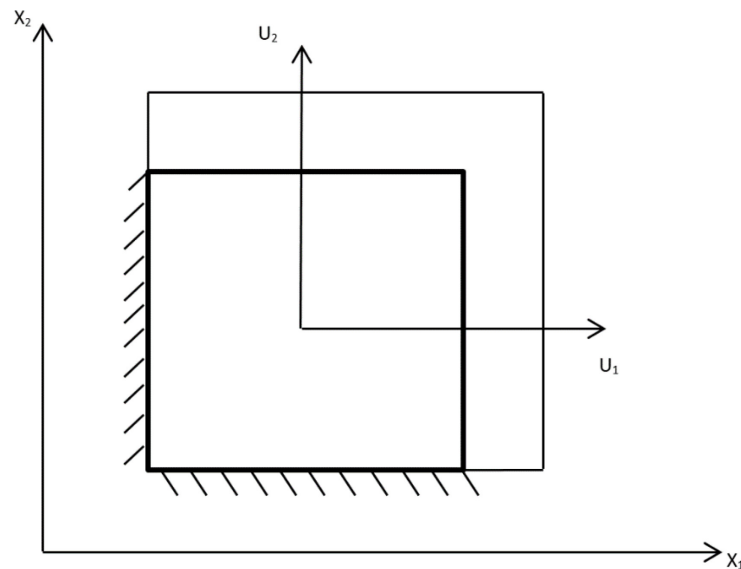


Figure 5-3 schematics of 2D homogeneous swelling

For a 2D homogeneous swelling, the relationship between displacement vectors and the coordinate system is as below

$$u_1 = \alpha X_1 \quad (5-25)$$

$$u_2 = \alpha X_2 \quad (5-26)$$

Since the applied stresses are equal in both directions α is the same coefficient in both Eq. (5-27) and Eq. (5-28). Therefore strains in X_1 and X_2 directions are defined as:

$$\varepsilon_{11} = \frac{\partial u_1}{\partial X_1} = \alpha \quad (5-27)$$

$$\varepsilon_{22} = \frac{\partial u_2}{\partial X_2} = \alpha \quad (5-28)$$

Hence, the constitutive law in the rate form for a homogeneous swelling problem when stress is equal in both directions can be written as below:

$$\Delta\sigma_{11} = C_{1111}\Delta\varepsilon_{11} + C_{1122}\Delta\varepsilon_{22} \quad (5-29)$$

$$\Delta\sigma_{22} = C_{2211}\Delta\varepsilon_{11} + C_{2222}\Delta\varepsilon_{22} \quad (5-30)$$

As it was discussed earlier $C_{1122} = C_{2211}$ due to the major symmetry of tangent moduli. Also, Eq. (5-29) and Eq. (5-30) can be simplified as below since $\Delta\varepsilon_{11} = \Delta\varepsilon_{22} = \Delta\alpha$ due to homogeneous swelling in both directions.

$$\Delta\sigma_{11} = (C_{1111} + C_{1122})\Delta\alpha \quad (5-31)$$

$$\Delta\sigma_{22} = (C_{2211} + C_{2222})\Delta\alpha \quad (5-32)$$

Therefore, three independent components of tangent moduli C_{1111} , C_{1122} and C_{2222} are required to find a stress strain curve for the homogeneous swelling of hyperelastic materials. The derivation of tangent moduli based on Flory's constitutive law is explained in section 5.2.4. Hence, according to Eq. (5-20) the independent components of tangent modulus are

$$C_{1111} = Nk_B T [J^{-1/3} H_{1111}] = Nk_B T [J^{-1/3} * \frac{1}{2} (4\bar{B}_{11})] \quad (5-33)$$

$$C_{1122} = Nk_B T [J^{-1/3} H_{1122}] = 0 \quad (5-34)$$

$$C_{2211} = Nk_B T [J^{-1/3} H_{2211}] = 0 \quad (5-35)$$

$$C_{2222} = Nk_B T [J^{-1/3} H_{2222}] = Nk_B T [J^{-1/3} * \frac{1}{2} (4\bar{B}_{22})] \quad (5-36)$$

Where all the terms have the same descriptions as defined in section 6.2.4. The values of C_{1111} , and C_{2222} are both nonlinear as a function of the Jacobian. It is also important to consider that, C_{2211} , and C_{1122} are both zero that means for a 2D problem based on the Flory's approach, deformation in one direction has no effect on the value of stress on the other direction, as oppose to normal Hookean materials that positive strain in one direction cause a negative strain in the other direction depending on the value of Poisson ratio.

Therefore, by discretising the value of $\Delta\alpha$ a nonlinear stress/ strain curve can be obtained from Eq. (5-31) and Eq. (5-32) in the first direction and the second direction respectively.

Figure 5-4 shows the analytical constitutive law in each direction, in which the horizontal axis shows the value of stretch and the vertical axis shows the value of stress.

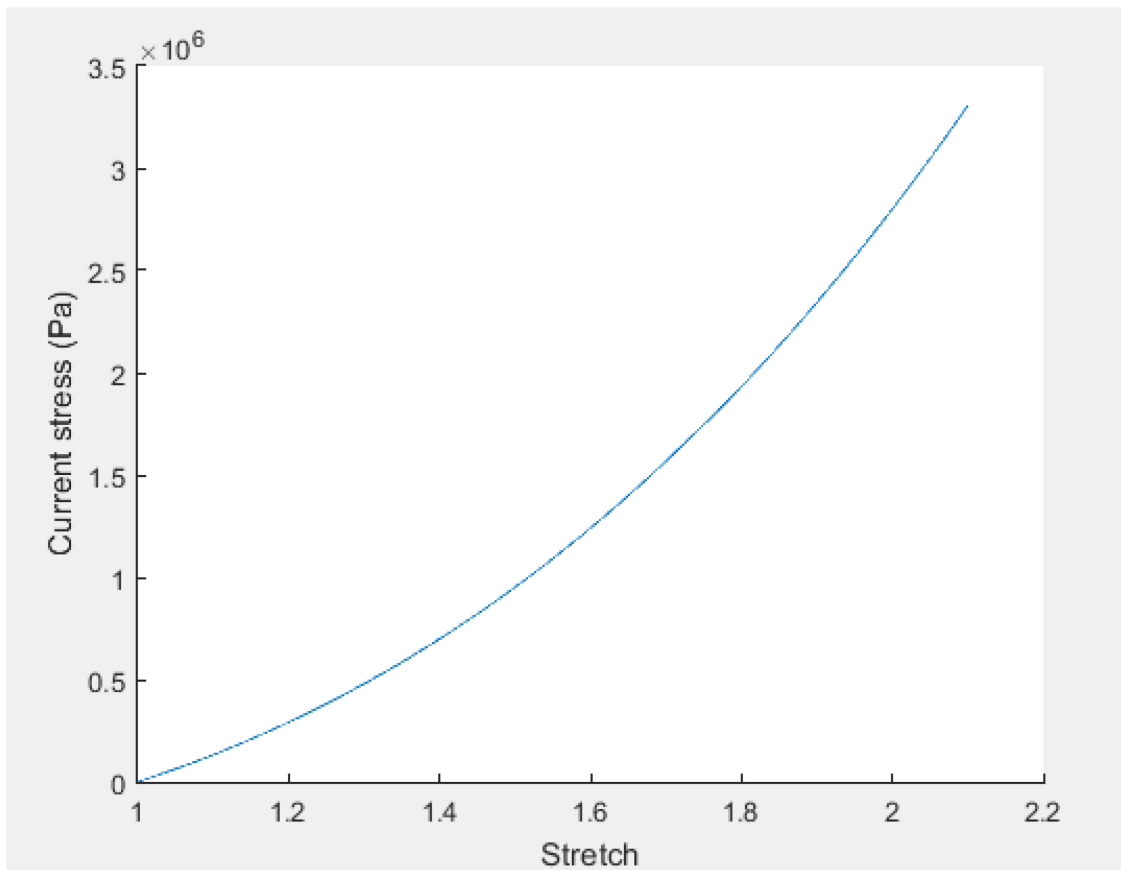


Figure 5-4 the stress stretch diagram

5.4.2 Uniform swelling results from the MPM code

In order to check the results from the MPM computer code with the analytical solution proposed in section 5.4.1, each time a swelling stress σ_0 should be defined, to get the final steady state stretch. Therefore, a series of different inputs for σ_0 is tested. Furthermore, at each test, the final value of stress should be converged to the same given value of σ_0 and the value of stretch should also be converged to the corresponding value of steady state stretch. In the next section, the results are shown for a various range of swelling stresses. Furthermore, it has been shown that the resolution of meshes does not change the results.

5.4.3 Test 1, the effect of the zero boundary layer

In test 1 the referenced body that is initially divided into a two by two elements is located in the middle of a domain of four by four elements. Figure 5-5 shows the initial

position of the referenced body and the extra material points that are defined around the referenced body to cover the total domain of deformation. The total number of material points in each element is 1600. The sintering stress is $\sigma_0 = 1100000$ (Pa), the shear modulus of elastomer for the referenced body is $Nk_B T = 600000$, and the shear modulus of elastomer for the boundary layer is $Nk_B T = 600$, the elements of the background mesh are squares of 1×1 mm and the thickness is 0.5 mm. The referenced body is a square of 2×2 mm and the thickness is 0.5mm which is located in the middle of a domain of four by four elements as shown in Figure 5-5, the damping coefficient is $C = 0.00035$ (Ns/m) and the initial density is 1000 (Kg/m³). In Figure 5-6 and Figure 5-8 the value of converged stress and steady state displacement are shown respectively. Furthermore, the deformed body after about 50% deformation is shown in Figure 5-8.

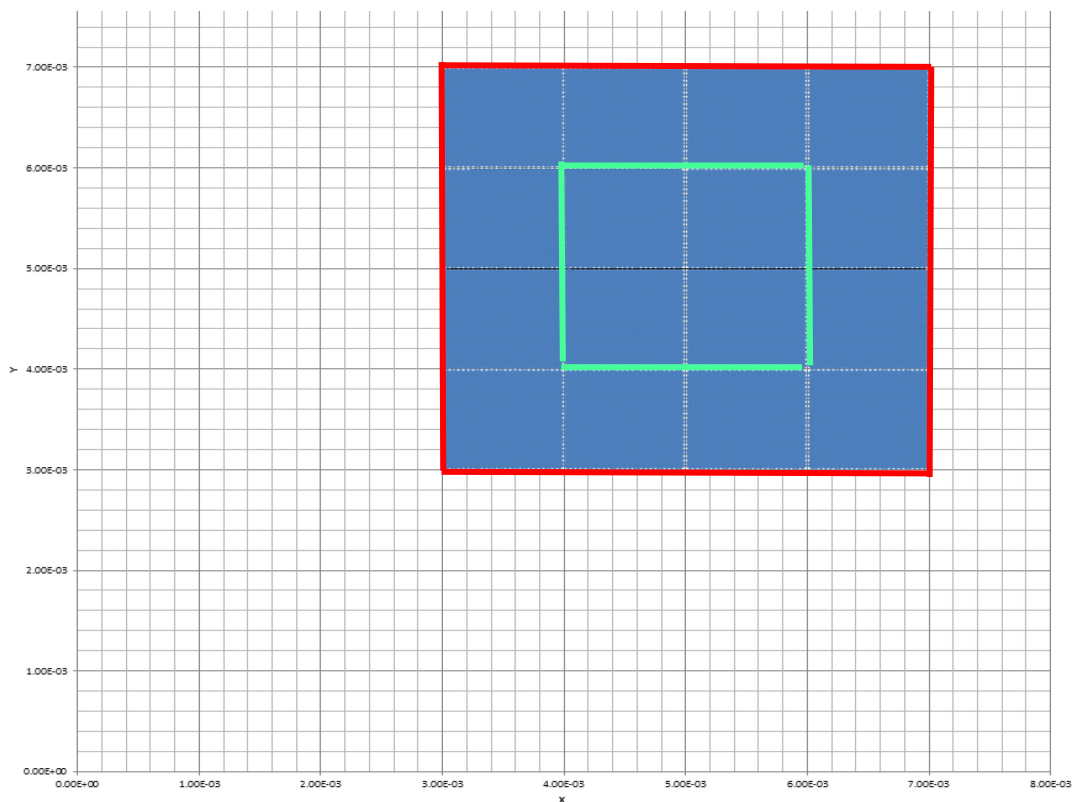


Figure 5-5 shows a four by four element set up for the initial un-deformed shape of the body. The middle two by two elements indicated by the green boundary is the main referenced body. The zero limits are also shown by red boundaries.

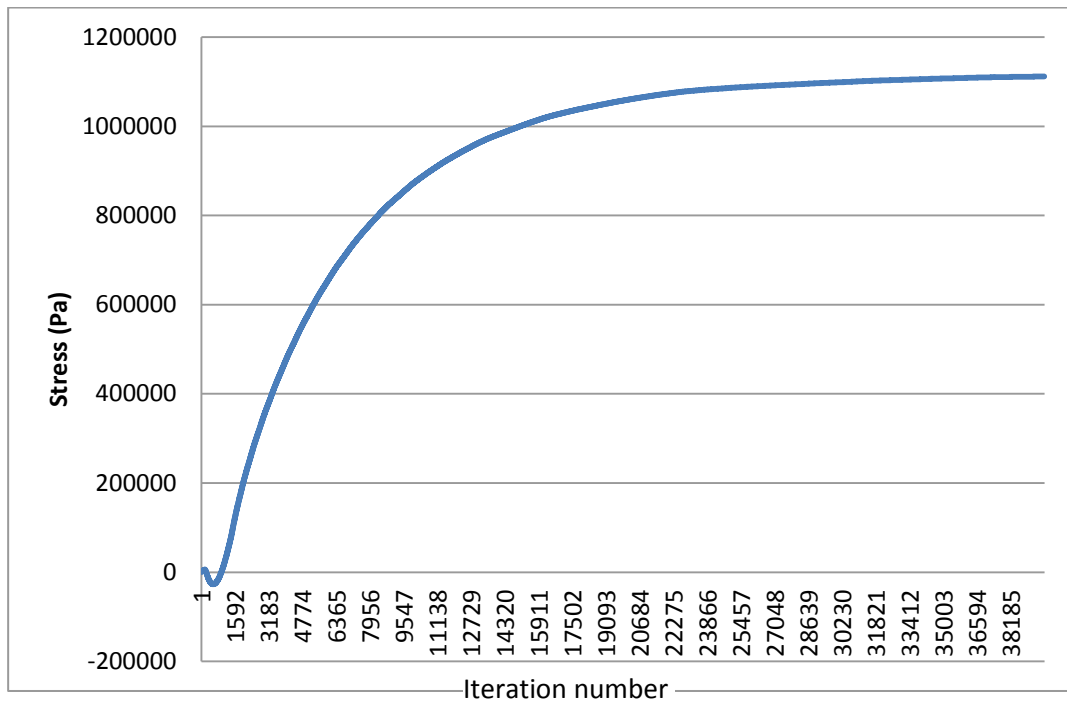


Figure 5-6 shows the converged stress value, the input sintering stress is $\sigma_0 = 1100000$ Pa. The iteration time step is $\Delta t = 0.001$.

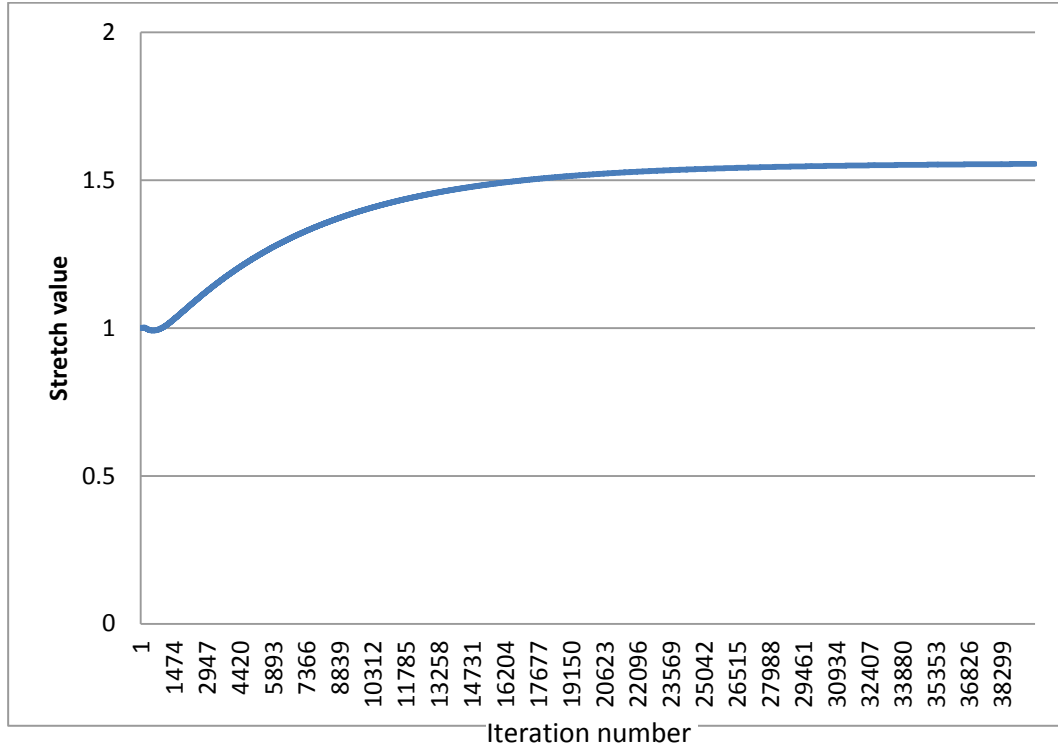


Figure 5-7 shows the steady state value of swelling deformation when sintering stress is $\sigma_0 = 1100000$ Pa. The iteration time step is $\Delta t = 0.001$.

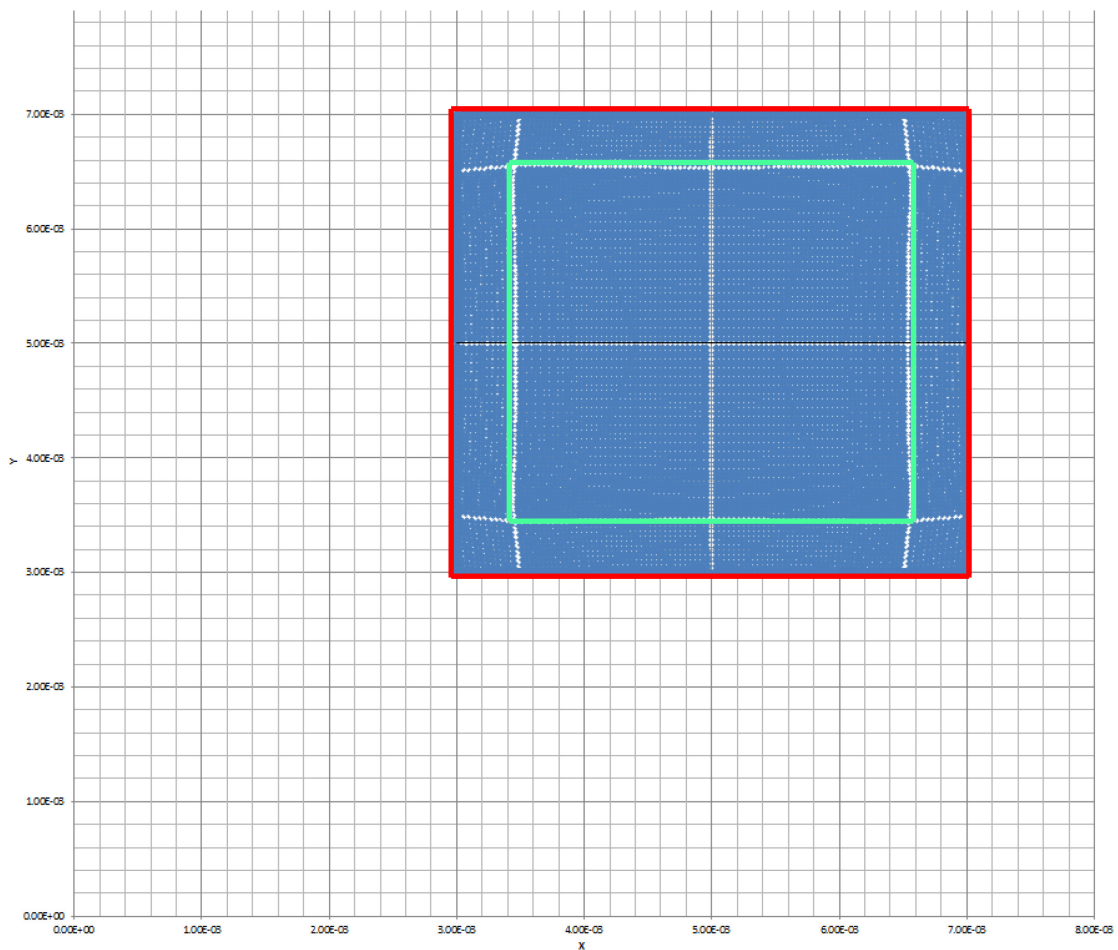


Figure 5-8 shows the deformed shape of the body when the value of stress is $\sigma_0 = 1100000$ Pa. The green boundaries represent the deformed main body. The zero limits are also shown by red boundaries.

As it is shown in the Figure 5-6 and Figure 5-7, at the early stage that the swelling stresses are applied, a small shrinkage can be seen. This is due to the out of balance forces at the of the nodes at the boundary layers. Because, these figures are the position of the material point located at the boundary layer, which is affected by the negative out of balance force at the beginning. After material points move to the next free element, the out of balance force will get a positive value, so that the material start swelling. This is due to the dynamic effect of the numerical method.

5.4.4 Test 2, the effect of the number of background elements

5.4.4.1 First case study

In test 2 two other examples are shown to prove the number of initial elements is not changing the final results of steady state swelling. Therefore, in the first case study, a

larger body was simulated with the same swelling stress, same shear modulus of elastomer for the referenced body and the same shear modulus of elastomer for the boundary layer. Also, the same size elements are taken for the computational mesh. The main body is a square of 8*8 Mm which is located in the middle of a 14*14 Mm domain. The total number of MPs in each element is 196. Other parameters such as damping coefficient and density are taken the same as the previous test. Figure 5-9 shows the un-deformed shape of the computational domain and Figure 5-10 illustrates the deformed shape. Similar to the previous example about 50% swelling deformation of the initial size can be shown in Figure 5-10, hence the main referenced body that is shown in green line in Figure 5-10 has gone through 50% swelling that is shown in Figure 5-10. Also, the converged stress value and the steady state displacement are exactly as the previous example that is shown in Figure 5-6 and Figure 5-7 respectively.

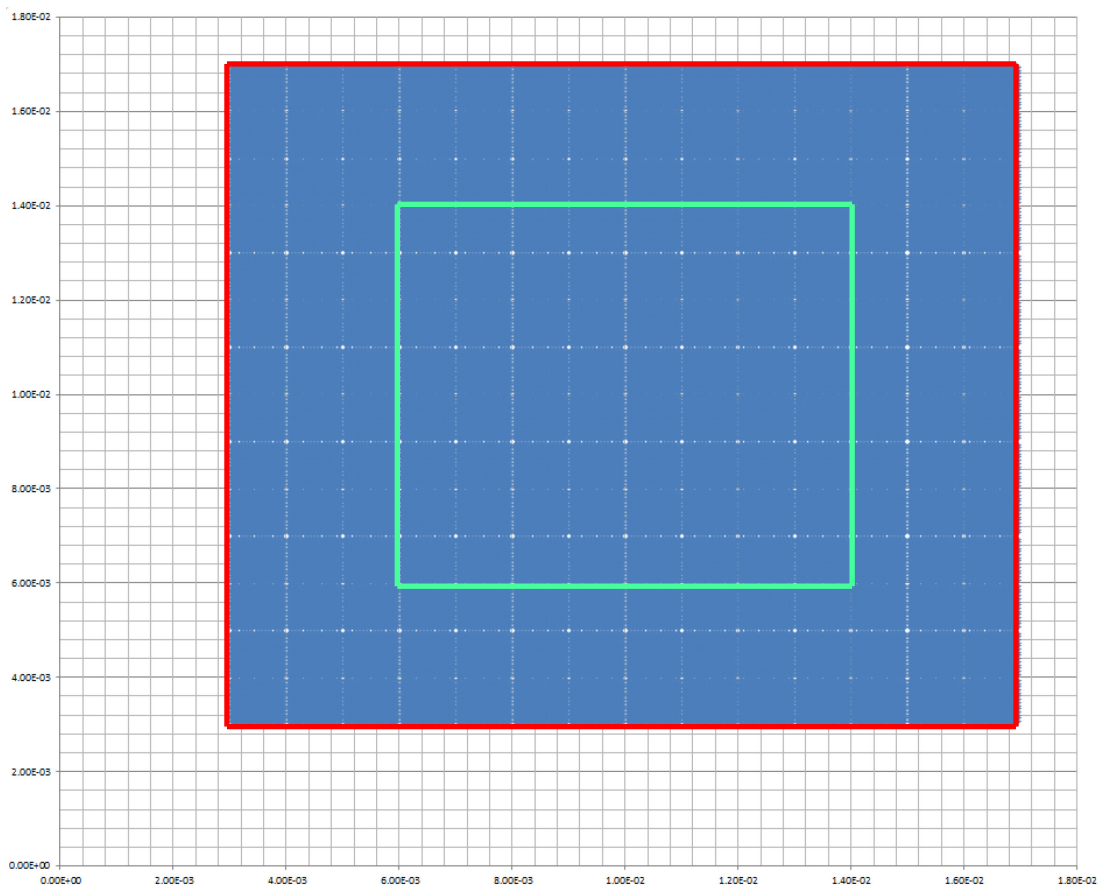


*Figure 5-9 shows a 14*14 element set up for the initial un-deformed shape of the body. The middle 8*8 elements indicated by the green boundary is the main referenced body. The zero limits are also shown by red boundaries.*

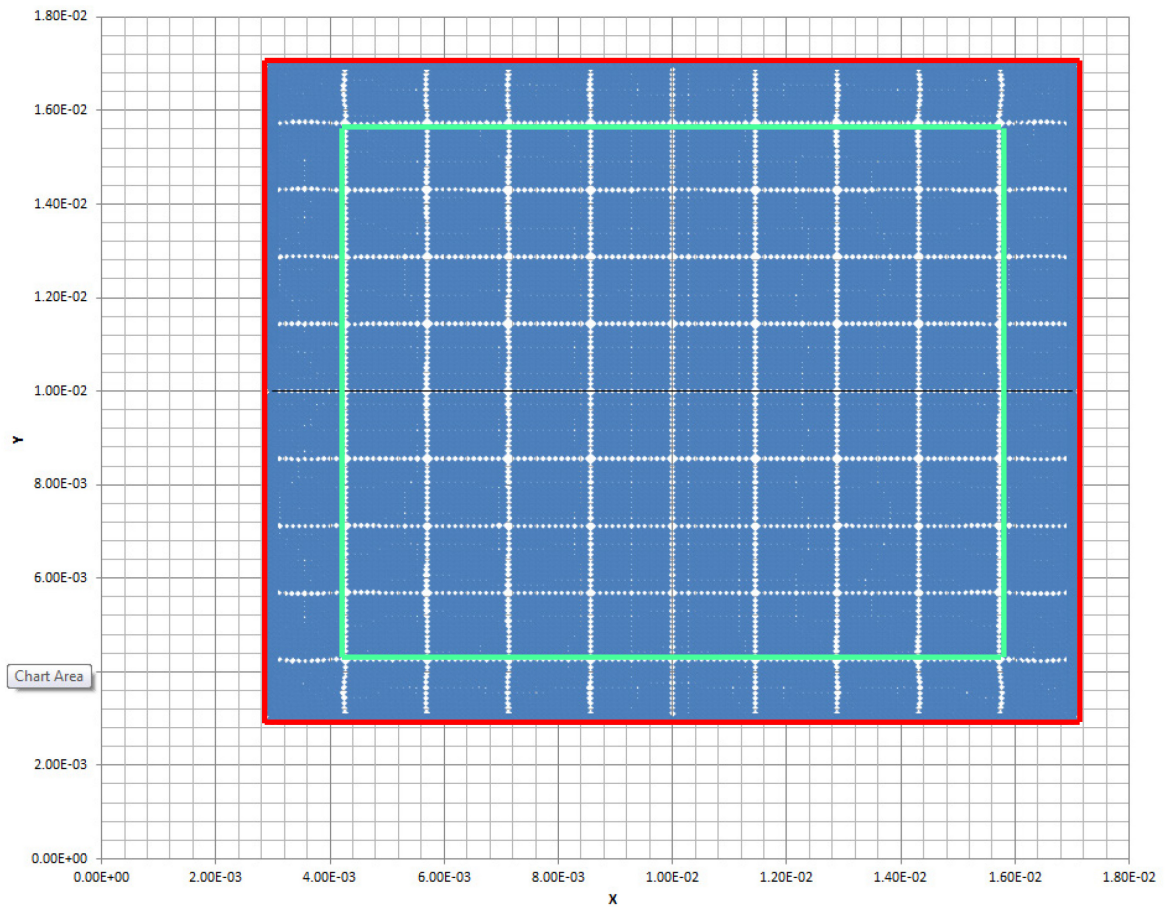


Figure 5-10 shows the deformed shape of the body when the value of stress is $\sigma_0 = 1100000$ Pa. The green boundaries represent the deformed main body. The zero limits are also shown by red boundaries.

5.4.4.2 Second case study

In the second case study, all the parameters have taken the same, but the size has changed. The main body is a square of 20*20 Mm which is located in the middle of a computational domain of 32*32 Mm. Figure 5-11 shows the un-deformed shape of the computational domain and Figure 5-12 illustrates the deformed shape. Similar to the previous example about 50% swelling is shown in Figure 5-12 as well.

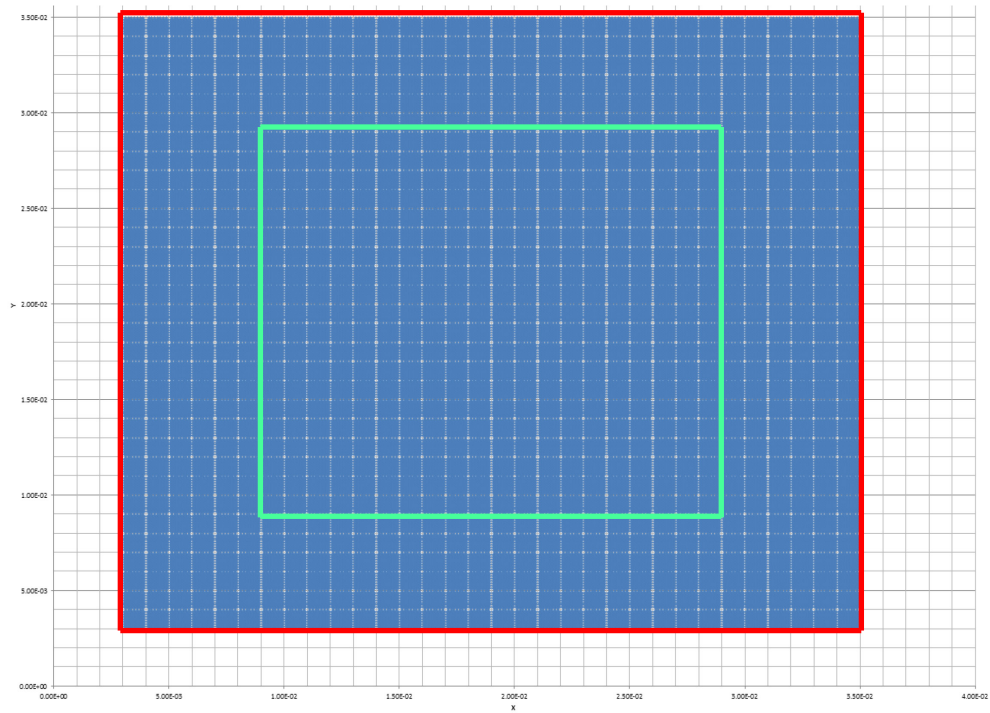


Figure 5-11 shows a 32*32 element set up for the initial un-deformed shape of the body. The middle 20*20 elements indicated by the green boundary is the main referenced body. The zero limits are also shown by red boundaries.

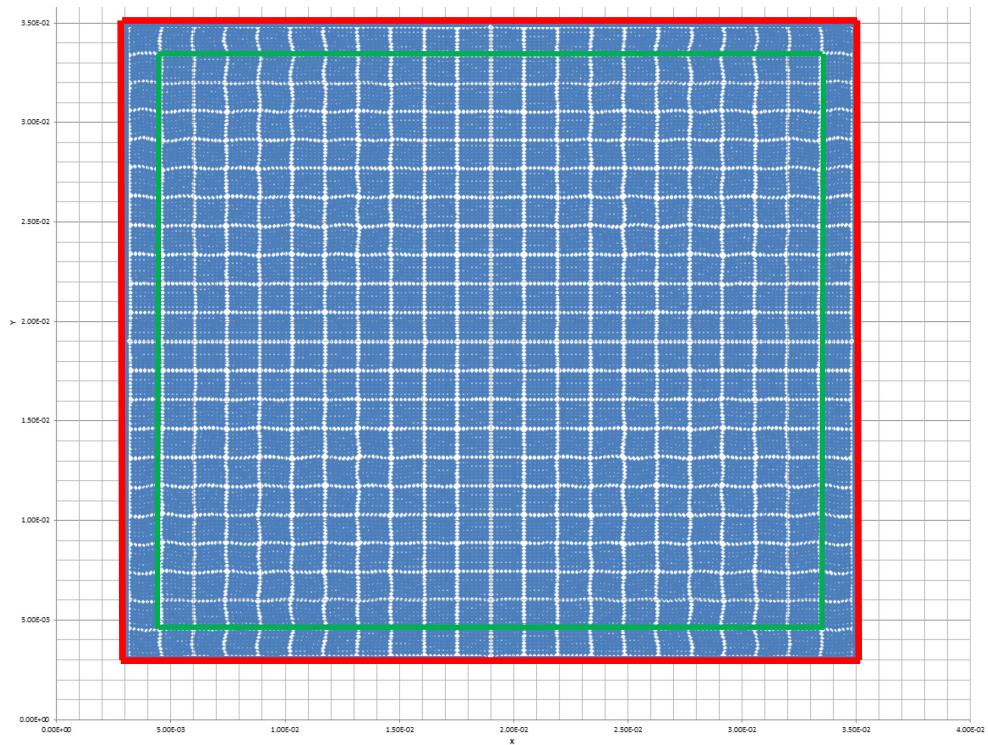


Figure 5-12 shows the deformed shape of the body when the value of stress is $\sigma_0 = 1100000$ Pa. The green boundaries represent the deformed main body. The zero limits are also shown by the red boundaries.

5.4.5 The effect of higher constant applied stress

5.4.5.1 First case study

In test 3 the total domain has been initially divided into a four by four element, and the total number of material points in each element is 1600. The swelling stress is $\sigma_0 = 1600000$ (Pa), the shear modulus of elastomer is $Nk_B T = 600000$, the width and height are 4 mm and the thickness is 0.5mm, the un-deformed referenced body is the same as shown in Figure 5-5, the damping coefficient is $C = 0.00035$ and the initial density is 1000 (Kg/m^3). In Figure 5-13 and Figure 5-14 the value of converged stress and steady state displacement are shown respectively. The final deformed shape is also shown in Figure 5-15.

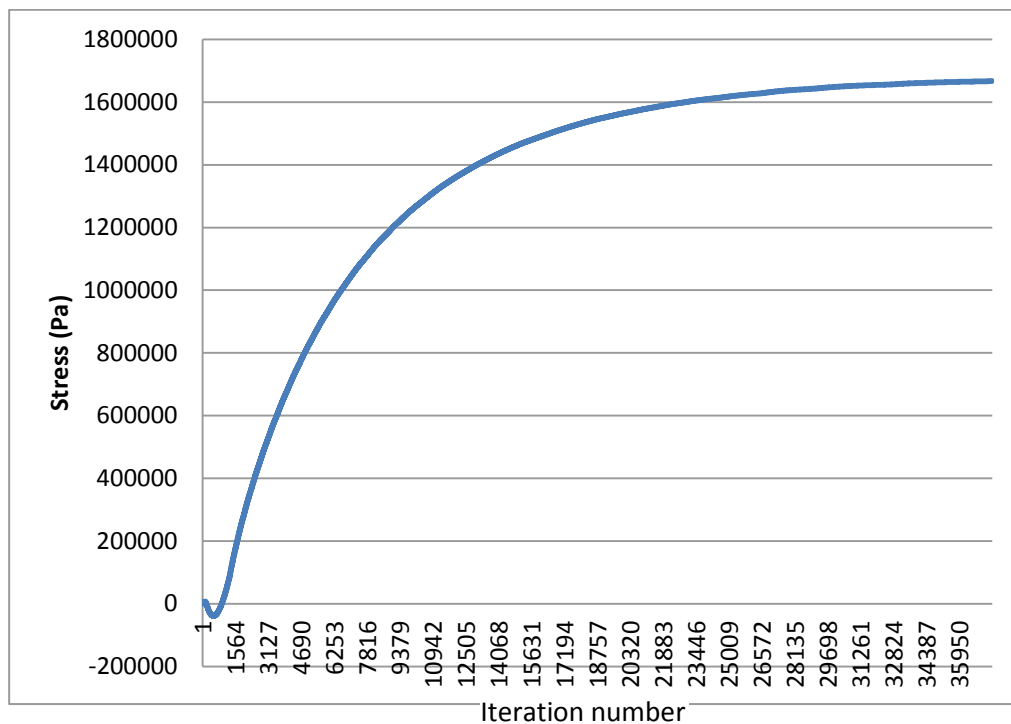


Figure 5-13 shows the converged stress value, the input sintering stress is $\sigma_0 = 1600000$ Pa. The iteration time step is $\Delta t = 0.001$.

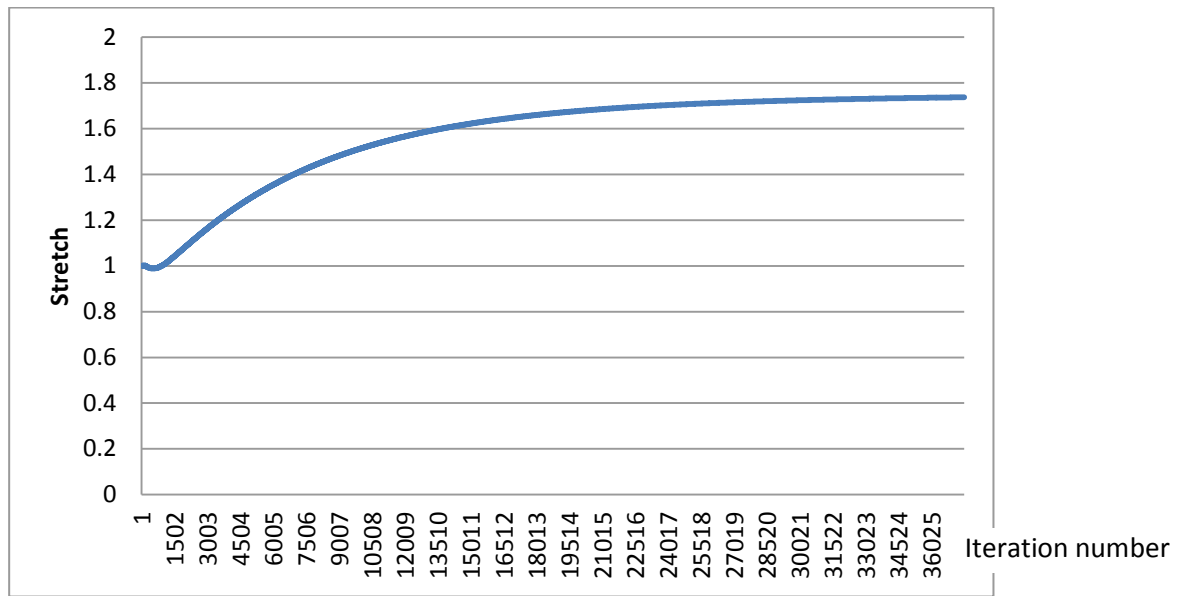


Figure 5-14 shows the steady state value of swelling deformation when sintering stress is $\sigma_0 = 1600000$ Pa. The iteration time step is $\Delta t = 0.001$.

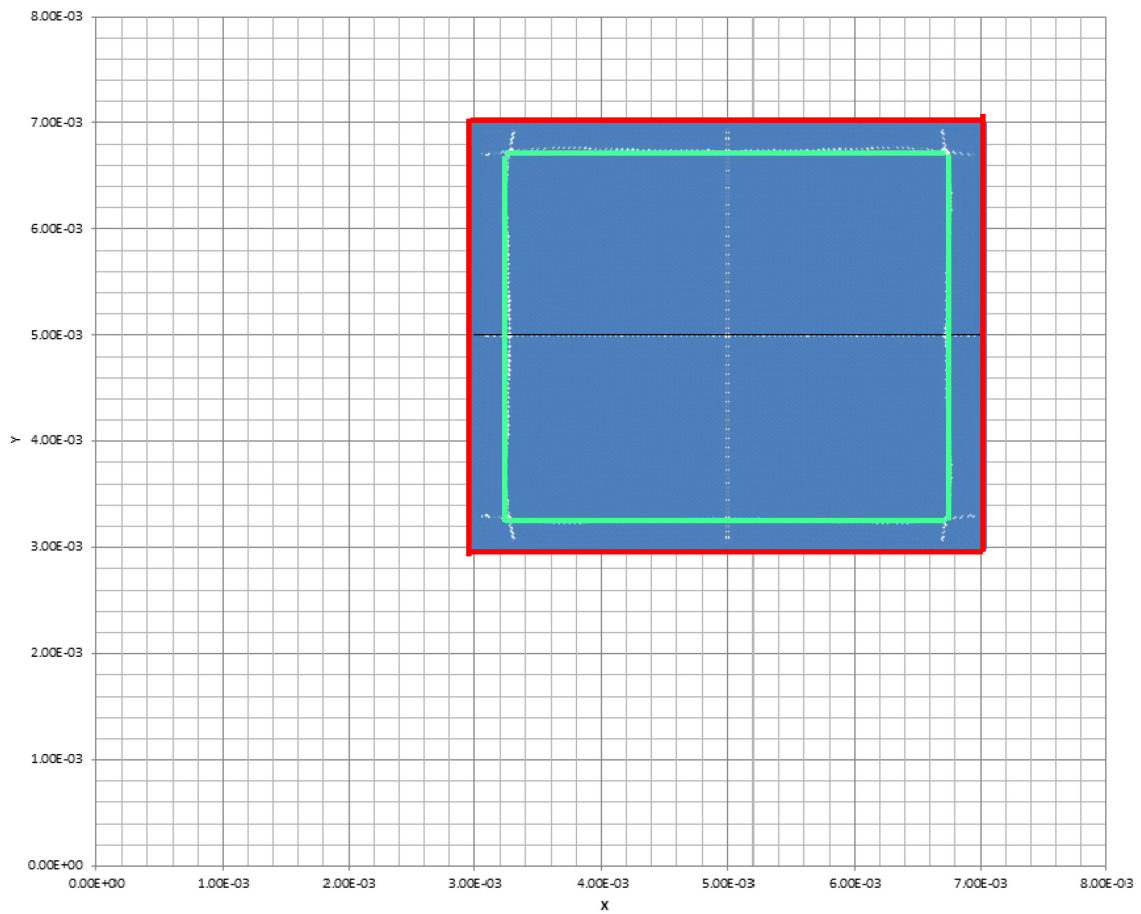


Figure 5-15 shows the deformed shape of the body when the value of stress is $\sigma_0 = 1600000$ Pa.

5.4.5.2 Second case study

In this section, the only parameter that is changed with respect to the previous test is the value of sintering stress that is $\sigma_0 = 2300000$. Hence, the un-deformed referenced body is as shown in Figure 5-5, also Figure 5-16 and Figure 5-17 represent the converged value of stress and the steady state swelling deformation respectively. The deformed shape after about 90% deformation is shown in Figure 5-18.

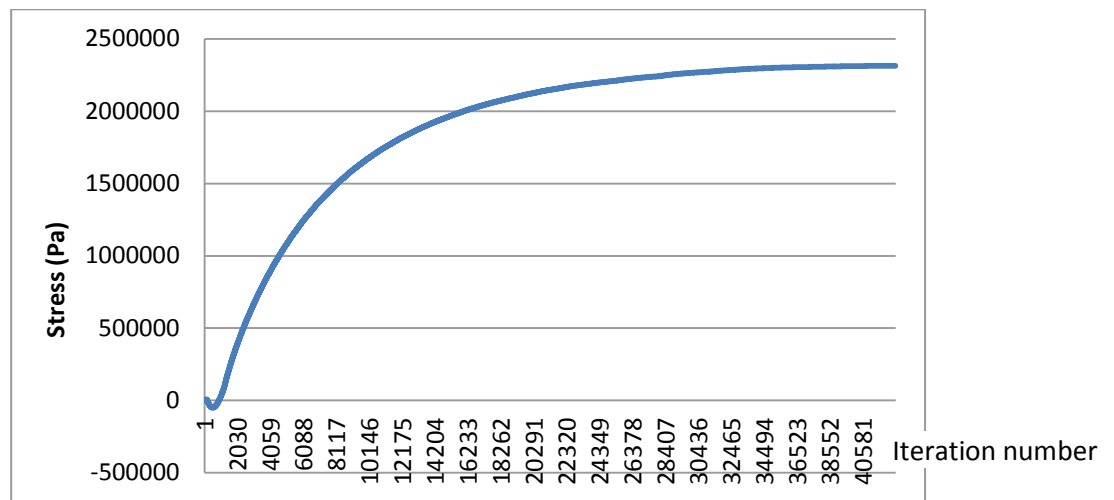


Figure 5-16 shows the converged stress value, the input sintering stress is $\sigma_0 = 2300000$ Pa. The iteration time step is $\Delta t = 0.001$.

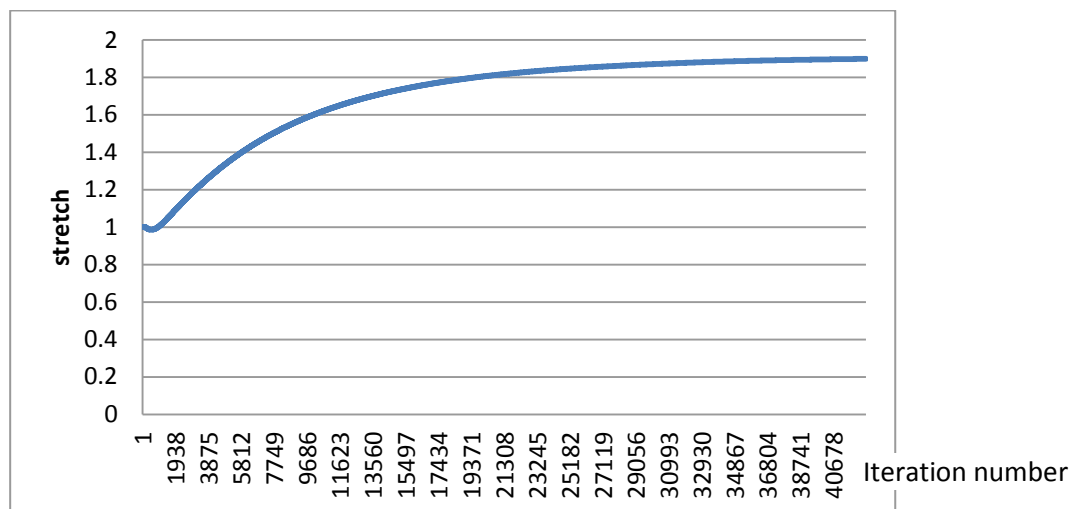


Figure 5-17 shows the steady state value of swelling deformation when sintering stress is $\sigma_0 = 2300000$ Pa. The iteration time step is $\Delta t = 0.001$.

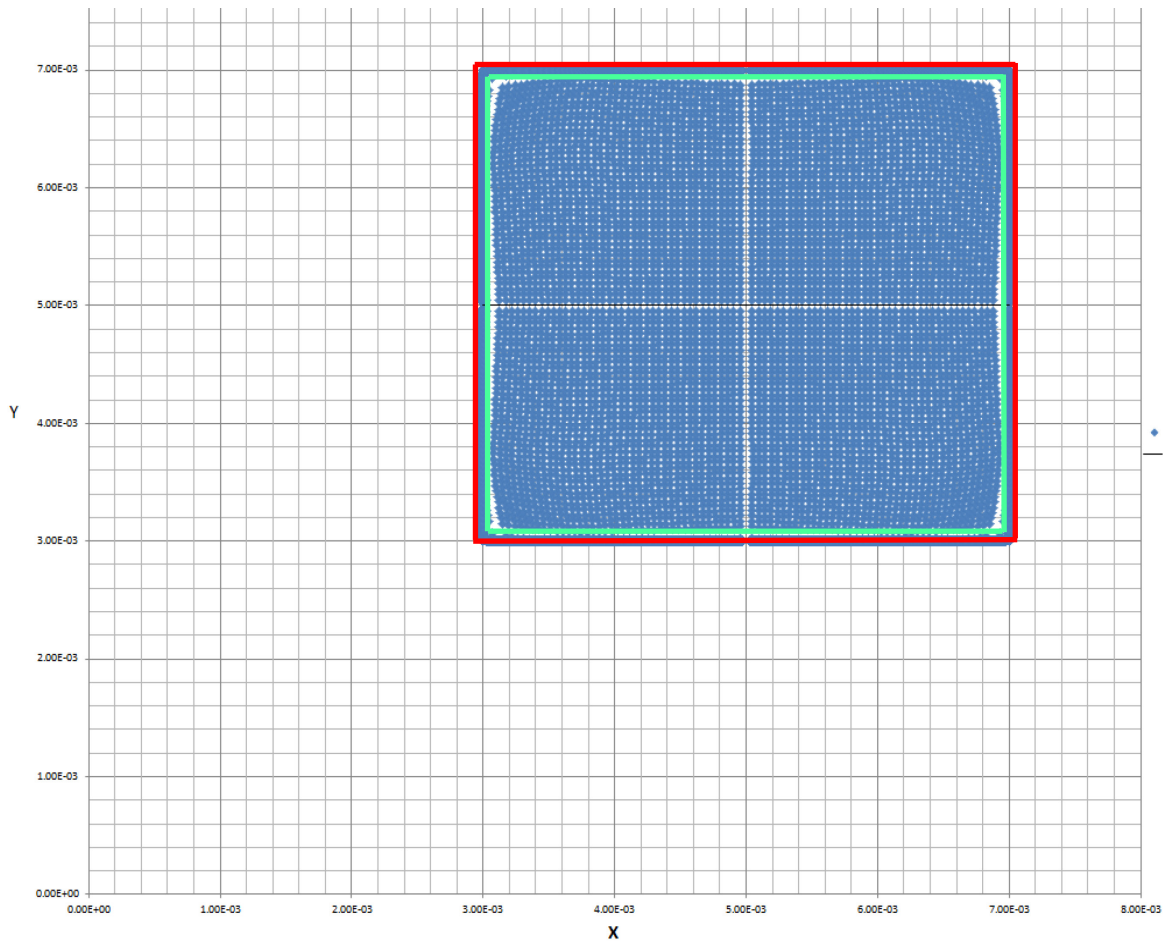


Figure 5-18 shows the deformed shape of the body when the value of stress is $\sigma_0 = 2300000$ Pa.

5.5 Model validation

According to the analytical results for the nonlinear swelling that was discussed in section 5.4.1 and comparing the numerical results from the MPM computer code that was shown in section 5.4.2, with the analytical results in Figure 5-4, a perfect match was obtained. In Figure 5-19 the red line shows the nonlinear analytical stress strain curve, and the blue stars show the results of the MPM code, that can be used to validate the code for large homogeneous swelling of polymers based on Flory's approach.

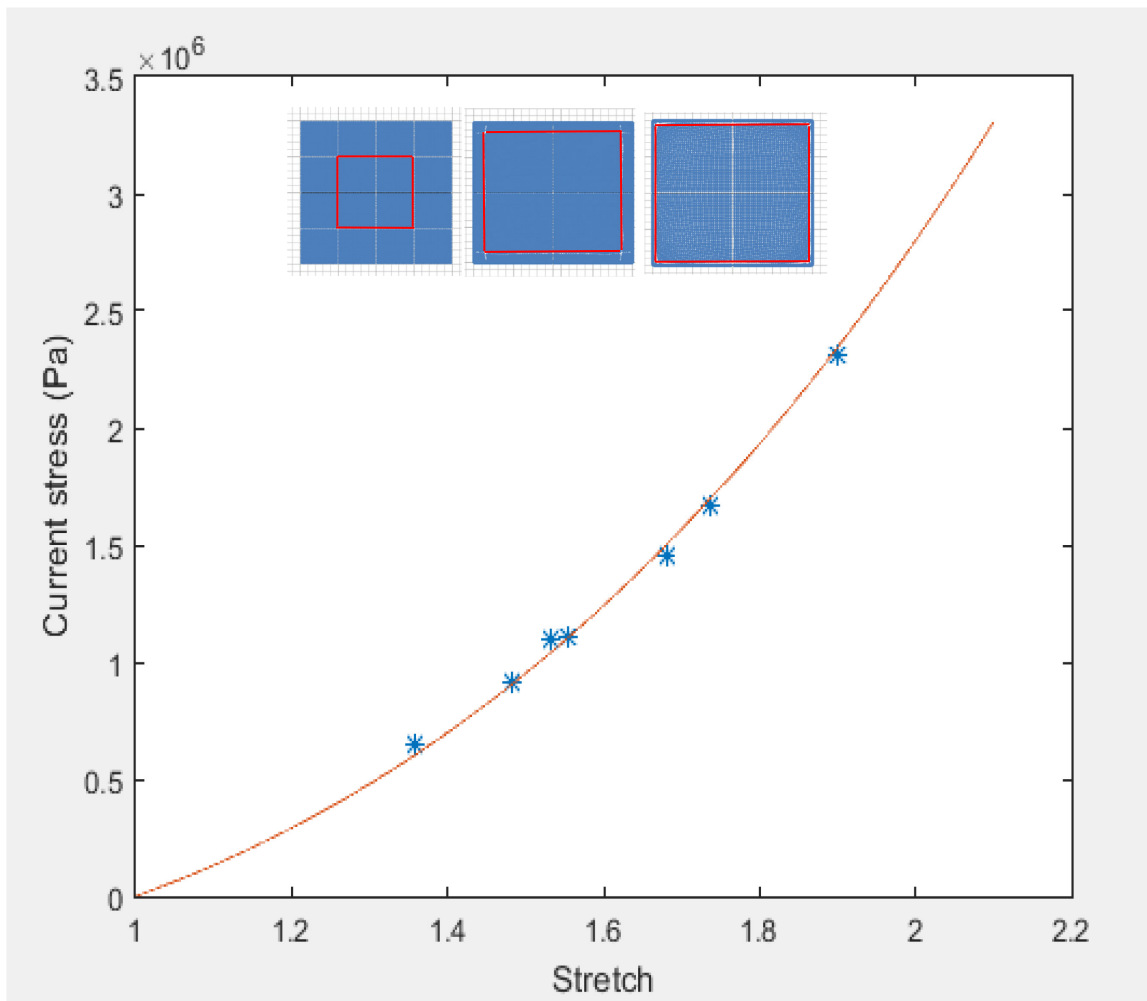


Figure 5-19 the vertical axis is the value of stress, and the horizontal axis is the value of the corresponding stretch. This figure shows a perfect match between the analytical results presented by the red line and the results from the MPM code that is represented by the stars. This is the most important figure in this chapter, as it tests the validity of MPM in large elastic deformation. The non-linear constitutive law which is based on Flory's constitutive law has been fed to the MPM code, and the results are perfectly matched with the analytical results, that were discussed in section 5.4.1.

5.6 Non-uniform swelling

One application of highly swellable materials is in controlled drug delivery systems, as these polymers can be used for the drug accommodator in tablets. These materials can quickly form a hydrogel and the solvent (water) can be diffused in and dissolve the drug and then diffuse the drug out of the hydrogel, and the polymer itself will be degraded eventually. The ultimate aim of the presented numerical approach in this thesis is to predict drug release profile. Polymers that are mainly used in the controlled release tablets can swell hugely and basically release most of the drugs before dissolution. Those polymers that are used in tissue engineering and engineering scaffolds and stent coatings swell to a much less extent, however, even a small swelling strain significantly accelerates drug release. Hence, controlling/ predicting the swelling behaviour of the polymer is a critical step in all the controlled drug delivery systems. There are two ways to tailor the swelling behaviour of a polymer device: (a) by manipulating the structural constraint and (b) by manipulating the polymer chemistry. Therefore, different drug release profile is achievable by combining the chemistry and structure design. In this section, we have focused on the structural design of the tablets that is including the size and shape of the tablet and also using multi-layers of different polymers. Multi-layers tablets with different rates of swelling, gelling, and erosion can control the rate of drug release in the body. Generally, once water penetrates the tablet, swelling occurs and a rubbery state of the polymer will be formed on the outer layer. During the swelling process, a distinctive interface between the swelling rubbery zone and the un-swelled glassy zone can be often observed as illustrated in Figure 5-20.

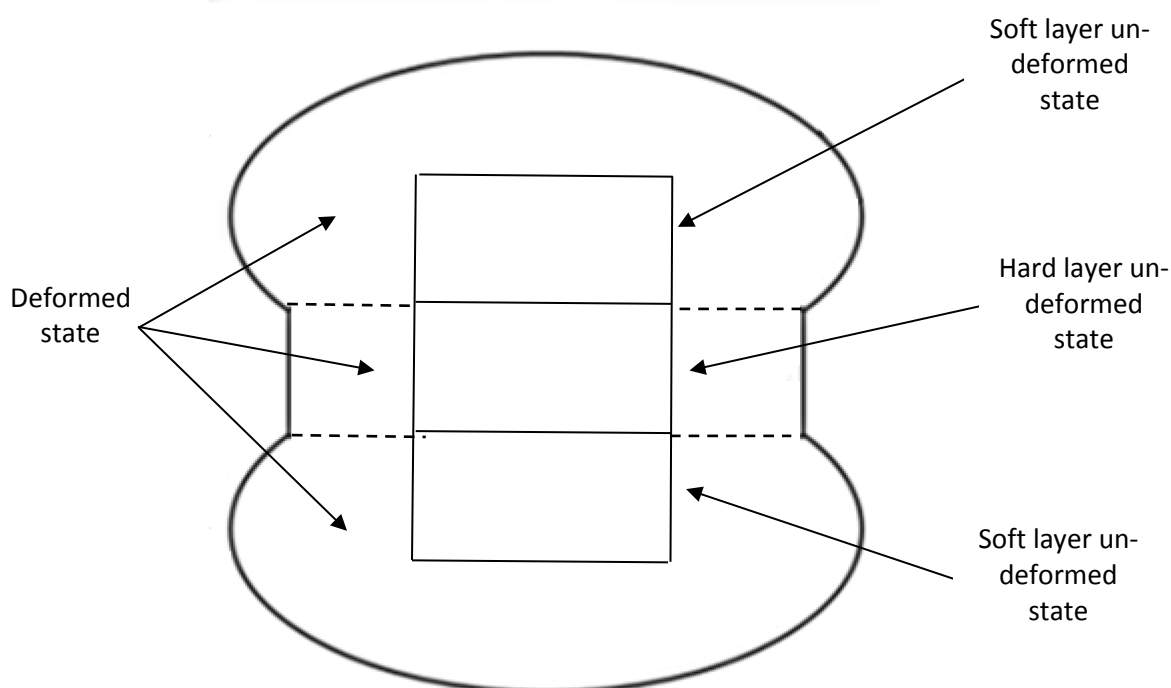


Figure 5-20 the schematic diagram of the multi-layered tablet during the non-uniform swelling, The un-deformed state, and the deformed state are shown.

5.6.1 Non-uniform swelling VS. Flory's theory

According to Flory's theory (1943), polymer swelling is driven by the reduction in the free energy of mixing between the polymer and the solvent and opposed by the entropy elasticity of the polymer network. Basically, this theory ignores enthalpy of mixing. The theory predicts an ultimate swelling ratio at equilibrium but does not deal with the kinetics of the swelling process. To calculate drug release from a swelling polymer, diffusion equations for the solvent and drugs should be solved on a swelling domain with migrating boundaries. A fundamental problem is that there is no theory of three dimensional deformations. Swelling strain was simply assumed to be uniform. Because swelling controls drug diffusion, such calculation of drug release cannot be valid in particular for multi-layered tablets. As the 2 dimensional MPM computer code was validated earlier for extremely large nonlinear deformation, in this section the same code is tailored to solve a non-uniform swelling problem. An initial three-layered polymer is defined as illustrated in Figure 5-20 to represent the multi-layered tablet, in which the black zone shows the hard core of the tablet, the two green zones on the top and bottom of the hard core are the soft zones, and the zero limits are also shown by

red boundaries. Basically, the difference between the soft and the hard zones are due to the concentration of the solvent molecules. Hence, the softer zones have absorbed more water. Therefore, the value of the constant stress which is applied in the soft zone is higher than the value of the constant stress in the hard zone. Therefore, the swelling ratio will be much bigger in the soft zone, rather than the hard zone.

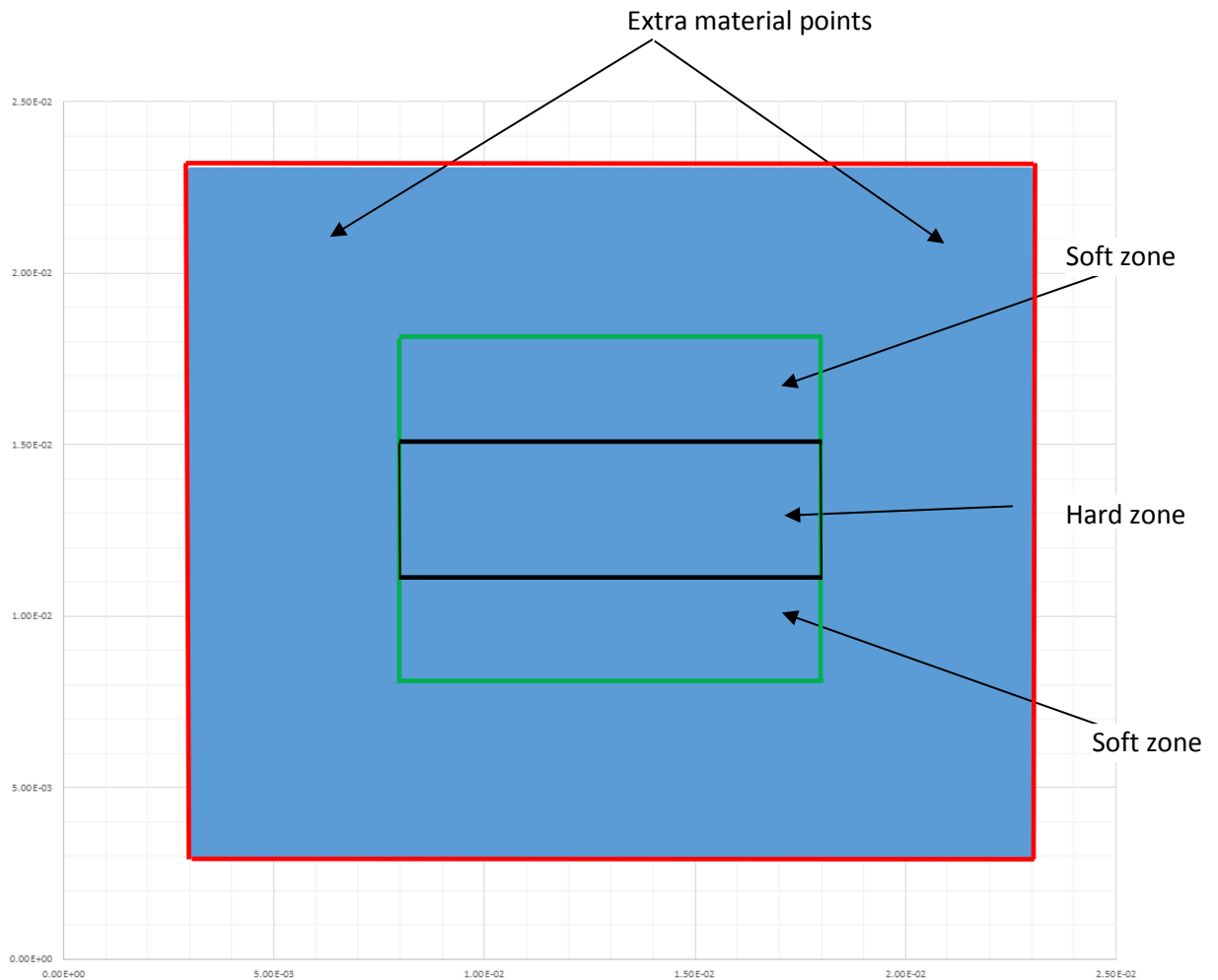


Figure 5-21 represent the multi-layered tablet, in which the black zone shows the hard core of the tablet, the two green zones on the top and bottom of the hard core are the softer zones, and the zero limits are also shown by red boundaries.

5.6.2 The results of non-uniform swelling

As it was discussed in section 5.3.3.2 in order to avoid the fatal numerical error due to the moving of the material points near to the free elements, the main computational domain (shown in green line in Figure 5-21) was defined such that, the overall

deformation of this domain still remains in the defined material points (shown in red line in Figure 5-21). Adding extra material points around the referenced body may not cause any problem for homogeneous swelling, but it is definitely not valid for non-uniform swelling, since extra material points around the referenced body cause constraint forces. Therefore, as it was discussed in section 5.3.3.3 in order to neglect the effect of extra material points on the overall simulation of non-homogeneous problems the shear modulus of elastomer, $Nk_B T$, is given a much smaller value for the extra material points around the referenced body. So, the value of stress generated in the extra layer of material points around the main body is much smaller than the value of stress generated in the main body, hence it can be ignored. The result of the non-homogeneous swelling is shown in Figure 5-22, and the value of stress in the hard core section is $\sigma_0 = 500000$ Pa, and stress in the soft sections are $\sigma_0 = 1000000$ Pa. The shear modulus of elastomer in both hard and soft core are $Nk_B T = 600000$, and the shear modulus of elastomer in the extra material points is $Nk_B T = 600$.

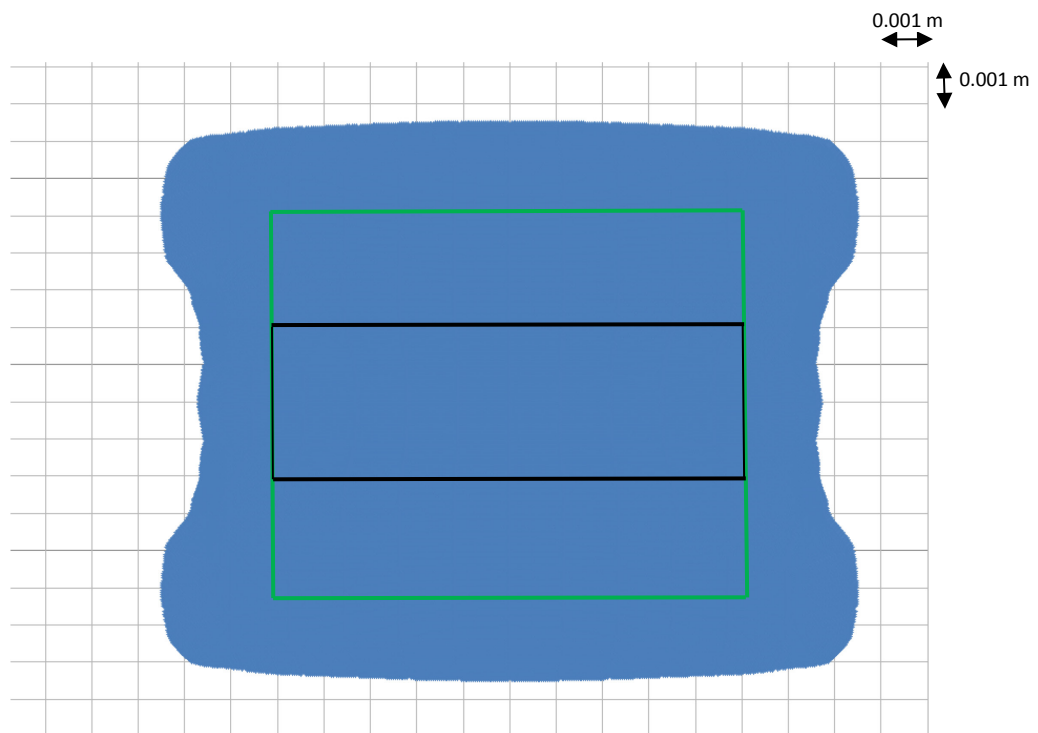


Figure 5-22 shows the non-uniform deformed shape of the body when the value of stress in the hard core section is $\sigma_0 = 500000$ Pa, and stress in the soft sections are $\sigma_0 = 1000000$ Pa. The shear modulus of elastomer in both hard and soft core are $Nk_B T = 600000$, and the shear modulus of elastomer in the extra material points is $Nk_B T = 600$.

In order to demonstrate the effect of the extra material points around the boundary layer in the non-uniform swelling, the same reference body in Figure 5-22 is shown in the middle of the total computational domain in Figure 5-23.

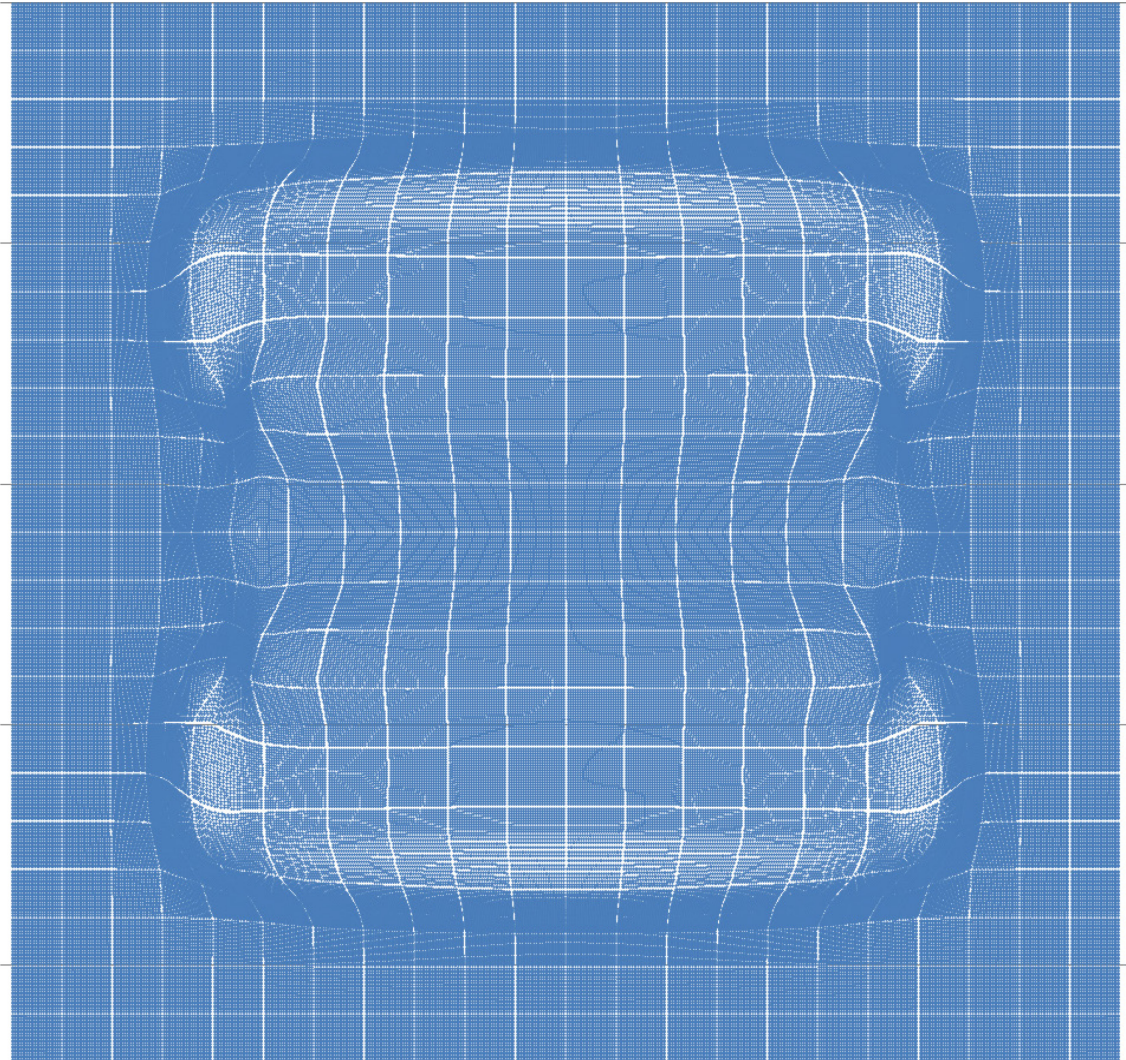


Figure 5-23 Non-uniform swelling of the referenced body in the middle of the extra material points around the boundary layer. The value of constant stress in the hard core section is $\sigma_0 = 500000 \text{ Pa}$, and the constant stress in the soft sections are $\sigma_0 = 1000000 \text{ Pa}$. The shear modulus of elastomer in both hard and soft cores are $Nk_B T = 600000$ and in the extra material points around the boundaries of the referenced body is $Nk_B T = 600$.

Furthermore, a stress contour of the deformed body is shown in the Figure 5-24 As it was discussed earlier the constant stress in the soft zones are higher than the hard zone

due to a higher concentration of water molecules. In Figure 5-24 the values of stresses in the X direction including the initial swelling stresses are shown.

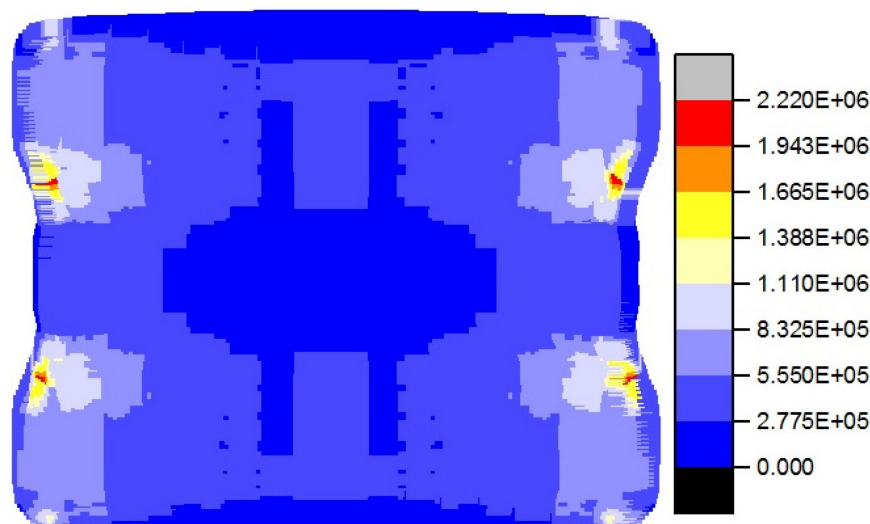


Figure 5-24 the colour-map contour of stresses in the X direction including the initial swelling stresses of the deformed body.

5.7 Simulating of degradation of highly swellable polymers

Degradation is the other important phenomenon that happens during the controlled drug release systems when the polymer undergoes a large swelling ratio. Basically, after the polymer reaches a certain volumetric strain it will be degraded. Erosion normally happens at the boundary layer of the systems due to bulk breakage of the polymer, while degradation is as a result of polymer chain breaking and can happen anywhere inside the polymer. Degradation and erosion are both nonhomogeneous and random phenomena.

Generally, polymer chains may break randomly at any point and either make oligomers if it is broken from either end of the chain or break from the middle and make two long polymeric chains, this phenomenon is called degradation which is a non-homogeneous and a random phenomenon by its nature.

5.7.1 The analytical approach in simulating of degradation of highly swellable polymers

In order to model the random and non-homogeneous degradation, a random variable is initially assigned to every material point. Hence, the normal (or Gaussian) distribution $N(\mu, \sigma)$ is defined by its probability density function, as introduced below

$$f(x) = \frac{1}{(2\pi)^{1/2} \sigma} e^{-\frac{(x-\mu)^2}{2\sigma^2}} \quad (5-37)$$

In which $x \in R$, μ is the mean value of the volumetric strain and σ is the standard deviation. The derivative of the above function is shown in Appendix III. For example, when the polymer undergoes 100% swelling in each side in 2 dimensional modelling, the mean value of the volumetric strain is $\mu = 4$, if we assume the standard deviation is $\sigma = 1$, hence the standard normal (Gaussian) distribution graph is as shown in Figure 5-25.

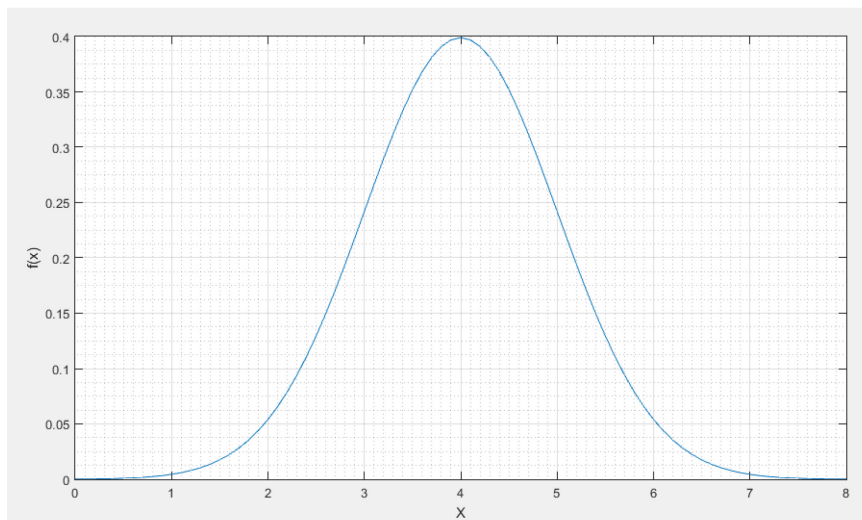


Figure 5-25 shows a normal (Gaussian) distribution of the volumetric strain when the mean value is $\mu = 4$ and the standard deviation is $\sigma = 1$.

Hence, the random volumetric strain is defined as below:

$$\varepsilon_{vr} = \mu + r \times \sigma \quad (5-38)$$

In which r is a random value that was initially assigned to every material point, μ and σ are the mean value of the volumetric strain and the standard deviation, respectively.

Finally, in order to simulate the erosion or degradation to the system, it is necessary to check the random value of volumetric strain which is normally distributed around the mean value as it was explained above with the actual volumetric strain in each time step. Therefore, in case the actual volumetric strain is equal or larger than the assigned random value the material point can be easily deleted.

If $\varepsilon_v \geq \varepsilon_{vr} \Rightarrow$ the material point will be deleted

There are a couple of different ways of deleting a material point in MPM. The simplest way is to zero the mass of the material point, or simply zero all the relative shape functions and shape functions' derivative of the corresponding material point. As we discussed in chapter 3, there is always a minimum required a density of the material points in each mesh in the MPM to have converged solution. Furthermore, in the simulation of extremely large and non-uniform swelling of highly swellable polymers a large number of material points should be initially assigned to each mesh, since in order to simulate the degradation phenomenon some material points will be deleted after they reach a certain value of volumetric strain, and the total number of the remaining MPs should endure the minimum required. On the other hand, using a large initial number of material points, cause some difficulties to present the results of degradation. Figure 6-26 shows the results of the same referenced body that were used in the previous section in Figure 5-21 while the mean value of the volumetric strain is set to be $\mu = 1.4$ and the standard deviation is $\sigma = 1$ as the two main criteria of the random degradation of highly swellable polymers. The value of constant stress in the hard core section is $\sigma_0 = 500000$ Pa, and the constant stress in the soft sections are $\sigma_0 = 1000000$ Pa. The shear modulus of elastomer in both hard and soft cores are $Nk_B T = 600000$ and in the extra material points around the boundaries of the referenced body is $Nk_B T = 600$.

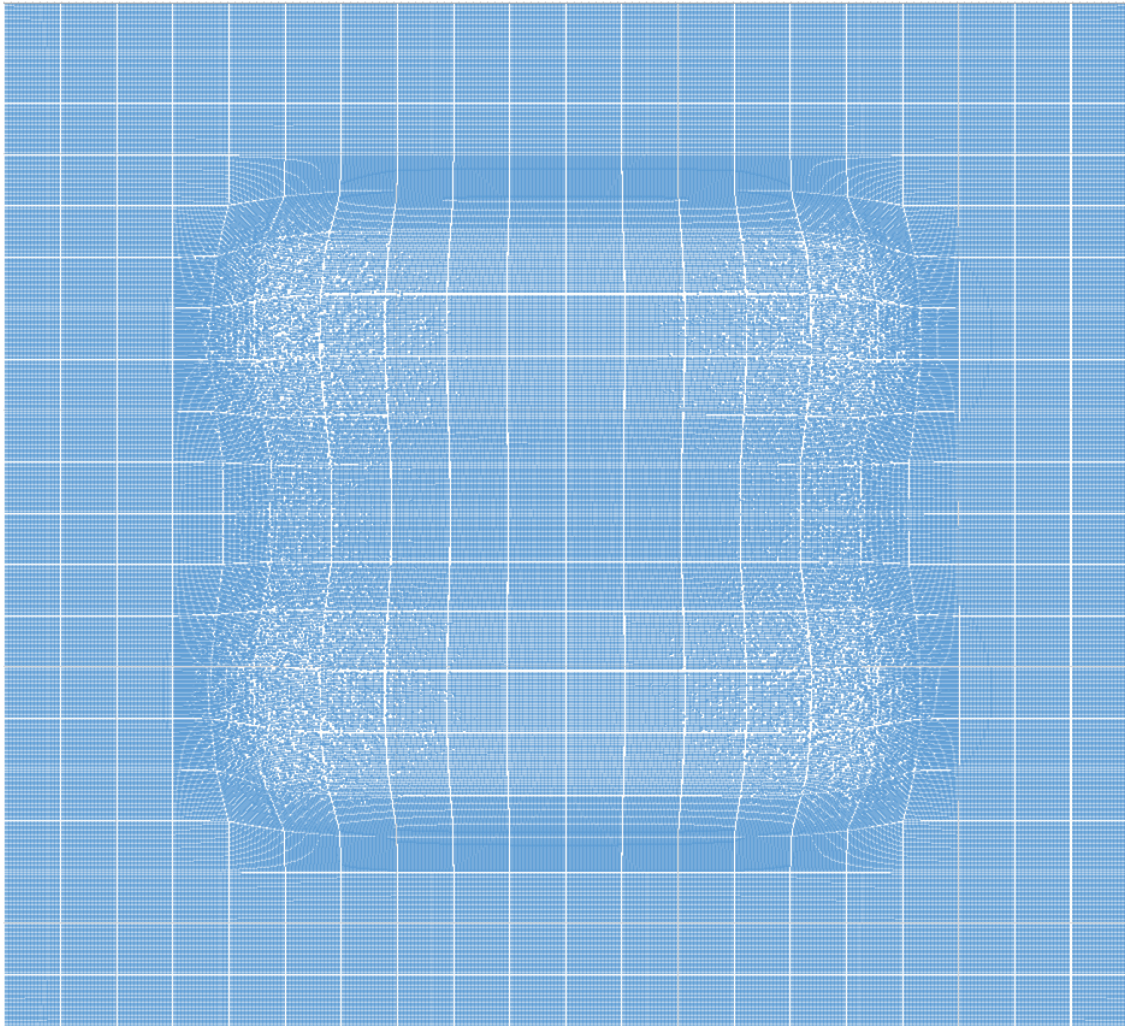


Figure 5-26 the mean value of volumetric strain is $\mu = 1.7$ and the standard deviation is $\sigma = 1$. The value of constant stress in the hard core section is $\sigma_0 = 500000 \text{ Pa}$, and the constant stress in the soft sections are $\sigma_0 = 1000000 \text{ Pa}$. The shear modulus of elastomer in both hard and soft cores are $Nk_B T = 600000$ and in the extra material points around the boundaries of the referenced body is $Nk_B T = 600$.

As it is shown in the Figure 5-26 degradation is mostly happened around the boundary of the deformed body where we have the maximum volumetric strains. However, degradation is assumed to be a random phenomenon, the possibility of degradation is higher where there is a higher volumetric strain.

5.8 Application of polymer degradation in controlled drug delivery systems

In recent years, there has been an increasing interest in the field of controlled drug delivery from water-swallowable matrix systems (hydrogels) in pharmaceutical industry. Hydroxypropyl methylcellulose (HPMC) is significantly used as a hydrophilic carrier material for the preparation of oral controlled drug delivery systems Siepmann J. and Peppas, (2000). Good mechanical properties of HPMC such as compression characteristics and also sufficient swelling properties (i.e. corresponding time and the degree of swelling) have made it a very commonly used hydrophilic carrier material. Swellability of the carrier material has a major effect on the release kinetics of an incorporated drug Siepmann J. and Peppas, (2000). Polymer networks upon contact with small molecules (e.g. water or biological fluid) form polymeric hydrogel Kang M.K. and Huang R., (2010). A hydrogel can swell considerably by absorbing the solvent molecules due to various environmental conditions (e.g. temperature) and finally degrades Kang M.K. and Huang R., (2010). The obviously mass concentration of the drug dramatically changes due to swelling of the polymer. According to the Fick's second law, diffusion of the drug out of the polymeric hydrogel is related to the mass concentration of the drug, and decreasing in mass concentration causes decreasing in drug diffusion. Thus, it is necessary to investigate polymer swelling in the drug delivery problem. Drug release mechanisms are very complex issues and involve three different moving boundaries which make the corresponding equations and boundary conditions so difficult. The three moving boundaries are usually called swelling, diffusion and erosion fronts, and the most complicated part of the polymer swelling mathematical model is dealing with the moving boundaries.

5.8.1 Drug release

In this simulation, a multi-layered tablet is assumed that the drug released profile increases mainly due to the degradation of the material points in the soft zone. Hence, an arbitrary drug dosage of $D_d = 0.5$ is assigned to each material point in the soft zone, and also an arbitrary drug dosage of $D_d = 0.1$ is assigned to each material point in the

hard zone. After the material point is degraded (deleted) the value of the drug dosage will be released. The drug release profile is shown in Figure 5-27.

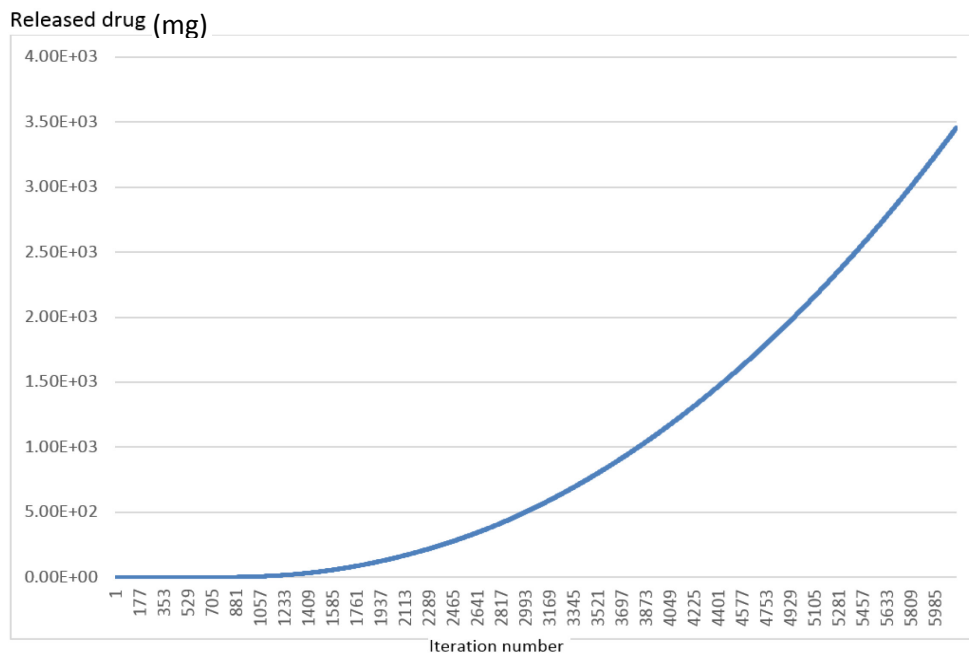


Figure 5-27 Drug released profile. $\Delta t = 0.001$

5.9 Summary of this chapter

In this chapter, MPM is firstly validated for the modelling of extremely large deformation of the materials via comparing the results with the analytical results of the large tensile test, in which the constitutive law is derived based on Flory's theory. Secondly, the capacity of MPM is demonstrated to model degradation of highly swellable materials during large swelling that is a very complex example of the current standard finite element method to handle. Following the work was done by M. Kang and R. Huang (2010), the rate form of Flory's constitutive law is calculated only based on the elastic free energy of hydrogels, and the Voigt form of the tangent modulus in 2D is developed. The constitutive law is fitted in the MPM code which is developed by the author and the results of 2D uniform swelling are validated by the analytical results of the 2D large tensile case study. A perfect match is observed between the analytical results and the MPM results for the large tensile test. Next, the same code is tailored for the non-uniform swelling and finally degradation during large elastic swelling is added to the simulation as a random phenomenon based on the normal distribution of the volumetric strain. Last but not least the drug release profile of the tablet in

controlled drug delivery systems for multi-layered tablets is presented as an example for an arbitrary multi-layered tablet.

Chapter 6. Implementation of MPM to Selective Laser Melting

The purpose of this chapter is to demonstrate the capability of the MPM to simulate difficult problems such as the simulation of Selective Laser Melting that is challenging for the traditional finite element method. The main concerns in the simulation of SLM manufacturing technique and the main inputs are discussed. A preliminary computer simulation of the SLM with MPM is presented that is mainly focused on the effect of scanning strategies to reduce the effect of the thermal stresses to avoid initial cracking due to the residual stresses. Furthermore, it is demonstrated that the MPM is a robust numerical method to simulate SLM and has significant advantages over traditional finite element methods.

6.1 Selective laser melting

Selective Laser Melting (SLM) is a new manufacturing process that has been developed over the last two decades. This method mainly enhances manufacturer to produce parts with very complex inner shape designs such as injection moulds with cooling channels, medical instruments and automotive parts which cannot be produced by conventional methods Laurent V. Belle, et al. (2012). A major problem in this process is the generation of high residual stress profile as a result of the strong temperature gradient in the manufactured parts. The main purpose of this chapter is to demonstrate Material Point Method as a robust numerical approach to model SLM process and simulate the residual stresses.

6.1.1 Introduction

Speeding the manufacturing process has always been manufacturer's main goal. Therefore, over the last few decades, rapid prototyping from CAD was changed to rapid manufacturing of the final net shapes parts usually used for parts with complex inner designs. The Rapid Tooling (RT) such as Warm and Arc Additive Layer Manufacturing (WAALM), Laser Metal Deposition (LMD) and Selective Laser Melting (SLM) are just

some examples of the recent developments towards this aim Laurent V. Belle, et al. (2012). In this chapter, we are focused on SLM technique and our efforts are to use Material Point Method which has been explained in chapter 2 to simulate the process and simulate the problem of residual stress generation in the parts due to a strong temperature gradient. SLM was first developed in 1995 by a research project at the Fraunhofer Institute ILT in Aachen, Germany. SLM is a technique to produce complex parts, layer by layer by fully melting the metallic powders with a laser radiation, and the product will be in the net shape and no post processing is required. The process begin with designing a multi-layer CAD model of the part, the suitable thickness of each layer is usually between 20-50 micrometres, and then the information will be transferred into the SLM machine Y. Wang, J. Bergström, C. Burman 2006; X. Su, Y. Yang (2012). Figure 6-1 shows the process after the SLM computer receives the input file L. Loh *et al.* (2015). At first, one layer of metallic powders with the designed thickness is deposited on the base plate that is located on the surface of a vertical piston. A wiper is used to make the powders uniform periodically through the process, then a laser beam is used to scan the pattern which has been planned in the CAD model at each layer and melt the metallic powders to make the solid materials after it cools down. The piston then moves down the platform when the first layer is finished. The height of moving is equal to the thickness of one layer. Then a new layer of powders will be laid on the surface of the solid structure and this process will be continued until a net body is produced K. Osakada, M. Shiomi (2006). There are a significant number of literature over the last few years to simulate the residual stress in the parts. L. V. Belle et al. (2012) used a numerical model which was based on a double mesh system with a multi-step birth and death technique of manufactured part. L. E. Loh et al. (2015) have developed an FE model on the SLM that simulate the powder-to-solid transition along with a method to calculate the volume shrinkage and the material removal. They have validated the model experimentally. P. Li et al. (2014) have developed a full scale 3D finite element model to investigate the microscopic deformation of the micro lattice structures and the microscopic stress and strain evolution in the solid struts of the micro lattice. The selective laser melting has been applied in many areas where parts to be fabricated is with complex geometries or structures with thin walls or holes, such as aerospace,

automobile, and medical industry. Commercial machines for SLM have been developed by several companies such as MCP, TRUMPF in Germany, MATSUUR in Japan and PHENIX in U.S.A. M. Vaezi *et al.* 2013; A. L. Jardini (2014). In this chapter, an FE method has been developed based on material point method. The model has been applied to a 2D structure, to calculate the microscopic deformation of the structure and also to investigate the microscopic stress and strain in the solid structure.

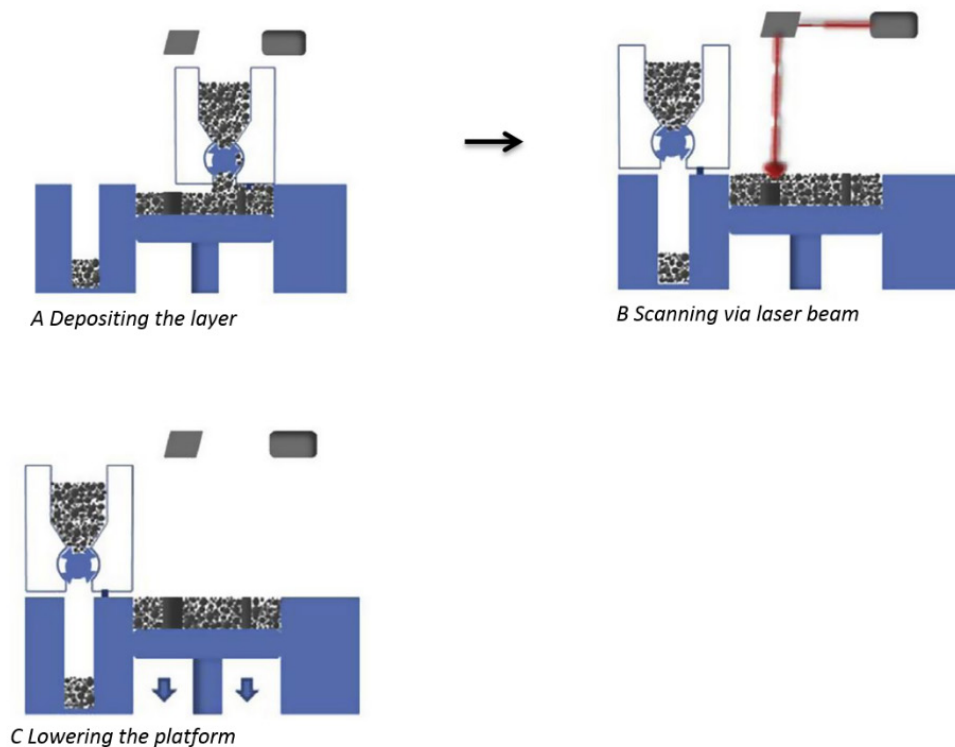


Figure 6-1 Schematic of the SLM process L. E. Loh *et al.* (2014)

6.1.2 The main problems and issues of SLM

There are a few different technical issues in the SLM process that need to be solved. The energy density of the laser has to be sufficient in order to ensure not only it melts the powder layer but also the current layer that has been scanned need to be fused together with the previous layer to avoid weak bonding T. Childs, C. Hauser and M. Badrossamay (2005). If the energy density applied to the metallic powder is too high, the temperature will continue rising after reaches the melting point. Evaporation will happen when the temperature exceeds the boiling point. The evaporated material will be removed with

the protection gas when not heated by the laser beam. The rest of the material cools down and solidifies. Meanwhile, the metallic powder will shrink in volume because the molten material seeps through the porous spaces E. Yasa, J.P. Kruth, J. Deckers (2011). The shrinkage causes an undesirable compressive thermal stress and it may lead to forming initial cracking. So it is essential to understand what will happen during the process of selective laser melting F. Verhaeghe et al. (2009). Figure 6-2 shows an example of cracked surfaces of Ti-6-4 specimens formed in the SLM process. S. Leuders et al. (2012).

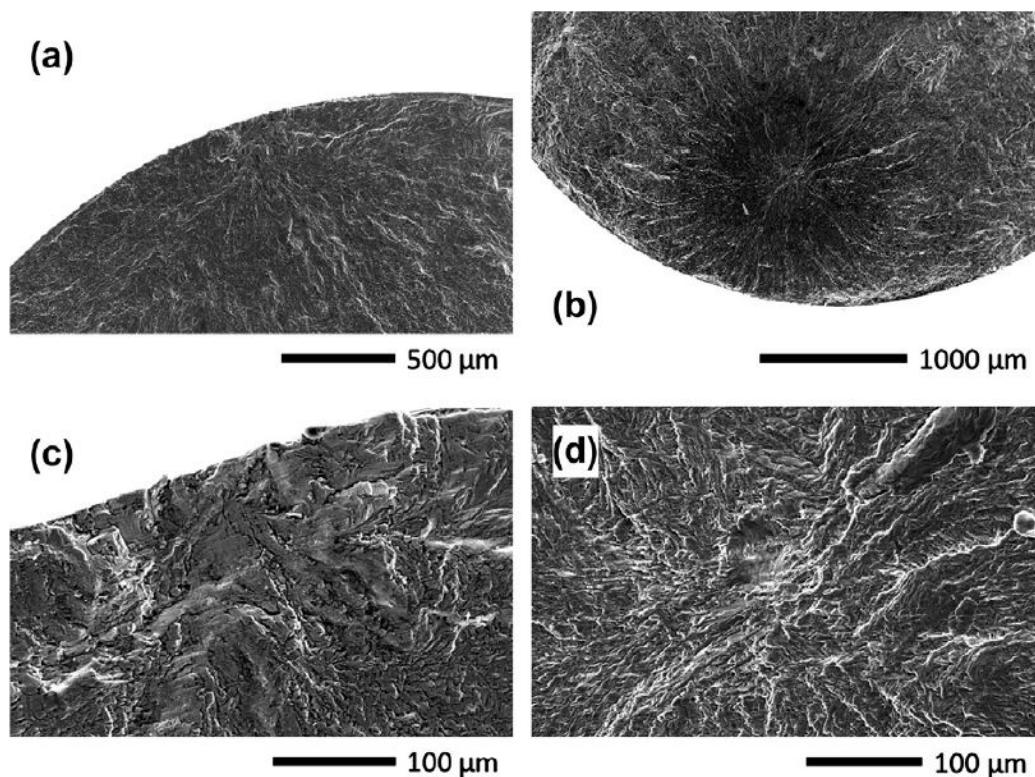


Figure 6-2 Crack surfaces of Ti-6-4 specimens following SLM processing, subsequent HIP treatment and fatigue at a stress amplitude of 620 MPa. Fatigue lives of the samples shown were fairly low (a, c: 188,103 cycles; b, d: 845,383 cycles) due to remaining porosity. The crack initiation sites for two different samples are shown in low magnification in (a) and (b); (c) and (d) depict the corresponding magnified view of the underlying defects. S. Leuders et al. (2012).

Recently, V. Cain et al. (2015) described the fatigue crack growth rate properties of selective laser melting from grade 5 Ti6Al4V alloy. They demonstrated low thermal stress relief can improve fracture toughness and fatigue crack growth resistance. S. Leuders et al. (2012) also tested the mechanical behaviours with titanium alloy TiAl6V4

and pointed out the material behaviour of crack growth is particularly influenced by internal stresses. Figure 6-2 shows a failure sample of cracking, in which the porous have been detected as an initial point of cracks S. Leuders et al. (2012).

In recent years, researchers have also investigated the thermal stresses generated by the SLM process. Several numerical methods have been developed to measure the temperature as well as thermal stress distribution of overhanging structures. A. Hussein et al. (2013) and D. Zhang et al. (2010), simulated the temperature distribution of selective laser melting with 90W–7Ni–3Fe powders and showed that lower thickness, narrower scan interval, and a slower scan velocity can improve the temperature in the powder bed. C. Casavola, S. L. Campanelli and C. Pappalettere (2008) have studied the residual stresses in SLM specimens produced from AISI Marage 300 steel by experiment. D. Leordean et al. (2015) have simulated the stress behaviour during the process of SLM for a multi-structured femoral prosthesis under different values of laser power. A. H. Nickel, D. M. Barnett and F. B. Prinz (2001) have numerically examined the effect of deposition patterns with finite element modelling and have drawn the conclusion that the different scanning strategies of the laser may affect the stress behaviour of the component. M. Shiomi et al. (2004) have measured the distribution of residual stress for the selective laser melting process and concluded that the largest (tensile) value in the top layer of the model irrespective of the scan speed.

6.2 The purpose of this chapter

The major advantage of MPM over the conventional FEM in simulating SLM is the capability of MPM to simply deal with adding/ losing material to the main body. In MPM, there is no need to extend or re-mesh the system during the solidification. Furthermore, it is straightforward to deal with separation of two material points as opposed to mesh splitting in the conventional FEM. Therefore, simulation of cracks could be effectively done by MPM F. Li, J Pan, C. Sinka (2011). Stress analysis with MPM is as accurate as conventional FEM, and also different constitutive laws can be used in MPM to model different materials with either plasticity theorems or elasticity theorems. In addition, modelling complicated geometries could be more convenient with MPM. As it is discussed in previous chapters, it is fairly easy to initially distribute the material points

in any arbitrary geometry. With regards to SLM simulation by MPM, scanned metallic powders can be represented by the material points. Therefore, MPM can effectively handle different scanning pattern and different geometries. In this chapter, MPM is combined with elasticity to demonstrate the capability of MPM to simulate fairly difficult geometries and different scanning patterns. Details of the numerical methodology are described in the next section. As the validation of the model in small deformation analysis is described in the previous chapter, elastic stress distribution of the SLM simulation is studied in this chapter. It is shown that MPM is a robust numerical tool that is suitable to simulate the SLM process and cover most of its difficulties.

6.3 Overall numerical algorithm

6.3.1 Adapt Material Point Method for SLM

The general formulation of MPM is described in chapter 3. Here an overall outline of the code is described briefly along with the discretised form of the MPM to consolidate the context for elastic small deformation of Selective Laser Melting. Furthermore, a new variable ξ is introduced to enhance the MPM code to simulate the scanning pattern. In the MPM, the motion of the material points represents the deformation of the solid body. As it was described in chapter 3 the deformation of the material points are calculated from the nodal velocities of the computational mesh that are determined from the nodal acceleration of the computational mesh, that is updated by calculating nodal forces, the same governing equation that was discussed in the small deformation processes will be valid here, since SLM is dealing with small deformations.

$$\begin{aligned}
 \sum_{p=1}^{N_p} M_p N^T(X_p) N(X_p) \dot{v} = & - \sum_{p=1}^{N_p} M_p B^T(X_p) \rho_p^{-1} \sigma(X_p) + \\
 \sum_{p=1}^{N_p} M_p \rho_p^{-1} B^T(X_p) C(X_p) V(X_p) + & \sum_{p=1}^{N_p} M_p B^T(X_p) \rho_p^{-1} \sigma_0(X_p) + \\
 \sum_{p=1}^{N_p} M_p N^T(X_p) b(X_p) + & \int_{\partial\Omega} N(X_p) \tau ds
 \end{aligned} \tag{6-1}$$

As it is discussed in section 6.1.1, in the SLM process a laser beam is used to melt the metallic powders and the solid structure will be formed after cooling down. In the material point method, each powder is represented by one material point. In this

preliminary simulation, the thermal stress analysis has been ignored, and instead, a sintering stress ($-\sigma_0$) which is a compressive stress is assumed that linearly reduced to zero after the cooling time t_c is passed. (i.e. sintering stress at $t = 0$ for the specific material point that is hit by the laser is equal to $(-\sigma_0)$ and at $t = t_c$ the sintering stress reduced to zero for the same material point). The discrete material powders are always quite near to each other. So several powders may be scanned by the laser beam at the same time and a melting pool is formed. Meanwhile, the material points around will also shrink due to the high heat transform of the melting pool. Interactions among the powders will lead to a compressive stress ($-\sigma_0$). This sintering stress should be calculated through thermal stress analysis of the system that is based on the power of the laser beam and heat transfer analysis of the structure, however, the material point method is flexible to any input from the heat transfer analysis that can be done within the same MPM code as a subroutine. Also, the cooling time t_c can be changed within the code accordingly. But heat transfer analysis is beyond the scope of this project and should be conducted via a different project.

The number of material points that is scanned by the laser at the same time depends on the laser spot size; also the temperature gradient depends on the heat transfer of the body. Therefore, in this project, the slope of the decreasing sintering stress can be simulated by the cooling time. (i.e. the sintering stress ($-\sigma_0$) is maximum when the laser hit the material point and get to zero after cooling time t_c has passed)

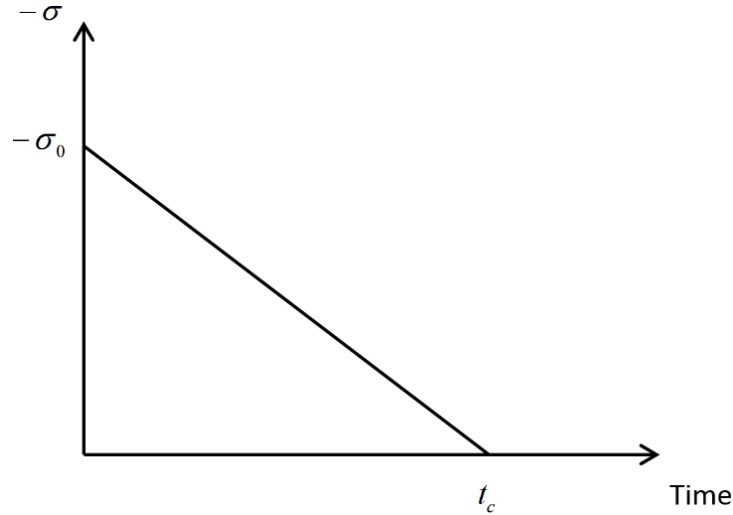


Figure 6-3 the distribution of the sintering stress on the material point over time.

Eq. (6-1) can be simply shown as below:

$$m\dot{v} = f^{int} + f^{ext} \quad (6-2)$$

In MPM instead of using the consistent mass matrix as it is shown on the left hand side of Eq. (6-1), lumped mass matrix in explicit time integration should be used which is defined in Eq. (6-3). In addition, the stresses σ are traced on material points. In order to calculate the volume integration in MPM, the density of each material point should be updated in every time step, therefore, in the first term on the right hand side of Eq. (6-1) material points are used as numerical integration points to calculate the volume integration. In SLM process, however, strains remain small, locally large solid rotations are still possible. Therefore, the same Jaumann rate of stress that is introduced in section 3.3.5, is also used in this model. The second term of the right hand side of Eq. (6-1) shows a damping system which is added to this model to damp the dynamic values to the final steady state solutions. The third term on the right hand side of Eq. (6-1) shows the possible body forces such as gravity that are applied on the material points, and the fourth term deals with surface traction τ that is applied to the computational mesh.

$$m = \sum_{p=1}^{N_p} M_p N^T(X_p) \quad (6-3)$$

The overall algorithm for numerical simulation of selective laser melting, which is based on the material point method is described as following.

1. Construct a collection of material points to represent a layer of powders that should be located on the surface of a constant background mesh. The background mesh should include any possible domain of movements of the material points.
2. Assign a new variable ξ to every material point that addresses the specific material points that are scanned by the laser. The value of ξ could be either one or zero, and if the material point is scanned by the laser the value is one and if it is not yet scanned it remain zero. Therefore, the laser path and laser scanning speed can be controlled if ξ is defined as a function of time. So by controlling this variable (defining the scanning pattern and scanning speed) those material points that are already scanned take into account as a part of the solid structure; otherwise for those material points that are not yet scanned by the laser, their mass will not contribute to the density integration and the stress rate calculation. Furthermore, with this method controlling of both the scan speed and the scan pattern is possible.
3. Compare the value of ξ to determine those material points that are scanned by the laser at each increment
4. Calculate the mass of the material points M_p to represent a solid structure, and initialise the state variables of the material points, including stresses, strains, velocities, and densities.

$$\rho = \sum_{p=1}^{N_p} M_p \tilde{\delta}(x - X_p)$$

(6-4)

The full algorithm for small deformation processes is described in chapter 3.

5. Updating the stresses, through calculating the Jaumann rate of stress $\sigma^{\nabla J}$ using the constitutive law as shown in Eq. (6-5) since in this project, we simulated the problem with the elasticity theorems; we have taken generalised Hook's law for the constitutive law.

$$\sigma_{n+1} = Q_{n+1} \cdot \sigma_n \cdot Q_{n+1}^T + \Delta t \sigma^{\nabla J} \quad (6-5)$$

6. Calculate the Von Mises stress, in order to be able to draw a colour map of stress distribution at each increment, through the current components of stress matrix $\sigma^{t+\Delta t}$. Therefore, the von Mises criterion can be simplified as

$$\sigma_{von-Mises} = \sqrt{\sigma_1^2 - \sigma_1\sigma_2 + \sigma_2^2 + 3\sigma_{12}^2} \quad (6-6)$$

As, it was discussed earlier, in order to have a uniform nodal mass density, the boundary of the system should be determined. In the SLM process, as there may be complicated geometries, every node of the background mesh should be checked at each increment to make sure if it is located on the boundary. Generally, for simple 4-noded rectangular background mesh, every node is surrounded by four elements. If all four surrounded elements are expired by the material points, so the corresponding node is not located on the boundary of the solid structure, otherwise if only one, two or three elements around the node are filled with material points then the nodal mass density for that node should be fixed accordingly with a factor of $\frac{1}{4}$, $\frac{1}{2}$, or $\frac{3}{4}$ respectively.

6.4 Pre-processing for different scanning strategy in SLM

In this project, one layer of a pipe with a separation wall is modelled as an example to analyse the stress distribution during the process of selective laser melting, with shape and dimension represented in Figure 6-4. Different scanning pattern, and scanning speed has been examined, and final Von Mises stress distribution has been shown in the results.

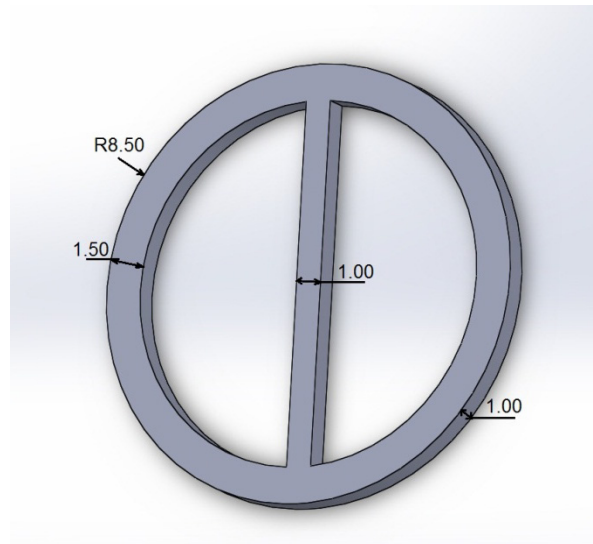


Figure 6-4 the geometry of the circular pipe with a separation wall. All the dimensions are in cm.

The programme is quite flexible with the elastic material properties. In this chapter, the properties of the material used are listed below:

Density (kg/m ³)	7700
Young's Modules (GPa)	80
Poisson Ratio	0.4

Three different scanning strategies are designed in this project, and the results of Von Mises stress are compared with each other. In the first strategy, the laser moves laterally while it is perpendicular to the plane of powders. As it is shown in Figure 6-5 the laser scans following the sequence of bottom layers to the top layer. Here in this particular pattern, the mid wall is scanned after the outside wall. In the second pattern, the laser moves on a circular base, perpendicular to the plain of powders again. In this method, the laser follows a polar coordinate system; it starts from one arbitrary point of the inner edge of the circular section of the pipe, and after scanning one whole circle, it moves one step in the radial direction and scans the second circle, until it finishes the pipe thickness and then scans the mid wall. Figure 6-6 shows the schematic of this pattern. In practice most of the times, the laser starts by scanning all the edges of the component

first to make it smoother. The third scanning pattern is following a polar coordinate system for the inner and outer edges of the circle and then it changes back to the normal Cartesian coordinate system. Next, scans the edges of the mid wall and then moves laterally and scans inside the circular walls and the mid wall as well. Figure 6-7 shows the schematic of this pattern.

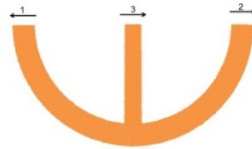


Figure 6-5 the laser moves laterally and is perpendicular to the plane of powders.

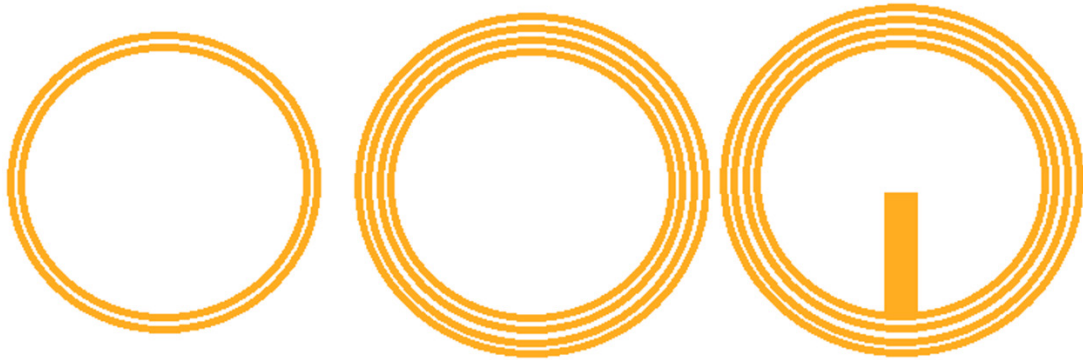


Figure 6-6 the laser moves on a circular base, perpendicular to the plain of powders

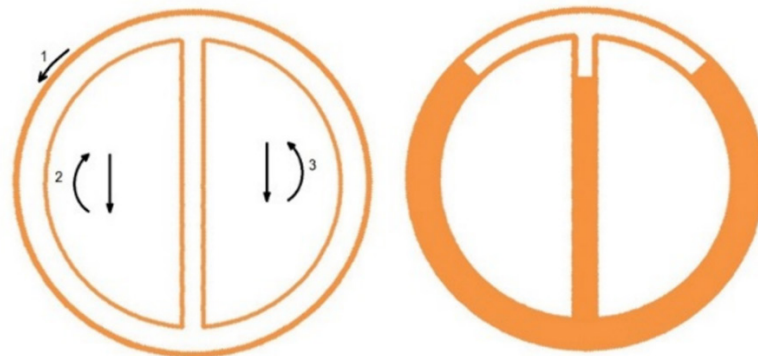


Figure 6-7 the laser first scans the edges and then scans between the edges.

All the three strategies are coded by FORTRAN as a part of the Material Point Method program. Therefore, the distribution of von Mises stress at any time during the whole process can be demonstrated as result of this project.

6.5 Results and discussion

The results presented in this section for case study 1 and case study 3 was carried out by Yu Zhou as his MSc project using my MPM code under my co-supervision. (Yu Zhou, 2013)

6.5.1 Distribution of von Mises stress for the first scanning strategy

Distribution of von Mises stress for the first strategy, as the scanning pattern was shown in Figure 6-5 the Von Mises distribution of the SLM process is shown at different times. In the first scanning method, 10200 material points have been scanned. Figure 6-8 shows how Von Mises stress behaves during the whole process of selective laser melting (with maximum sintering stress $\sigma_0 = -500MPa$, and $t_c = 500$ that means the effect of the laser will vanish after 500 iterations, and it is assumed the laser hit only 1 material point at each iteration)

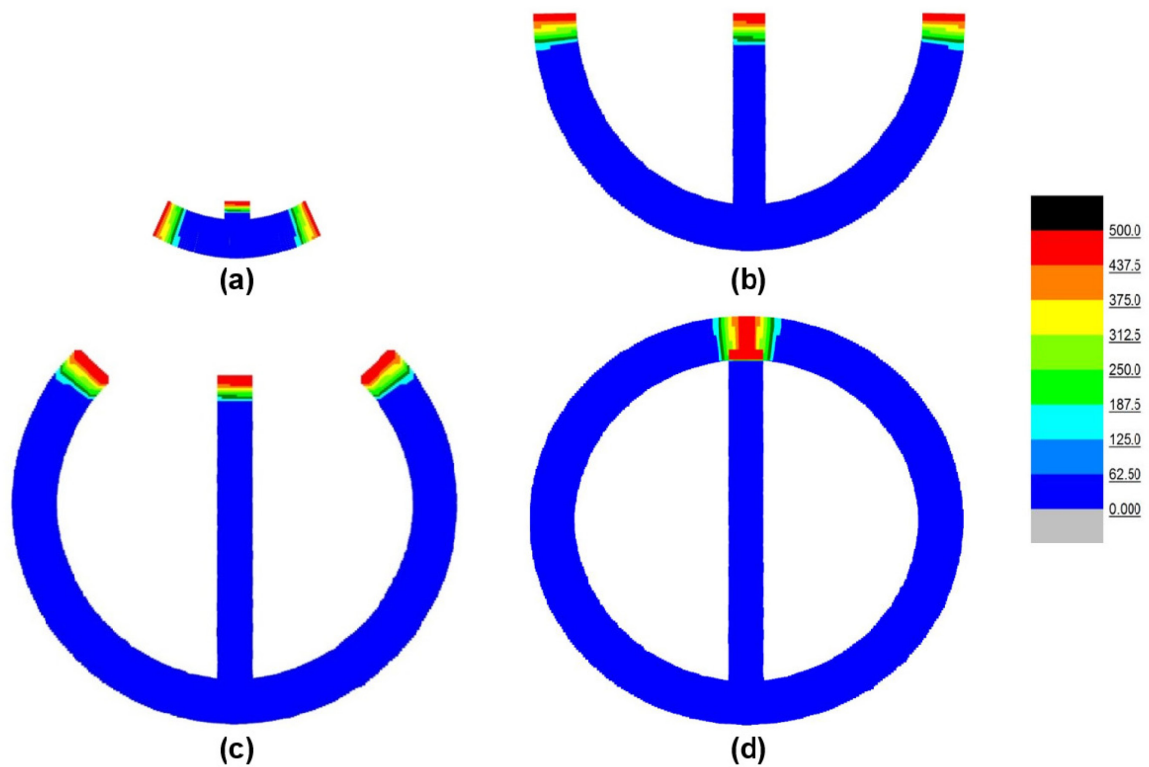


Figure 6-8 Distribution of von Mises stress for the first scanning strategy with cooling time $t_c = 500$ and maximum sintering stress $\sigma_0 = -500 \text{ MPa}$ (All the units in the figure are $-\text{MPa}$).
The number of scanned material points: (a) 1530; (b) 5100; (c) 7650; (d) 10200

The Von Mises stress reaches a maximum when the laser beam hit the material point and the value is almost σ_0 . This means the power of the laser is the dominant factor to Von Mises stress. Then, Von- Mises stress keeps decreasing after the laser passed the heated material point, and finally it reaches almost zero after a period of time because only elastic deformation is taken into account in this project. However, MPM is quite flexible to use plasticity theories and will be able to calculate the residual stresses; it is beyond the scope of this project and further research is required.

6.5.2 Distribution of von Mises stress for the second scanning strategy

Von Mises stress distribution for the second strategy that is shown in Figure 6-6 when the circular section is following the polar coordinate system is shown in Figure 6-9. In this method 8200 MP has been scanned in total with the same sintering stress $\sigma_0 = -500 \text{ MPa}$ and cooling time of $t_c = 500$.

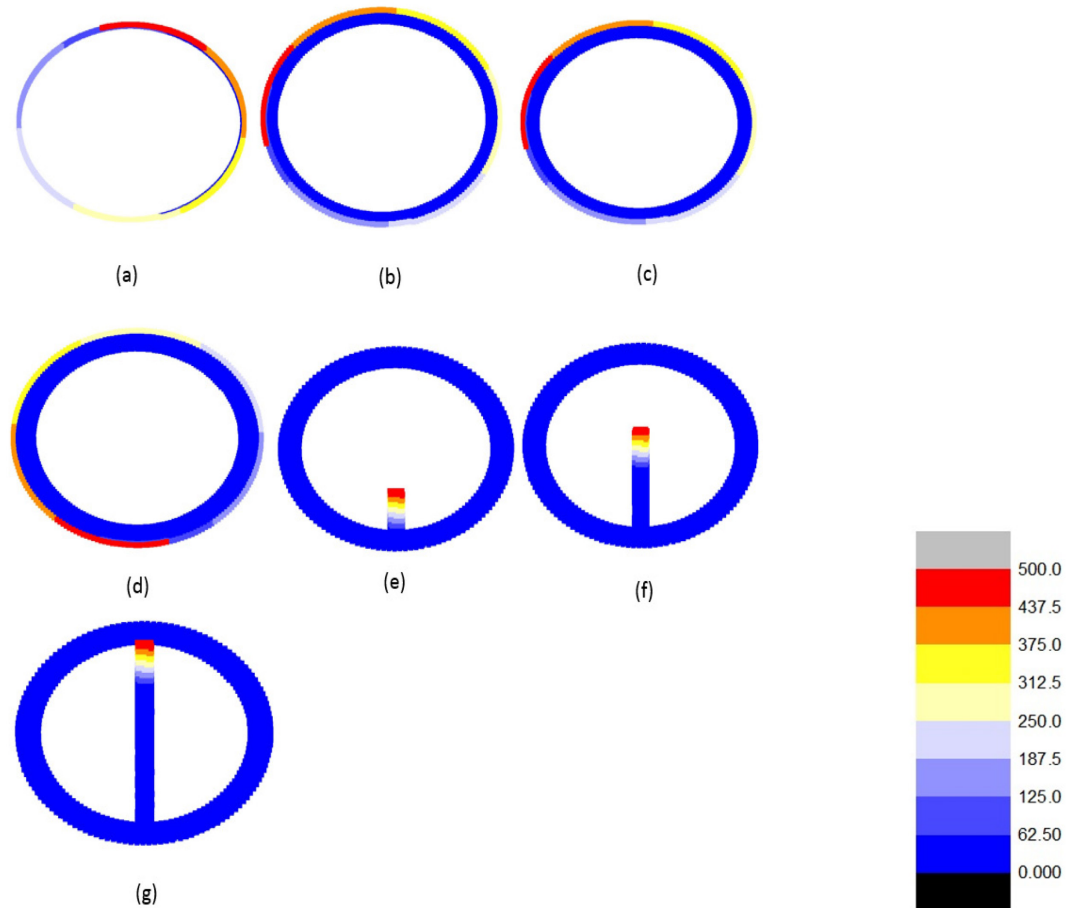


Figure 6-9 Distribution of von Mises stress for the third strategy with cooling time $t_c = 500$ and maximum sintering stress is $\sigma_0 = -500\text{MPa}$ (All the units in the figure are $-\text{MPa}$). The number of material points: (a) 600 ;(b) 3500 ;(c) 4500(d) 6150;(e) 6500 ;(f) 7200;(g) 8000

6.5.3 Distribution of von Mises stress for the third scanning strategy

As it is discussed in section 6.4, in the third scanning strategy first the edges are scanned, and then the laser moves between the edges to scan inside the thickness of the pipe. The total number of material points in this method is 12600, and the distribution of the Von Mises stress is shown in Figure 6-10. Here it is assumed that the laser spot only scans one material point at a time, however, in practice always a melting pool will be formed around the laser spot. Such situation that material point is scanned repeatedly happens frequently during the whole process. This can cause a high temperature and thermal stress, which results in initial cracks. More attention should be paid to this issue during practical fabrication.

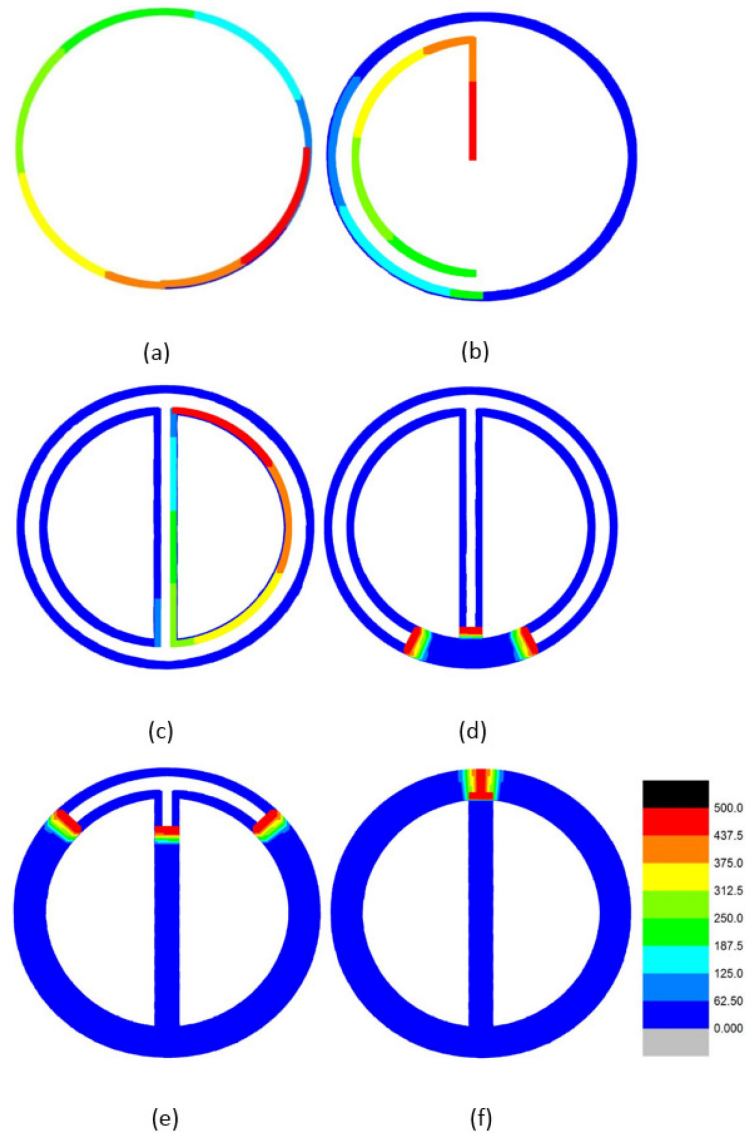


Figure 6-10 Distribution of von Mises stress for the third strategy with cooling time $t_c = 500$ and maximum sintering stress is $\sigma_0 = -500\text{MPa}$ (All the units in the figure are $-\text{MPa}$). The number of material points: (a) 500 ;(b) 1100 ;(c) 2400 (d) 3930 ;(e) 10050 ;(f) 12600

6.5.4 Distribution of von Mises stress with different length of cooling period t_c

Different values of cooling time t_c are used to represent how the distribution of von Mises stress behaves in a different situation. The behaviour is tested with a cooling time of shrinkage stress $t_c = 20, t_c = 100, t_c = 500$. Figure 6-11 shows the distribution of von Mises stress for the first strategy with 1530 material points with different cooling time t_c . The period that Von Mises stress exists is positively proportional to the cooling time of shrinkage stress. Therefore, as it is demonstrated this factor can be easily adjusted in

this model. Figure 6-11 shows the comparison of thermal stresses under the different cooling time of shrinkage stress. In Figure 6-11 (a) and Figure 6-11 (b) when laser begins to scan the body of the component, it repeats scanning the material points of the edge that have already been totally cooled down. In practical production, it is better to take into account the property of shrinkage stress when deciding the material.

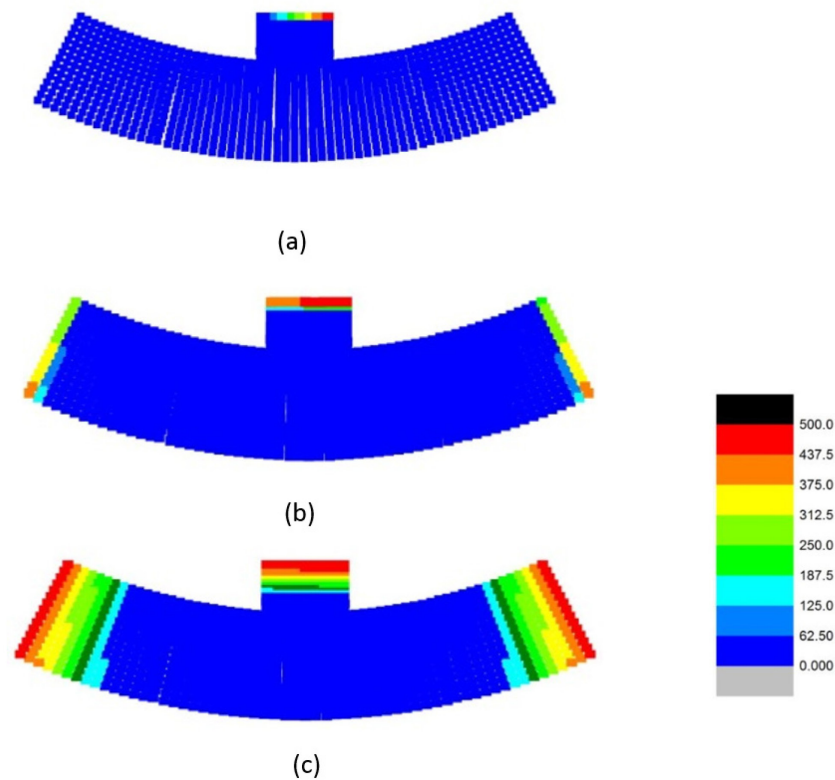


Figure 6-11 Distribution of von Mises stress for the first strategy with maximum sintering stress $\sigma_0 = -500\text{MPa}$, the number of material points 1530 (All the units in the figure are -MPa).

Cooling time t_c is: (a) 20; (b) 100; (c) 500.

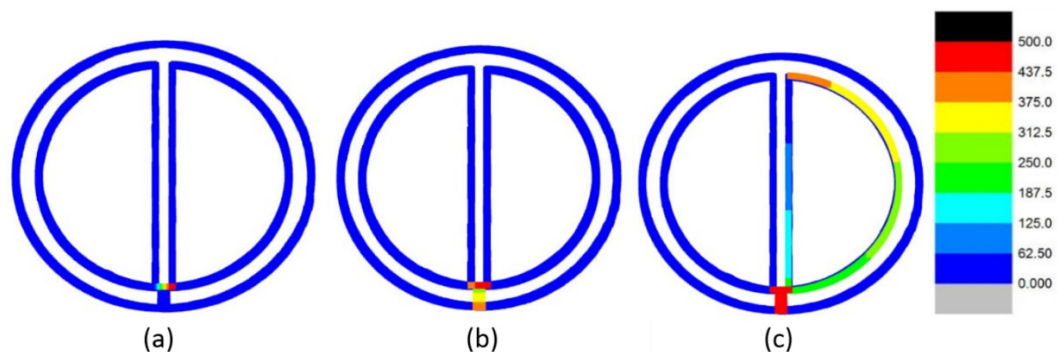


Figure 6-12 Distribution of von Mises stress for the third strategy with maximum sintering stress $\sigma_0 = -500\text{MPa}$, (All the units in the figure are -MPa). Number of material points 2502

and cooling time t_c is: (a) 20; (b) 100; (c) 500.

6.6 Summary

In this chapter, the application of Material Point Method has been demonstrated in a simulation of Selective Laser Melting (SLM) process. MPM is a strong numerical tool to calculate the residual stresses inside the material due to the distribution of thermal stresses during the process of SLM. As it was discussed in this process laser scanning pattern also play an important role in the distribution of the residual stresses that can lead to cracks. Here, we have modified the MPM code for small deformation and tailored it to be able to simulate the effect of laser scanning pattern. Three different strategies have been considered and the results of Von Mises stress distribution have been compared. The results are suitable for a wide range of materials and values of laser power due to the flexibility of the programme used in this project. Further improvement can be done to the program by using plasticity theorems instead of elasticity theorems that are used in this program. Also, thermal analysis enables the program to investigate heat transfer in the material that could be used to accurately calculate the residual stresses due to the shrinking. The major advantage of MPM over the conventional FEM in simulating SLM is the capability of MPM to simply deal with adding/ losing material to the main body. The strong side of MPM is its flexibility that can fit in any conditions, whether plasticity is used or elasticity for the governing equation. Also, the initial sintering stress can be separately calculated and be fed into the program. For example, sintering stress can be separately evaluated in a different subroutine via a transient heat transfer analysis and be used as σ_0 in Eq. (6-1) in each time step in SLM process. As we have used elastic constitutive law, the residual stresses cannot be calculated, therefore the sintering stress caused by the laser is always the dominant factor in the von Mises stress distribution. That is the reason why, the stress field around the laser spot is always much higher than the rest of the body, and also the stress field away from laser spot is almost zero.

Chapter 7. Conclusion

In this thesis mainly Material Point Method (MPM) is used as a robust numerical tool based on Lagrangian- Eulerian description of motion to model complex problems such as degradation of highly swellable polymers during large elastic swelling. Also, a rigorous validation of the MPM is shown against simple problems to fully validate MPM in extremely large deformation analysis. This advanced numerical method is further demonstrated to model an additive manufacturing technique called Selective Laser Melting that is currently difficult to handle for standard Finite Element Method (FEM). It is demonstrated that MPM can be perfectly tailored to fulfil the requirements of modelling problems dealing with discrete parts and continuum parts at the same time, such as SLM.

The main advantages of MPM over the conventional FEM are first due to the constant background mesh that can be chosen arbitrary, that avoids fatal mesh distortion which is a common problem in FEM especially in large deformation analysis. Therefore, no re-meshing technique or iterative contact algorithms are necessary for the MPM. The second appealing feature of the MPM is the flexibility of this method to deal with the material disintegration or material consolidation which means during the computational process material can be added or removed from the main computational domain without any re-meshing or iterative schemes. Therefore, in this thesis simulation of polymer degradation during large swelling and modelling of Selective Laser Melting are chosen as two complex examples to demonstrate the robustness and simplicity of the MPM over the conventional FEM for complex problems.

The Material Point Method is validated in this thesis using a series of analytical solutions for simple tensile problems and vibration problems. Therefore, it is demonstrated that the method is reliable and the numerical results are of high confidence. Nonetheless, the effortless and strength and accuracy of this numerical method makes it a very authoritative technique to tackle very complex problems beyond the scope of polymer degradation during large swelling that was discussed in this thesis.

The focus of this thesis, however, is on the capacity of the Material Point Method to tackle polymer swelling and polymer degradation for highly swellable polymers. In chapter 2 non-equilibrium thermodynamic theory was introduced and the framework was presented to model the swelling behaviour of the highly swellable materials. It is discussed that the equilibrium thermodynamic theory does not consider the short time limit of the polymer swelling and only focuses on the long time limit and the final swelling ratio of the hydrogel. Since the swelling process is a fast phenomenon in highly swellable materials and a short time limit of the process is of high importance, so equilibrium thermodynamic theory cannot be used to explain the swelling behaviour of highly swellable materials. Therefore, the non-equilibrium thermodynamic theory is presented. Also, polymer swelling is brought about by the concentration of the solvent molecules which is diffused inside the polymer due to the chemical potential. Hence, the nominal stresses and the chemical potential (i.e. the governing equation) that are shown in Eq.(2-14) and Eq.(2-15) must be solved. Also, non-equilibrium thermodynamic theory stated that there is a linear relationship between the applied body force (nominal stresses) and displacement of the materials as shown in Eq. (2-18). Therefore, the focus of this thesis is to model the large elastic deformation of the hydrogel as a consequence of the nominal stresses, rather than solving the actual governing equations. Hence, the computer program based on the MPM is designed to work for a range of arbitrary constant stresses that is applied to all the material points which are representing the mass of the body. Hence, instead of solving the actual governing equations for nominal stresses and chemical potential, alternatively, it is assumed a range of known constant stresses are applied to the polymer like an initial body force. Therefore, it is shown that the computer program is capable of working for more realistic values of stresses and chemical potential when required.

In Chapter 3 the mathematical framework of the MPM is explained in detail, and the topological system which is designed for the main computer program for this thesis is discussed. Furthermore, in MPM the material points can be easily positioned within a global coordinate system and build a large collection of material points in multi-dimensional space with specific boundary profile. Therefore, modelling and discretising of structures with difficult geometries are easy to handle with MPM, while it could be a

challenging task for standard FEM, however, then a fairly complicated topological system is required to track the material points at every time step, especially in large deformation problems that material points move far from their initial computational cell. The topological system that is discussed in this chapter can accurately track down the material points, and remember the state variables such as position, velocity, accelerations, and stress values from the last time step and use them to update for the current time step. The framework that is designed contains two subroutines to relate the nodal numbers to the surrounding cell's index number and also cell's index number to the four node's index number of the computational cell. Furthermore, three subroutines are designed to count the total number of material points per cell at each time step, and also to find the current cell's index number for a specific material point's index number, and last but not least, to find the index number of all the current material points per cell's index numbers. In addition, either global or local mesh refinement is possible with the MPM. But, a common issue that often happens in the MPM is when there are a few number of material points in a computational element that can happen due to moving of the material point to a new element which usually occurs in the boundary of the system. This problem is discussed in chapter 3 in detail and a smoothing technique which is offered by Sulsky et al. (1995) is presented, however, their smoothing technique is useful in small deformation analysis, it will not be helpful for extremely large deformation analysis. Therefore, in chapter 5 a unique technique is presented by the author of this thesis to solve this issue for extremely large deformation problems.

A rigorous validation of the MPM against an analytical solution of some simple problems is conducted in chapter 4 in 1D and 2D for small deformation analysis. Hence, the dynamic response of the vibrational system is simulated in 1D and 2D and the results of the simulation by the MPM and the FEM are shown having a good match and can be also analytically justified. Furthermore, it is shown that the number of material points per cell is an important factor for the accuracy of the results of the MPM. Therefore, a range of different vibration simulations with different mechanical properties and different boundary conditions and load conditions are fulfilled to verify the computer program based on the MPM. The next step in the validation of the computer program

based on the MPM is to validate the accuracy of the constitutive law and the stress/strain values. Hence, a tensile test is carried out to validate the accuracy of the linear constitutive law that is fitted in the MPM computer program for small elastic deformation analysis. Therefore, the reliability of the computer program based on the MPM is firmly demonstrated in 2D small deformation analysis, by comparing the steady state response of the 2D vibrational system with the analytical solution. Also, the results of the stress and strain values of the MPM simulation are used to verify Young's modulus and Poisson's ratio using Hooke's law, and these results have been compared with the initial inputs. A perfect match between the initial inputs of Young's modulus and Poisson's ratio and that of calculated by the MPM perfectly validate the computer program. A damping system is designed to damp the dynamic response of the MPM results about the steady state values. It is shown that for a range of different mechanical properties and boundary conditions and load conditions the results of the computer program have a perfect match with the analytical solutions.

In chapter 5, degradation of highly swellable polymers during non-uniform and extremely large deformation is used as an example of the capability of the MPM in the simulation of such a complex problem that is impossible to handle for the conventional FEM. The complexity of this problem can be shown in random degradation of the polymer during extremely large deformation, while in the conventional FEM random re-meshing of the discretised system due to the mass loss is impossible. Hence, firstly the computer program based on the MPM is validated for the modelling of extremely large deformation of the materials or structures, against the analytical result of the large tensile test. Secondly, the capability of MPM is shown in the modelling of random degradation of highly swellable polymers during non-uniform large swelling. Following the work was done by M. Kang and R. Huang (2010), the rate form of Flory's constitutive law is calculated only based on the elastic free energy of hydrogels and is used as the material constitutive law of highly swellable polymers in the computer program based on the MPM to update the stresses. A perfect match is found between the numerical results and analytical results of the 2D uniform large tensile test. Therefore, the computer program is then tailored to model a non-uniform swelling by changing the reference body to a multi-layered polymer with different values of applied stresses. Last

but not least, polymer degradation is modelled as a random phenomenon based on the normal distribution of the volumetric strain. The main difficulty in the numerical simulation of the non-uniform extremely large swelling based on the MPM is to deal with the boundary layer of the system when the material points move to the new empty elements of the background mesh, that cause inaccurate high nodal accelerations. The fatal numerical issues of implementation of the MPM and also a novel technique to solve the problem is presented in sections 5.3.2 and 5.3.3 respectively.

Part of the work in this chapter was presented in the 5th International Conference on Computational Methods (ICCM2014) Cambridge, UK.

The details of the conference presentation and poster presentation is given in APPENDICES.

In chapter 6 the capacity of the MPM is demonstrated in the modelling of Selective Laser Melting (SLM) manufacturing process. It was shown that the MPM can be simply modified and be applied to simulate SLM manufacturing technique, since not only it can easily deal with adding/removing materials to the main computational body during the process due to the consolidation of metals powders which are melted by the laser, but also it can easily deal with complicated geometries which are the main advantage of the MPM over the conventional FEM in simulating of the SLM manufacturing technique. The simple birth/death technique that is designed and presented in section 6.3.1 in parallel with the MPM, is claimed to be much easier than the conventional birth/death technique since re-meshing of the system is not required when the material is added to the system due to the consolidation of the melted powders. Therefore, it is demonstrated that study of the effect of different laser patterns is easy to handle with the MPM. Laser scanning pattern is an important factor which can directly effect on the residual stresses due to the thermal stresses that are maximum around the laser spot. Furthermore, in the conventional FEM, in order to study the effect of the laser spot size, or to study the local thermal residual stresses or to study the potential micro-cracks due to the thermal residual stresses and also to apply the birth/death technique, it is required to use an extremely refined mesh that cause an enormous increase in the computational costs Lian Y.P., Zhang X., Liu Y., (2012). Hence, the study of the real size parts is extremely difficult and expensive by the conventional FEM. But, in the MPM

since each powder can be defined by one material point and also all the state variables are defined on the material points a much larger background mesh can be used that reduces the computational costs. Therefore, the study of the larger industrial size of the machine parts is possible with the MPM. Also, MPM can be easily modified to use the plasticity theorem and to calculate the distribution of thermal stresses due to conduction, or radiation in order to analyse the residual stresses that are beyond the scope of this thesis.

References:

Achilleos E.C., Christodoulou E.C., Kevrekidis I.G., (1999) A transport model for swelling of polyelectrolyte gels in simple and complex geometries. *Computational and Theoretical Polymer Science*. 11 (2001) 63-80

Arruda E. M., and Boyce M., (1992) A three-dimensional constitutive model for the large strength behaviour of rubber elastic materials. *J. Mech. Phys. Solid*. 41, 2, 389-412.

Aydt E.M., Hentschke R., (1999) Swelling of a model network: A Gibbs-ensemble molecular dynamics study. *JOURNAL OF CHEMICAL PHYSICS*. 112(12).

Belle L.V., Vansteenkiste L.V., Boyer J. C. (2013) Comparisons of numerical modelling of the Selective Laser Melting.

Belytschko T., Liu W. K., and Moran B., (2000). *Nonlinear Finite Elements for Continua and Structures*. WILEY

Belytschko T., Kam Liu W., and Moran B., (2005). *Nonlinear Finite Element for Continua and Structures*. West Sussex England, John Wiley.

Bettini R., Catellani P.L., Santi P.L., Massimo G., Peppas G., and Colombo P., (2001). Translation of drug particles in HPMC matrix gel layer: effect of drug solubility and influence on release rate. *Journal of Controlled Release*. 70(3).383-391

Biot M.A., (1941). The general theory of three dimensional consolidation. *J. Appl. Phys.* 12 (2), 155-164.

Bouklas N., Landis C.M., and Huang R., (2015). A nonlinear, transient finite element method for coupled solvent diffusion and large deformation of hydrogels. *Journal of the Mechanics and Physics of Solids* 79. 21-43

Djekic L., Krajisink D., Martinovic M., Djoidjevic D., Primorac M., (2015). Characterization of gelation process and drug release profile of thermosensitive liquid lecithin/poloxamer 407 based gels as carriers for percutaneous delivery of ibuprofen. *International Journal of Pharmaceutics*. 490.1-2. 180-189

Flory P.J. (1953). *Principles of Polymer Chemistry* Cornell University Press, Ithaca, NY.

Fowler R.H., Guggenheim, E.A. (1941). Statistical Thermodynamics. Journal of Chemical Education. 18(4),p 198, DOI: 10.1021/ed0 18p198.3.

Fyfe C.A., Blazek A.I., (1997). Investigation of hydrogel formation from hydroxypropylmethylcellulose (HPMC) by NMR spectroscopy and NMR imaging techniques, macromolecules. 30 6230-6237

Gibbs J.W., (1878). The Scientific Papers of J. Willard Gibbs. Pp. 184,201,215. Digital copy of the book is freely available at <http://books.google.com/>.

Gleadall A., Pan J., Krufft MA., Kellomaki M., (2014) Degradation mechanisms of bioresorbable polyesters, part 1: effects of random scission, end scission, and autocatalysis. Acta Biomaterialia, 10, 2223-2232.

Han X., (2011). Degradation models for polyesters and their composites. Ph.D. thesis, University of Leicester

Hettich T. and Ramm e., (2006) Interface material failure modelled by the extended finite element method and level sets, Computer Methods in Applied Mechanics and Engineering, 195,37-40, 4753-4767

Hong W., Zhou J., and Suo Z., (2007). A theory of coupled diffusion and large deformation in polymeric gels. Journal of The Mechanics and Physics of Solids. 56.1779-1793

Kang M.K., and Huang R., (2010). A variational approach and finite element implementation for swelling of polymeric hydrogels under geometric constraints. Journal of Applied Mechanics. Vol. 77 / 061004-1

Kill S. and K. Dam-johanson K., (2003). Controlled drug delivery from swellable hydroxypropylmethylcellulose matrices: model-based analysis of observed radial front movements. Journal of Controlled Release. 90(1).1-21

Krank J. (1975). The Mathematics of Diffusion. Oxford, Pa: Clarendon Press.

Kuhn W., Hargitay B., Katchalsky A., and Eisenberg H., (1950). Reversible Dilation and Contraction by Changing the State of Ionization of High-Polymer Acid Networks. Nature (London). 165.514-516

- Li F., (2008). Interactions between fine particles. Ph.D. thesis, University of Leicester
- Li F., Pan J. and Sinka C. (2011), Modelling brittle impact failure of disc particles using material point method, *International Journal of Impact Engineering*, 38, 653-660
- Li P., Wang Z., Petrinic N., Siviour C.R., (2014). Deformation behaviour of stainless steel microlattice structures by selective laser melting. *Material Science and Engineering. A* 614 (2014), 116-121.
- Lian Y.P., Zhang X., Liu Y., (2012) An adaptive finite element material point method and its application in extreme deformation problems. *Computer methods in applied mechanics and engineering*.
- Loh L., Chua C., Yeong W., Song J., Mapar M., Sing S., Liu Z., Zhang D., (2014). Numerical investigation and an effective modelling on Selective Laser Melting (SLM) process with aluminium alloy 6061. *INTERNATIONAL JOURNAL OF HEAT AND MASS TRANSFER*. 80, (2015), 288-300.
- Lucantonio A., Nardinocchi P., Teresi L., (2012) Transient analysis of swelling-induced large deformations in polymer gels. *Journal of the Mechanics and Physics of Solids* 61 (2013) 205-218
- Ma S., Zhang X., and Qiu X., (2008). A comparison study of MPM and SPH in modelling hypervelocity impact problems. *International Journal of Impact Engineering* 36 (2009) 272-282.
- Ma X., Zhang D., Giguere P. T., Liu C., (2013) Axisymmetric computation of Taylor cylinder impacts of ductile and brittle materials using original and dual domain material point methods. *International Journal of Impact Engineering*. 54, 96-104.
- Narasimhan B., and Peppas N.A., (1997). Molecular analysis of drug delivery systems controlled by dissolution of the polymer carrier. *Journal of Pharmaceutical Sciences*. Vol. 86(3). 297-304
- Painter P. C., Coleman M. M., (2009). *Essential of Polymer Science and Engineering*. Lancaster, Pa: DEStech Publications, Inc.

Phuong N.T.V., Van To A.F., Elkadi A.S.K., Rohe A., (2015) Numerical investigation of pile installation effects in sand using material point method, *Computers and Geotechnics* 73 (2016)58-71

Siepmann J., and Peppas N.A., (2000). Modelling of drug release from delivery systems based on hydroxypropyl methylcellulose (HPMC). *Advanced Drug Delivery Reviews*. Vol. 48. 139-157.

Smith I. M., and Griffiths D.V., (2004). *Programming the Finite Element Method*. West Sussex England, John Wiley.

Sun W., Chaikof, Levenston M.E., (2008). Numerical Approximation of Tangent Moduli For Finite Element Implementation Of Nonlinear Hyperelastic Material Models. *Journal of Biochemical Engineering*. 130 / 061003-1.

Sulsky A.I., Zhou S., and Schreyer H. L., (1995). Application of a particle-in-cell method to solid mechanics. *Computer Physics Communications*. Vol.87.236-252.

Wang B., Vardon B., Hicks M.A., (2016) Investigation of retrogressive and Progressive slope failure mechanisms using the material point method. *Computers and Geotechnics*. 78, 88-98.

Wing K.L., Chang H., Chen J., Belytschko T., (1988) Arbitrary lagrangian-eulerian petrov-galerkin finite elements for nonlinear continua, *Computer Methods in Applied Mechanics and Engineering*, 68,3,259-310

Wineman A., (2004) Some results for generalized neo-Hookean elastic materials. *INTERNATIONAL JOURNAL of NON-LINEAR MECHANICS*. 40 (2005) 271-279

Yan H., 2013. A dynamic model for swelling induced by moisture absorption. Master's degree dissertation, University of Leicester

Zhang Y., Matsumoto E.A., Peter A., Lin P.C., Kamien R.D., Yang S., (2008). One-Step Nanoscale Assembly of Complex Structures Via Harnessing of an Elastic Instability. *Nano Lett.* 8. 1192-1196

Zhang J., Zhao X., Suo Z., Jiang H., (2009) A finite element method for transient analysis of concurrent large deformation and mass transport in gels. *J. Appl. Phys.* 105(9), 093522.

Zhou Y. (2013). Computer simulation of Selective Laser Melting. Master's degree dissertation, University of Leicester.

APPENDICES

Conference Presentations

Ali Tabatabaeian Nimavardi, et al., 2014. A variational approach and finite element implementation for controlled drug delivery. The 5th International Conference on Computational Methods (ICCM2014), 28-30 July .2014, Cambridge, UK.

Ali Tabatabaeian Nimavardi, et al., Numerical modelling of selective laser melting based on the Material Point Method. Festival of postgraduate research University of Leicester, July 2015, Leicester, UK.

Ali Tabatabaeian Nimavardi, et al. 2013. One day meeting on advanced numerical methods, run by the Engineering and Mathematics department, University of Leicester March 2013.

Ali Tabatabaeian Nimavardi, et al., 2012. Phase Field model and a variational approach for controlled drug delivery systems. Engineering department, University of Leicester. October 2012.

Appendix I **Reynold's theorem of material time derivative**

Deformation gradient is an important variable in characterization of the deformation, which is defined by

$$F_{ij} = \frac{\partial \Phi_i}{\partial X_j} \equiv \frac{\partial x_i}{\partial X_j} \equiv (\nabla_0 \Phi)^T \quad (\text{AI-1})$$

Where $\Phi(X, t)$ is the equation of motion as shown in Eq. (AI-2), x_i and X_j refer to the computational coordinates and the material coordinates respectively, and ∇_0 which is the left gradient operator with respect to the material coordinate.

$$x = \Phi(X, t) \quad (\text{AI-2})$$

The determinant of the F is indicated as J and called *Jacobian determinant*, or determinant of the deformation gradient

$$J = \det(F) \quad (\text{AI-3})$$

With the Jacobian determinant the integrals in the current and reference configurations can be related, Eq. (AI-4) relates the two configuration

$$\int_{\Omega} f(x, t) d\Omega = \int_{\Omega_0} f(\Phi(X, t), t) J d\Omega_0 = \int_{\Omega_0} f(x, t) J d\Omega_0 \quad (\text{AI-4})$$

Where f is an arbitrary function, Ω_0 and Ω are initial state of the configuration and the current configuration respectively.

The time derivative of Eq. (AI-5) gives

$$\frac{dJ}{dt} = J \frac{\partial v_i}{\partial x_i} = J \nabla \cdot (v) \quad (\text{AI-5})$$

In Eq.(AI-5) v is the velocity vector and Einstein summation is used. By applying the time derivative on Eq. (AI-5) it gives

$$\frac{d}{dt} \int_{\Omega} f(x, t) d\Omega = \frac{d}{dt} \int_{\Omega_0} f(\Phi(X, t), t) J d\Omega_0 = \frac{d}{dt} \int_{\Omega_0} f(x, t) J d\Omega_0 \quad (\text{AI-6})$$

As the initial configuration is time independent Eq. (AI-6) can be simplified as

$$\begin{aligned}
\frac{d}{dt} \int_{\Omega} f(x,t) d\Omega &= \int_{\Omega_0} \frac{d(f(x,t)J)}{dt} d\Omega_0 = \int_{\Omega_0} \left[\frac{df(x,t)}{dt} J + \frac{dJ}{dt} f(x,t) \right] d\Omega_0 = \\
\int_{\Omega_0} \left[\frac{df(x,t)}{dt} J + \operatorname{div}(v) J f(x,t) \right] d\Omega_0 &= \int_{\Omega_0} J \left[\frac{df(x,t)}{dt} + \operatorname{div}(v) f(x,t) \right] d\Omega_0 = \quad (A1-7) \\
\int_{\Omega} \left[\frac{df(x,t)}{dt} + \operatorname{div}(v) f(x,t) \right] d\Omega
\end{aligned}$$

Appendix II Derivatives of tangent modulus based on Flory's constitutive law

Tangent modulus derivatives based on the Flory's theory:

Formulation of a numerical approach for inhomogeneous swelling is inevitable. Therefore, rate form constitutive law has been derived below based on work done by M. K. Kang and R. Huang that is following the work done by Hong et al. based on the Flory's theory.

Flory has suggested the below functional form of Energy, in which the first term is related to the elastic free energy density which is a function of deformation gradient tensor F . The second term on the right hand side of Eq. is due to free energy of mixing that is a function of solvent concentration C .

$$U(F, C) = U_e(F) + U_m(C) \quad (\text{AII-1})$$

M. K. Kang and R. Huang (2010) based on the statistical mechanics model of rubber elasticity, suggested an elastic free energy density and free energy of mixing for hydrogels based on Flory's work.

$$u_e(F) = \frac{1}{2} Nk_B T [\lambda_1^2 + \lambda_2^2 + \lambda_3^2 - 3 - \ln(\lambda_1 \lambda_2 \lambda_3)] \quad (\text{AII-2})$$

$$u_m(C) = \frac{\Delta F_m}{V_0} = \frac{k_B T}{\nu} \left(\nu C \ln \frac{\nu C}{1 + \nu C} + \frac{\chi \nu C}{1 + \nu C} \right) \quad (\text{AII-3})$$

Note that the principal stretches $\lambda_1, \lambda_2, \lambda_3$ in equation (AII-2) and are defined with respect to the dry state as the reference, which assume to be isotropic. And χ is a dimensionless quantity that characterizes the interaction energy between the solvent and polymer.

A Legendre transformation of the free energy density function is introduced by M. K. Kang and R. Huang (2010).

$$\hat{U}(F, \mu) = U(F, C) - \mu C \quad (\text{AII-4})$$

In which, μ is the chemical potential which is again suggested by M. K. Kang and R. Huang (2010) in Eq. (AII-5)

$$\mu = \frac{\partial u}{\partial C} = k_B T \left[\ln \frac{\nu C}{1 + \nu C} + \frac{1}{1 + \nu C} + \frac{\chi}{(1 + \nu C)^2} + N\nu \left(\frac{1}{\lambda} - \frac{1}{\lambda^3} \right) \right] \quad (\text{AII-5})$$

Therefore, by substituting Eq. (AII-2), Eq. (AII-3) and Eq. (AII-5) as well as $C = (J - 1)/\nu$ into Eq. (AII-4) the Legendre transformation can be written as

$$\hat{U}(F, \mu) = \frac{1}{2} N k_B T (I - 3 - 2 \ln J) + \frac{k_B T}{\nu} \left[(J - 1) \ln \frac{J - 1}{J} + \chi \frac{J - 1}{J} \right] - \frac{\mu}{\nu} (J - 1) \quad (\text{AII-6})$$

Where $I = F_{ik} F_{ik}$. The suggested method needs a long derivation for the true (Cauchy) stress and its variation with respect to the current state in terms of a fourth-order tangent modulus tensor.

The nominal stress is given in Eq. (AII-7)

$$s_{ik} = \frac{\partial \hat{U}}{\partial F_{ik}} = \frac{\partial \hat{U}}{\partial I} \frac{\partial I}{\partial F_{ik}} + \frac{\partial \hat{U}}{\partial J} \frac{\partial J}{\partial F_{ik}} \quad (\text{AII-7})$$

According to the literature, the Kirchhoff stress is

$$J \sigma_{ij} = s_{ik} F_{jk} = \left(\frac{\partial \hat{U}}{\partial I} \frac{\partial I}{\partial F_{ik}} + \frac{\partial \hat{U}}{\partial J} \frac{\partial J}{\partial F_{ik}} \right) F_{jk} \quad (\text{AII-8})$$

Where, σ_{ij} is the true stress at the current state. Hence, by using the free energy function that was defined in Eq. (AII-4)

$$\frac{\partial \hat{U}}{\partial I} = \frac{1}{2} N k_B T \quad (\text{AII-9})$$

$$\frac{\partial \hat{U}}{\partial J} = \left[-\frac{1}{J} + \frac{1}{N\nu} \left(\ln \frac{J - 1}{J} + \frac{1}{J} + \frac{\chi}{J^2} - \frac{\mu}{k_B T} \right) \right] \quad (\text{AII-10})$$

Also, it can be shown that

$$\frac{\partial I}{\partial F_{ik}} = 2 F_{ik} \quad (\text{AII-11})$$

$$\frac{\partial J}{\partial F_{ik}} = \frac{1}{2} e_{ijk} e_{KQR} F_{jQ} F_{kR} \quad (\text{AII-12})$$

Hence, by substituting Eq. (AII-9), (AII-10), (AII-11) and (AII-12) into Eq. (AII-8) an explicit formula for the true stress can be obtained as

$$\sigma_{ij} = Nk_B T \left[J^{-1/3} \bar{B}_{ij} + \frac{\delta_{ij}}{N\nu} \left(\ln \frac{J-1}{J} + \frac{1-N\nu}{J} + \frac{\chi}{J^2} - \frac{\mu}{k_B T} \right) \right] \quad (\text{AII-13})$$

Where, $\bar{B}_{ij} = J^{-2/3} F_{ik} F_{jk}$ is the deviatoric stretch tensor and δ_{ij} is the Kronecker's delta.

The variation of the Kirchhoff stress gives that

$$\delta(J\sigma_{ij}) = Nk_B T \left[\frac{2}{3} J^{-1/3} \bar{B}_{ij} \delta J + J^{2/3} \delta \bar{B}_{ij} + \frac{\delta_{ij}}{N\nu} \left(\ln \frac{J-1}{J} + \frac{1}{J-1} - \frac{\chi}{J^2} - \frac{\mu}{k_B T} \right) \delta J \right] \quad (\text{AII-14})$$

It can be shown that

$$\delta J = J \delta D_{kk} \quad (\text{AII-15})$$

$$\delta \bar{B}_{ij} = H_{ijkl} \left(\delta D_{kl} - \frac{\delta_{kl}}{3} \delta D_{mm} \right) + \bar{B}_{kj} \delta W_{ik} - \bar{B}_{ik} \delta W_{kj} \quad (\text{AII-16})$$

$$\delta D_{ij} = \frac{1}{2} (\delta L_{ij} + \delta L_{ji}) \quad (\text{AII-17})$$

$$\delta W_{ij} = \frac{1}{2} (\delta L_{ij} - \delta L_{ji}) \quad (\text{AII-18})$$

$$\delta L_{ij} = \frac{\partial}{\partial x_j} (\delta u_i) \quad (\text{AII-19})$$

$$H_{ijkl} = \frac{1}{2} (\bar{B}_{jl} \delta_{ik} + \bar{B}_{ik} \delta_{jl} + \bar{B}_{jk} \delta_{il} + \bar{B}_{il} \delta_{jk}) \quad (\text{AII-20})$$

In the above equations, δu_i is the variation displacement, δD_{ij} is the symmetric part of the deformation gradient, and δW_{ij} is the antisymmetric part (spin). It should be noticed that, all the above quantities are variational quantities with respect to the current state.

Therefore, Eq. (AII-14) can be written as

$$\delta(J\sigma_{ij}) = J C_{ijkl} \delta D_{kl} + J (\sigma_{kj} \delta W_{ik} - \sigma_{ik} \delta W_{kj}) \quad (\text{AII-21})$$

The second term on the right hand side of Eq. (AII-21) represent the rotation of the local coordinates. From Eq. (AII-21) an explicit formula for the tangent modulus tensor at the current state can be obtained as

$$C_{ijkl} = Nk_B T [J^{-1/3} H_{ijkl} + \frac{1}{N_V} (\ln \frac{J-1}{J} + \frac{1}{J-1} - \frac{\chi}{J^2} - \frac{\mu}{k_B T}) \delta_{ij} \delta_{kl}] \quad (\text{AII-22})$$

The second term on the right hand side of Eq. (AII-22) represent the rotation of the local coordinates. The first term on the right hand side of Eq. (AII-22) gives tangent modulus for an incompressible neo-Hookean material.

Appendix III Expected value of a function of random variable

It is assumed that X is a random variable defined on a probability space (Ω, F, P) .

Hence, $E[X]$ is signified as the expected value of the random value X that is defined as Lebesgue integral.

$$\mu = E[X] = \int_{\Omega} X(\omega) \cdot P(d\omega) \tag{AIII-1}$$

If $f(x)$ is an admitted probability function of X , then

$$\mu = E[X] = \int_{-\infty}^{\infty} x \cdot f(x) dx \tag{AIII-2}$$

With this introduction, the normal (Gaussian) distribution $N(\mu, \sigma)$ can be defined by its probability density function,

$$f(x) = \frac{1}{(2\pi)^{1/2} \sigma} e^{-\frac{(x-\mu)^2}{2\sigma^2}} \tag{AIII-3}$$

In which $x \in R$, μ is the mean value of the volumetric strain and σ is the standard deviation. For a case of $\mu = 0$ and $\sigma = 1$ the distribution graph is shown in Fig. AIII-1.

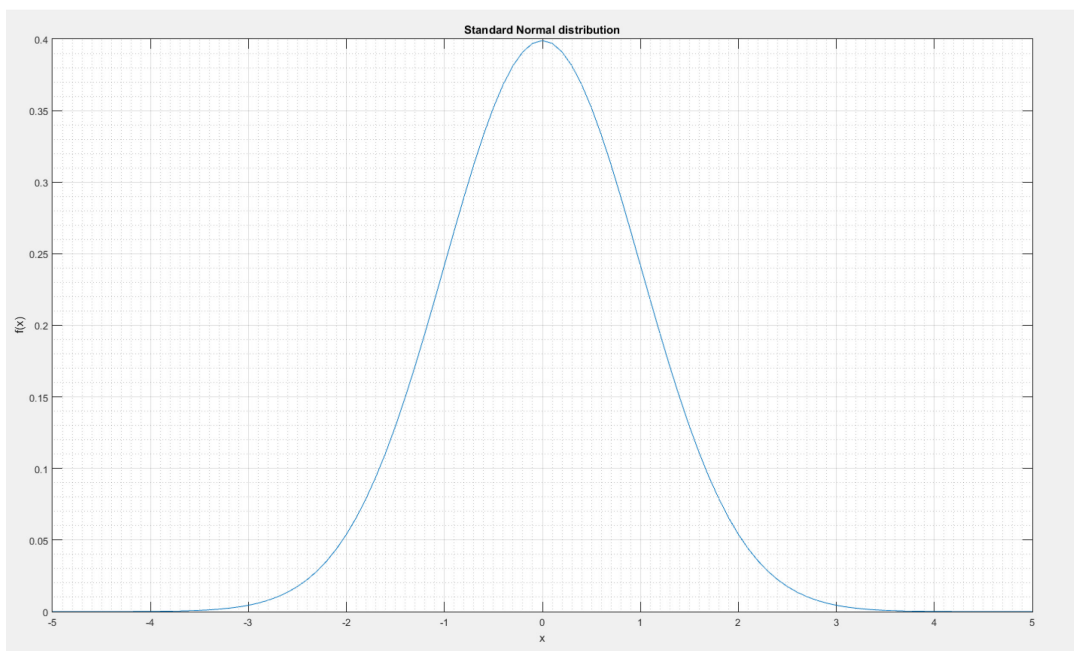


Fig. AIII-1 Standard normal distribution, $\mu = 0$ and $\sigma = 1$.

So, in this case the probability density function will be reduced to

$$f(x) = \frac{1}{(2\pi)^{1/2}} e^{-\frac{x^2}{2}} \quad (\text{AIII-4})$$

First, it should be proved that $f(x)$ is a probability density function,

$$\int_{-\infty}^{\infty} f(x) dx = \frac{1}{(2\pi)^{1/2}} \int_{-\infty}^{\infty} e^{-\frac{x^2}{2}} dx = 1 \quad (\text{AIII-5})$$

In order to prove Eq. (AIII-5), let

$$I = \int_{-\infty}^{\infty} e^{-\frac{x^2}{2}} dx \quad (\text{AIII-6})$$

Therefore,

$$I^2 = \left(\int_{-\infty}^{\infty} e^{-\frac{x^2}{2}} dx \right) \cdot \left(\int_{-\infty}^{\infty} e^{-\frac{y^2}{2}} dx \right) = \int_{R^2} e^{-\frac{x^2+y^2}{2}} dx \cdot dy \quad (\text{AIII-7})$$

Next, by converting Eq. (AIII-7) to polar coordinates and substituting $x = \rho \cos \theta$, $y = \rho \sin \theta$, and the Jacobian determinant $J(\rho, \theta)$ is shown in Eq. (AIII-8)

$$J(\rho, \theta) = \begin{vmatrix} \frac{\partial x}{\partial \rho} & \frac{\partial x}{\partial \theta} \\ \frac{\partial y}{\partial \rho} & \frac{\partial y}{\partial \theta} \end{vmatrix} = \begin{vmatrix} \frac{\partial \rho \cos \theta}{\partial \rho} & \frac{\partial \rho \cos \theta}{\partial \theta} \\ \frac{\partial \rho \sin \theta}{\partial \rho} & \frac{\partial \rho \sin \theta}{\partial \theta} \end{vmatrix} = \begin{vmatrix} \cos \theta & -\rho \sin \theta \\ \sin \theta & \rho \cos \theta \end{vmatrix} = \rho \cos^2 \theta + \rho \sin^2 \theta = \rho \quad (\text{AIII-8})$$

Therefore Eq. (AIII-7) can be written as,

$$I^2 = \left(\int_0^{2\pi} d\theta \right) \cdot \left(\int_0^{\infty} e^{-\frac{\rho^2}{2}} |J(\rho, \theta)| d\rho \right) = 2\pi \cdot \int_0^{\infty} \left(e^{-\frac{\rho^2}{2}} \right) \rho d\rho = 2\pi \quad (\text{AIII-9})$$

Hence, $I = (2\pi)^{1/2}$ and it leads to $\int_{-\infty}^{\infty} f(x) dx = 1$. In a general case, by substituting

$\eta = \frac{x - \mu}{\sigma}$ into Eq. (AIII-3), the same result will be obtained.

Now, let $\eta = \frac{x - \mu}{\sigma}$ also it can be shown $dx = \sigma d\eta$ therefore,

$$\begin{aligned} E[X] &= \int_{-\infty}^{\infty} xf(x)dx = \frac{1}{(2\pi)^{1/2}\sigma} \int_{-\infty}^{\infty} xe^{-\frac{(x-\mu)^2}{2\sigma^2}} dx = \frac{1}{(2\pi)^{1/2}\sigma} \int_{-\infty}^{\infty} (\sigma\eta + \mu)e^{-\frac{\eta^2}{2}} \sigma d\eta \\ &= \frac{\sigma}{(2\pi)^{1/2}} \int_{-\infty}^{\infty} \eta e^{-\frac{\eta^2}{2}} d\eta + \mu \left(\frac{1}{(2\pi)^{1/2}} \int_{-\infty}^{\infty} e^{-\frac{\eta^2}{2}} d\eta \right) \\ &= 0 + \mu = \mu \end{aligned} \tag{AIII-10}$$

Therefore, Eq. (AIII-10) proves that $f(x)$ is an admitted probability function.